UNIVERSITY OF SOUTHAMPTON

AC electrokinetic analysis of chemically modified microparticles

By

Diego Morganti

A thesis submitted in partial fulfilment for the
degree of Doctor of Philosophy

In the

Faculty of Physical and Applied Sciences
School of Electronics and Computer Science

UNIVERSITY OF SOUTHAMPTON

<u>ABSTRACT</u>

FACULTY OF PHYSICAL AND APPLIED SCIENCES

SCHOOL OF ELECTRONICS AND COMPUTER SCIENCE

<u>Doctor of Philosophy</u>

By Diego Morganti

Electrokinetic manipulation offers a flexible and versatile tool to analyse and precisely handle microparticles, it is non invasive and can be easily implemented in microfluidic devices. Those characteristics make the electrokinetic methods appealing in the field of medical diagnostics because of their ability to perform analysis on a single particle basis, for example to detect binding events of biomolecules such as antibodies and nucleic acids. The detection is performed without fluorescent tags or chemical modifications, because it uses the electrical properties of the surface of the particles as label. The aim of this project is to study the electrical properties of microparticles according to the chemical properties of their surface using electrokinetic on a single particle basis.

A new method to analyse single particles that relies on electrorotation and electroorientation has been introduced. Using quadrupolar electrodes it has been possible to obtain both spectra for the same particle allowing a combined fitting of the data. Rod shaped particles have been analysed after each step of the biochemical modifications needed to obtain a surface functionalised with antibodies. We found that the chemical modifications happen mostly in the bulk of the particles, therefore not many charges were available onto the surface. Anyway, it has been possible to distinguish different types of particles using the surface conductance of the particles and their permittivity.

Along with biochemically modified particles, also metal coated particles have been analysed to study the electrical double layer under different conditions, like different suspending medium conductivities and surface functionalisations. Particles of different shapes were metal coated with gold after a suitable chemical modification to sensitize their surface. The gold coating is an autocatalytic electroless process; therefore it has been used to plate particles in suspension without the need of an external current source. Metal coated particles' behaviour is dominated by the double layer at low frequency, but the results are only in qualitative accord with the theory due to the roughness of the metal surface.

Table of Contents

List of Figures

List of Tables

List of Chemical Reactions

Declaration of authorship

I, Diego Morganti declare that the thesis entitled AC Electrokinetic analysis of chemically modified microparticles and the work presented in the thesis are both my own, and have been generated by me as the result of my own original research. I confirm that:

- this work was done wholly or mainly while in candidature for a research degree at this University;
- where any part of this thesis has previously been submitted for a degree or any other qualification at this University or any other institution, this has been clearly stated;
- where I have consulted the published work of others, this is always clearly attributed;
- where I have quoted from the work of others, the source is always given. With the exception of such quotations, this thesis is entirely my own work;
- I have acknowledged all main sources of help;
- where the thesis is based on work done by myself jointly with others, I have made clear exactly what was done by others and what I have contributed myself;
- parts of this work have been published in number of publications (see Appendix 1 for a list)

Signed: ……………………………………………………………………….

Date:………………………………………………………………………

Acknowledgements

Here it comes the moment of the acknowledgements...

I would like first to thank Prof. Hywel Morgan for have me allowed to work in the excellent facilities of the University of Southampton. It has been a wonderful experience I will never forget. I would like also to thank him for make me understand what working in the Academia really is and how to do research. Then I would like to say thank you to all my past (!) colleagues for the amazing time and conversations and lunches... and for course for all your help at work! You really helped me growing up professionally.

In the second paragraph I usually thank friends. I will not change that tradition, therefore here I will express gratitude to all the amazing friends I made here in UK, but especially to Marta, Barbara and Simone. They managed to cheer me up when I was feeling down and really helped me in growing up as a person.

Of course I am very grateful to my parents for putting up with my bad character and helping me in the moments of need. You are all in my heart.

I will not forget to express my gratitude to my amazing boyfriend Raul, which got to know me in a moment were I was hyper-stressed and probably not at my (social) best. You always find a way to cheer me up.

Finally I want to say thanks and dedicate this work to Me. Myself and I, with the advice of thinking twice before doing things. We went through a lot and I do not want to stop now.

Chapter 1

Introduction

This work is concerned with the study of the motion of particles in alternating electric fields. This type of manipulation is called electrokinetics and in a more broad meaning can include also the manipulation of fluids using electric fields. In this chapter electrokinetics will be introduced through its different embodiments using DC or AC fields at high or low frequency. DC electrokinetics refers to electrophoresis and Quincke rotation, which refers to the translational motion of charged particles and rotation (respectively) in a DC electric field. AC electrokinetics uses AC electric fields to move particles, which has advantages because it explores a richer variety of frequency dependent behaviour in particles, along with reduced electrolysis at the electrodes. AC electrokinetics embraces many different effects but we shall confine our attention to dielectrophoresis (DEP), electroorientation (EO), electrorotation (ROT) and travelling wave dielectrophoresis (TW). An introduction to the phenomenology related to AC fields at low frequency will be provided.

Every object whose dimensions are less than 10^{-3} metres (Figure 1-1) is usually defined as particle. These objects exhibit specific electrical properties that depend on the shape, on the internal structure and on the composition. Those properties and the properties, both electrical and chemical, of the surrounding environment determine their behaviour in electric fields. In this context "particle electrokinetics" is the study of the forces and/or torques exerted on particles through the action of electric fields and the dynamics of the resultant motion. In the general case, the electric field can be imposed by external means or induced by other particles,
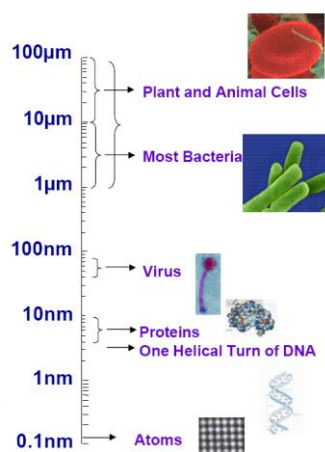
Figure 1-1. Sub-millimetre particles cover a wide range of object shapes and sizes, ranging from cells to viruses to atoms, each one in a specific range of dimensions. Electrokinetic analysis is typically applied to objects greater than 100 nm.

but for our purpose we will take into account just the case of external fields, either DC or AC fields.

1.1 Electrophoresis

It is common knowledge that a charged particle placed in an electric field will experience a Coulomb force that will push it along or against the electric field. This effect is known as electrophoresis and is now a common laboratory technique for separation of molecules based on their charge/mass. Electrophoresis (EP) is usually performed using two electrodes in a gel to allow a better separation between different species. The gel provides a molecular matrix with a certain retention power to "trap" molecules above a certain dimension that will experience a greater drag force than smaller particles. In a similar way particles with a larger charge will experience a stronger force and therefore will move more than less charged species. Different species can be identified by the distance they move in a given time (called *bands*). An example of a gel EP apparatus is shown in Figure 1-2.

Gel EP is commonly used to separate proteins and nucleic acids (DNA, RNA). Nucleic acids have a negatively charged backbone composed of phosphate groups and sugars, therefore will move towards the positive electrode. Proteins are instead usually denatured because their tertiary structure (how they are folded) can influence the drift due to the electric field. In this way they can be separated only on the basis of the molecular weight.
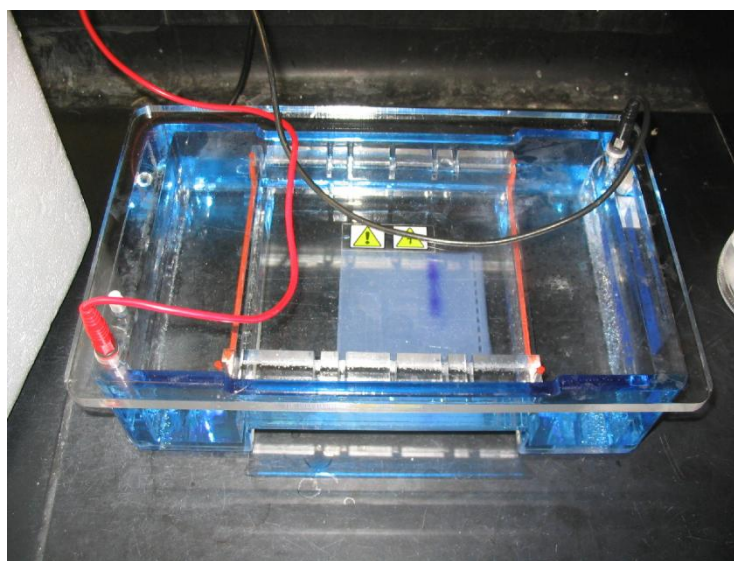
Figure 1-2. Electrophoresis apparatus[1]. The red and black leads connect the electrodes in the gel tray (blue) to the power supply (not shown). In this case the electric field goes from left to right.

The development of EP as separation method is credited to Smithies in the 1955 [1] and won him a Nobel Prize. EP as it is known today can be traced back to 1959 with the introduction of acrylamide gel as supporting medium for electrophoresis [2], and to the work of Weber and Osborn where they introduced SDS as denaturing agent for proteins [3]. Swartz and Cantor discovered a method to separate large DNA molecules using pulsed electric fields along different directions [4] and Görg introduced in 1988 a 2D EP method to separate proteins using a pH gradient to perform isoelectric focussing [5][6]. In a similar way, instead of using a gel, the fluid flow inside the lumen of a capillary tube can retard the movement of particles and allow separation based on charge and hydrodynamic radius. This separation technique is called capillary electrophoresis and depends on the fluid flow generated in a glass capillary by a DC electric field acting on the counter-charges in the electrolyte accumulated at the charged wall. This technique can be downscaled to perform capillary electrophoresis in 10 μm wide channels etched in glass [7]. A recent review on this subject has been published [8]. Electrophoresis is not strictly relevant to this work but it provides a simple model from which to start the discussion on AC electrokinetics, which will be developed in Chapter 2.

1.2 Dielectrophoresis (DEP)

The term dielectrophoresis (DEP) was coined by Pohl in 1951 [9] to define the motion of polarisable particles (charged or uncharged) in a non-uniform alternating electric field. The cause of this motion is the polarization induced by the electric field in the particle and

---

[1] http://www-che.syr.edu/faculty/boddy_group/pages/electrophoresis.jpg, found on 6/3/2011

depends on many parameters such as the electric field non-uniformity, and the dielectric properties of medium and particle [10]. Uncharged particles will not move in a uniform electric field because the force acting on each of the parts of the induced dipole is the same but opposite in direction. In the case of a spatially non-uniform electric field, the two forces are no longer balanced and this gives rise to a net force acting on the particle. The direction of this force depends on the frequency and the electrical properties of the particle/medium system. According to the behaviour of the particles, we have positive DEP (pDEP) when they are attracted to the high electric field strength or negative DEP (nDEP) when they are driven towards low strength electric field regions. The behaviour of sub-micrometre particles depends largely on their surface properties [11][12], which means that DEP can be used to investigate and measure changes in the composition of particle surfaces like binding of antibodies [13][14].

Many different electrode shapes have been used in the literature, but the more frequent types are the castellated electrodes [15][16] and the interdigitated electrodes [17] as shown in Figure 1-3. Particles can accumulate at the edges of the electrodes (positive DEP) or in regions of low electric field gradient (negative DEP), according to their properties. In this regard the castellated electrodes are more useful as they have closed regions (the "bays" of the electrodes) where particles experiencing negative DEP can be trapped. While the castellated and interdigitated electrodes can be arranged easily in extended arrays, the quadrupolar electrodes (Figure 1-3c) are usually used in *stand alone* configuration because of the need for four electrical contacts. Many shapes of electrodes have been studied in order to obtain a field gradient as homogeneous as possible [18] and the best choice are the polynomial electrodes which have a hyperbolic shape [19] and produce a quadratic electric field gradient in the centre.
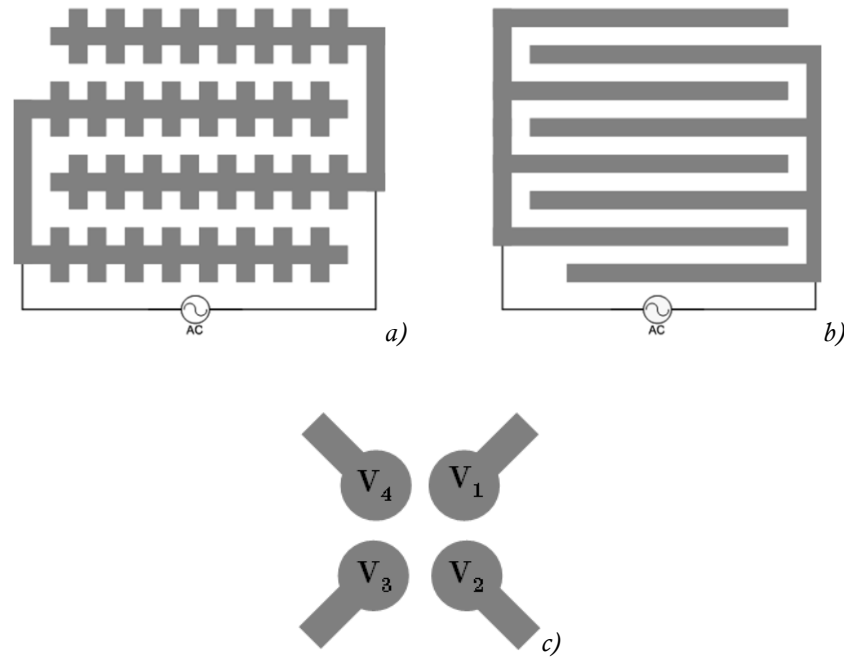
Figure 1-3. Schematic representation of a) interdigitated castellated electrodes, b) interdigitated linear electrodes and c) quadrupolar electrodes (the four electrodes have an AC electric signal with different phase applied to each electrode). They are usually fabricated with titanium and gold patterned on a glass substrate with characteristic dimensions in the micrometer range.

Because dielectrophoresis is a non-invasive technique, it has been widely used in biophysics and medical research on living cells. Its applications span from separation of cancer cells from blood cells [15] or sorting labelled cells [20] to trapping nanotubes in order to build gas sensors [21]. DEP has always been a very versatile technique, in particular in the lab-on-a-chip framework, where in a chip of a few square centimetres we want to place a complete set of tools to analyse particles, with microfluidic channels (to handle the suspending fluid with the particles within), and sorting and focussing elements. In this context particles are usually focussed in a narrow line to allow easier sorting and analysis on a single particle basis. nDEP has been used to focus particles in the middle of a microfluidic channel using a set of 4 electrodes as shown in [22]-[24]. The difference between hydrodynamic focussing and focussing based on nDEP is shown in Figure 1-4: DEP can confine the particles in the middle of the channel, while traditional hydrodynamic focussing only confines in the horizontal axis. Hydrodynamic 2D focussing can be achieved by means of more complicated devices [25][26] while DEP focussing only requires electrodes on the top and bottom of the channel. From that point of view the DEP focussing is more efficient and can be achieved with simple devices.
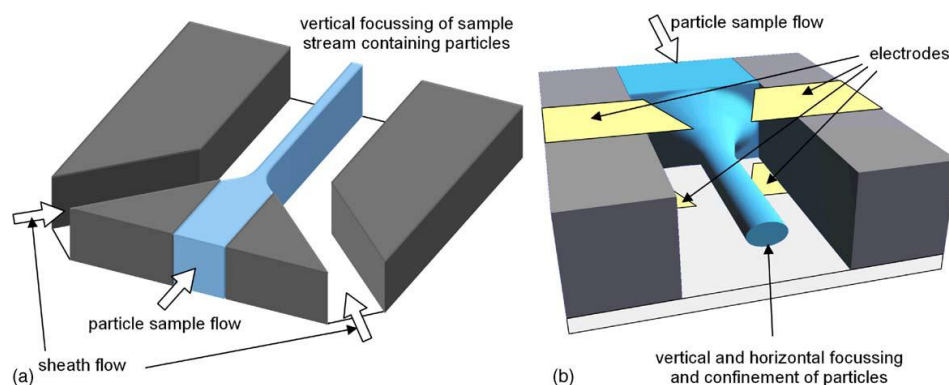
Figure 1-4. Different focussing methods of particles in a microfluidic channel. a) Standard hydrodynamic focussing using two sheet flows compresses the central stream with the particles to focus only in the horizontal plane while in b) nDEP from the electrodes allows to focus the particles in a narrow stream in the middle of the channel. Image taken from [22].

Analysis of isolated particles in microfluidic devices is usually performed using electrorotation with quadrupolar electrodes (see Figure 1-3c) as explained in Section 1.4 but is not common due to the amount of time (and processing of data) required to analyze large numbers of particles.

DEP has been used to obtain the electrical properties of microparticles studying their motion in AC electric fields to obtain DEP spectra. One possible way to achieve that is looking at the rate of change of the optical absorbance of a particle suspension when the particles – starting from being dispersed – collect in specific regions of the electrodes array [27][28]. The rate of change of the optical absorbance is related to DEP force, but this method only allows the analysis of particles in batches. Other methods have been presented in the literature, which allow the analysis of single particles. Kaler *et al.* presented a setup based on a needle and plane electrode pair which creates a non-homogeneous AC electric field able to make particle levitate. The height of the particle depends on the competitive contribution of DEP force and gravity, and allows the acquisition of single particle DEP spectra [29][30]. Single particle spectra can be acquired also using quadrupolar electrodes and measuring the time a particle takes to move between two ideal concentric circles cantered in the electrode array [31][32]. In this case the speed is directly related to the DEP force and no other forces are involved.

Particle separation using DEP is more commonly used to characterize particles flowing in a channel, and thereby to sort them. Usually two different strategies are used to separate two populations: one population experiences pDEP while the other nDEP, in this case the first one is retained on the electrodes (for example castellated electrodes [15]) while the second can flow freely in the channel, or both populations experience nDEP to a different degree. The use of interdigitated electrodes in the channel at an angle with respect to the stream lines will

cause the two populations to slowly separate into two different streams [33]. The second method works better because there is no crowding of particles on the electrodes, limiting the number of particles that can be trapped efficiently: both populations flow freely therefore continuous separation occurs.

One of the major problems with very early applications of DEP was the need for large applied voltages in order to effectively move the particles. This limitation was overcome by fabricating smaller electrodes and therefore creating stronger electric field gradients comparable to the characteristic dimension of the particles under investigation, hence achieving DEP with applied voltages of the order of the volt. Submicron particles are subject to Brownian motion, a stochastic motion caused by their interaction with the molecules of the surrounding fluid, which can counteract the DEP. This problem has been solved by scaling down the electrodes to increase even more the electric field gradients and therefore the strength of the DEP force. Through the use of micrometer scale electrodes, submicron particle such as viruses and nanoparticles can be manipulated [34].

1.3 Electroorientation (EO)

Electroorientation (EO) is the alignment of a particle in a steady homogeneous (AC) electric field. To observe EO it is necessary that the analysed particles are anisotropic, which means that one (or more) of their physical or electrical properties are different along different axes. This means that the induced dipole moment is greater along one axis than the others, causing the particle to align in the field. This orientation is frequency dependent and depends on the electrical properties of the particles, shape, surface, conductivity and structure [35] and can lead to a parallel or perpendicular alignment to the electric field as shown in Figure 1-5. Unlike DEP no gradient in the electric field is needed because the electric forces acting on the two halves of the dipole create a torque. Traditionally only the points where no orientation is observed are studied, that is the frequency of the applied AC electric field at which the polarization is the same along perpendicular axes. This method is not used usually on a single particle basis and needs to be coupled to electrorotation measurements in order to produce quantitative data.
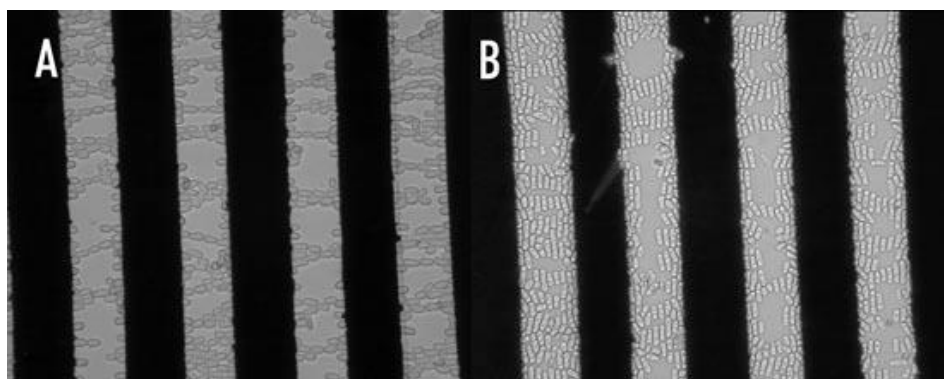
Figure 1-5. Electroorientation of yeast cells. The electrodes used had a spacing and width of 40µm; the applied voltage was 10Vpp. a) Orientation along electric field lines at 1MHz; b) Orientation perpendicular to electric field at 50MHz. Image taken from [36].

First measurements of the orientational behaviour of elongated particles were carried out in 1948 on salt crystals [37]. The first observation of frequency-dependent orientation of cells like protists and bacteria dates from 1960 [38] since then, many other cells have been studied. For example, Griffin studied human and avian red blood cells [39] and Miller and Jones [40] ellipsoidal erythrocytes. They used the points of zero orientation at different suspending medium conductivities to determine the internal conductivity of the cell. *Schizosaccharomyces pombe*, a yeast, has been extensively studied with this method because of its elongated shape [41]-[43]. *S. pombe* has also been studied by Kriegmaier [44] where electroorientation and electrorotation are used at the same time to estimate cell electrical properties: the method used for electroorientation consists of mapping the orientation of the particles at different medium conductivities in order to define the points of zero orientation. Bacteria have also been studied [45], particularly under different chemical stresses [46]-[48] or to study the effect of antibody binding on their electrical properties [49][50]. Also retinal receptors [51] have been studied, along with cellular substructures like mitochondria in different states [52] and microtubules [53]. The latter is the only work in the literature that tries to use the actual alignment torque of the particles instead of using the points of zero alignment in order to determine the microtubules electrical properties. The experimental approach is based on the analysis of videos of the particles moving at different frequencies, and estimation of the frequency of no movement. Some groups tried a more simple batch analysis using the change in absorbance of the dispersed (elongated) particles using a polarized light [54][55].

DEP and EO can occur at the same time for elongated/asymmetric particles, while for symmetric particles only DEP occurs. In this case particles can be trapped in regions of high electric field density forming biofilms [56], structures called by some authors *microniches* [57][58], replicating structures found in nature. EO (with DEP) can provide a useful tool to build cell structures more similar to their natural environment, e.g. referece [59] where the
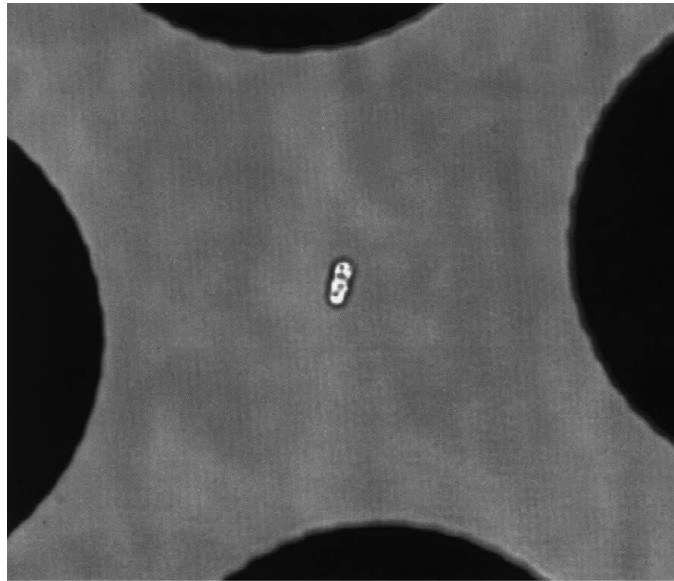
Figure 1-6. Image of a cell of S. pombe in an ROT chamber consisting of four circular microelectrodes. The distance between the opposite electrodes is 100 μm. Taken from [44].

authors assembled a tissue-like structure using cardiac myocytes. Reviews on tissue engineering have been published by Markx [36] and Alp *et al.* [60]. EO and DEP has also been used to form three-dimensional interconnections of carbon nanotubes [61]. However, electroorientation is not often used for characterization of particle properties.

1.4 Electrorotation (ROT)

Electrorotation (ROT) is the rotation of a particle induced by an electric field with directional non-uniformity. The electric field induces a dipole whose direction follows the applied electric field with a lag that depends on the frequency and the electrical properties of the system. This lag causes a torque and makes the particle rotate. ROT can be seen on particles of any shape, unlike EO. The motion is asynchronous and it can be against or with the electric field rotation, according to the frequency of the rotating field and the electrical properties of the system.

Usually in order to measure ROT a homogeneous rotating electric field is used. Like DEP and EO, ROT depends on size and shape [35][62] but also on internal and surface properties of the particles. Because of this, ROT has been extensively used to study cells and characterize their internal structure, which is accessible only at high frequencies due to the capacitive shielding effect of the cell membrane. The analysis of the motion of the particles is usually simpler than in the case of DEP because the rotation is constant (for a given frequency and voltage) and usually the particle is trapped by nDEP in the middle of the quadrupole

electrodes (see Figure 1-6), allowing longer measurements to be taken. The quadrupolar nDEP trap is not closed and it resembles a funnel, therefore gravity is needed to counteract the force pushing the particle up away from the electrodes and keep it contained. The popular choice of 4 electrodes is also not related to the performance of trap itself, as it is possible to use any arbitrary number (bigger than 2) of electrodes to create a rotating electric field using the correct phase shift between different channels. More electrodes should give a more homogeneous field over a larger area, but usually the choice of 4 electrodes is adequate. Commercially available function generators used to apply the electric signal to the electrodes usually have 4 output channels.

An improvement is the octupolar configuration [57]: two sets of quadrupolar electrodes are place opposite each other at the top and the bottom of a microfluidic channel, defining a 3D trap which does not rely on gravity. Fabrication of this type of devices is more complicated as a micrometer scale alignment of the electrodes is required but that is easily reachable with cleanroom microfabrication methods. Research on using the octupolar electrodes are been published by Fuhr's group [63][64][65], where they noted that breaking the symmetry of the octupolar cage can lead to a more efficient functioning. The cage is showed in Figure 1-7.

The first observation of small particles rotating in a rotating electric field dates from 1892 [66]. Early experiments were aimed at investigating the theoretical background needed to interpret the particle behaviour in a rotating electric field. The theoretical framework that is now widely accepted relies on the so called surface conductance of the particle [67][68], which is a measure of how easily charges can move along the particle surface. A great deal of work has also been done on electrode geometries and their characterization, showing that polynomial electrodes produce a more homogeneous rotating electric field [18][69][70]. Different groups also tried to combine different types of electrodes (i.e. DEP, ROT, etc.) on the same device [71][72] in order to improve the overall performance.

Figure 1-7. A cell trapped in an octupolar cage with broken symmetry. The electrodes are patterned on the top and bottom of a 40 μm deep channel, and their planes have been twisted by 20 degrees. The bar is 100 μm. Image taken from [64].

Since 1980, the field has mostly concentrated on cell study and manipulation. In particular scientists used electrorotation to study the electrical properties of many different type of cell, for example plant protoplasts [73], erythrocytes [74] or parasites [75], with the aim of measuring their biophysical properties in different conditions. This trend continues and it is possible to find studies on algal cells [76] or yeast cells [44]. The latter paper represents a good example of how to use electrorotation (and electroorientation). Cells have two relaxations, related respectively to the membrane and cytoplasm properties. From the position of the peaks at different suspending medium conductivities it is possible to evaluate electrical parameters like membrane capacitance and conductance. The majority of the work is aimed at studying how their electrical properties (especially the membrane conductance and capacitance [77]) change under different conditions, like electric fields [78], nanoparticles [79][80], or various chemical compounds [81]-[84] mostly using a simpler version of the same method as described in reference [44]. ROT was presented for the first time by Arnold and Zimmerman [85], and it is widely used to study cells because it allows the determination of membrane capacitance and membrane conductance without the need to fit a full ROT spectrum. A large number of measurements is taken at different medium conductivities to produce a mean value for the membrane conductance and capacitance. This method works because at low suspending medium conductivities (1 – 4 mS/m) the position of the low frequency electrorotation peak times the radius of the particle is proportional to the medium conductivity. In this thesis a different approach was chosen to perform single particle measurements: ROT and EO were performed simultaneously on the same particle in order to perform a full fit of the data.

1.5 Quincke rotation (QR)

Quincke rotation (QR) refers to the spontaneous rotations of small cylindrical or spherical object suspended in a dielectric when subjected to a strong DC electric field. Unlike ROT, QR has a threshold in the strength of the applied electric field below which no motion is observed. Moreover the threshold itself depends on the electric properties of particle and medium (permittivity and conductivity) and in some case may not exist at all. The direction of the rotation is random, but the rotation axis always lays in a plane perpendicular to the electric field. The origin of this break in the symmetry of the system is due to the accumulation of charges at opposite poles of the particles forming an induced dipole. Under particular conditions this induced dipole can have an orientation opposite to the electric field (see Figure 1-8) and therefore the particle will be in a condition of unstable equilibrium and will start to move after any small perturbation of the equilibrium. Once the movement starts the dipole will reform again opposite to the electric field driving the rotation in the same direction and repeating the cycle.
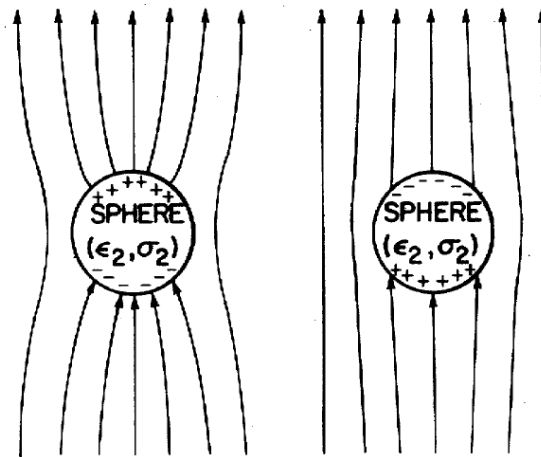
Figure 1-8. Schematic representation of the condition for QR (right) and no QR (left). When the induced dipole is aligned to the electric field there is no torque acting on the particle. When it is formed opposite to the direction of the electric field the particle is in a condition of unstable equilibrium and a torque will appear. Image taken from [86].

The first observation of this phenomenon was in 1896, when Quincke reported small spherical objects rotating in DC electric fields [87]. The first to propose the correct explanation for the movement was Lampa [88], who related it to the charge relaxation time of particle and suspending dielectric. The phenomenon was rediscovered much later by Sumoto [89], whose work was a foundation for a paper from Secker where QR was used to create an electric motor [90][91]. It has been noted that QR of particles in a fluid can decrease viscosity [92] and increase conductivity [93] due to the fluid moved by the rotation of the particles. The theory of QR has been extended to the case where the double layer thickness cannot be
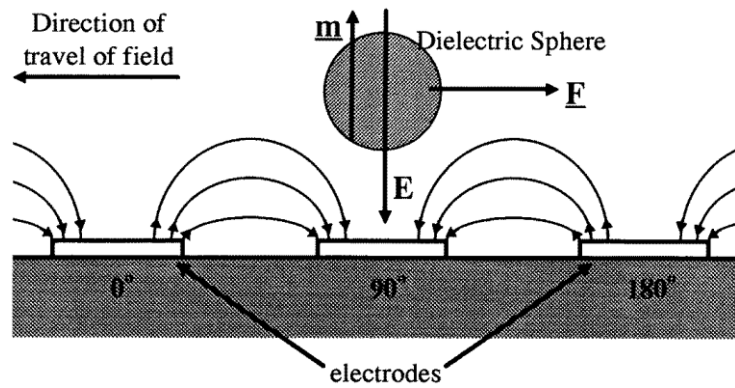
Figure 1-9. The diagram shows the different electrical forces acting on a particle in a travelling wave dielectrophoresis setup. The total force acting on the particle is a propelling force against the phase of the field. Only three of the four electrodes forming a basic building block are shown. Taken from [95].

ignored compared to the size of the particle. In that case the rotation of the particle is no longer independent of its size [94].

1.6 Travelling-wave dielectrophoresis (TW)

Travelling wave dielectrophoresis (TW) is conceptually close to ROT. In ROT the electrodes are arranged to wrap the phase of the AC signal on itself and produce a rotating electric field, while in TW the phase is unwrapped to obtain a wave moving in one direction. This effect can be achieved using a long series of linear electrodes which are energized with a 90 degree phase shift between following electrodes. In this particular arrangement the particles can experience DEP, pushing them towards or away from the electrodes, and another force in the direction (or against) of the travelling wave as suggested in Figure 1-9. This second force depends again (as in ROT) on the lag between the induced polarization in the particle and the electric field. In TW the force is no longer a torque but it has the effect of propelling the particle in one direction asynchronously with the electric field wave.

TW was described for the first time and used to separate small particles by Masuda *et al.* [96][97]. Since then, the main attraction of TW has been the possibility of separating populations of particles such as viable from non viable yeast cells [98], or red blood cells from white blood cells [95] using the different force experienced by different types of cells. The Morgan group has been active not only in developing TW applications but also on the theoretical characterization of TW electrodes [99]-[101]. TW devices were not only used in conjunction with electrowetting to concentrate samples in droplets [102], but also for manipulation of particles inside more complicated devices [103], where the TW plays the role of a conveyor belt to connect different parts of the device. Induced fluid flow can compete

with TW in moving the suspended particles, but it can also be exploited to act like a pump [104].

1.7 AC electrokinetics - Low frequency phenomena

The mechanisms involved in AC electrokinetics, such as DEP and ROT, rely on particle polarization at the interface with the suspending fluid. At low frequency that process may not show any torque because its characteristic time scale is in the MHz range. However the movement of charges in the liquid can give rise to another type of polarization in the sub-kHz range. At this frequency the electric field can interact with electrolytes giving rise to an asynchronous steady fluid flow.

Arnold *et al.* [67] noticed that the behaviour of spherical microparticles in a low frequency field was substantially different from the theory. Particles at low frequency experience another relaxation due to the concentration polarizant of the electrical double layer around the particle. In other terms, the electric field induces a change in the concentration of charges around the particle which causes asymmetry in the double layer. The characteristic time of this relaxation is the order of magnitude of the diffusion time of the charges in the electrical double layer around the particle. Therefore it is usually in the kHz range or lower, depending on the size of the particles. The general theory of this process has been developed by Grosse and Shilov [105], who showed that the total rotation is the sum of the rotation induced by the electric torque on the particle plus the rotation due to the fluid moving around the particle [106]. That theory is valid in the approximation of low voltages, which means a voltage drop across the particle lower than the thermal voltage of 25 mV.

For metallic particles the situation is more complicated, because the electric double layer can in fact screen the metallic surface making it appear as an insulator at low frequency [107], while at high frequency the electrical double layer does not have time to charge up, leaving the conductor exposed. For high voltages (>25 mV) and low frequencies, the electrical double layer is no longer stable and the ions moving from the bulk of the electrolyte generate a fluid flow. This fluid flow is generated by a non-uniformity of the electric field on the metal surface. At this point two scenarios are possible: the metal surfaces are in fact electrodes, or the metal structures are immersed in an electric field. The first case represents AC electroosmosis (ACEO) and has been investigated by studying the fluid flow generated by symmetric planar electrodes by Ramos *et al.* and Green *et al.* [108][109], where the fluid flow was mapped using fluorescent microparticles as shown in Figure 1-10a. Given that the fluid flow depends on the lateral dimensions of the electrodes, the same phenomenon was used to pump fluids using asymmetric electrodes [110][111], where the asymmetry gave rise to a steady flow in one particular direction. The second case has been called induced charge electroosmosis (ICEO) [107] by Squires and Bazant who defined the concept of ICEO to
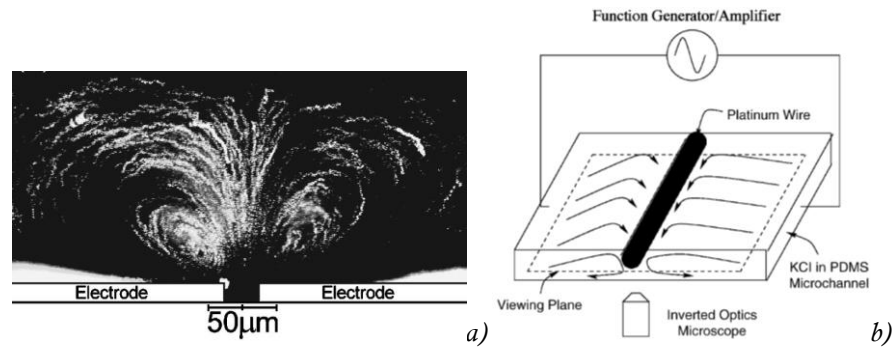
Figure 1-10. a) Composite image showing fluorescent particles moving because of AC electroosmosis. The image was obtained by superimposing successive video frames from the footage of the fluid flow generated by the electrodes, which were energized with a 2V at 100Hz AC signal. Picture taken from [103]. b) Schematic representation of the setup that Levitan et al. used to imagine ICEO generated by a metal wire in an electric field. Image taken from [112].

stress the small differences with ACEO. The two phenomena rely on a non-homogeneous distribution of charges to generate a fluid flow, though in two different ways. In the case of ACEO the metal structures (electrodes) are energised with an AC electric field. The field will not be homogeneous along all the surface of the electrodes giving rise to a non-homogeneous charge distribution and a fluid flow. In the case of ICEO the structures around which the flow is created are left floating while exposed to an external AC electric field, which induces a non-homogenous distribution of induced charges on the metal surfaces and therefore a fluid motion.

Bazant's group first work on ACEO [112] used a metal pillar lying flat on a surface (see Figure 1-10b) to obtain a flow. They presented a theoretical model to explain the fluid flow observed around metal structures such as pillars or other 3D structures [107][113] when exposed to a low frequency and high frequency electric field. Under this condition the electric field generates a non-homogeneous charge distribution on the metal structure and therefore an electric field which is not normal to the surface. Ions in the surrounding electrolyte move accordingly creating a fluid flow. Solid state pumping, i.e. pumping fluids with no moving parts, is a major subject of Bazant's group. 3D electrodes were developed to optimize the fluid flow [114][115]: electrodes of different sizes produce a fluid flow because the recirculation patterns in a specific direction are modified to produce a net flow as in Figure 1-11a. A more homogeneous flow can be achieved using 3D electrodes because the smaller recirculations are enclosed in a niche as shown in Figure 1-11b. Gangwal *et al.* studied the effect of breaking the symmetry on metal coated polymer microbeads (called Janus particles) [116]: having only half of the surface coated with metal caused the particle to move in a peculiar way in AC electric field. The Janus particles not only move with the usual rules seen for DEP, but can also move sideways because of ICEO.
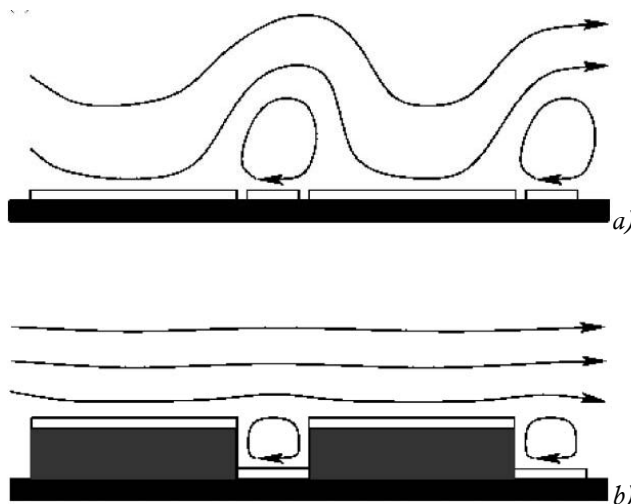
Figure 1-11. Difference between the flow above a) planar and b) 3D electrode configuration in ICEO pumping. In the 3D configuration (Fluid Conveyor Belt) the small counter rotating vortices above the smaller electrodes are not disturbing the fluid flow drive by the larger electrodes. Images taken from [114].

1.8 Electrokinetic methods as tool for biosensing

Biosensing is the detection of analytes using biological sensitive elements coupled with a physiochemical transducer/detector. Biosensors find application in many fields, for example the instrument to measure blood glucose levels is a biosensing device. In the context of this work, biosensing would be the detection of biomolecule binding events (for example nucleic acids or antibodies) to a functionalised substrate using electrokinetic methods. It has been shown in this Chapter that the electrokinetic methods (such as ROT and EO) are a versatile and flexible tools to study and manipulate particles on a single particle basis. They rely on the polarizability of the particles, which determines direction and speed of the motion. The addition of materials (for example biomolecules or cells) to the surface of particles changes their polarizability and therefore their electrokinetics behaviour. That leads to the idea of exploiting that change for biosensing. Some aspects of it have already been explored in the literature, for example Vykoukal *et al.* showed that adding different monolayers of long biomolecules to gold coated latex microspheres changes their DEP behaviour in a way that they can be differentially manipulated [117]. Adding proteins (IgG) to the surface of latex beads has been proved to change their electrokinetic behaviour, in a way that a mixture of beads and beads with proteins can be spatially separated by DEP [13][118]. Moreover Hughes *et al.* showed that adding antibodies and secondary antibodies to latex beads changed their surface charge [119]. Zhou *et al.* [120] and Hodgson *et al.* [121] showed that adding bacteria to the surface of latex beads changed the bead ROT spectra, and used that information to determine the viability of the bacteria itself. Not only latex beads but also cells were used as

substrate: Huang *et al.* changed the dielectrophoretic properties of *Salmonella* bacteria adding gold nanoparticles to their surface in order to separate them from *E. coli* using DEP [122].

1.8.1 Requirements for particles to be used in biosensing

The electrokinetic behaviour of a particle depends on their electrical properties – especially of their surface – but also on their structure. Particles with no inner structure and non-porous should be preferred as substrate because of the easier interpretation of their electrokinetic spectra. Non-living materials such as polymers offers an ideal substrate to develop a biosensing method using electrokinetics because their electrical properties represented in the electrokinetic spectra are "simple" due to the lack of internal structures [35]. Shelled particles such as cells have more complicated electrokinetic spectra and they can show up to one relaxation for each interface [123]. Polymeric particles and metal particles are therefore the best choice because of their simple structure.

Particles should be big enough to be captured by a common optical microscope but small enough to fit in the depth of field of a microscope objective if fluorescence measurements are to be taken: which means a lateral dimension of about 10 μm. This requirement rules out the commercially available metal particles, which usually are in the nanometre range.

Detecting the rotation of spherical objects is not an easy task for a computer or a human operator, therefore particle with an elongated shape should be preferred in order to develop an optimal biosensing method. Compared to spherical particles, elongated particles have the advantage that their rotation can be easily analysed and also they can be studied using ROT, EO as well as DEP. Simple polymeric elongated particles show only one orientation in AC electric fields (with the major axis aligned to the electric field) [53], while shelled elongated particles may have different orientations (any of the three principal axes aligned with the electric field) for different frequencies of the applied electric field [44]. The particles that are commercially available are spherical, therefore microfabrication is necessary to make particles with an elongated shape.

The microfabrication of particles relies on the use of photoresists to be patterned using photolithographic masks and UV light: the best choice among the photoresists used in the University of Southampton cleanroom is SU-8. That is due to the actual resolution achievable with photolithography, to the experience with the chemistry related to its modifications gained in the Morgan group and to the chemical resistance of the material itself, strong enough to withstand solvent based chemical reactions aimed at the functionalisation of the particle surface.

Polymers are usually negatively affected by solvents, they can swell or even dissolve. Solvents are necessary for SU-8 chemical functionalisation, but the particles used for biosensing should

be solvent resistant and not swell when exposed to solvents or at least they should come back to the original size once resuspended in water. This condition derives from the fact that in the case of porous substrates the conductivity of the surface might be masked by the conductivity of the bulk in a non-trivial way.

There are many possible choices of elongated particle design, for example rods or square parallelepipeds. Rod shaped particles should be preferred as their friction when moving on the glass is lower due to the circular cross-section. They can be easily fabricated as pillars using photolithography.

1.8.2 Aim of the project

The aim of this project is to develop a methodology for sensing of binding of biomolecules (antibody or DNA) using electrokinetics. In this project ROT and EO were used on a single particle basis to study the electrical properties of microparticles in AC electric fields according to the chemical properties of their surface. The motion in AC electric field of microparticles depends strongly on their surface charge density, therefore their motion can be used to develop an electrical label free assay where fluorescent labelling (commonly used in biomedical assays) is not used. Target molecules bind to their complementary molecules on the surface of the particles, and therefore change the particle surface conductance and hence their motion in AC electric fields.

In this thesis, SU-8 elongated particles were chemically modified to have different surface chemistry and their electrical properties were obtained using ROT and EO. The chemical modifications performed represent the common functionalisation steps needed to obtain a surface rich with the biomolecules of interest, for example antibodies. The aim is to asses if those modifications change the ROT and EO spectra of the particles and in which way, and from that quantify the electrical properties of those particles. Spherical and elongated particles were analysed as well after a gold coating process to study the EDL relaxation and the effect of gold modification with uncharged molecules.

1.9 Conclusions

In this chapter the different electrokinetic phenomena and methods were introduced, specifically EP, DEP, EO, ROT, QR and TW. These are all closely related through the particle polarizability, which describes how a particle reacts to an external electric field. Generally the particles have an induced dipole whose direction and magnitude depend on the particle and fluid properties.

The DEP force depends on the gradient of the applied field created by the electrodes, therefore the actual motion of a particle depends on position with respect to the electrodes

and is intrinsically limited in space due to the limited extent of the electrodes themselves. DEP is often used on a batch basis to separate different particle populations or to study the electrical properties of particles. Batch DEP analysis is done for example looking at the rate of change in optical absorbance to obtain a DEP force spectrum; or just looking at the frequencies[2] at which the particle experiences no motion, i.e. no positive or negative DEP, as function of the medium conductivity. Nonetheless, DEP can be used also on a single particle basis, for example studying the levitation of particles against gravity or the speed of movement in spatially non-homogeneous AC electric fields to obtain their electrical properties.

EO is used for batch analysis of particles. Like DEP, the motion is studied to determine the frequencies at which particles do not move. This is done using a large number of particles in order to generate statistical data. The information that is obtained is similar to the data from DEP as both technques depend in the same way on the particle polarizability.

ROT is performed on single particles. This method works better if the particles do not show positive DEP, which would drive them towards the electrodes, stopping the motion. To solve that problem optical tweezers (laser traps) can be used to keep the particles in place. Unfortunately reflective particles (i.e. metal particles) cannot be trapped making the measurements more complicated. ROT is often coupled with DEP or EO because it can provide independent information on particle polarizability. TW is used mostly for separation purposes and it is not often used to study the electrical properties of particles because of the complex relation between fluid flow, buoyancy, and electric field geometry.

Low frequency electrokinetics has applications in microfluidics, especially for pumping and mixing. Many conditions can affect the behaviour of the system such as voltage, electrolyte concentration and frequency of the applied field, giving rise to unusual behaviour like flow reversal during pumping. QR today has no application in the Life Science field, especially because it is unable to provide information on the internal structures of cells, given that a DC field cannot pass through the cell membrane which can be considered as a capacitor.

Electrokinetics as tool for biosensing was also discussed showing how in the literature researchers changed the properties of particles by adding materials to their surface, such as biomolecules, metal nanoparticles or even cells. Considerations on the requirements for an optimal particle design for biosensing were presented along with the aim of this project.

---

[2] Those points are called *crossover frequency*. According to the structure of the particles and medium conductivity, there can be more than one. For a shelled particle the maximum number is one for each interface.

1.10 Thesis structure

In this work a novel method of combining EO and ROT which allows single particles analysis is developed. A method to electrolessly gold coat SU-8 is shown and also the ROT spectra obtained for gold coated elongated particles (not previously published in literature) was obtained.

Chapter 2 contains the theoretical background of this work, where all the relevant equations of the motion are derived. In Chapter 3, the experimental setup is introduced along with the programs written to perform the experiments and fit the data. Chapter 4 explains the fabrication of the elongated SU-8 particles and their chemical modifications. Chapter 5 explains the development of the electrokinetic method. Chapter 6 contains the experimental results (ROT and EO spectra) for the biochemically modified SU-8 particles. In Chapter 7, the gold coating process is explained for beads and SU-8 particles, and the electrokinetic characterization of the metal coated particle is presented. Chapter 8 contains the conclusions drawn from this work.

Chapter 2

Theory

In this chapter, the background theory is presented. Firstly, the interaction of particles with the suspending liquid will be presented, including an explanation of the electrical double layer (EDL). Then, the interaction of particles with electric fields will be treated: the cases of DC and AC electric field will be treated separately, dividing the latter into high frequency and low frequency phenomena.

2.1 Dielectric relaxation and Maxwell-Wagner relaxation

The motion of a polarisable particle in an electric field depends on the frequency. For the case of DEP, a change in behaviour can be observed that describes the change from positive to negative DEP (or the other way round). This phenomenon is explained by introducing a loss mechanism, which is a decrease in energy storage of the system due to the polarization of the dielectric. At low frequencies the system has sufficient time to align the dipoles with the electric field and the energy stored per cycle is at maximum whilst the energy dissipated per cycle is zero. Increasing the frequency toward the characteristic frequency of the specific process (which is the inverse of the time the system needs to achieve maximum polarization), means that the time the dipoles have to align decreases. The energy dissipated per cycle by the system increases, and the energy storage per cycle decreases. When the frequency is the same as the characteristic frequency of the process, the energy dissipated by the system is at maximum. When the frequency is higher than the characteristic frequency, polarization can
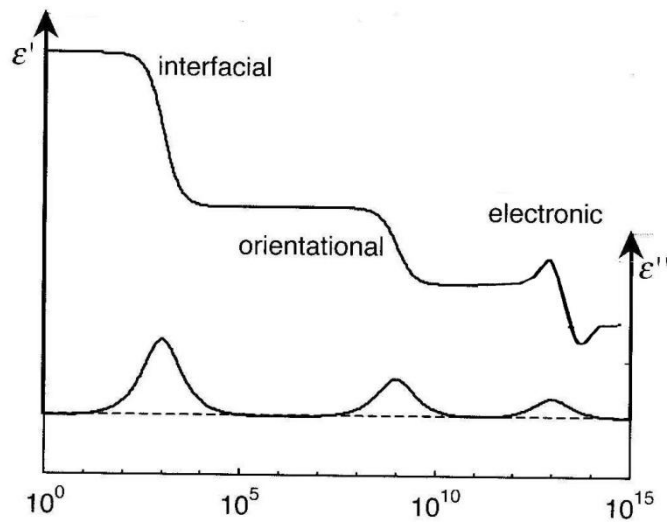
Figure 2-1. The frequency variation of the complex permittivity of a dielectric, taking into account the typical relaxations mechanism. Adapted from [124].

no longer reach the maximum because the system reaction time is long, the energy dissipated per cycle drops, as does the stored energy. At very high frequencies the system does not polarize and energy is neither dissipated nor stored. This behaviour affects the complex permittivity of dielectrics and appears as a relaxation, with a typical characteristic frequency that depends on the details on the process involved. The significant processes are sketched in Figure 2-1. As an example the drop in the relative permittivity of water from ~80 below 10^8 Hz to ~2 Hz at frequencies greater than 10^{11} Hz is due to the orientation of the water molecular dipoles.

Interfacial polarization arises when the electric field passes through different dielectrics. At each interface induced surface charges are created, for example on the surface of a dielectric particle suspended in water. These surface charges depend on the difference of complex permittivity between the medium and particle, and are related to the ability of the material to polarize in response to an external electric field. A dielectric with higher permittivity therefore polarizes more than one with lower permittivity producing more induced charges at the interface in order to preserve the continuity of the electric field. In this way we can explain positive or negative DEP as a force that acts on the resultant dipole formed by the induced charges at the interface (see Figure 2-2). This process is called Maxwell-Wagner relaxation and acts every time an interface between dielectrics with different properties is involved, such as a particle suspended in an electrolyte.
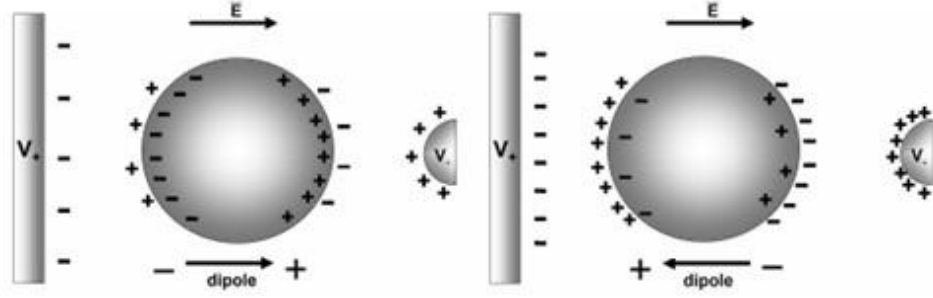
Figure 2-2. Sketch of the effect of an inhomogeneous electric field on a lossy dielectric sphere in a lossy dielectric medium at different frequency. Negative DEP on the left and positive DEP on the right. Copied from [124].

The Maxwell-Wagner relaxation can be illustrated with the parallel plate capacitor model drawn in Figure 2-3, containing two layers of lossy dielectric with different electrical properties, thickness d_1 and d_2, permittivity ε_1 and ε_2, and conductivity σ_1 and σ_2 respectively. This system can be thought as series of two capacitors each one with one dielectric between the plates. The total impedance of the two capacitors therefore is:

$$Z = Z_1 + Z_2 = \frac{R_1}{1 + j\omega R_1 C_1} + \frac{R_2}{1 + j\omega R_2 C_2} \tag{2.1}$$

where we defined:

$$R_i = \frac{d_i}{\sigma_1 A}$$
$$C_i = \varepsilon_i \frac{A}{d_i} \tag{2.2}$$

in which A is the area of the plates and $i=1,2$. Equation (2.1) can be thought of as a single capacitor with a complex permittivity defined in the form of a Debye relaxation [124]

$$\varepsilon = \varepsilon' - j\varepsilon'' = \varepsilon_0 \left[\varepsilon_{hf} + \frac{\varepsilon_{lf} - \varepsilon_{hf}}{1 + \omega^2 \tau^2} \right] - j\varepsilon_0 \left[\frac{\varepsilon_{lf} - \varepsilon_{hf}}{1 + \omega^2 \tau^2} \omega\tau + \frac{\sigma}{\varepsilon_0 \omega} \right] \tag{2.3}$$

where ε_{hf} is the high frequency permittivity, ε_{lf} is the low frequency permittivity, τ the relaxation time and σ the system conductivity, given by:

$$\varepsilon_{hf} = \frac{d\varepsilon_1\varepsilon_2}{d_1\varepsilon_2 + d_2\varepsilon_1} \qquad \varepsilon_{lf} = \frac{d\left(d_1\varepsilon_1\sigma_2{}^2 + d_2\varepsilon_2\sigma_1{}^2\right)}{\left(d_1\sigma_2 + d_2\sigma_1\right)^2}$$
$$\tau = \varepsilon_0 \frac{d_1\varepsilon_2 + d_2\varepsilon_1}{d_1\sigma_2 + d_2\sigma_1} \qquad \sigma = \frac{d\sigma_1\sigma_2}{d_1\sigma_2 + d_2\sigma_1} \tag{2.4}$$
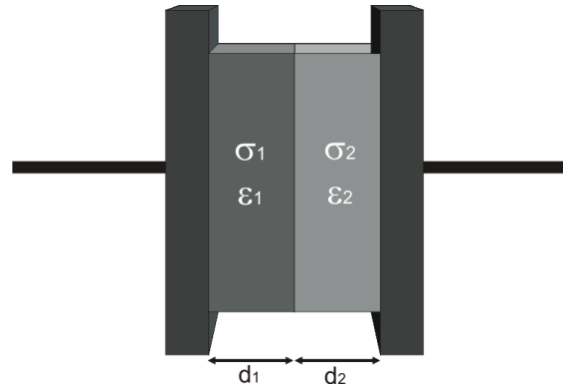
Figure 2-3. The Maxwell-Wagner relaxation can be represented with a parallel capacitor with two different lossy dielectrics between the plates. Dielectrics have conductivities σ_i, permittivity ε_i and thickness d_i (i=1,2).

As shown by this toy-model derivation, a dispersion in the permittivity arises just from the difference in permittivity and conductivity of the two dielectrics at the interface. Actually this is a very general phenomenon that appears when interfaces of two different materials are crossed by an electric field. For example a dielectric sphere in a dielectric medium in an electrical field generates a dipole from the accumulation of charges at opposite sites.

2.2 Interaction of particles with the suspending fluid

2.2.1 Stern layer and diffuse layer

Suppose a particle with a certain surface charge is suspended in an aqueous electrolyte. The system reacts to the charges at the interface, moving ions from the bulk of the solution and water molecules (which have a small dipole moment) to the interface to preserve large scale neutrality. A simple example is an aqueous solution of ions. Water molecules respond to the electric field of the ions and orientate their dipoles, counteracting the ion field. This screening effect can be quantified by the Debye length, which is the distance over which the ion potential drops to $1/e$ of its maximum value:

$$\lambda_D = \sqrt{\frac{D\varepsilon}{\sigma_m}} \qquad (2.5)$$

where D is the diffusion constant of the ions, $\varepsilon=\varepsilon_0\varepsilon_r$ and σ_m are the permittivity and the conductivity of the medium respectively. The region of polarized water is named the *ionic atmosphere* and the molecules in this region can be considered bound to the ion (they are not free to orientate) causing a drop in the permittivity in this region.
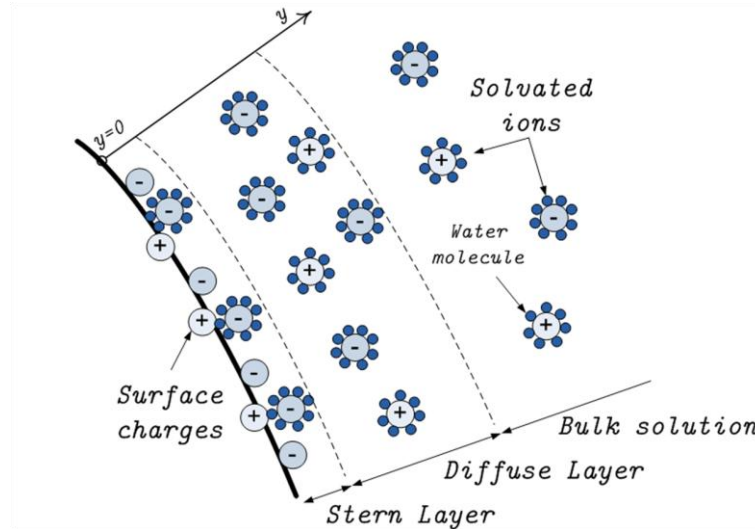
Figure 2-4. Schematic representation of the double layer for a positively charged surface in water. The Stern layer is formed by counterions (negative), solvated counterions and water molecules tightly associated onto the surface; the diffuse layer is formed by solvated ions and counterions (the majority), and they are free to move. Outside is the bulk medium. The axis y is normal to the surface and measures the distance from it.

For charged particles or electrodes immersed in electrolytes this region has a complicated structure formed by ions, counterions and water molecules as shown in Figure 2-4. Looking at the surface, there are two regions – the *Stern layer* and the *diffuse layer* – that together form the *electrical double layer*. In the *diffuse layer* water molecules and ions (solvated) are free to move but the density of counter ions is higher than in the bulk because of the charges on the surface, while the co-ions are repelled from the surface. Between the *diffuse layer* and the surface there is a thin layer – one or two solvated ions thick – named *Stern layer*. In this region the counterions (not solvated) and hydrated ions are adsorbed onto the surface along with water molecules, and are not free to move. The Stern layer is therefore essentially static. In order to keep neutrality the total charge in the electrical double layer must be the same (but of different sign) to the charges on the surface.

Many models have been proposed to describe the double layer, but in a simplified form it can be considered as just the diffuse layer (ignoring the Stern layer). There are no general analytical models but some approximations have been presented, for example the Gouy-Chapman theory [124].

This theory is as follows. Assume that *y=0* defines the position of a surface, as in Figure 2-4, with charge density ρ_d in the diffuse layer, and ϕ the potential of the surface. Those quantities are related by the Poisson equation

$$\nabla^2 \phi = -\frac{\rho_d}{\varepsilon} \tag{2.6}$$

The charge density can be obtained from the Boltzmann equation which relates the density of ions $n(y)$ at a distance y to the bulk concentration n_0. For ions of valence z_j this is

$$n_j(y) = n_{0,j} e^{-\phi(y)\frac{qz_j}{k_BT}} \tag{2.7}$$

For different ion types j, the total charge density is given by

$$\rho_d = q \sum_j n_{0,j} z_j e^{-\phi(y)\frac{qz_j}{k_BT}} \tag{2.8}$$

Equation (2.8) can now be used in equation (2.6) to obtain the Poisson-Boltzmann equation, whose solution is the potential as a function of distance from the surface:

$$\nabla^2 \phi(y) = -\frac{q}{\varepsilon} \sum_j n_{0,j} z_j e^{-\phi(y)\frac{qz_j}{k_BT}} \tag{2.9}$$

Equation (2.9) has an analytical solution for planar surfaces (i.e. thin double layer limit for a particle) for the diffuse layer only. The first step is to define the dimensionless potential function $\Psi = (q/k_BT)\phi$. In the case of a symmetric electrolyte, equation (2.9) gives:

$$\frac{d^2\Psi}{dy^2} = -\frac{q^2}{k_BT}\frac{zn_0}{\varepsilon}\left(e^{-z\Psi} - e^{+z\Psi}\right) \tag{2.10}$$

With the boundary conditions $d\Psi/dy=0$ and $\Psi=0$ at $y= \infty$, the previous equation can be solved to give the electric field as function of ion concentration and distance from the surface, and therefore the potential:

$$\phi = \frac{2k_BT}{q}\ln\left(\frac{1+\gamma e^{-\kappa y}}{1-\gamma e^{-\kappa y}}\right) \approx \frac{4k_BT}{q}\gamma e^{-\kappa y} \tag{2.11}$$

where $\gamma = \tanh(q\phi_0/4k_BT)$. At this point the variation in ion concentration can be derived substituting (2.11) in equation (2.7). The factor κ^{-1} is the characteristic decay length of the potential and it is usually referred to as the Debye length with value

$$\kappa^{-1} = \sqrt{\frac{\varepsilon k_BT}{2z^2 q^2 n_0}} \tag{2.12}$$

In case of $z=z^+=z^-$ (that is a symmetric electrolyte). The diffuse layer, despite the exponential distribution of the charge density, can be thought of as a conductive layer surrounding charged particles.

2.2.2 Surface conductance

The electrical properties of a particle can be obtained by considering a spherical particle with a given surface charge in an electric field. Following [35], from classic electrostatic theory it is known that the electrostatic potential of a spherical particle of radius R in an electric field is

$$\Phi_1 = -E_0 r \cos\theta + \frac{A\cos\theta}{r^2} \quad , \quad r > R$$
$$\Phi_2 = -Br\cos\theta \qquad , \quad r < R$$

(2.13)

where A and B are unknown terms to be determined using boundary conditions: the potential Φ must be continuous at the interface between particle and medium, i.e. at $R=r$, the electric field must satisfy the continuity equation. In spherical coordinates, this means

$$\begin{cases} \Phi_1^*(r=R,\theta) = \Phi_2^*(r=R,\theta) \\ i\omega\left(\varepsilon_1^* E_{r1}^* - \varepsilon_2^* E_{r2}^*\right) + \nabla\cdot\overline{J}^* = 0 \end{cases}$$

(2.14)

where $\overline{J}$ is the surface current density and ∇ is the divergence operator; $E_r=-\partial\Phi/\partial r$ and $E_\theta=-r^{-1}\partial\Phi/\partial\theta$ are the radial and tangential components of the electric field.

Assume that there is a thin layer around the particle that can support an ohmic or a displacement current (see Figure 2-5). If the surface current density does not have any component along r and is proportional to the tangential electric field then it is

$$\overline{J}^* = i\omega\varepsilon_S^* E_\theta \hat{\theta}$$

(2.15)

where $\varepsilon_S^*=\varepsilon_S+K_S/i\omega$ is the surface complex permittivity, which is composed of the surface permittivity (in Farads) and surface conductance K_S (in Siemens). Solving the system yields

$$A = \frac{\varepsilon_2^{*\prime} - \varepsilon_1^*}{\varepsilon_2^{*\prime} + \varepsilon_1^*} R^3 E_0$$

(2.16)

where $\varepsilon_2^{*\prime}=\varepsilon_2^* + 2\varepsilon_S^*/R$. If we consider the limit $\varepsilon_2 >> \varepsilon_S/R$, the expression for $\varepsilon_2^{*\prime}$ becomes

$$\varepsilon_2^{*\prime} = \varepsilon_2 + \frac{\sigma_2 + \dfrac{2K_S}{R}}{i\omega}$$

(2.17)
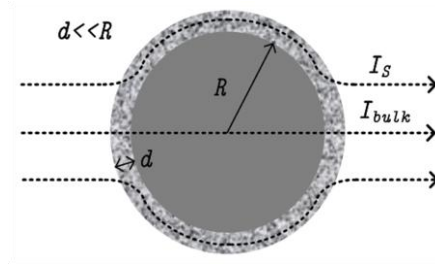
Figure 2-5. Diagram of a particle of radius R surrounded by a thin conductive layer of thickness d<<R. Dashed lines represent current flow in response to an external electric field (not shown). In the overall conductivity there is the contribution of the bulk conductivity and the conductivity of the external layer.

This expression appears as a generalization of expression (2.41) where the conductivity σ_2 is the bulk conductivity of the particle and $2K_S/R$ is the surface conductivity. Concluding, the conductivity of the particles can be divided into a bulk component and a surface component independent of the size of the particle:

$$\sigma_p = \frac{2K_S}{R} + \sigma_{bulk} \tag{2.18}$$

For polymer particles a common choice assumes the bulk conductivity equals zero, meaning that the overall particle conductivity depends only on surface effects.

The surface conductivity can in turn be expressed as a function of the ion mobility [124], linking surface conductance to surface charge density:

$$K_S = \sum_j \sigma_{density,j}\mu_j \tag{2.19}$$

where $\sigma_{density,j}$ is the surface charge density and μ_j the mobility for all the ions j.

Following [125] and [126] and 1.12.1, the surface conductance can be divided in two components: one relative to charge movement in the Stern layer and another relative to the diffuse layer. Equation (2.18) now becomes

$$\sigma_p = \sigma_b + \frac{2K_{Stern}}{a} + \frac{2K_{Diff}}{a} \tag{2.20}$$

The Stern layer conductance is given by

$$K_{Stern} = \rho_{q,Stern}\mu_{Stern} \tag{2.21}$$

where $\rho_{q,Stern}\mu_{Stern}$ are the equivalent surface charge density and ion mobility in the Stern layer.

The conductance of the diffuse layers can be divided in two components: one related to electroosmosis of fluid $K_{Diff,eo}$, and the other related to charges moving with respect to the liquid $K_{Diff,m}$. the diffuse layer conductance can be therefore be expressed as

$$K_{Diff} = K_{Diff,m} + K_{Diff,eo} = \frac{4F^2cz^2D\left(1+3m/z^2\right)}{RT\kappa}\left(\cosh\left[\frac{zq\zeta}{2k_BT}\right]-1\right) \qquad (2.22)$$

where ζ is the zeta potential, D is the diffusion coefficient of the excess free charge in the diffuse layer, z the valence of the counterions, F the Faraday's constant, R the gas constant, k_B the Boltzmann's constant, q the charge of the electron and T the temperature. The inverse Debye length is given by

$$\kappa = \sqrt{\left(2czF^2\right)/\left(\varepsilon_m RT\right)} \qquad (2.23)$$

where c is the electrolyte concentration in moles per litre. The dimensionless parameter m describes the contribution of the electroosmotic ion flux to the diffuse layer conductance

$$m = \left(\frac{RT}{F}\right)\frac{2\varepsilon_m}{3\eta D} \qquad (2.24)$$

where η is the viscosity of the suspending medium. Equation (2.22) can be rewritten using equation (2.23) to express its dependency on $\sqrt{c}$:

$$K_{Diff} = \frac{4F^2cz^2D\left(1+3m/z^2\right)}{RT}\sqrt{\frac{\varepsilon_m RT}{2czF^2}}\left(\cosh\left[\frac{zq\zeta}{2k_BT}\right]-1\right) \propto \frac{c}{\sqrt{c}} = \sqrt{c} \qquad (2.25)$$

K_{diff} therefore is a monotonically increasing function of c.

2.3 Electrical forces acting on particles

2.3.1 Electrophoresis

A particle with charge z sits in a DC electric field $\bar{E}$. The force acting on the particle can be expressed as:

$$\bar{F} = z\bar{E} \qquad (2.26)$$

For a more realistic case where the charged particle is suspended in a viscous fluid, the equation of the motion can be written as:

$$z\bar{E} - 6\pi\eta rv = 0 \qquad (2.27)$$

where the viscous drag of the fluid is proportional to the velocity v of the particle, to the viscosity η, to the Stokes radius r_S and where inertia has been neglected. The Stokes radius is defined as $r_S = \frac{k_B T}{6\pi\eta D}$ where k_B is the Boltzmann constant, T is the temperature, and D is the diffusion coefficient. It simply follows from equation (2.27) that the particle will move with the speed

$$v = \frac{z\bar{E}}{6\pi\eta r_S} = \mu_p \bar{E} \qquad (2.28)$$

where the electrophoretic mobility μ_p is defined as a function of the Stokes radius r_S and z [126]-[128]:

$$\mu_p = \frac{z}{6\pi\eta r_S} \qquad (2.29)$$

This is the case for gel electrophoresis for example. The actual theory that describes the motion of particles through a polymer net is more complicated and its treatment here is not necessary, but the simplified model already shows how the speed of a particle in an electric field is a function of its charge and its hydrodynamic radius. The bigger the particle radius and the viscosity the slower it will move, and the bigger the charge the faster the movement.

In the case of charged particles suspended in an aqueous electrolyte, as shown in Figure 2-6, it is more convenient to express the electrophoretic mobility μ_p in terms of the ζ potential. The charges present on particle surface will attract by electrostatic force counter ions from the solution to form what is called the *electrical double layer* (EDL). The ions in the mobile part of the double layer will experience the same electrophoretic force as the ions in the bulk and will move towards the electrode of the opposite sign. Because the ions in the mobile region are solvated, their movement will also drag the surrounding electrolyte, creating an electroosmotic flow. The electroosmotic flow around the particle is opposite to the particle movement and appears as a force slowing down the particles, the *retardation force*, which is weaker for thicker EDL.
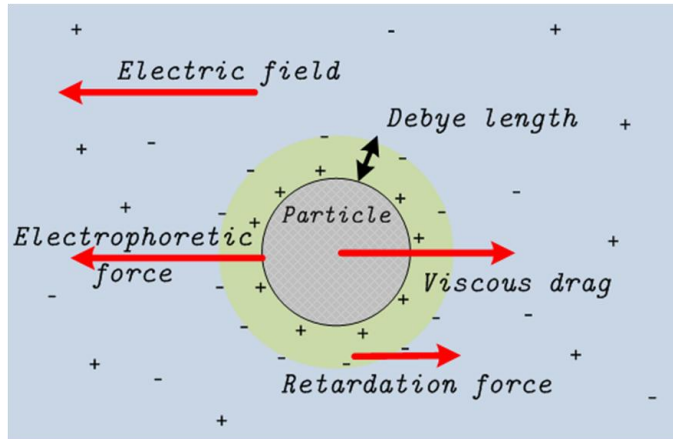
Figure 2-6. Illustration of all the different forces acting on a charged particle suspended in an electrolyte and sitting in a DC electric field. The particle has an intrinsic positive charge, therefore its EDL is mostly formed by negative charges. The thickness of the EDL is represented by the Debye length.

An analytical expression for the particle mobility that is valid in all cases does not exist, but various approximations have been proposed, see references [125][129]. The most common case is the approximation of a thin EDL, described by the Smoluchowski model [130]. That offers a powerful simplification because it is independent of the shape and concentration of particles. The condition of thin EDL is expressed by *κa>>1*, which relates the Debye length to the particle size. In this case the mobility is:

$$\mu_p = \frac{\varepsilon_0 \varepsilon_r \zeta}{\eta}$$

(2.30)

where $\varepsilon_0 \varepsilon_r$ is the permittivity of the solution and ζ is the zeta potential of the capillary wall. The zeta potential is the electric potential in the EDL at the point of the slip plane compared to a point in the bulk solution far away from the particle [129]. It exists because surfaces may present fixed charges either on the surface or adsorbed from the surrounding medium.

The *κa<<1* limit (thick EDL) is described by the Hückel formula:

$$\mu_p = \frac{2}{3} \frac{\varepsilon_0 \varepsilon_r \zeta}{\eta}$$

(2.31)

This equation is applied mostly for nanoparticles in very low ionic strength electrolytes, where the EDL thickness is comparable to the particle dimensions.

The Smoluchowski and the Hückel equations ignore the contribution of the surface conductance to the particle mobility. Many models have been proposed for the case *κa>>1* which take into account surface conductance [125], for example Shubin *et al.* [131], where

$$\frac{\eta q}{\varepsilon kT}\mu_p = \bar{\zeta} + \frac{2Du}{1+2Du}\left\{\frac{2\ln 2}{z} - 2\ln\left[1+\exp\left(\frac{z\bar{\zeta}}{2}\right)\right]\right\} \tag{2.32}$$

Where $\bar{\zeta} = \zeta q/kT$ and *Du* is the *Dukhin number*, which reflects the relative importance of the surface conductivity to the bulk conductivity. *Du* is defined as

$$Du = \frac{K_p}{K_m a} \tag{2.33}$$

Where K_p and K_m are the particle and electrolyte conductivity respectively, and a is the particle dimension. The Smoluchowski and the Hückel equations are therefore valid for the case of *Du<<1* and *κa>>1*, while equation (2.32) is valid for *Du>>1* and *κa>>1*. Using equation (2.22) and (2.24) *Du* can be expressed as a function of ζ potential [125][129]:

$$Du = \frac{2}{\kappa a}\left(1+\frac{3m}{z^2}\right)\left[\cosh\left(\frac{ze\zeta}{2kT}\right)-1\right]\left(1+\frac{K_{Stern}}{K_{diff,m}}\right) \tag{2.34}$$

2.3.2 Force on an infinitesimal dipole

The simplest case of particle electromechanics is an infinitesimal dipole located in an electrical field $\bar{E}$ as in Figure 2-7. If the dipole consists of two charges, *+q* and *–q*, at distance $\bar{d}$, then the force acting on the dipole can be expressed as

$$\bar{F} = q\bar{E}\left(\bar{r}+\bar{d}\right) - q\bar{E}\left(\bar{r}\right) \tag{2.35}$$

where $\bar{r}$ is the position vector of *–q*. If $\bar{d}$ is small compared with the length scale of the electric field it is possible to expand the expression for the electric field in equation (2.35) using a truncated Taylor series:

$$\bar{E}\left(\bar{r}+\bar{d}\right) = \bar{E}\left(\bar{r}\right) + \bar{d}\cdot\nabla\bar{E}\left(\bar{r}\right) \tag{2.36}$$

where the higher terms of order d^2, d^3 and so on, have been neglected. This is a good approximation because the electrodes (or their features) are often bigger than the particles and this means that the variation in length scale of the electric field is bigger than the dimensions of the particles. Inserting equation (2.36) in equation (2.35) leads to

$$\bar{F} = q\bar{d}\cdot\nabla\bar{E} = \bar{p}\cdot\nabla\bar{E} \tag{2.37}$$

if we take the limits $\left|\bar{d}\right| \to 0$ in such a way that $q\bar{d} \equiv \bar{p}$ remains finite. Therefore there is no force acting on the dipole (the so called *ponderomotive force*) if the field is uniform.
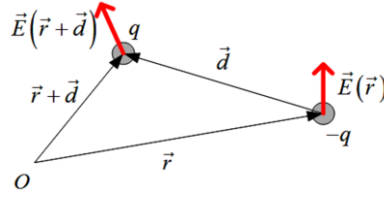
Figure 2-7. Forces on a dipole formed by two charges (q and -q) at distance d by an electric field E. O is the arbitrary origin of the coordinate system.

2.3.3 Torque on an infinitesimal dipole

A dipole in an electrical field is subjected not only to the ponderomotive force but also to a torque acting around the centre of the small dipole because of the different sign of charge at each end:

$$\bar{T}^e = \frac{\bar{d}}{2} \times q\bar{E} + \frac{-\bar{d}}{2} \times \left(-q\bar{E}\right) = q\bar{d} \times \bar{E} = \bar{p} \times \bar{E} \tag{2.38}$$

where we have used again the first order approximation in $\bar{d}$. In this case the torque does not depend on the gradient of the field but just on its direction, therefore a torque can exist in a uniform field.

2.3.4 Spherical particles in an electric field

Equations (2.37) and (2.38) refer to an abstract infinitesimal dipole which could be either a permanent moment or an induced dipole. The latter is the one we are interested in, because particles in general do not possess a permanent moment and their polarization depends on the external field and on the intrinsic electrical properties of the suspending medium. In order to relate the system parameters to the behaviour of the particles we use the formalism of the *effective moment*. The dipole moment $\bar{p}$ (see equation (2.37)) will be calculated as an equivalent dipole producing the same electric field as the polarized particle.

The simplest case is an ideal dielectric sphere in an ideal dielectric medium (Figure 2-8) with uniform electric field of magnitude E_0. From classic electrostatic theory [35] we know that the sphere behaves as a dipole of magnitude

$$p_{eff} = 4\pi\varepsilon_1 K R^3 E_0 \tag{2.39}$$

where R is the radius of the sphere, ε_1 is the permittivity of the medium and K is the Clausius-Mossotti function also known as polarization factor. The Clausius-Mossotti function
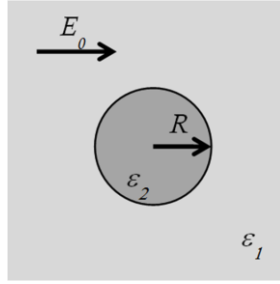
Figure 2-8. Dielectric spherical particle of radius R in a homogeneous electric field
E_0 *suspended in a dielectric medium with different permittivity.* ε₂ *is the particle permittivity,* ε₂ *is the medium permittivity.*

expresses the magnitude of the induced dipole and its direction as a function of ε_1 and ε_2 and is defined for a sphere as

$$K\left(\varepsilon_1, \varepsilon_2\right) = \frac{\varepsilon_2 - \varepsilon_1}{\varepsilon_2 + 2\varepsilon_1} \tag{2.40}$$

It is easy to see that, depending on the relative properties of particle and medium, the dipole lies parallel or antiparallel to the field, because a substance with higher permittivity produces more induced charges at the interface (Figure 2-9).

2.3.5 Generalizations of the model for lossy systems

The model presented above describes the behaviour of perfect systems with no loss. Real world systems instead are usually lossy, which means they are not perfect insulators but always show a certain amount of current flowing through once placed in an AC electric field.

The first step in the generalization to introduce lossy systems [35] is changing the definition of ε_i to ε^*_i:

$$\varepsilon_1^* = \varepsilon_1 + \frac{\sigma_1}{i\omega}$$
$$\varepsilon_2^* = \varepsilon_2 + \frac{\sigma_2}{i\omega} \tag{2.41}$$
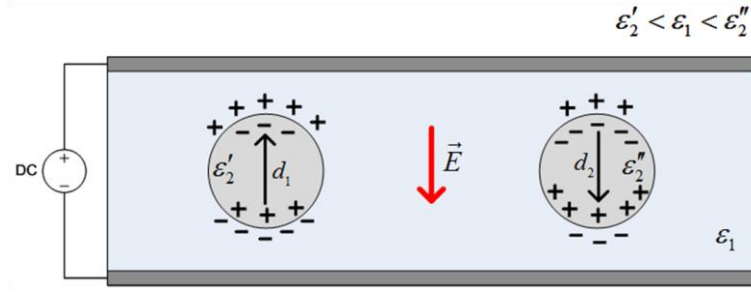
Figure 2-9. Two particles with different permittivity (ε_2', ε_2") suspended in a medium of permittivity ε_1 in a homogeneous electric field $\vec{E}$. The particle on the left has lower permittivity than the surrounding medium, therefore it polarizes less than the medium; the particle on the right has a bigger permittivity and polarizes more than the medium. d_1 and d_2 are the directions of the resulting dipole moments.

where σ_1 and σ_2 are the conductivity of the suspending medium and of the particle. Using these expressions we get:

$$\bar{p}^*_{eff} = 4\pi\varepsilon_1 K^* R^3 \bar{E}^*_0$$

$$K^*\left(\varepsilon_2^*, \varepsilon_1^*\right) = \frac{\varepsilon_2^* - \varepsilon_1^*}{\varepsilon_2^* + 2\varepsilon_1^*} \tag{2.42}$$

where p_{eff} is $\bar{p}_{eff}(t) = \mathrm{Re}\left[\bar{p}^*_{eff}\exp(i\omega t)\right]$ and $\bar{E}_0 = \mathrm{Re}\left[\bar{E}^*_0\exp(i\omega t)\right]$. All the information about frequency dependencies and phase lag are described by the Clausius-Mossotti factor K^*, which in this case is complex. The generalization to lossy systems, and the consequent introduction of the frequency dependence in the induced dipole, leads to the equations for dielectrophoresis, electrorotation and electroorientation.

2.3.6 Generalization of the model to represent cell-like particles

The first step in describing cell-like particles is introducing a shelled sphere model, which has an inner core, radius R_2 and permittivity ε_3^*, and outer shell, radius R_1 and permittivity ε_2^*, see Figure 2-10. If the suspending medium has permittivity ε_1^* we obtain

$$K^*\left(\varepsilon_2^{*\prime}, \varepsilon_1^*\right) = \frac{\varepsilon_2^{*\prime} - \varepsilon_1^*}{\varepsilon_2^{*\prime} + 2\varepsilon_1^*} \tag{2.43}$$

$$\varepsilon_2^{*\prime} = \varepsilon_2^* \left\{ \frac{\gamma^3 + 2\left(\frac{\varepsilon_3^* - \varepsilon_1^*}{\varepsilon_3^* + 2\varepsilon_1^*}\right)}{\gamma^3 - \left(\frac{\varepsilon_3^* - \varepsilon_1^*}{\varepsilon_3^* + 2\varepsilon_1^*}\right)} \right\} \tag{2.44}$$
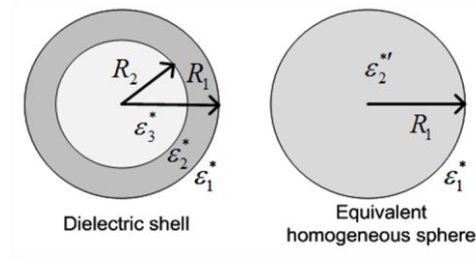
Figure 2-10. Model of shelled particle of radius R_1 composed of a core of permittivity ε^*_3 and radius R_2 and a shell of permittivity ε^*_2, suspended in medium of permittivity ε^*_1. On the right, the equivalent particle of same radius but permittivity $\varepsilon^{*'}_2$.

where $\varepsilon^{*'}_2$ is the equivalent permittivity of the whole sphere (Figure 2-10) and $\gamma=R_1/R_2$.

It is possible to modify the shelled particle model to describe cells or other structures composed of a thin membrane surrounding a lossy dielectric. Taking into account that the cell radius R is usually much bigger than membrane thickness d, we introduce the conductivity and capacitance of the cell membrane per unit area:

$$C_m = \frac{\varepsilon_2}{d}, \quad G_m = \frac{\sigma_2}{d} \tag{2.45}$$

and the revised expression for the Clausius-Mossotti factor [44]:

$$K^* = \frac{RC_m^*\left(\varepsilon_i^* - \varepsilon_e^*\right) - \varepsilon_i^* \varepsilon_e^*}{RC_m^*\left(\varepsilon_i^* + 2\varepsilon_e^*\right) + 2\varepsilon_i^* \varepsilon_e^*} \tag{2.46}$$

where $C^*_m = C_m + G_m/i\omega$, ε^*_1 and ε^*_e are the complex permittivity of the cytoplasm (or the solution inside the membrane) and of the medium respectively.

2.3.7 Dielectrophoresis (DEP)

As we shall see, the time scale of the movement of the particles on microelectrodes is usually bigger than the period of the applied AC electric field (~µs), so it is convenient to consider the time average of the force acting on a particle [29]. According to the previous definition of *effective moment* in an AC field we obtain, from equation (2.37):

$$\left\langle \bar{F}_{DEP}\left(t\right)\right\rangle = \left\langle \bar{p}^*_{eff} \cdot \nabla \bar{E}^*\right\rangle = \frac{1}{2}\mathrm{Re}\left[\bar{p}^*_{eff} \cdot \nabla \bar{E}^{*\dagger}\right] \tag{2.47}$$

where $\left\langle f\left(t\right)\right\rangle$ means the time average of the function f and $\dagger$ complex conjugation. Using equation (2.42) the ponderomotive force is:

$$\left\langle \bar{F}_{DEP}\left(t\right)\right\rangle = \pi\varepsilon_1 R^3 \, \mathrm{Re}\left[K^*\left(\omega\right)\right]\nabla\left(\bar{E}^{*2}\right) \tag{2.48}$$

The force is directed along the gradient of the squared electric field, and the direction is defined by the real part of the Clausius-Mossotti factor, which contains the electrical properties of the particle and the surrounding medium. A general expression for spherical homogeneous lossy dielectric particles in a lossy dielectric medium is:

$$K^*\left(\omega\right) = \frac{\varepsilon_2^* - \varepsilon_1^*}{\varepsilon_2^* + 2\varepsilon_1^*} = \frac{\varepsilon_2 - \varepsilon_1 - i\left(\sigma_2 - \sigma_1\right)/\omega}{\varepsilon_2 + 2\varepsilon_1 - i\left(\sigma_2 + 2\sigma_1\right)/\omega} \tag{2.49}$$

In this simple case the real part of the Clausius-Mossotti factor (related to DEP) takes the shape of a smoothed step function with the following behaviour, as shown in Figure 2-11:

$$\mathrm{Re}\left[K^*\right] \rightarrow \begin{cases} \dfrac{\sigma_2 - \sigma_1}{\sigma_2 + 2\sigma_1} & for \quad \omega\tau_{MW} = 1 \\[3mm] \dfrac{\varepsilon_2 - \varepsilon_1}{\varepsilon_2 + 2\varepsilon_1} & for \quad \omega\tau_{MW} \, ? \, 1 \end{cases} \tag{2.50}$$

where we have introduced the characteristic Maxwell-Wagner relaxation time constant

$$\tau_{MW} = \frac{\varepsilon_2 + 2\varepsilon_1}{\sigma_2 + 2\sigma_1}. \tag{2.51}$$

The behaviour depends on the sign of $\mathrm{Re}[K^*]$ which in turn depends on the properties of the particle and the suspending liquid. If it is positive, we have positive DEP (the particle is attracted to high electric field strength regions and repelled from low strength regions) or negative DEP when it is negative (with opposite behaviour). In this context it is easy to define a function that describes this behaviour, defining the frequency where no positive or negative DEP is observed, the so called *crossover frequency*:

$$f_X = \frac{1}{2\pi\varepsilon_0}\sqrt{\frac{\sigma_2^{\,2} + \sigma_2\sigma_1 - 2\sigma_1^{\,2}}{\varepsilon_2^{\,2} + \varepsilon_2\varepsilon_1 - 2\varepsilon_1^{\,2}}} \tag{2.52}$$
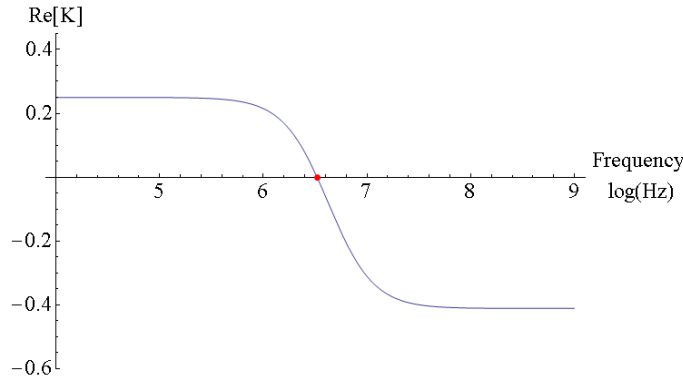
Figure 2-11. Real part of the Clausius-Mossotti factor for a non-conductive sphere.
$\varepsilon_1=80\varepsilon_0$, $\varepsilon_2=10\varepsilon_0$, $\sigma_1=0.01 S/m$, $\sigma_2=0.02 S/m$. *The dot at 6.5 indicates the position of the crossover frequency.*
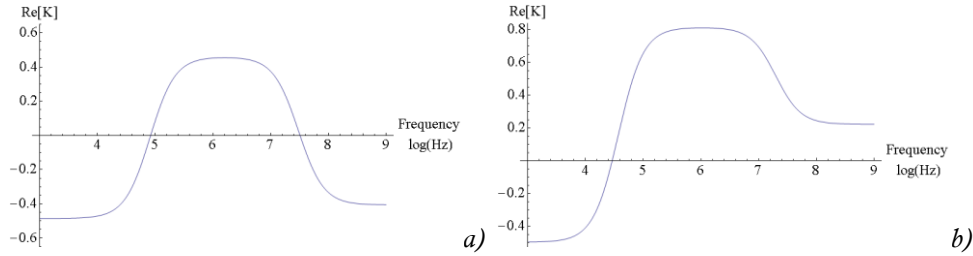
Figure 2-12. Real part of the Clausius-Mossotti factor for a) shelled particle and b) cell-like particle in the approximation of very thin shell. In a) the following parameters were used: $\varepsilon_1=80\varepsilon_0$, $\varepsilon_2=15\varepsilon_0$, $\sigma_1=1$ mS/m, $\sigma_2=0.001$ mS/m, $\varepsilon_3=10\varepsilon_0$, $\sigma_3=0.2$ S/m, $\gamma^{-1}=0.95$; in b) $\varepsilon_e=80\varepsilon_0$, $\varepsilon_i=150\varepsilon_0$, $\sigma_e=0.02$ S/m, $\sigma_i=0.3$ S/m, $C_m=0.015$ F/m, $G_m=5$ Ω/m, $R=10$ μm.

The calculations for shelled particles are similar but of course more complicated. Because there are two interfaces, a maximum of two relaxations and two crossover frequencies are expected. In general there is a relaxation for each interface (plus intrinsic relaxations), the behaviour of which depends on the properties of the interface. Examples of the real part of the Clausius-Mossotti factor for a shelled particle and a cell-like are shown in Figure 2-12, where the theoretical spectra are obtained from equation (2.48) using the definitions of K^* given in 2.3.6.

2.3.8 Electrical torque on spherical particles

As described by equation (2.38), a dipole that is not aligned to an electric field experiences a torque that forces it to align with the field. For the case of a spherical particle, for symmetry reasons no torque is expected in a steady AC field, but it is possible to demonstrate the
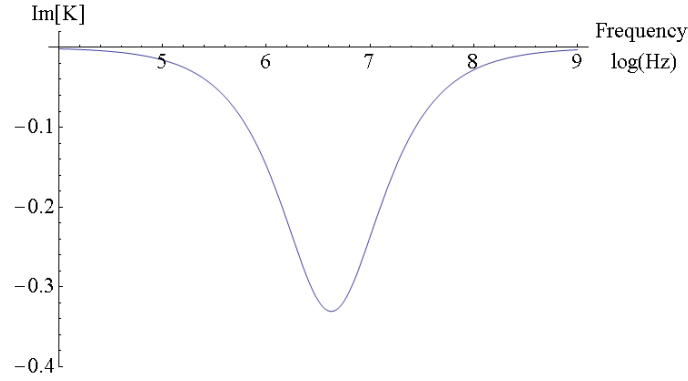
Figure 2-13. Imaginary part of the Clausius-Mossotti factor for a non-conductive sphere. $\varepsilon_1=80\varepsilon_0$, $\varepsilon_2=10\varepsilon_0$, $\sigma_1=0.01$ S/m, $\sigma_2=0.02$ S/m.

existence of a torque for a rotating electric field (or in general a field whose orientation changes with time). The time averaged torque on a particle is:

$$\left\langle \bar{T}^e(t) \right\rangle = \frac{1}{2}\operatorname{Re}\left[\bar{p}^*_{eff} \times \bar{E}^{*\dagger} \right] \tag{2.53}$$

$$\bar{E}^* = E_0\left(\hat{x} - i\hat{y} \right) \tag{2.54}$$

$$\left\langle \bar{T}^e(t) \right\rangle = \frac{1}{2}\operatorname{Re}\left[\det \begin{pmatrix} \hat{x} & \hat{y} & \hat{z} \\ p^*_x & p^*_y & p^*_z \\ E^{*\dagger}_x & E^{*\dagger}_y & E^{*\dagger}_z \end{pmatrix} \right] =$$

$$= \frac{1}{2}\operatorname{Re}\left[\det \begin{pmatrix} \hat{x} & \hat{y} & \hat{z} \\ p^*_x & p^*_y & 0 \\ E^{*\dagger}_x & E^{*\dagger}_y & 0 \end{pmatrix} \right] = \frac{1}{2}\operatorname{Re}\left[ip^*_x E_0 - p^*_y E_0 \right] \tag{2.55}$$

$$\left\langle \bar{T}^e(t) \right\rangle = -4\pi\varepsilon_1 R^3 \operatorname{Im}\left[K^*(\omega) \right] E_0^2 \hat{z} \tag{2.56}$$

where we assume that the electric field is a right circularly polarized vector of magnitude E_0 (equation (2.54)). In this case the torque spectrum (the direction of rotation and the rotation rate) is determined by the imaginary part of the Clausius-Mossotti factor. For a spherical particle the imaginary part of K^* appears as a peak centred at the Maxwell-Wagner relaxation as shown in Figure 2-13.

For a shelled particle, there is a peak for every interface (plus intrinsic relaxations), with sign and magnitude that depend on the properties of the interface. For cells the spectrum has an anti-field rotation at lower frequencies and a co-field rotation at higher frequencies (Figure 2-14). The former depends on the relaxation of the membrane that acts as a (lossy) capacitor, while the latter is the Maxwell-Wagner relaxation between the cytoplasm and the medium (at that frequency the membrane is short circuited).
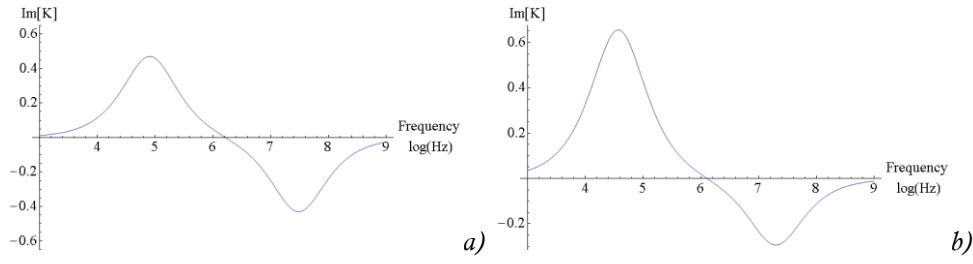
Figure 2-14. Imaginary part of the Clausius-Mossotti factor for a) shelled particle and b) cell-like particle in the approximation of very thin shell. In a) the following parameters were used: $\varepsilon_1=80\varepsilon_0$, $\varepsilon_2=15\varepsilon_0$, $\sigma_1=1mS/m$, $\sigma_2=0.001\ mS/m$, $\varepsilon_3=10\varepsilon_0$, $\sigma_3=0.2\ S/m$, $\gamma^{-1}=0.95$; in b) $\varepsilon_e=80\varepsilon_0$, $\varepsilon_i=150\varepsilon_0$, $\sigma_e=0.02\ S/m$, $\sigma_i=0.3\ S/m$, $C_m=0.015\ F/m$, $G_m=5\ \Omega/m$, $R=10\ \mu m$.

2.3.9 Quincke rotation of spheres in a DC electric field

Assume a spherical particle suspended in a dielectric fluid in a DC field. To ease the calculation it is possible to fix the reference frame to the particle in order to a have a fixed particle and a linearly polarized rotating electric field. Similar to the case of electrorotation, the electric field is defined as $\bar{E}=E_0\left(\hat{x}-i\hat{y}\right)e^{i\Omega t}$, while the effective dipole is:

$$\bar{p}_{eff}=4\pi\varepsilon_1 K^* R^3 E_0\left(\hat{x}-i\hat{y}\right)e^{i\Omega t} \tag{2.57}$$

where K^* is the complex Clausius-Mossotti factor introduced before, ε_1 is the real permittivity of the suspending fluid and Ω is the angular speed of the rotating field. The electric torque on the particle can be calculated from $\left\langle\bar{T}_Q\left(t\right)\right\rangle=1/2\operatorname{Re}\left(\bar{p}_{eff}\times\bar{E}^\dagger\right)$ to obtain:

$$\left\langle\bar{T}_Q\left(t\right)\right\rangle=\frac{1}{2}\operatorname{Re}\left[\det\begin{pmatrix}\hat{x} & \hat{y} & \hat{z}\\ p_{eff,x} & p_{eff,y} & 0\\ E_{0,x}^\dagger & E_{0,y}^\dagger & 0\end{pmatrix}\right]=\operatorname{Re}\left[4i\pi\varepsilon_1 K^* R^3 E_0^{\,2}\right]\hat{z}=4\pi\varepsilon_1 R^3 E_0^{\,2}\operatorname{Im}\left(K^*\right)\hat{z} \tag{2.58}$$

The previous expression can be rewritten in a more convenient form following [80]:

$$T_Q=\left\langle T_Q\left(t\right)\right\rangle=\frac{6\pi\varepsilon_1 R^3 E_0^{\,2}\left(1-\tau_1/\tau_2\right)\Omega\tau_r}{\left(1+2\varepsilon_1/\varepsilon_2\right)\left(1+\sigma_2/2\sigma_1\right)\left[1+\left(\Omega\tau_r\right)^2\right]} \tag{2.59}$$

where the following substitutions have been made:

$$\tau_i=\frac{\varepsilon_i}{\sigma_i}\quad\tau_r=\frac{\varepsilon_2-\varepsilon_1}{\sigma_2-2\sigma_1}$$

where τ_i is the charge relaxation time of $i=1,2$ for suspending fluid and particle. The substitution $\Omega=-\omega$ changes the reference from the one fixed to the particle to another one
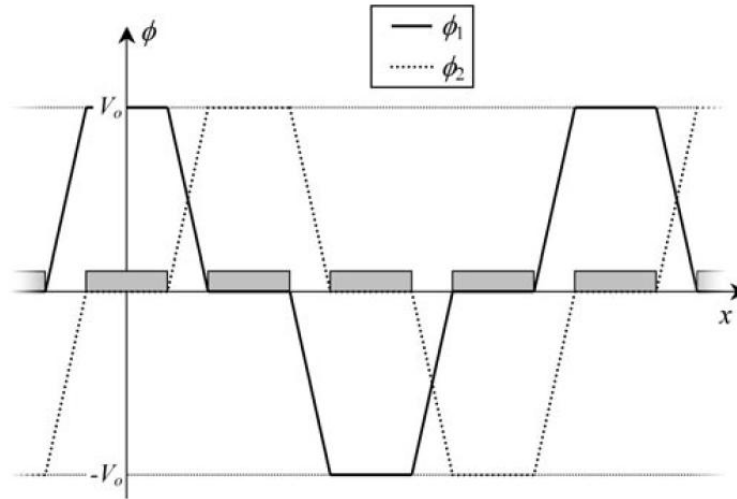
Figure 2-15. Boundary conditions for potential functions ϕ_1 and ϕ_2 generated by two adjacent electrodes. The electrostatic potential is the superposition of the two and was used to derive the forces acting on a particle in a TW device. The amplitude is the same but shifted by $\pi/4$ to the right. Image taken from [132].

fixed with respect to the electric field. For $\Omega=0$ the torque is always 0 but any small perturbation can induce a movement if $\tau_1/\tau_2<1$ because the torque is in the same direction as the rotation of the particle, providing a positive feedback to the motion. For $\tau_1/\tau_2>1$, the torque is negative so it is opposite to the movement of the particle which means the particle is in a position of stable equilibrium and will not move. The maximum torque is when $\Omega=\tau_r^{-1}$, which is actually the Maxwell-Wagner relaxation frequency for that system. It can be shown [80] that the critical electric field necessary for movement is:

$$E_{crit} = \sqrt{\frac{8\eta_1\tau_1}{3\varepsilon_1\varepsilon_2}}\frac{1+\sigma_1/2\sigma_2}{\sqrt{1-\tau_1/\tau_2}} \tag{2.60}$$

In the case of $\tau_1/\tau_2>1$, E_{crit} is not defined and no moment is allowed.

2.3.10 Travelling-wave dielectrophoresis

The derivation of the force is rather cumbersome and it will be summarized only briefly, the full derivation can be found in [132].

Assume an infinite array of interdigitated electrodes with a 90° phase shift in the applied AC electric signal between adjacent electrodes. The electrodes have lateral dimension d equal to the space between them. A particle is suspended at a distance y above the electrodes in an electrolyte. Intuitively, a travelling wave electric field will generate a DEP force perpendicular to the electrodes and a force in the direction of the travelling wave, in the same way as a rotating field would apply a torque to the particle. A full analytical solution to the problem is

not possible, but using Fourier series it is possible to obtain an analytical solution for a particle some distance away from the electrodes with the assumption of a linear potential function between neighbour electrodes as shown in Figure 2-15. The time averaged DEP component of the force is [132]:

$$\langle F_{DEP} \rangle = -0.372 \frac{vV_0^{\,2}}{d^3} \mathrm{Re}\left[K^* \right] e^{-\pi y/2d} \tag{2.61}$$

Where v is the volume of the particle and V_0 is the amplitude of the potential applied to the electrodes. This expression is valid only for distances >1.5d, in case of smaller distance higher order effects should be taken into account. Equation (2.61) is valid for positive and negative DEP, but for the common TW applications usually only negative DEP is required, as the particles must levitate above the electrodes. That is possible because the force decreases exponentially with the distance from the electrodes while the gravitational force ($F=mg$) is constant and therefore a point of equilibrium is possible.

The time-averaged component of the force parallel to the electrodes is calculated as:

$$\langle F_{TW} \rangle = -0.372 \frac{vV_0^{\,2}}{d^3} \mathrm{Im}\left[K^* \right] e^{-\pi y/2d} \tag{2.62}$$

This expression is very similar to the electric torque imposed by a rotating electric field. Also in this case the force decreases exponentially, therefore the velocity of the particles depends also on their distance from the electrodes. Different particles will experience different DEP force and will levitate at different heights, and will be propelled with different forces, scaled according to the distance from the electrodes. Given these complicated dynamics, TW-DEP is mostly used in a phenomenological way to separate populations of different particles and not actually to get any information on particle electrical properties.

2.4 Torque on elongated particles in electric fields

While spherical particles can only show DEP and electrorotation, elongated particles can show also electroorientation, due to differences in the induced dipole along different axes.

Elongated particles can be approximated to ellipsoids for which the Clausius-Mossotti factor can be expressed analytically. Assuming a lossy dielectric ellipsoid with semi-axes $a>b>c$ (see Figure 2-16) suspended in a lossy dielectric, it is possible to define three different Clausius-Mossotti factors for every semi-axis of the ellipsoid [35]:

$$K_\alpha^* \equiv \frac{\varepsilon_{2,\alpha}^* - \varepsilon_1^*}{3\left[\varepsilon_1^* + \left(\varepsilon_{2,\alpha}^* - \varepsilon_1^* \right) L_\alpha \right]} \quad , \quad \alpha = a,b,c \tag{2.63}$$
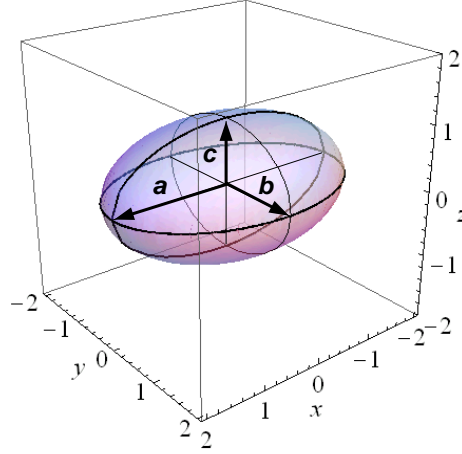
Figure 2-16. Ellipsoid with semi-axes a>b>c. In this case a=2, b=√2, c=1.

where L_α is the depolarization factor and is defined by an elliptical integral along the arbitrary distance s:

$$L_\alpha = \frac{abc}{2} \int_0^\infty \frac{ds}{\left(s+a^2\right)\sqrt{\left(s+a^2\right)\left(s+b^2\right)\left(s+c^2\right)}} \qquad (2.64)$$

and $\varepsilon_{2,\alpha}{}^* = \varepsilon_2 + \sigma_{2,\alpha}/i\omega$ is the complex permittivity of the particle along the axes α. Following [133], the definition of σ_2 can be generalized introducing three different conductivities, one for each axis of the particle:

$$\sigma_{2,c} = \frac{(a+b)K_S}{ab} \qquad \sigma_{2,b} = \frac{(a+c)K_S}{ac} \qquad \sigma_{2,a} = \frac{(b+c)K_S}{bc} \qquad (2.65)$$

with K_S the surface conductance of the particle, and a, b, c the dimensions of the relative semi-axes.

We can recast equation (2.42) and define a specific induced moment dipole for every axis:

$$\left(\overline{p}_{eff}^*\right)_\alpha = 4\pi abc\varepsilon_1 K_\alpha^* \overline{E}_{0,\alpha} \qquad (2.66)$$

2.4.1 Electrorotation of ellipsoidal particles

Assume an ellipsoid with axis a and b parallel to the surface as in Figure 2-16. Fix the coordinate system with the axes of the particle ($a\rightarrow x$, $b\rightarrow y$, $c\rightarrow z$) and a rotating electric field parallel to the x-y plane. Inserting equations (2.54) and (2.66) in equation (2.55) gives the rotational torque:
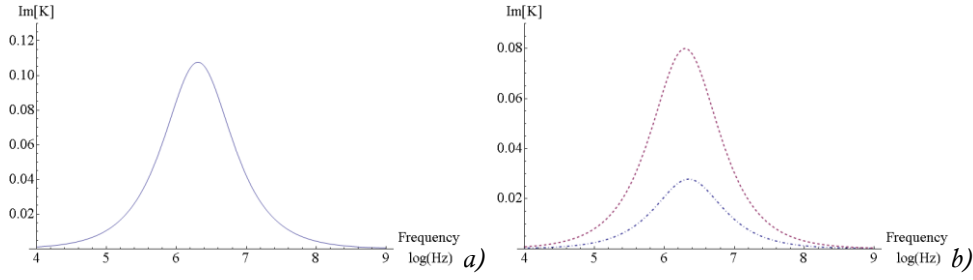
Figure 2-17. a) Imaginary part of the Clausius-Mossotti factor for an ellipsoidal particle, b) the contributions from the longer (small peak) and shorter axis (big peak). a=20 μm, b=5 μm, σ_1=0.01 S/m, K_p=1 nS/m, ε_1=80ε_0, ε_2=15ε_0.

$$\left\langle \bar{T}^e(t) \right\rangle = \frac{1}{2}\text{Re}\left[p_a^* E_y^{*\dagger} - p_b^* E_x^{*\dagger} \right]\hat{z} = \frac{1}{2}\text{Re}\left[ip_a^* E_0^* - p_b^* E_0^* \right]\hat{z} \tag{2.67}$$

$$\begin{aligned} \left(p_{eff}^* \right)_a &= 4\pi abc\varepsilon_1 K_a^* E_0 \\ \left(p_{eff}^* \right)_b &= -i4\pi abc\varepsilon_1 K_b^* E_0 \end{aligned} \tag{2.68}$$

$$\left\langle \bar{T}^e(t) \right\rangle = 2\pi abc\varepsilon_1 E_0^{\ 2}\,\text{Re}\left[iK_a^* + iK_b^* \right]\hat{z} = -2\pi abc\varepsilon_1 E_0^{\ 2}\,\text{Im}\left[K_a^* + K_b^* \right]\hat{z} \tag{2.69}$$

The electric torque acting on the particle depends on the combined effect of the dipoles along different axes. An example of a theoretical Im[K_a^*+K_b^*] for an ellipsoidal particle is shown in Figure 2-17, where also the contribution for each axis is plotted.

2.4.2 Electroorientation of ellipsoidal particles

Consider an ellipsoidal particle as previous, and a linearly polarized electric field forming an angle θ with the principal axis of the particle: E_x^*=$E_0\cos(\theta)$, E_y^*=$E_0\sin(\theta)$, E_z^*=0. Using the new definition of the electric field in equation (2.55) and (2.66) gives:

$$\begin{aligned} \left\langle \bar{T}^e(t) \right\rangle &= \frac{1}{2}\text{Re}\left[\det\begin{pmatrix} \hat{x} & \hat{y} & \hat{z} \\ p_a^* & p_b^* & p_c^* \\ E_x^{*\dagger} & E_y^{*\dagger} & E_z^{*\dagger} \end{pmatrix} \right] = \\ &= \frac{1}{2}\text{Re}\left[\det\begin{pmatrix} \hat{x} & \hat{y} & \hat{z} \\ p_a^* & p_b^* & 0 \\ E_x^{*\dagger} & E_y^{*\dagger} & 0 \end{pmatrix} \right] = \frac{1}{2}\text{Re}\left[p_a^* E_y^{*\dagger} - p_b^* E_x^{*\dagger} \right]\hat{z} \end{aligned} \tag{2.70}$$

$$\begin{aligned} \left(p_{eff}^* \right)_a &= 4\pi abc\varepsilon_1 K_a^* E_0 \cos\theta \\ \left(p_{eff}^* \right)_b &= 4\pi abc\varepsilon_1 K_b^* E_0 \sin\theta \end{aligned} \tag{2.71}$$
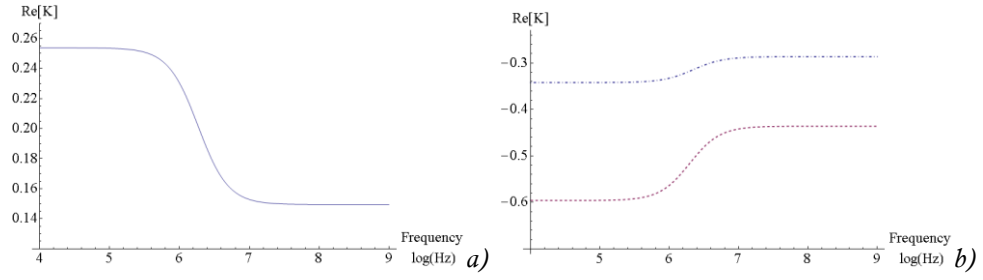
Figure 2-18. a) Real part of the Clausius-Mossotti factor for an ellipsoidal particle; b) the contributions from the longer (higher curve) and shorter axis (lower curve). a=20 μm, b=5 μm, σ_1=0.01 S/m, K_p=1 nS/m, ε_1=80ε_0, ε_2=15ε_0.

$$\left\langle \overline{T}^e\left(t\right)\right\rangle = \pi abc\varepsilon_1 E_0^{\ 2}\,\mathrm{Re}\left[K_a^* - K_b^*\right]\cdot\sin\left(2\theta\right)\hat{z} \tag{2.72}$$

In this case the electric torque depends on the combined effect of two *competitive* dipoles. From equation (2.72) it follows that spherical particles do not undergo any orientational torque. Figure 2-18 is a plot of Re[K_a^*-K_b^*], with the contribution of the two components along different axes.

2.5 Particle movement in electric fields

The actual motion of microparticles in suspension under the effect of an electric field can be derived taking into account the viscosity of the suspending medium and the negligible mass of the particle. Following [53], the viscous counter-torque for an elongated particle ($a>b=c$) is defined as

$$\Gamma_V = -\pi a^3\eta C_R\frac{d\theta}{dt} \tag{2.73}$$

where the viscosity η has a value of 1.0x10^{-3} Pa·s for a typical aqueous suspending medium, and the form factor C_R is

$$C_R = \frac{1}{3\left(\ln\left(a/b\right)-\frac{1}{2}\right)} \tag{2.74}$$

2.5.1 ROT motion of ellipsoidal particles

The equation of motion can be derived from equation (2.69) and equation (2.73) for a particle with $a>b=c$ starting from

$$-2\pi ab^2\varepsilon_1 E_0^{\ 2}\,\mathrm{Im}\left[K_a^* + K_b^*\right]-\pi a^3\eta C_R\frac{d\theta}{dt}=0 \tag{2.75}$$

to get:

$$\theta_{ROT} = -2\varepsilon_1 E_0^2 \frac{b^2}{a^2} \frac{\text{Im}\left[K_a^* + K_b^*\right]}{\eta C_R} t + \theta_0 \tag{2.76}$$

Given a particular frequency of the applied field, the particle rotates with a constant angular speed. If we define the scaling factor

$$F = 2\frac{\varepsilon_1 E_0^2}{\eta C_R} \frac{b^2}{a^2} \tag{2.77}$$

we obtain a simplified version of equation (2.76) that describes the actual motion of the particle in a rotating electric field

$$\theta_{ROT} = -F \, \text{Im}\left[K_a^* + K_b^*\right] t + \theta_0 \tag{2.78}$$

Using some realistic choice of parameters: $\varepsilon_1 = 80\varepsilon_0$, $a/b = 4$, $\eta = 10^{-3}$ Pa/s, $C_R = 0.38$ and $E_0 = 50000$ V/m, the factor F can be estimated as 600 rad/s. For any particular experimental system, the factor F is fixed, which means that studying the motion of a particle at different frequencies enables the reconstruction of the expression $\text{Im}[K_a^* + K_b^*]$, which contains all the information about the electrical properties of the particle and the suspending dielectric. Theoretical spectra for ROT of ellipsoidal particles are shown in Figure 2-19(a,c) and in Figure 2-20(a,c) for different values of the electrical properties of particle and suspending dielectric.
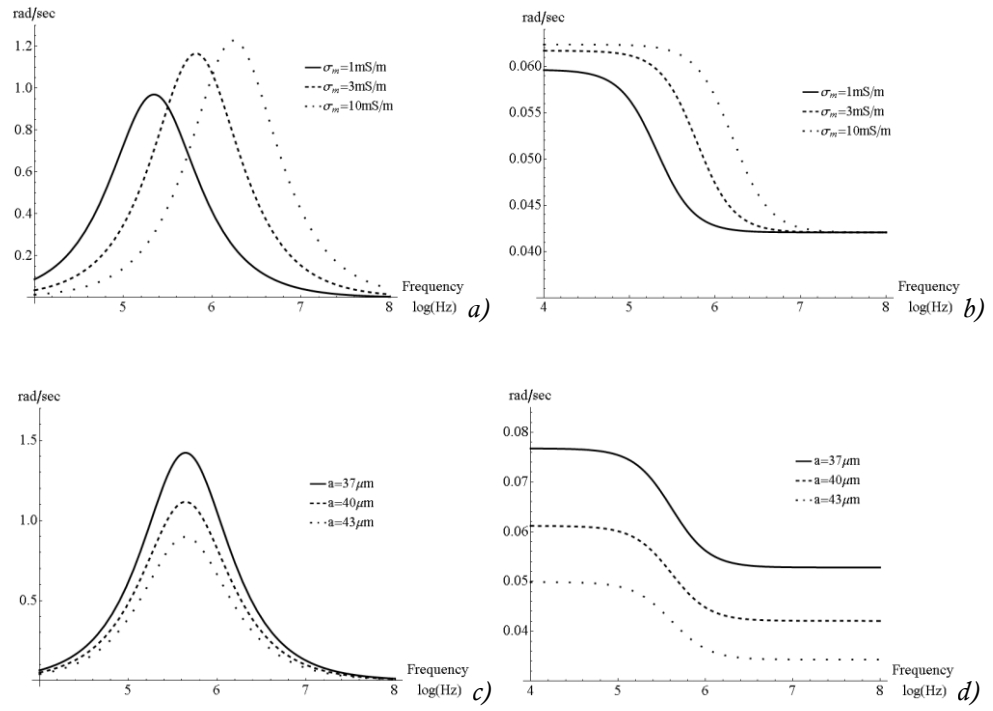
Figure 2-19. Theoretical ROT (a,c) and EO (b,d) spectra for different particles and suspending media. ROT and EO spectra for: (a,b) Different medium conductivities with 2a = 40 μm, 2b=2c=10 μm, K_S=0.1 nS, ε_p=10ε_0, ε_m=76ε_0; (c,d) Different particle shapes with 2b=10 μm, K_S=0.1 nS, ε_p=10ε_0, σ_m=2mS/m, ε_m=76ε_0.
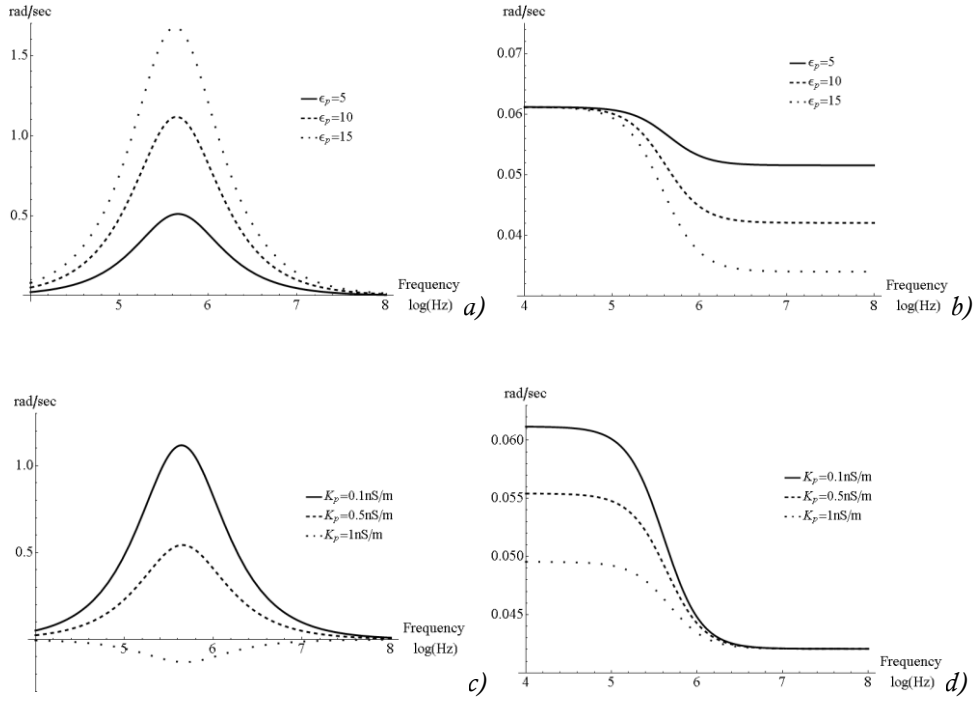
Figure 2-20. Theoretical ROT (a,c) and EO (b,d) spectra for different particles and suspending media. ROT and EO spectra for: (a,b) Different particle permittivities with 2a = 40 μm, 2b=2c=10 μm, K_S=0.1 nS, σ_m=2 mS/m, ε_m=76ε_0; (c,d) Different particle surface conductances with 2a = 40 μm, 2b=2c=10 μm, ε_p=10ε_0, σ_m=2mS/m, ε_m=76ε_0.

2.5.2 EO motion of ellipsoidal particles

The orientational motion of a particle can be derived from equation (2.72) in the same way

$$\pi ab^2 \varepsilon_1 E_0^{\ 2} \, \mathrm{Re}\Big[K_a^* - K_b^* \Big] \cdot \sin\big(2\theta\big) - \pi a^3 \eta C_R \frac{d\theta}{dt} = 0 \qquad (2.79)$$

$$\theta_{EO} = \arctan\left[\exp\left(2\varepsilon_1 E_0^{\ 2} \frac{b^2}{a^2} \frac{\mathrm{Re}\Big[K_a^* - K_b^* \Big]}{\eta C_R} \cdot t + const\big[\theta_0\big] \right) \right] \qquad (2.80)$$

Equation (2.80) describes the angular alignment of a particle with a time constant τ given by

$$\frac{1}{\tau} = 2\varepsilon_1 E_0^{\ 2} \frac{b^2}{a^2} \frac{\mathrm{Re}\Big[K_a^* - K_b^* \Big]}{\eta C_R} = F\,\mathrm{Re}\Big[K_a^* - K_b^* \Big] \qquad (2.81)$$

where F is the same as in equation (2.77). A spectrum of the inverse of the time constant is a representation of $\mathrm{Re}[K_a^* - K_b^*]$, similar to the case for ROT. Theoretical spectra of EO are

shown in Figure 2-19(b,d) and Figure 2-20(b,d) for different values of the electrical properties of particle and suspending dielectric.

2.5.3 ROT motion of spherical particles

In the simple case of a spherical particle of radius R suspended in a viscous fluid the viscous counter-torque has the form:

$$\Gamma_V = -8\pi R^3 \eta \frac{d\theta}{dt} \tag{2.82}$$

and therefore from equation (2.56):

$$-4\pi R^3 \varepsilon_1 E_0^{\ 2} \operatorname{Im}\left[K^*\right] - 8\pi R^3 \eta \frac{d\theta}{dt} = 0 \tag{2.83}$$

$$\theta_{ROT} = -\frac{\varepsilon_1 E_0^{\ 2} \operatorname{Im}\left[K^*\right]}{2\eta} t + \theta_0 \tag{2.84}$$

The motion of the particle is independent of particle size, steady and proportional to the electric torque. Equation (2.84) describes the motion for an arbitrary spherical particle; shelled particles or cells can be treated in the same way, only the factor K^* should be chosen accordingly.

2.6 Discussion on the combined use of ROT and EO

The importance of EO measurements of ellipsoidal particles can be understood by comparing how the ROT and EO spectra vary with a single parameter of the system. In Figure 2-19 and Figure 2-20 show the effect of changing suspending medium conductivity, particle aspect ratio, particle permittivity and surface conductance. Changing the particle permittivity or surface conductance leads to a change in the height of the rotational peak, with no change in its position. Only changing the medium conductivity modifies the position.

It is clear that ROT by itself cannot provide enough information to determine how two particles with different spectra are different, especially regarding permittivity and surface conductance. EO on the other hand separates the contribution of permittivity and surface conductance in different regions of the spectrum, respectively in the high frequency and low frequency region. Measuring DEP spectra could provide similar information to what can be obtained with EO because both depend on the real part of the Clausius-Mossotti factor. Nevertheless, both DEP and ROT depend on $K_a^*+K_b^*$ therefore their spectra are not independent but are related through the Kramers-Kronig relation that relates the real and imaginary part of a function. Hence measuring DEP and ROT does not provide two independent sets of measurements. Moreover, elongated particles tend to align to external

electric fields, therefore their DEP spectra depend also on their orientation compared the electric field.

The ROT and EO spectra instead form together an independent set of measurements, because the two are not related by the Kramers-Kronig relation. Comparing graphs, the surface conductance, suspending medium conductivity and particle permittivity form a set of independent parameters that can be used to fit EO spectra, because three parameters are enough to describe these curves. Unfortunately a scaling factor (the parameter F) must be added to take into account variations in electric field strength and the viscosity of the medium, which are often unknown. In order to recover the uniqueness of the fit, the fitting was extended to ROT spectra. In this way an independent measurement is added, which gives one more independent parameter without losing uniqueness.

In case of particles experiencing only nDEP (or only pDEP), the measurement of single particle DEP spectra is complicated because of the need to reposition the particles using an external means, such as laser tweezers. Combining EO and ROT on a single device using polynomial electrodes as demonstrated in Chapter 3 allows the acquisition of the spectra ina simpler way and, unlike when measuring DEP spectra, the details of the electric field distribution are not needed and the eventual reposition of particles (needed for EO) can be achieved selecting the appropriate electrode pair.

2.7 Linear and non-linear phenomena at low frequency

The properties of the electrical double layer are directly related to the charges on the surface of the particles. This means that uncharged polymer particles, such as unfunctionalized latex beads, will have a thicker double layer (if any) compared to particles functionalized with charged groups such as carboxyl or amine groups. A special case is represented by perfectly polarisable particles, for example metal particles, or even metal coated particles. Metal particles do not have charges on the surface, but they strongly polarize in a field with a thick double layer. This double layer is polarized according to the direction of the electric field, therefore an AC electric field will induce an alternating polarization moving the ions in the double layer along the surface of the particle.

The standard theory for this phenomenon is described in the work of Grosse and Shilov [105]. Because the actual derivation of the equations is rather cumbersome the results will be only briefly explained. Assume an insulating particle of radius a with surface charge σ suspended in an electrolyte. The ions in the condensed part of the double layer (Stern layer) are immobile, which means the surface of the particle is assumed to be at the boundary between the condensed layer and the diffuse layer and the surface potential is the potential at this point as well. From this assumption, the surface charge is the charge inside this boundary. A

further assumption is the condition of weak electric field *Ea<25mV* which restricts analysis to phenomena linear in *E*. The authors demonstrated that the angular speed of a particle is the sum of the angular speed of the particle with its double layer (given by an electric torque) plus the angular speed of the particle with respect to the outer boundary of the double layer (given by the electroosmosis). This leads to an angular speed for the particle of $\omega=\omega_d+\omega_{eo}$. The angular speed ω_d is related to the induced dipole formed by the electric field which polarizes the charges around the particle. The process of moving charges across the particle in the opposite direction is slow, therefore the relaxation time is in the kHz range; much lower in frequency than the Maxwell-Wagner relaxation, which is in the MHz range. The angular speed ω_{eo} is related to the electroosmotic slip on the particle, which is caused by zero total torque, because it has the same value but opposite direction in the two different parts of the EDL. In other words, the fluid flow around the particle is driven by two different phenomena: electroosmosis and what in the paper is called *capillary osmosis* [105]. Electroosmosis depends on the gradient of the electric field along the surface. Capillary osmosis is the movement of liquid driven by a gradient in salt concentration along the surface of a particle and for symmetry reasons does not give rise to any torque on the particle. Both ω_d and ω_{eo} depend on the imaginary part (in AC) of the concentration changes around the particle with frequency, which is the analogous to the Clausius-Mossotti factor for a particle that experiences a Maxwell-Wagner relaxation. The relative importance of the two components to the net angular speed of the particle can be evaluated analytically for a symmetric electrolyte (ion charge is ±z) in the two extreme cases of very low and very high ζ-potential. In the first case (*zζ<<0.05V*) the ratio is [105]:

$$\frac{\omega_d}{\omega_{eo}} = -\frac{4\lambda_{db}}{3a} \tag{2.85}$$

Where λ_{db} is the Debye screening length. In the case of high ζ-potential (zζ>>0.05V)

$$\frac{\omega_d}{\omega_{eo}} = -\frac{2(1+3m)\lambda_{db}}{3a}e^{z\zeta/2}$$

$$m = \frac{2\varepsilon}{3\eta D}\left[\frac{k_B T}{ze}\right] \tag{2.86}$$

Where *D* is the diffusion coefficient of the ions, k_B the Boltzmann constant, *T* the temperature, η the viscosity of the suspending fluid and ε its absolute permittivity. Therefore the electric torque and the electroosmotic slip always have opposite signs, but at low ζ-potential the electroosmotic slip is bigger and the particles move with the electric field, whilst in case of high ζ-potential the electric torque is bigger and the particle moves against the electric field.

For the case of metal particles the situation is similar, because of the EDL. When an electric field is applied, at the time $t=0$ the field lines are normal to the surface of the metal, therefore the ions in the solution are driven towards the surface of the particle and trapped there. This accumulation of charge will screen the particle leading to a condition similar to the non-conductive particles. In fact at frequencies below the charge relaxation time $\sigma_{medium}/\varepsilon_{medium}$ of the medium, the metal surface is screened by the double layer capacitance, and will behave like an insulating particle. At higher frequencies the capacitor formed by the double layer is short-circuited exposing the metal surface to the electric field.

In conclusion, AC electrokinetic phenomena (at low voltages and low frequencies) occur when an applied electric field acts on a static double layer in equilibrium with the bulk solution, while electroosmotic flow occurs when an applied electric field along the surface puts the double layer into motion. All the forces described above, as well as the fluid flow, exist at the nanometre scale of the double layer.

For larger applied voltages, the zeta potential presents a significant additive contribution ζ_i, in phase with the external field, to be added to the value at the equilibrium ζ_{eq}: $\zeta=\zeta_{eq}+\zeta_i(t)$. The added contribution is always in phase with the applied AC fields and therefore can give rise to a net contribution to the induced fluid flow [134]. The difference in the ζ-potential is the most important difference when compared with classical electrokinetic effects: in the classical framework of electrokinetics the EDL arises from the surface charge at the solid-liquid interface and is in equilibrium with the solution. In the non-linear regime where ICEO and ACEO happen, the EDL is induced by an external electric field, and is generally not uniform along the surface. For a sufficiently low frequency AC electric field ($\omega\tau_c<<1$) the induced part of the double layer varies in phase with the external electric field, where $\tau_c=\lambda_D L/D$, L is the characteristic length of the structure involved (such as electrode length or particle diameter), λ_D is the Debye length and D is the diffusion coefficient. In this case the fluid flow is [134]:

$$v_{ICEO} \propto \frac{\varepsilon E_0 \zeta_i^0}{\eta} \propto \frac{\varepsilon E_0^2 L}{\eta} \tag{2.87}$$

The equilibrium ζ_{eq} component of the ζ-potential of course gives a zero net contribution. Equation (2.87) shows the non-linear dependence on the electric field, but there is no reference to the ionic strength of the solution. In fact, experimentally it has been found that salt concentrations >10 mM can suppress the fluid flow but no explanation has been provided yet. Also, fluid reversal was observed at very high applied voltages. This mechanism accounts for the fluid motion around structures, such as metallic wires, in electric fields [112] but also for the fluid flow generated by two electrodes, a mechanism that can be used to pump fluid [113]. Indeed, fluid pumping is an important application of ACEO, where a break in the symmetry of the electrodes can generate asymmetric fluid rolls and therefore a fluid flow in a

specific direction. Like classical electrokinetics, the fluid flow exists just outside the EDL. ICEO can also exist in DC electric fields, because the only condition is $\omega\tau_c<<1$ which defines the presence (or not) of the induced ζ-potential, i.e. at high frequency the EDL cannot form and therefore only ζ_{eq} is present.

2.7.1 A closer look at a spherical conductive particle in a rotating electric field

The electric potential on the outside of a conductive sphere in an electric field can be described in polar coordinates (r,θ) as:

$$\phi = -E_0 r \cos(\theta) + \frac{A}{r^2}\cos(\theta) \tag{2.88}$$

Where ϕ is the potential, E_0 the applied electric field and A is a factor correlated to the dipole moment of the particle $p=4\pi\varepsilon A$ that can be obtained using the appropriate boundary conditions for the problem. In this case they can be written as:

$$\sigma\frac{\partial\phi}{\partial r} = i\omega q_s = i\omega C_{DL}\phi \tag{2.89}$$

Where σ is the medium conductivity, ω is the angular frequency of the rotating electric field, q_s is the local (induced) charge in the surface of the particle and C_{DL} is the double layer capacitance.

Solving the equations leads to the following value for A:

$$A = E_0 a^3 \frac{i\Omega - 1/2}{i\Omega + 1} \tag{2.90}$$

Where $\Omega=\omega C_{DL}a/2\sigma$. Now that the dipole moment has been found, the real and imaginary part of the Clausius-Mossotti factor can be calculated as usual to obtain:

$$\begin{aligned}\mathrm{Re}[K] &= \frac{\Omega^2 - 1/2}{1+\Omega^2} \\ \mathrm{Im}[K] &= \frac{3\Omega/2}{1+\Omega^2}\end{aligned} \tag{2.91}$$

Therefore the presence of the double layer induces a relaxation (similar to the Maxwell-Wagner relaxation), with characteristic angular frequency $2\sigma/aC_{DL}$.

2.8 Conclusions

In this chapter the theoretical background needed in this work has been presented. The concept of dielectric relaxation was introduced and its phenomenology explained. Dielectric relaxation is a ubiquitous phenomenon that happens in many frequency ranges due to different phenomena such as interface, orientational or electronic relaxation. A relaxation causes a drop in the real part of the permittivity and a peak in the imaginary part, due to the balance between the stored energy and the dissipated energy provided by an external AC electric field.

The interaction of charged surfaces with the surrounding fluid was then introduced, and the concept of electrical double layer (EDL) presented. An EDL is formed because charges from the surrounding fluid are attracted to opposite charges onto the surface, forming in this way a layer that acts like a capacitor. The bigger is the surface charge density of the surface the thinner is the EDL and therefore the bigger is its capacitance. The presence of surface charges and of the EDL leads to the concept of surface conductivity, which measures how easily an electric current can flow along a surface.

The electric forces and torques acting on particles of different shape were derived starting from the simple ideal case of a charged particle and an electric dipole in an electric field. The equations of the motion were derived considering also the viscosity of the surrounding fluid. In particular, we derived the equations in the case of elongated particles because these can show electrorotation (ROT) and electroorientation (EO). Both ROT and EO depend on the polarizability of the particle, but through its imaginary and real part respectively. The axial dependence of ROT and EO implies that measuring them for the same particle provides two independent measurements of the electrical properties of the particles. Compared to ROT spectra, EO spectra have the advantage of separating the effect of particle permittivity and surface conductance in different regions of the spectrum: different surface conductances will change the spectra at low frequency, while different permittivities will change the spectra at high frequency. In the ROT spectra instead the two contributions are entangled with peak height.

These theoretical results suggest that using elongated particles and measuring their ROT and EO spectra provides a way to obtain their permittivity and surface conductance through a simultaneous fit of both spectra.

Chapter 3

Experimental Setup

3.1 Experimental setup

The experimental setup is shown in Figure 3-1 and comprises a computer connected to a digital camera and a 4-phase function generator connected to a glass chip with the microelectrodes. The chip is fixed on a PCB, placed on an inverted microscope. The microscope is fixed on a bread board to keep the system aligned with a laser trap, which is used to adjust the position of the particles in the middle of the electrodes or to remove unwanted particles. The computer is connected through GPIB to the function generator and by USB to the digital camera. The function generator and the camera are synchronized to record and analyze particle motion in real time.

3.1.1 Micro-electrodes

The electrodes were manufactured on glass using standard photolithographic techniques [118]. The electrodes are composed of 200 nm of gold (Au) sandwiched between two layers of 20 nm of titanium (Ti). The Ti surface layer is used to protect the Au layer. The electrodes had characteristic dimensions of 250 μm or 500 μm between opposing electrodes and a hyperbolic shape to obtain a well defined parabolic electric field gradient [19]. A picture of the 500 μm gap electrodes is shown in Figure 3-2: the final device is a square of 1 cm by 1 cm of glass with the electrodes in the middle and the electric contacts at the corners.
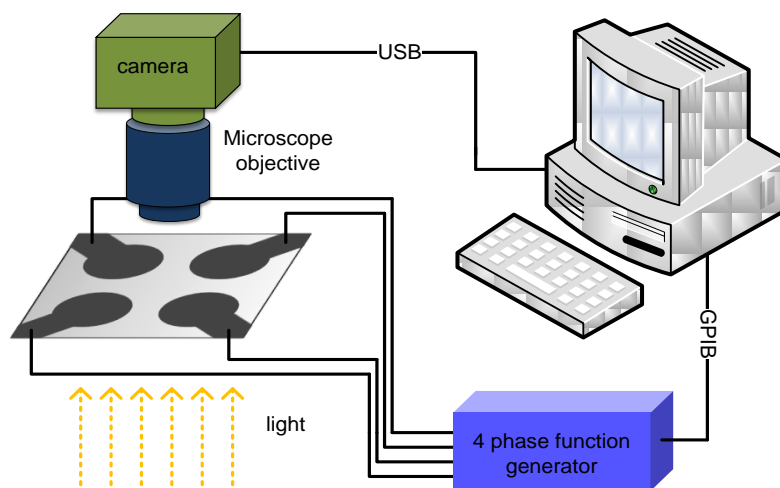
a)
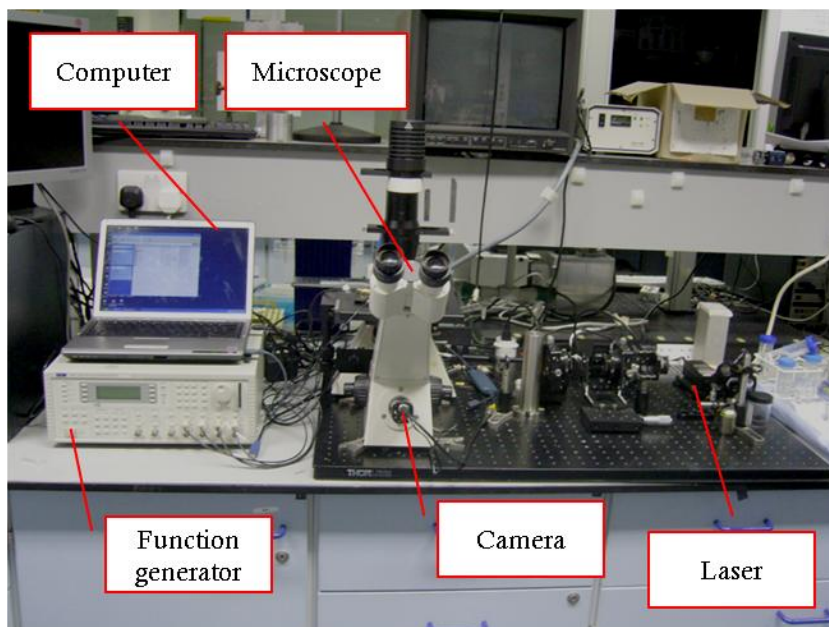
b)

Figure 3-1.   a) Diagram of the setup used for electrorotation and electroorientation measurements. The setup comprises a glass chip with four electrodes. Particles are placed in the centre of the chip, and a four phase function generator to apply the voltage to the electrodes. Particle movement is observed through a camera connected to a microscope (not shown). A computer controls the function generator and allows analysis and recording of the video. b) The actual setup.
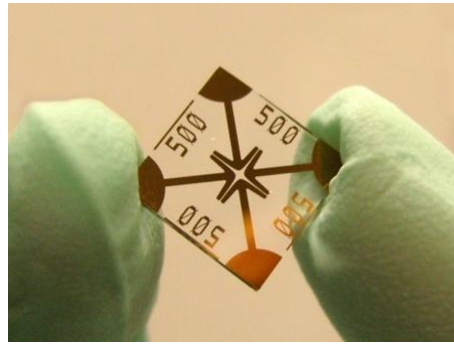
Figure 3-2. A sample of the electrodes used in this work. The ones in the picture have 500 μm gap between opposing electrodes.

3.1.2 The PCB holder

The electrodes were mounted on a PCB with electrical connections to interface the glass chip with the function generator. The design of the PCB, shown in Figure 3-3a, was optimized to be used on a microscope stage as it has the same size as a normal microscope slide. The path of each electrode has the same length in order to avoid phase delay between different channels. The PCB was fabricated using an acetate mask to expose the resist in a UV box. The developed copper tracks were covered in solder to protect them, and the square where the chip should be placed was cut out using a milling machine. The final result is shown in Figure 3-3b.

a)

b)
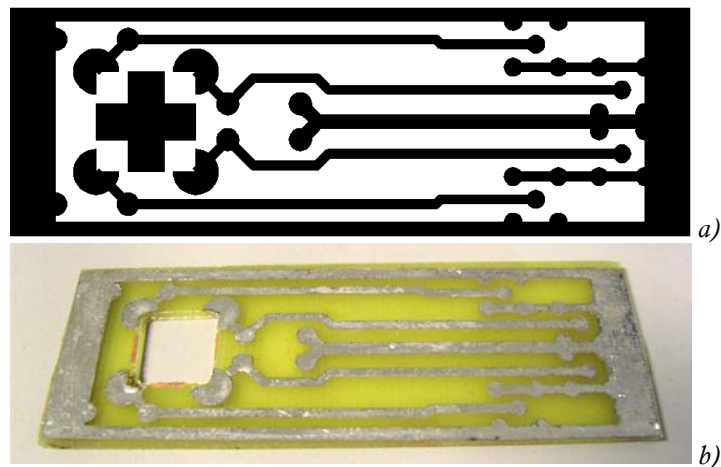
Figure 3-3. a) Design of the mask used to make the PCB for this work; b) picture of a PCB used in this work, the copper tracks are coated with solder to protect the copper and ease the soldering of the other components.
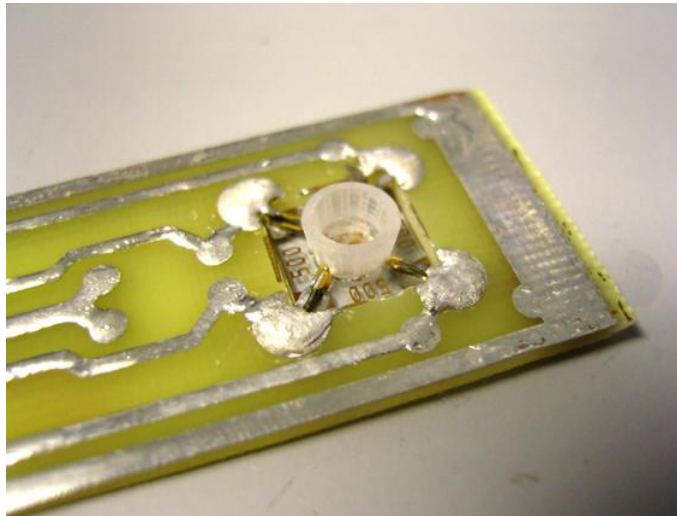
Figure 3-4. Detail of a PCB with the spring connectors soldered in place, the chip with the electrodes, and the chamber made from the crown of a 10 μl pipette tip.

To ease the handling of the samples during the measurements, a chamber was build on the chip using the cut top of a 10 μl pipette tip. The tip was put in place and fixed using Super Glue (gel type) as shown in Figure 3-4. This chamber can contain about 50 μl of liquid and can be closed with a microscope slide to reduce the evaporation of the medium, which may cause a change in the medium conductivity.

The electrical contact between the PCB tracks and the chip was made using metal spring connectors (SEI-120-02-G-S-AT, Toby Electronics) soldered on the PCB as in Figure 3-4. Because the spring connectors cannot lock the chip in position, a microscope coverslip was
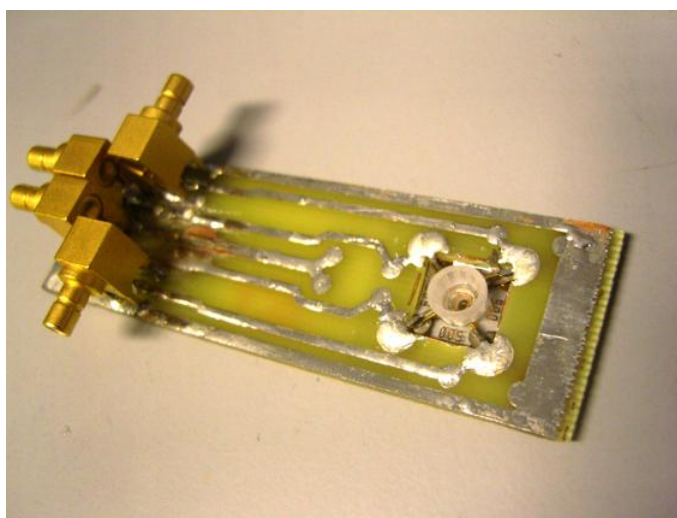
Figure 3-5. A PCB with all the components in place. On the left the four SNB connectors.
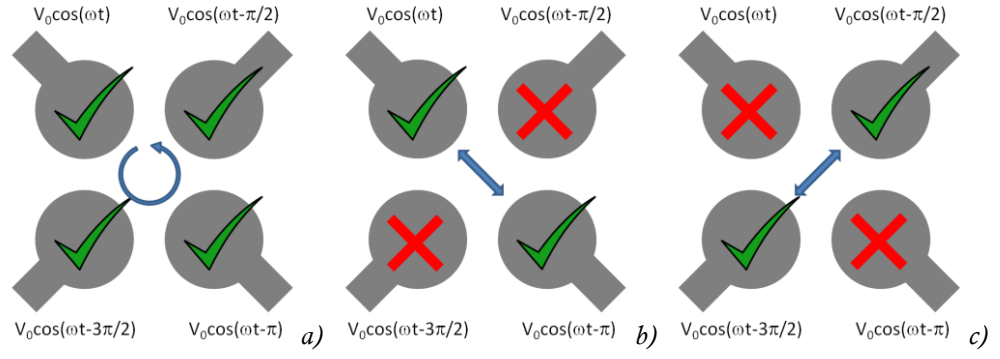
Figure 3-6. The picture shows the quadrupolar electrodes (in gray) with the signal function applied with frequency ω, amplitude V_0 and phase. The arrow indicates the direction of the electric filed in the different cases. a) configuration for electrorotation, all the electrodes are energized to obtain a circularly polarized electric field; b-c) for EO measurements only two electrodes at the time are energized, alternating them after each measurement.

attached on the bottom of the chip to the PCB (using Super Glue) to keep the chip in place. To protect the interface between the spring connectors and the chip, 1 μl of conductive paint (101-5621, RS) was used on each point of contact after the chip was put in position. The super glue and the conductive paint can be removed easily using acetone in an ultrasonic bath allowing the release of the glass chip without damaging it. Connection of BNC cables was by SNB connectors (295-5716, RS) soldered to the metal tracks, Figure 3-5. Each electrode was driven by a TTi TGA12104 4-channel function generator.

For ROT, each electrode was energized using a sinusoidal signal with 90 degree phase shift between adjacent channels. In this configuration an approximate rotating field was generated between the electrodes (Figure 3-6a). For EO, the relative electrode phase was the same as for ROT but only two opposing electrodes were energized leaving the others two floating. In this case the field generated between the electrodes is an approximated steady uniform electric field (Figure 3-6b,c).

3.2 The laser trap

A laser trap (also known as optical tweezers) is composed of a tightly focused laser beam that allows the 3D manipulation of microparticles. The mismatch of refractive index between a transparent particles and the surrounding environment creates a force gradient that keeps the particle in the beam waist, which is the narrowest point of the focused beam [135].

In this work the optical tweezers were built to allow the repositioning of particles and the removal of small contaminants from the centre of the polynomial electrodes. The setup comprised of a red LED laser (LRD-0635, λ = 635 nm, Laserglow Technologies), a beam
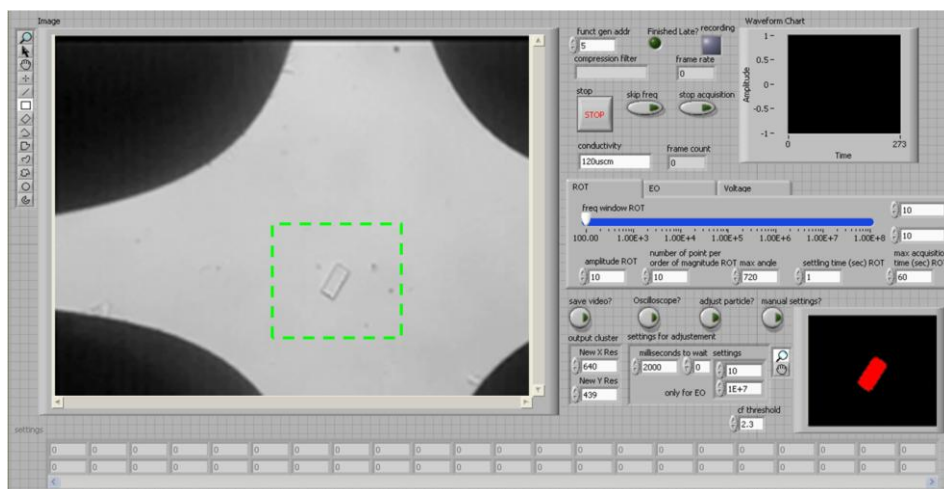
Figure 3-7. Sketch of the front panel of the acquisition and analysis software written with Labview. In the front panel are placed all the controls needed to set up EO and ROT experiments. On the left is shown the video from the camera with overlaid the green selection area that the program will analyze. The detected particle is shown on the bottom right corner in red.

expander and a dichroic beam splitter (Di01-R635-25x36, Semrock). The beam expander was composed (in the order of beam propagation) of a divergent lens (LC1120, f = -100 mm, Thorlabs) and a convergent lens (LA1461, f = 250 mm, Thorlabs). The lenses were mounted and aligned in Galilean configuration with the focus of the convergent lens placed in the virtual focus of the divergent lens, giving and expansion factor of 2.5. That expansion factor allowed the laser beam to fill all the aperture of the microscope 20x objective. The dichroic beam splitter was mounted on a custom stand inside the microscope to allow the laser beam (parallel to the bread board) to enter vertically upward in the objective. The beam splitter prevented any reflection from the glass chip from reaching the camera or the eyepiece, while allowing normal illumination to be used for imaging.

3.3 The software for control, acquisition and analysis

Data acquisition and analysis can be time consuming; therefore software was written to speed up data analysis and acquisition. This was written in Labview [www.ni.com/labview]. Fitting of the spectra was done using Mathematica [www.wolfram.com].

3.3.1 Acquisition program

The movement of particles was captured using a digital camera [Watec WAT-902H2] and recorded in digital format using a custom made software written in Labview. The program, whose user interface is shown in Figure 3-7, allows the computer to interface with the camera (via USB) and the function generator (via GPIB) and to synchronize them.

Once started, the program opens a dialog windows to setup the camera acquisition properties (such as the number of pixels in the image and the frame rate), then a GPIB connection to find the function generator and to setup the 4 channels for the measurements. The program then enters a loop to permit a continuous acquisition from the camera, to allow focusing and positioning of the particles. Drawing a selection rectangle on the screen triggers the program to create a folder to deposit all the saved data of the experiment and to start a measurement. Once a measurement is started, the program performs video acquisition with the set frame rate. For each frame acquired the program analyses the content of the selected area to detect a particle. This is done through a threshold defined as a function of the brightness of the background (i.e. the brightness of the majority of the pixels) tuned to search for particles darker than the background. Because the SU-8 is transparent, particles will appear as a dark line defining the shape of the particle. The program transforms the result into a binary image, and fills the shape of the particle to provide a solid object for analysis. Particles touching the borders will be deleted as well as particles too small compared to the expected dimensions. The final result is then analysed to produce the angle of the major axis of the particle with respect to the horizontal axis of the image.

The program can automatically scan frequencies or voltages; the voltage window goes from 0 to 20V and the frequency window from 100Hz to 40MHz, which is the maximum frequency that the function generator can produce. The operator can choose the range of frequencies to be analysed in the experiment and the density of points in the spectra per decade. The program will always start a measurement and the recording of the motion of the particle from the highest frequency (or lower voltage). For each frequency point the program will produce a snapshot of the view of the camera and a text file which contains a timestamp and the orientation of the particle for each frame (up to 15 frames per second). The text files contain also, embedded in the name, important annotations used during the analysis, such as the voltage and the frequency applied. A video can be saved for each frequency point if the relevant button is pressed. The snapshot is used by another program to calculate particle dimensions. Analysis is performed by a third program that opens the files and, one by one, lets the operator adjust the data to remove the noise.

3.3.1.1 Particle detection

In the acquisition software only the area inside the rectangular selection is analysed by the algorithm shown in Figure 3-8. The first step is the calculation of the intensity distribution of the pixels with the evaluation of the mean value and the standard deviation. If the particle is small compared to the background then the mean value of the intensity will have the same value (or very close to the background). A particle can therefore be selected using a threshold, discarding all the pixels brighter than:
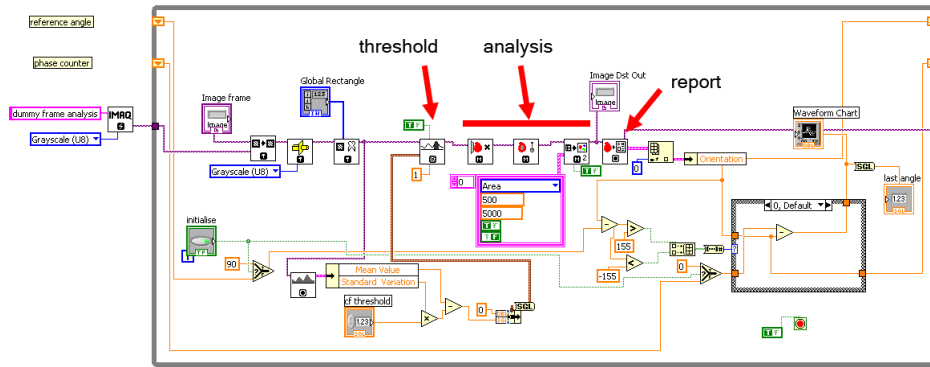
Figure 3-8. Extract of the acquisition software showing the Labview code for the identification and analysis of the orientation of the particles.

$$threshold = meanvalue - stdev \cdot cf \qquad (3.1)$$

Where *stdev* is the standard deviation and *cf* is an empiric coefficient. A value of *cf*=2.1 is typical. This particular definition of the threshold was chosen to make it independent of the actual brightness of the image. The application of a threshold function transforms the gray tones in the image into a binary image, composed of 0s (background) and 1s (particles). The particles touching the border of the selection are removed. SU-8 is a transparent material, so only the edges of the particles are dark, therefore in the binary image particles are defined as contours. The contour is filled to give a solid particle whose area (now representative of the particle size in a more efficient way) can be used to filter out unwanted particles such as dust (see Figure 3-9 for an example of the particles filtering steps). At this point, only the particle under analysis is left in the selection region and its orientation is measured as the angle between the longest axis of the particle and the horizontal axis of the image.
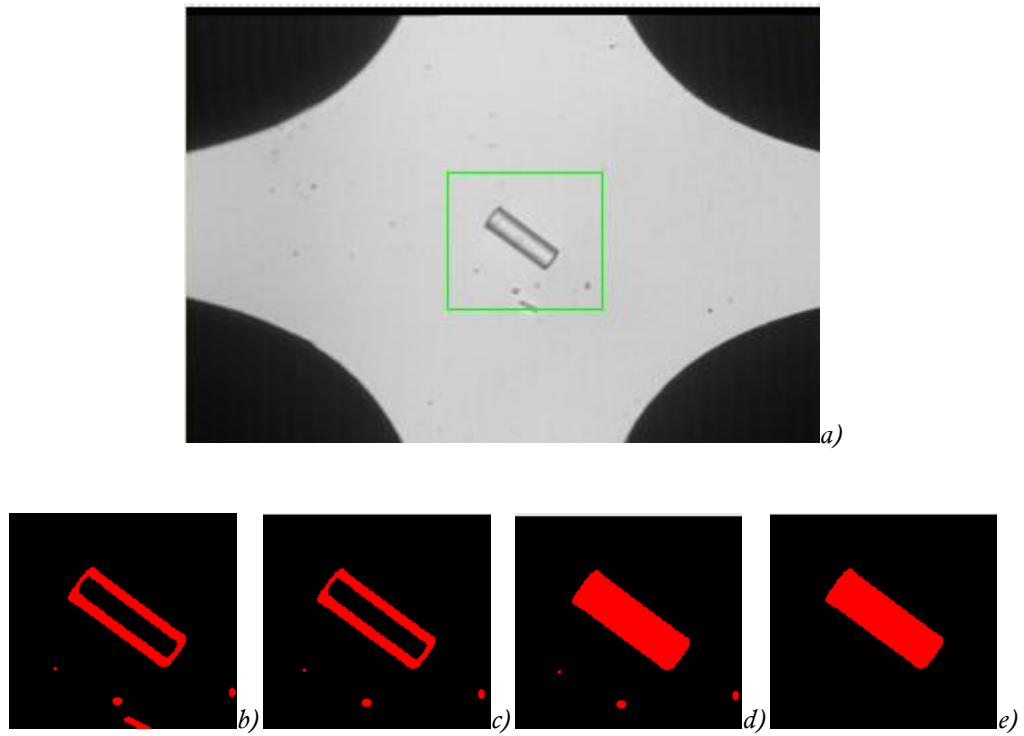
Figure 3-9. Filtering process involved in the particle orientation analysis. a) Original picture captured by the camera with the region of interest in green. b) Binary image showing the result of the threshold applied to the region of interest. c) The particles touching the edge of the image are removed. d) The holes in the particles are filled. e) Particles whose area is significantly smaller than the expected particle are removed; the orientation of the particle can now be calculated.

3.3.2 Snapshot analyser

This program obtains the dimensions of the analyzed particle from the snapshot saved by the acquisition program. The program (front panel shown in Figure 3-10) uses the same algorithm used in the acquisition program to obtain the particle shape and the dimensions in microns (after calibration). For each analysed image the program writes a file with the name, the dimensions of major axis and minor axis, and their ratio. Once all the images of a certain experiment are analysed, the program gathers all the data and writes an Excel file for further analyses.
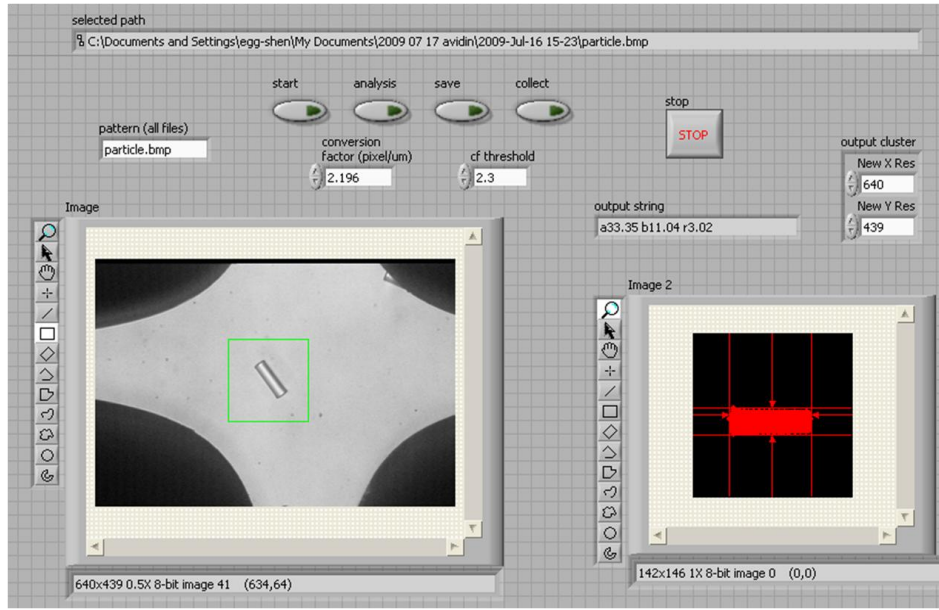
Figure 3-10. Front panel of the snapshot analyser program. The analysed picture is shown on the left with the region of interest, how the particle is seen by the software is shown on the right. The "output string" shows the dimensions in μm and the ratio between axes.

3.3.3 Motion analyser

The text files saved by the acquisition program contain the raw data of particle motion, which sometimes needs to be filtered to produce a good fit. This is due to the particle moving and touching the border of the selected region and therefore disappearing because of the filtering in 1.21.1.1. This problem usually arises at the beginning or at the end of the recordings, so filtering consists of cutting out the initial or the final data points.

Once a file is opened, the program decides from the name if it is related to ROT or EO and recovers the value of the voltage applied in order to rescale the result of the fit. For EO measurements, the data are treated to show a motion that starts from 90 degrees orientation to zero degrees. The filtered data are fitted using a linear fit for ROT data and a non-linear fit in case of EO. The fitting was performed with the following equations (see equations (2.76) and (2.80)) using the simplified form on the right hand side:

$$\theta_{ROT} = -2\varepsilon_1 E_0^2 \frac{b^2}{a^2} \frac{\mathrm{Im}\left[K_a^* + K_b^* \right]}{\eta C_R} t + \theta_0 = At + B \tag{3.2}$$

$$\theta_{EO} = \arctan\left[\exp\left(2\varepsilon_1 E_0^2 \frac{b^2}{a^2} \frac{\mathrm{Re}\left[K_a^* - K_b^* \right]}{\eta C_R} \cdot t + const\left[\theta_0\right] \right) \right] = \arctan\left[\exp\left(Ct + D \right) \right] \tag{3.3}$$
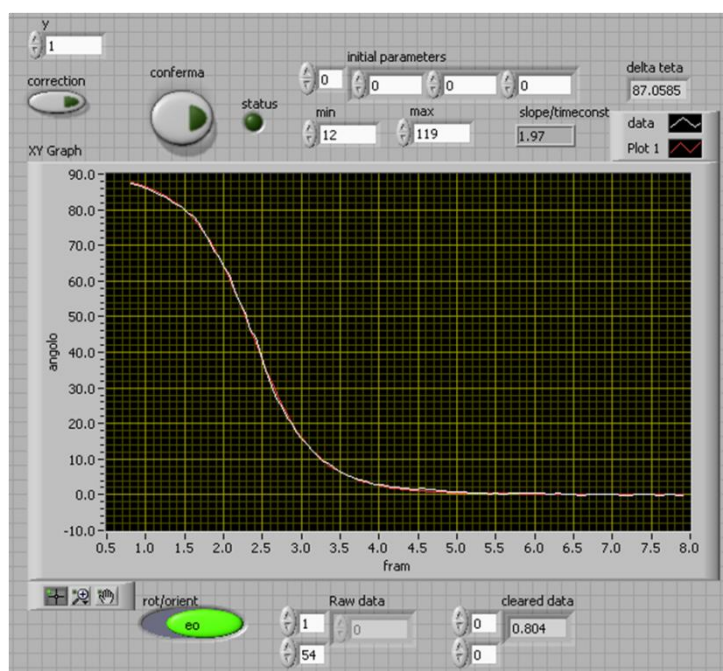
Figure 3-11. Front panel of the motion analyzer program. The settings for the fitting can be seen at the top of the image. The graph shows the motion data for the orientation.

The coefficients A, B, C, D were calculated by fitting the data for each frequency and the value of the parameter A and C was kept in memory until the analysis for all frequencies was complete. The program writes an Excel file containing, in the name, an identifier of the particle analysed and two columns containing the frequencies scanned and the relative value of the fit.

3.3.4 Fitting spectra using Mathematica

Fitting of the data was done in Mathematica, using an ancillary Excel file built with all the data from all the files produced in one experiment. That file contains all the spectra for ROT, EO and particle dimensions in a structured way that can be imported using Mathematica. The script starts importing the Excel file and reorganizing the data and eliminating missing data points (the script is reproduced in Appendix 2). Missing data points are usually caused by unwanted objects detected as particles by the acquisition program. This is usually not a problem given the number of points acquired for each spectrum (at least 5 per order of magnitude). The analytical expressions of the ROT and EO spectra are calculated as symbolic expressions and used in the fitting. There is no predefined function in Mathematica to fit two functions with two datasets, therefore a minimization function that makes use of the least squares method was implemented to fit the ROT and EO spectra at the same time.

Figure 3-12. Extract of the Mathematica script used to fit the data. The script performs the minimization of the least squares difference between data and model for each particle in the dataset. NMinimize is the function that actually performs the minimization of the function in the curly brackets. The full script can be found in Appendix 2.

The function calculates the least square function for both ROT and EO data and adds them together as shown in the extract of the script shown in Figure 3-12. A numerical minimization algorithm (chosen automatically by the software between "differential evolution" and "Nelder-Mead") is used then to find a minimum of the total least squares function. This custom made fit was performed using 4 different free parameters: the conductivity of the suspending electrolyte, the surface conductance of the particle, the permittivity of the particle, and also a scaling factor to represent the medium viscosity and the electric field in the chamber. The script fits all the particles (with the same initial conditions) and provides statistics about the results, such as average, standard deviation (or standard error) and correlation in order to evaluate the goodness of the fit.

3.3.5 Phase correction program

Despite the use of a commercially available 4-phase function generator, it was found that the difference in phase between channels was linearly dependent on the frequency. To measure this, a different PCB was used with two connectors on two adjacent channels near the glass chip. Another Labview program was written to measure the difference in phase between channels as a function of the applied signal using an oscilloscope.

The program interfaces with the TTi function generator and a two channel digital oscilloscope [Agilent DSO3202A] and measures the amplitude and the phase difference between the two signals. At the end of the process the program calculates a linear regression of the relative phase against frequency. The same measurement is repeated until all the different channels are characterised. This process provides three numbers that are used by the acquisition program to adjust on the fly the relative phase of the channels during the measurements. This
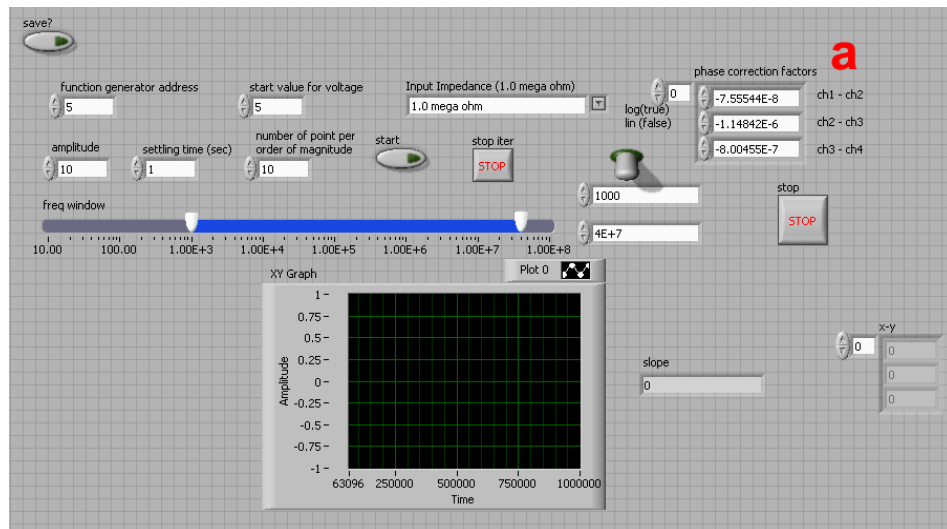
Figure 3-13. Front panel of the phase correction program. On the top left there are the settings for the function generator and oscilloscope; on the top right the output of the program (marked with A).

method does not provide a complete solution to the problem of unstable phase difference, but improves the quality of the data, especially with ROT measurements at high frequency. Further improvement could be achieved using a 4 channel oscilloscope connected to the chip and measuring amplitude and phase difference between channels in real time.

Chapter 4

Materials and Methods

4.1 Introduction

In this chapter the fabrication method of the rod-shaped particles and the chemical modifications aimed to change their surface properties will be explained. The fabrication is based on the use of SU-8, which is a negative photoresist known for its chemical and thermal resistance. SU-8 can be patterned easily in elongated particles using photolithography and the chemistry related to the modification of its epoxide rings is well known. The particles were fabricated from SU-8 [www.microchem.com], using photolithography. SU-8 is an epoxy-based negative photoresist based on the molecule shown in Figure 4-1. SU-8 was developed and patented by IBM [136] to be used as negative photoresist in microelectronics.
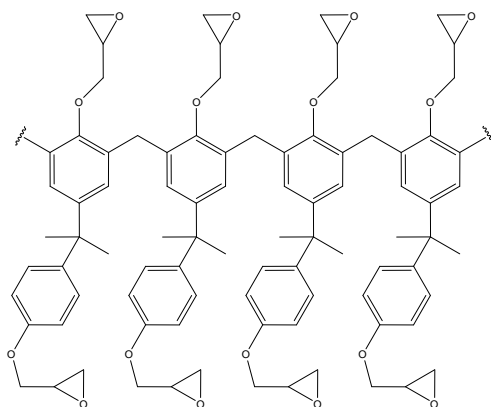
Figure 4-1. Molecular structure of a SU-8 oligomer. The cross-linking process depends on the triangular epoxide rings to react with the ones from nearby oligomer forming a covalent bond. This provides a very high cross-link level and the chemical strength of the material.
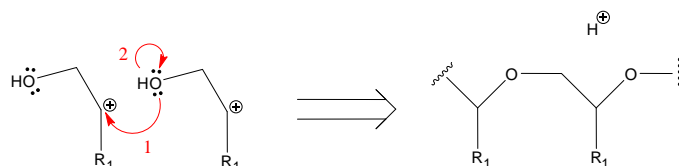
Reaction 4-1. The SU-8 oligomers crosslink when an open epoxide ring reacts with a similar neighbour. R_1 is an unspecified residue that does not participate in the reaction, which is the rest of the SU-8 oligomer molecule. Arrows indicate the movement of the electrons in the reaction.

The SU-8 is available in different formulations, such as SU-8 5, SU-8 25, SU-8 50: the difference is in the content of solvent, adjusted to have different resist viscosities and therefore thicknesses when spun on a wafer. Formulations with different solvents are available to improve the adhesion or to produce very thin layers. According to the manufacturer it is possible to obtain spin-coated thicknesses from 0.1 μm up to 2 mm [137][138]. Its thermal and chemical resistance, biocompatibility, and the sensitivity to UV radiation in the range 300-400 nm (therefore compatible with normal photolithographic equipment), made it also very suitable for micromachined applications and especially for bio-MEMS applications (for example in microfluidics). In fact, SU-8 is transparent in the near UV region, making possible to obtain structures with vertical walls and aspect ratios of 190 and more [139][140] as shown in Figure 4-2. The SU-8 formulation also contains a photoinitiator that under UV light exposure (maximum absorption at 365 nm) generates a strong acid that opens the epoxide rings to make them reactive. In this condition a nucleophilic addition occurs between adjacent former epoxide rings with the oxygen donating an electron to the now positively charged carbon ion as shown in Reaction 4-1. Given the high number of active groups in the
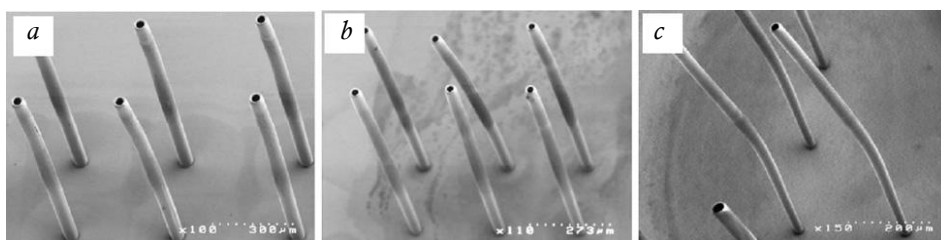
Figure 4-2. Image of 150 μm high microcylinders with wall thicknesses and internal diameters, respectively of a) 10 μm and 45 μm, b) 8μm and 30 μm and c) 6 μm and 20 μm. Structures were fabricated using a special technique to tackle the diffraction at the interface of mask and resist. Image taken from [140].

molecule, the extent of crosslinking of the SU-8 is very high, so the mechanical and chemical stability of the crosslinked resist is also high.

The good chemical and thermal resistance of crosslinked SU-8 has led to its use as a structural component in many different applications, from microfluidic structures [141][142], to microparticles to be used as drug carriers or for bioanalysis [143]-[145]. SU-8 is biocompatible [146][147] but the hydrophobicity of the crosslinked structures imposes limitations for biological applications. Surface modifications have been developed to modify the surface properties of SU-8, most of them based on the use of the residual epoxy groups on the surface as reactive sites [148]. Different chemical modification pathways have been explored, some of them dry modification techniques that use plasma treatment to change the wettability [149][150] or chemical functionalization using the decomposition of ammonia [151]. Wet methods provide more flexibility for modification: they range from strong acid treatment to provide hydroxyl groups [152][153] to direct reaction of amino-functionalized biomolecules, such as DNA or PEG, with the epoxide rings [154]-[156]. The direct reaction of primary amines and epoxy rings is usually the first step towards successive modifications, such as with antibodies [144][145]. A topical review on SU-8 exploring all the different characteristics of the resin has been published by Del Campo [140]. Of particular interest is metal coating of SU-8 structures [157] as gold is often used to bind thiolated biomolecules [117] and antibodies [158]. The process gold coating will be discussed din more detail in Chapter 7 .

4.2 Particle fabrication

Rod-shaped particles provide a means to study not only the rotation but also the orientation of a particle, while offering a reduced contact with the substrate because of the circular cross-section. Cylindrical particles can be easily fabricated using a simple photolithographic mask composed of circles, leaving the length of the rod dependent on the thickness of the resist.
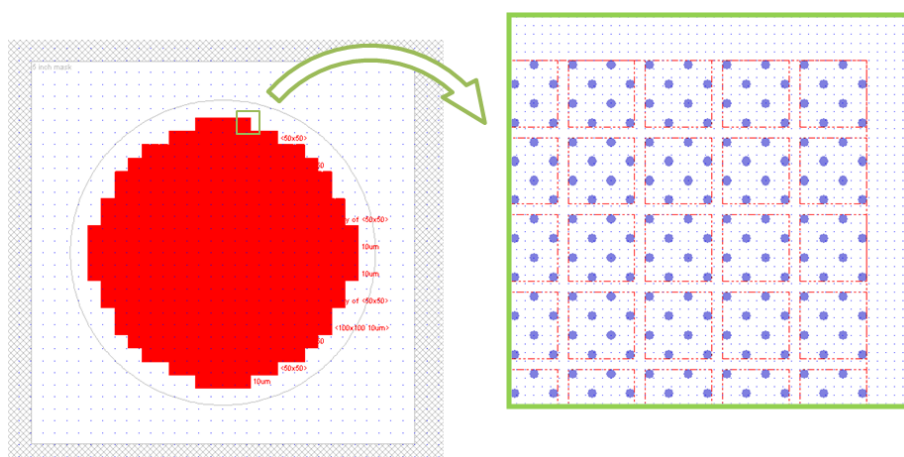
Figure 4-3. Left) Design of the photolithographic mask used to make the rod-shaped particles. The large white square defines the boundaries of the mask; the circular region defines the boundaries of the 4" wafer used in the fabrication. The red area is where the particles are. The edge of the wafer is kept clean from the particles to avoid the edge-bead, common during spin coating. Right) Detail of the mask, showing the contours of the elementary cell (red dashed lines) used to draw the mask. The blue dots define the position of the particles.
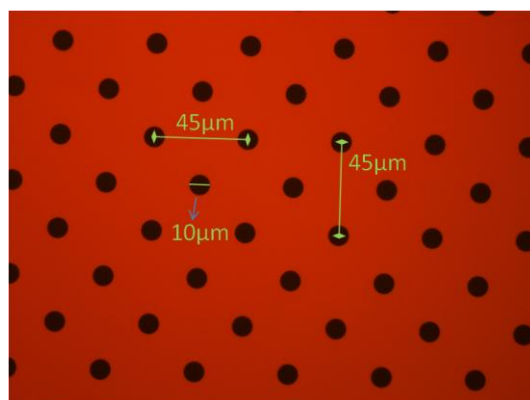
Figure 4-4. Detail of the finished photolithographic mask used to fabricate the rod-shaped particles. Bright parts are chromium; dark circles are quartz, i.e. holes in the mask. Picture taken with a 50x objective, reflected light.

4.2.1 The photolithographic mask

The photolithographic mask used for this thesis consisted of a vast array of dots, 10 μm diameter, giving a total number of 5,840,000 particles, as shown in Figure 4-3 and Figure 4-4. The mask was made of chromium on a 5" quartz substrate (Compugraphics [www.cgi.co.uk]), to be used with 4" wafers.
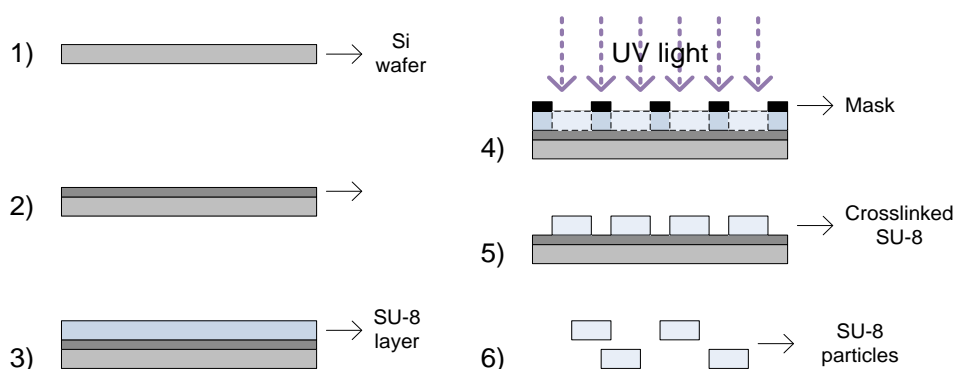
Figure 4-5. Process steps of SU-8 rods preparation by photolithography. (1) The process starts with a silicon wafer, (2) a 50 nm Al layer is deposited on the surface of the wafer, (3) SU-8 5 is spun with defined thickness on the Al layer, (4) the wafer is exposed to UV light using a negative mask, (5) the wafer is baked to cross-link the SU-8 (post-exposure bake) and developed, (6) exposing the particles to dimethylformamide (or alternatively etching the sacrificial layer) will release the SU-8 pillars from the wafer.

4.2.2 Fabrication method

The particles were made on a 4" silicon wafer with 50 nm aluminium coating. The aluminium layer was not used as sacrificial layer, like other work from our group [144], but just as an adhesion layer.

The work flow for the fabrication of the particles is shown in Figure 4-5. A clean wafer was left overnight in an oven at 210°C to dehydrate the surface. To improve the adhesion of the SU-8 to the aluminium, Ti-Primer [www.microchem.com] was spun onto the wafer at 3000 rpm for 30 seconds and baked on a hot-plate at 120°C for 2 minutes. About 4 ml of SU-8 25 was poured on the wafer and spun at 1000 rpm. The actual thickness depends on the age of the SU-8 and the spinner used, therefore the thickness of the resulting layer was measured to calibrate the exposure rate. The wafer was then soft-baked on a hot-plate at 65°C for 5 minutes and then at 95°C for 15 minutes to allow the solvent to evaporate. Using an EVG 620 mask-aligner the soft-baked samples were exposed through the mask with a dose of 200mJ/cm^2. After exposure, the wafer was baked at 65°C for one minute and then at 95°C for 4 minutes to crosslink the SU-8 and form the pattern. The resist was then developed in acetone for 30 seconds, and then rinsed with clean acetone, isopropyl alcohol (IPA) and blown dry.

The standard procedure suggested by the manufacturer recommends the use of EC Solvent, which is a proprietary developer from Microchem. Given the geometry of the pattern, the EC Solvent was found to be ineffective in removing the non-crosslinked SU-8. Because of the strong chemical stability of the crosslinked SU-8, the EC Solvent was replaced with acetone
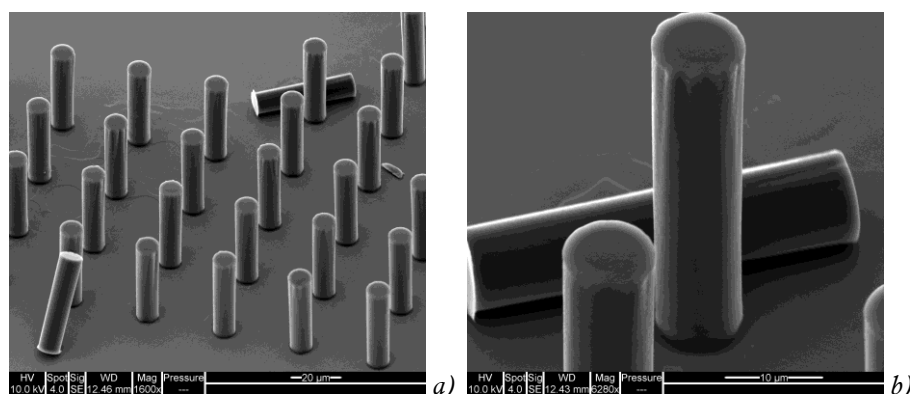
Figure 4-6. a) SEM picture of rod-shaped particles on a wafer after a partial lift-off; b) detail of the particles. Samples were coated with ~10 nm gold before imaging.

as a developer, see [http://memscyclopedia.org/su8.html 12/10/2010] and [159]. Acetone has a lower surface tension and is more aggressive than the EC Solvent, consequently the developing time was about 30 seconds in a Petri dish. After that time the wafer was washed with clean acetone and rinsed with IPA. If white traces were still present, the wafer was rinsed again with acetone using a squeezing bottle and rinsed again with IPA. Care was taken not to let the acetone dry out on the sample to avoid thermal stress of the particles. The resulting particles are shown in Figure 4-6.

Release of the particles from the substrate can be achieved using MF-319 [Shipley], but this metal etchant is usually acid[3] (also alkaline formulations can be found) and in an acid or basic environment the epoxide rings can open producing a surface rich in the much less reactive hydroxyl group (-OH). To preserve the reactivity of the surface, dimethylformamide (DMF) was used instead. DMF is a common solvent for chemical reactions but is also a well known paint stripper because it can penetrate most plastics to make them swell. The same happens to SU-8, allowing a quick release from the substrate because of the mechanical stress on the relatively small contact area. Lift-off of the particles was done in a 12 cm Petri dish using 10 ml of DMF. After 1 minute in an ultrasonic bath, all the particles were detached from the wafer and could be collected using a pipette. For a better recovery rate, the wafer and the Petri dish were washed with additional DMF. All the DMF was then collected in a 50 ml falcon tube and centrifuged to concentrate the particles, which were then transferred into a 2 ml eppendorf tube and washed once with clean DMF. The SU-8 rods were subsequently washed three times (3 x 1 ml) in methanol to remove the DMF, distributed in 10 different eppendorf tubes and vacuum dried in a desiccator. The actual dimensions of resulting dry particles are shown in Table 4-1.

---

[3] http://www.microchemicals.com/technical_information/aluminium_etching.pdf, retrieved on 05/03/2011.

	Particle sizes (aver ± std dev)
A (μm	44 ± 1
B (μm)	11.0 ± 0.3

Table 4-1. Average dimensions of 13 dry particles obtained after the lift-off and wash steps. A is the length of the rod, B is the diameter.

4.3 Chemical modification of particles

The surface conductance, which is related to the surface charge density, can be used as an electrical label to identify changes in particles. Commonly, a fluorescent label is used, that is a biomolecule complementary to the analyte under study, such as complementary DNA strands or an antibody-antigen pair which has been chemically modified to have a small fluorescent molecule covalently bound. The amount of target molecule is quantified by the amount of light measured after coupling to the probe molecule. This method, although simple, requires complicated chemical modification steps. An electrical labelling based on changes in the surface conductance may distinguish whether a binding event has happened or not without chemical modification. The surface conductance is related to the surface charge density of the particles, therefore changing the surface chemical properties of particles (for example by adsorption of proteins) should lead to a change in surface conductance

In this work particles with different surface chemistry were studied. Unfunctionalized SU-8 particles provide the starting point to all measurements and all chemical modifications. In a step by step process, the surface of the particles was changed according to the "road map" of Figure 4-7. All the different functionalisation steps aim to change the type (positive or negative) and number of charges on the surface of the particles, and to evaluate these changes with ROT and EO.

Native SU-8 particles do not carry a net charge at neutral pH but they have a surface rich in epoxide rings which are negatively polarized due to the oxygen in the ring. The epoxide rings (Table 4-2, P01) are very reactive because of the strain imposed on the oxygen atom, and can be used to covalently bind other molecules to obtain a surface with different chemical properties. Amine groups (Table 4-2, P02) carry a positive charge at neutral pH because they are in the form $-NH_3^+$. Particles modified with Jeffamine or polyethylene glycol (PEG) (Table 4-2, P03 - P04) will have a surface rich with amine groups but with a spacer. Carboxyl groups (Table 4-2, P05) instead give a negatively charged surface at neutral pH, of the form $-COO^-$.
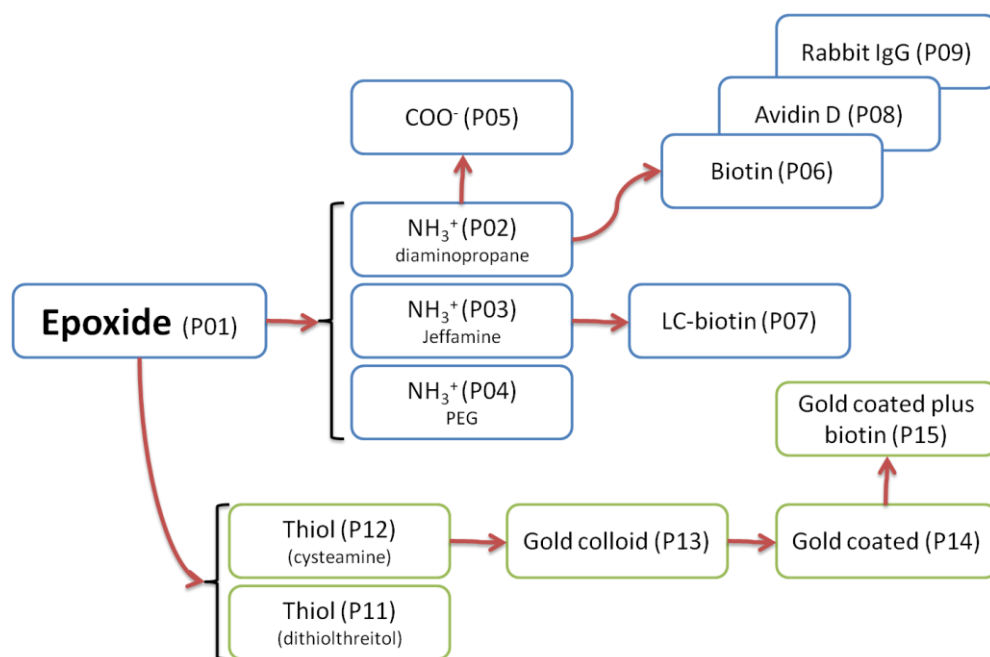
Figure 4-7. Road map of the different chemical modifications of the SU-8 particles performed in this work. The functionalisation routes in blue are described in this chapter, and the green ones are described in Chapter 7 .

Biotin modified particles (Table 4-2, P06 – P07) do not have a net charge, but they are used as intermediate step prior to functionalisation with avidin. Similar to epoxide rings, biotin has a polarised oxygen atom. Avidin is a protein which has a strong affinity for biotin (K_d=10^{-15} M^{-1}); it can bind 4 biotin molecules as shown in Figure 4-8a. The affinity is so high that the avidin-biotin complex can only be taken apart by using conditions so harsh as to denature the protein. Particles modified with avidin (Table 4-2, P08) should have a high charge density given by both positive and negative charges because proteins have a high number of carboxyl and amine groups. The actual net charge when suspended in an electrolyte depends on the isoelectric point (pI) of the protein, which is the pH at which the protein carries no net charge. At a pH below the pI, proteins carry a net positive charge; above the pI they carry a net negative charge. Avidin is used to immobilize biotinylated molecules, that are molecules that have been chemically modified to have one (or more) biotin moieties. In this work biotinylated IgG was immobilized onto avidin (Table 4-2, P09). IgGs are a class of antibody molecules composed of 4 peptide chains: two heavy chains and two light chains as shown in Figure 4-8b; each IgG has two antigens binding sites at the extremes of its characteristic "Y" shape. The immobilisation of the antibodies should increase the net surface charge density after the immobilization of avidin.

a)   b)
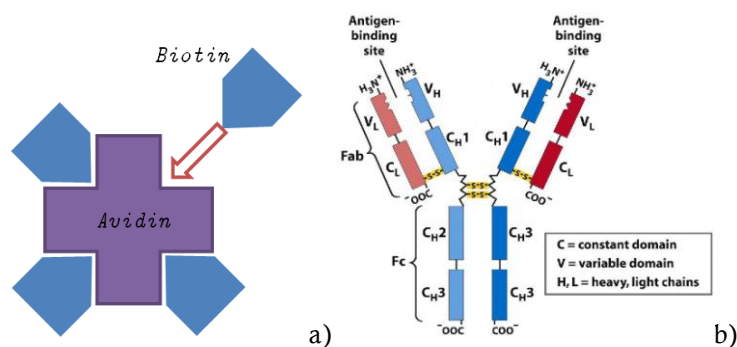
Figure 4-8. a) Avidin is a protein that has 4 binding sites for biotin. The interaction is very specific and strong; the bond can be broken only by denaturing the protein. b) Sketch of the molecular structure of IgG. The binding site is the active part of the molecule and depends on the targeted antigen. Adapted from http://chemistry.umeche.maine.edu/CHY431/Antibody2.jpg.

P01: native SU-8 particle.

P02: amino modified SU-8 particle using diaminopropane.

P03: amino modified particle with a Jeffamine spacer.

P04: amino modified particle with a PEG spacer.

P05: carboxyl modified SU-8 particle.

P06: biotin modified SU-8 particle

P07: biotin modified SU-8 particle with a spacer.

P08: Avidin immobilized onto biotinylated particle.

P09: IgG immobilized onto avidin.

Table 4-2. Summary of all the different types of particles studied in this chapter. Each of these particles has been studied using ROT and EO.

4.3.1 Modification with amine groups

The native SU-8 particles have residual surface (and bulk) epoxide rings which may not have participated in the crosslinking reaction and can therefore be used to change the properties of the particles. An example of the ring opening of the epoxide ring is shown in Reaction 4-2. The reaction is a nucleophilic addition under basic conditions, with the nucleophile attacking the less substituted carbon as shown in Reaction 4-2.
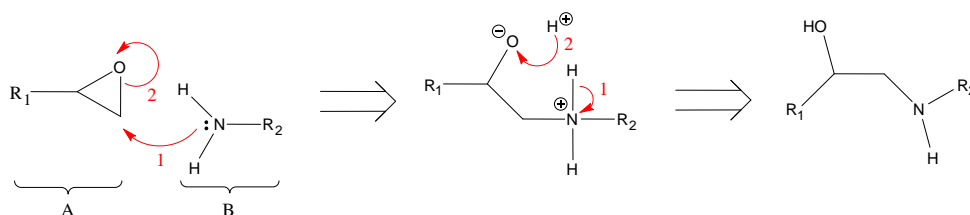
Reaction 4-2. Ring opening reaction by an amine group under basic conditions. Compound A is the native SU-8 particle, compound B is any molecule containing a primary amine. R_1 and R_2 are unspecified residues that do not participate in the reaction. Arrows indicate the movement of the electrons in the reaction.

The primary amine donates an electron to the carbon and causes the ring to open. There is then a proton transfer between the positively charged ammonium ion and the negatively charged oxygen, favoured thermodynamically towards the uncharged final molecule. This reaction is used in this work to obtain a surface rich in amine groups. This has been done using the three different molecules shown in Figure 4-9, to act as *B* in Reaction 4-2.
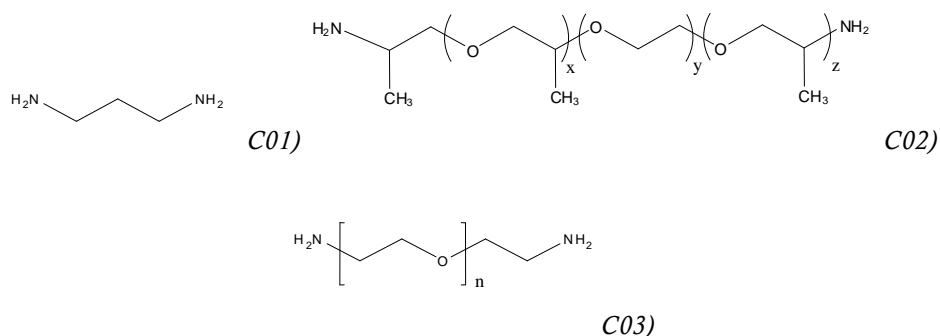
Figure 4-9. Molecules used to obtain a surface rich in amine groups. C01) diaminopropane, used to obtain particles P02; C02) Jeffamine ED-900 ($y \approx 12.5$, $x+z \approx 6$), used to obtain particles P03; C03) bis(amine) PEG, $n \approx 66$, used to obtain particles P04.

Diaminopropane (C01), Jeffamine ED-900 (C02) and bis(amine) PEG (C03) have two amine groups at opposite ends. C01 has a very short carbon chain, therefore the reaction of both the amine groups with epoxide rings is not favourable; on the other hand, C02 and C03 have

longer carbon chains, which means a number of them will react, binding both ends to the epoxide rings, not leaving any amine group exposed. Moreover, the molecules may fold over on themselves because the amine groups are positively charged, while all the oxygen atoms are slightly negatively polarized.

4.3.1.1 Modification with diaminopropane (C01)

Materials: Diaminopropane (D23602, Sigma), N,N-Diisopropylethylamine (DIPEA, 496219, Sigma), DMF

Methods: 2 mg of dry particles were resuspended in a solution composed by 20 μl of diaminopropane and 2 μl of DIPEA in 1 ml of DMF. The eppendorf with the mixture was left in a mixer overnight (~16 hrs) at room temperature. The following day the sample was washed three times with DMF (3 x 1 ml) and three times with methanol (3 x 1 ml) and the supernatant removed as much as possible. The eppendorf was then put in a vacuum desiccator for 4 hrs to dry the sample.

4.3.1.2 Modification with Jeffamine (C02)

Materials: Jeffamine ED-900 (14527, Sigma), DMF.

Methods: A solution composed of 500 μl Jeffamine and 500 μl DMF was added to 2 mg of SU-8 particles. The reaction mixture was then agitated at 50°C overnight. Particles were then washed 4 times (4 x 1 ml) in DMF and three times (3 x 1 ml) in methanol and then dried in a vacuum desiccator.

4.3.1.3 Modification with PEG (C03)

Materials: bis(amine) PEG-3000 (14502, Sigma), N,N-Diisopropylethylamine (DIPEA, 496219, Sigma), DMF

Methods: To the SU-8 particles (2 mg) was added a solution composed of 30 mg of PEG, 2 μl of DIPEA and 1 ml of DMF. The reaction mixture was then agitated on at 50°C overnight. Particles were then washed 4 times (4 x 1 ml) in DMF and three times (3 x 1 ml) in methanol and then dried in a vacuum desiccator.

4.3.2 Modification with succinic anhydride (C04)

Particles P05 can be obtained from P02 through succinilation using the molecule C04 in Figure 4-10. The reaction, which is again a nucleophilic addition, gives as final product carboxyl groups as explained in Reaction 4-3

C04)
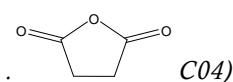
Figure 4-10. Molecule of succinic anhydride, used in the reaction of succinilation of primary amine groups to obtain a carboxyl group.
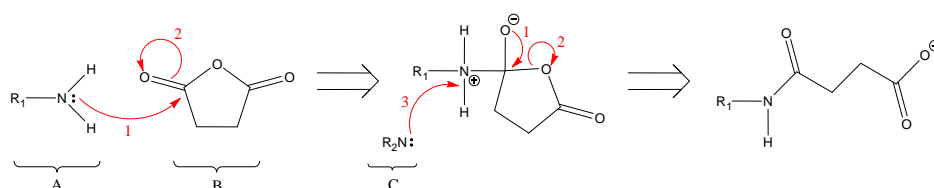
Reaction 4-3. Reaction of succinilation of a primary amine group. A is particle P02, B is succinic anhydride C04, C is an organic base in solution. R_1 and R_2 are unspecified residues that do not participate in the reaction. Arrows indicate the movement of the electrons in the reaction.

Materials: Succinic anhydride (239690, Sigma), 4-(Dimethylamino)pyridine (DMAP, 522805, Sigma), N,N-Diisopropylethylamine (DIPEA, 496219, Sigma).

Methods: 2 mg of amino-functionalised particles was added to a solution composed by 4 mg of succinic anhydride, 4 mg of DMAP and 2 μl of DIPEA in 1 ml of DMF. The mixture was left overnight (~16 hrs) on a mixer at room temperature. The following day the sample was washed three times with DMF (3 x 1 ml), three times with methanol (3 x 1 ml) and the supernatant removed as much as possible. The eppendorf was then put in a vacuum desiccator for 4 hours to dry the sample.

4.3.3 Biotinylation

A further modification of the SU-8 particles is obtained using particles P02 to obtain particles with a surface rich in biotin, i.e. particles P06 and P07. Those particles are obtained using the molecules in Figure 4-11.

C05)

C06)
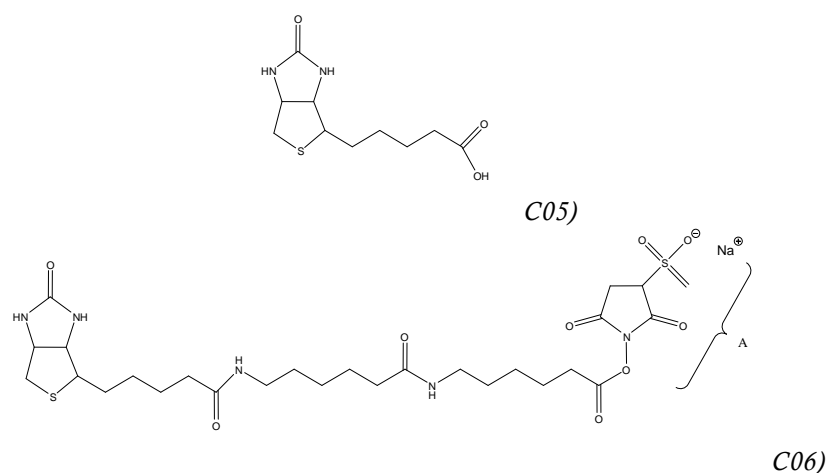
Figure 4-11. Molecules used to obtain a surface rich in biotin. C05) biotin; C06) sulfo-NHS-LC-LC-biotin. LC stands for "long chain", sulfo-NHS is the part marked with A. C06 is the biotin molecule C05 with already bound a spacer and a pre-activated carboxyl group at the right end side of the molecule.

Particles P06 are obtained from P02 through a preactivation of the biotin's carboxyl group and the reaction with the amine group from P02. The preactivation is needed to favour the reaction and is done using sulfo-NHS. Sulfo-NHS binds to the biotin's carboxyl group with a weak bond as in Reaction 4-4, and facilitates the reaction with a primary amine.
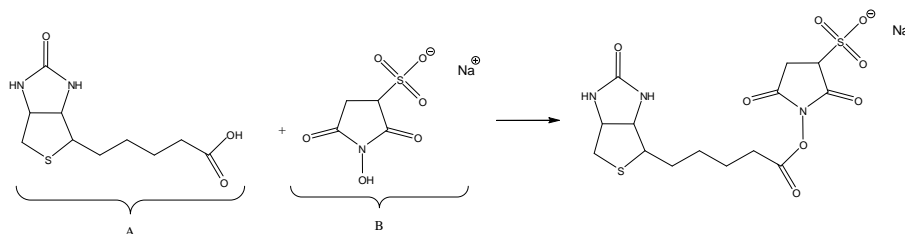
Reaction 4-4. Preactivation of the biotin's carboxyl group. The sulfo-NHS (B) is weakly bound to biotin (A), to facilitate the reaction with a primary amine.

The preactivated biotin molecule, which is an unstable compound, reacts with a primary amine to form a stable amide covalent bond and release the sulfo-NHS in solution as shown in Reaction 4-5.
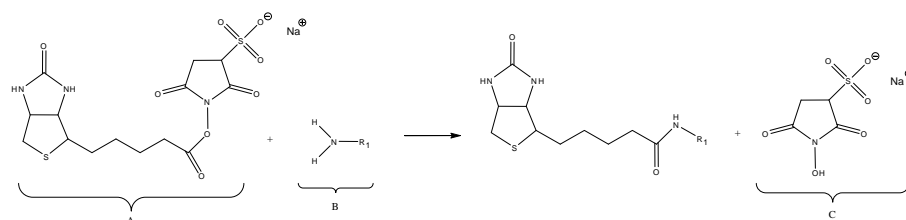
Reaction 4-5. Reaction scheme of a preactivated biotin molecule (A, following Reaction 4-4) with a primary amine. The amine group comes from particle P02 (B), to form an amide bond. At the end of the reaction the sulfo-NHS (C) is released in solution. R_1 is an unspecified residue that does not participate in the reaction.

Particles P07 are obtained from P03 using sulfo-NHS-LC-LC-biotin (C06). C06 consists of a molecule of biotin bound to a 3 nm spacer, ending with a carboxyl group already preactivated with sulfo-NHS. C06 forms a bond with primary amine in the same way as C05 in the preactivated form as seen in Reaction 4-4.

4.3.3.1 Modification with biotin (C05)

Materials: Biotin (B4639, Sigma), N-(3-Dimethylaminopropyl)-N′-ethylcarbodiimide hydrochloride (EDC.HCl, 03449, Sigma), N-Hydroxysulfosuccinimide sodium salt (sulfo-NHS, 56485, Sigma), MES sodium salt (M5057, Sigma), NaCl, Tween-20.

Methods: An activation buffer was prepared using 100 mM MES, 150 mM NaCl and 0.02% Tween-20 in DI water. The buffer was then adjusted to pH 6 using 1 M HCl. 2 mg of amino-modified particles were suspended in a mixture composed of 20 mg of biotin, 1 mg EDC.HCl and 1 mg sulfo-NHS in 1 ml of activation buffer and agitated at room temperature overnight. The sample was then washed four times in de-ionised (DI) water (4 x 1 ml) to remove the chemical reagents.

4.3.3.2 Modification with sulfo-NHS-LC-LC-biotin (C06)

Materials: EZ-Link Sulfo-NHS-LC-LC-biotin (21338, Thermo), Phosphate Buffer Saline (PBS)

Methods: 2 mg of amino-modified particles were added to a mixture of 4 mg of Sulfo-NHS-LC-LC-biotin in 1 ml of PBS and agitated overnight. The sample was then washed three times with PBS and 0.02% Tween-20

4.3.4 Immobilization of proteins

Particles P08 are obtained from P07 by exposing them to a suspension of avidin. Biotin binds firmly to avidin with a dissociation constant of $K_d = 10^{-15}$ M^{-1}. Avidin has 4 binding sites;

therefore after the immobilization onto the surface of particles P07 there will be free binding sites that can be used to immobilize other molecules or proteins. In our case biotinylated IgG is immobilized onto P08 by exposing these particles to a suspension of IgG.

4.3.4.1 Immobilization of avidin

Materials: Rhodamine-labelled avidin D solution (A-2002, Vector), PBS, Tween-20.

Methods: 25 μl of avidin D was added to 1 ml of PBS with 0.02% Tween-20. 2 mg of biotin-functionalised particles were then resuspended in the PBS solution and left overnight on gentle shaking. The sample was then washed 4 times (4 x 1 ml) in PBS and 0.02% Tween-20.

4.3.4.2 Immobilization of IgG

Materials: Biotinylated rabbit IgG (BI-1005, Vector), PBS, Tween-20.

Methods: 100 μl of rabbit IgG suspension, was added to 1ml of PBS with 0.02% Tween-20. 2 mg of avidin-functionalised particles were then resuspended in the PBS solution and left overnight on gentle shaking. The sample was then washed 4 times (4 x 1 ml) in PBS with 0.02% Tween-20.

4.4 Preparation of the suspending electrolyte

Every electrokinetic measurement in this work was done using the same suspending electrolyte in order to have comparable results. Particles were washed three times in the suspending electrolyte before measurements. The buffer should have a low conductivity and a stable neutral pH to allow the analysis of particles with either amine or carboxylic groups on the surface. HEPES was used, because it is a low conductivity zwitterionic organic buffer agent.

Materials: 4-(2-Hydroxyethyl)piperazine-1-ethanesulfonic acid (HEPES, 54459, Sigma), KCl, NaOH, Tween-20.

Methods: The suspending electrolyte was prepared using 10 mM KCl, 20 mM HEPES in DI water. The solution was buffered with NaOH to pH=7.0 using a pH-meter, then diluted 1:100 and 0.02% Tween-20 was added. The solution had a conductivity of 2.01 mS/m, measured with a calibrated conductivity meter. The buffer prepared was divided into 50 ml falcon tubes and frozen until use. The Debye length associated with the buffer can be estimated for the final concentration of KCl; using a concentration of 0.1 mM the Debye length is λ_D=30 nm. The contribution of the HEPES can be ignored to a first approximation because the diffusion coefficient is 4 times smaller than KCl.

Chapter 5

Method development

5.1 Introduction

In this Chapter the optimal measurement methodology will be presented. We will show how the equations of the motion in Chapter 2 will be used to fit the electrokinetic spectra to take into account the observation that the motion of particles during ROT and EO differs, due to contact with the glass substrate in the case of EO. The effect of water evaporation on the calculated electrical properties of particles and suspending electrolyte will be investigated in the case of sample chamber open and closed. In the case of sample chamber closed with a coverslip, it will be demonstrated that the change in electrolyte conductivity during the first minutes is negligible.

5.2 Fitting strategy

During the ROT experiment it was observed that negative DEP causes the SU-8 rods to float above the glass, while moving on the glass during EO measurements. This difference in the position of the particles is due to the stronger DEP force created when using 4 electrodes (ROT) rather than 2 (EO). The stronger force is due to the fact that when performing ROT the energy delivered is double because there are 2 more electrodes applying a voltage in the chamber. Particles also experience a higher viscous drag when moving near the glass. To take this into account, the scaling factor for the EO measurements was defined as equal to the

ROT scaling factor multiplied by an additional factor (smaller than one). Using 10 native unmodified SU-8 particles, the result of each fit was studied by changing the permittivity of the particle ε_p in a stepwise manner (i.e. it was not a free parameter) and leaving the scaling factor (*Scaling factor*), the additional factor for the EO measurements (*Adjustment factor*), the conductivity of the medium and the particle surface conductance as free parameters. A fit was performed for values of the particle relative permittivity ranging from 4 to 12 and the average results for all the particles are reported in Table 5-1.

$\varepsilon_p/\varepsilon_0$	Scaling factor	Adjustment factor	K_S	σ_m
4	11.6	0.511	/	0.0024
5	9.3	0.65	/	0.0023
5.5	8.5	0.71	/	0.0024
6	7.9	0.78	0.0008	0.0024
6.5	7.5	0.82	0.02	0.0024
7	7.8	0.81	0.11	0.0024
7.5	8.4	0.77	0.21	0.0024
8	9	0.73	0.32	0.0024
9	10.8	0.64	0.55	0.0024
10	200	0.4	0.92	0.0025
10.5	400	0.29	1.3	0.0027
11	810	0.05	1.84	0.0032
12	740	0.011	2.1	0.0033
13	640	0.0127	2.3	0.0033
14	550	0.0151	2.4	0.0033

Table 5-1. Results of the fit for the different particle permittivities (left column). The resulting values for the Scaling factor, the Adjustment factor, the particle surface conductance K_S, and the electrolyte conductivity σ_m are reported in the corresponding columns. The significant digit was chosen according to the standard deviation measured (not reported).

Values of particle relative permittivity lower than 6 did not produce any physically meaningful result ($K_S < 0$). On the other hand values higher than 10 produced a wrong result for the suspending electrolyte conductivity and a correction factor that was too low. The value of the surface conductance increases with particle permittivity (in the range 6-10 $\varepsilon_r/\varepsilon_0$) while the electrolyte conductivity does not change, therefore the values of the *Scaling factor* and the *Adjustment factor* at different frequencies were compared to find an optimum value for the *Adjustment factor*. From Figure 5-2 the point of maximum *Adjustment factor* and minimum *Scaling factor* was chosen as the optimum, giving to a value of *Adjustment factor=0.82*. The fact that the *Adjustment factor* is smaller than one does not reflect a difference in the electric field distribution but a difference in the viscous drag acting on the particles moving onto the glass substrate.
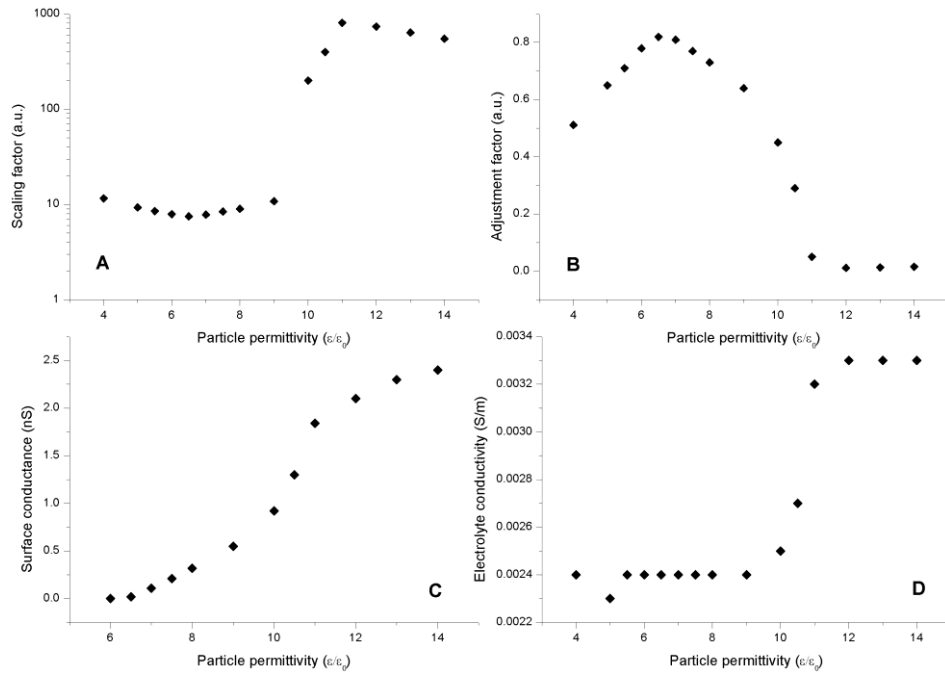
Figure 5-1. Dependence of the 4 fit parameters as a function of the particle permittivity. Data were obtained keeping the particle permittivity fixed and fitting the ROT and EO spectra to obtain a value for the 4 different parameters, the fit was then repeated with a different particle permittivity.
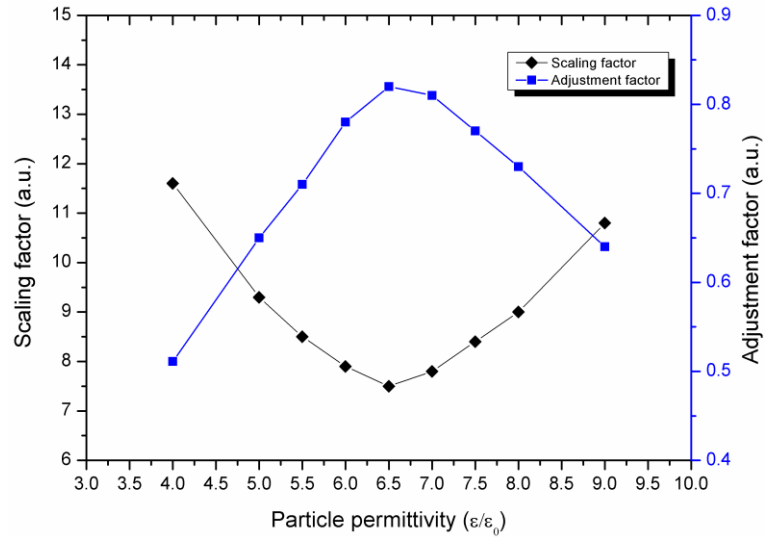
Figure 5-2. Extract of the data in Figure 5-1. The value of Scaling factor and Adjustment factor are compared for different particle permittivity values. The extract of the data show a correlation between the two.

5.3 Effect of evaporation: chamber open and chamber closed

The effect of evaporation was investigated by measuring the change in the electrical properties of suspending electrolyte and particles with time. Two different experiments were run, one with an open chamber and one with a coverslip closing the chamber. A single particle was placed in the middle of the electrodes and the ROT and EO spectra were acquired continuously every 13 minutes for a total of 8 runs.

5.3.1 Chamber open

A particle was placed in the middle of the quadrupolar electrodes and the chamber was left open. A series of a ROT spectrum and an EO spectrum were taken in sequence one after the other to analyse the time dependence of the system. The data were fitted using the average dimensions of the particle ($2a=50.3 \pm 0.1$ μm, $2b=11.8 \pm 0.2$ μm) for each snapshot and the results are in Figure 5-3. The change of suspending electrolyte conductivity was measured from the data in Figure 5-4c (through linear fit) to be 18 ± 1 μS m^{-1} min^{-1}.

5.3.2 Chamber closed

The same test was repeated with a different particle but in a closed chamber. The particle used in this second test had dimensions equal to $2a=51.2 \pm 0.1$ μm and $2b=12.0 \pm 0.2$ μm. The experiment was repeated in the same way and the results are shown in Figure 5-5. In the case of a closed chamber, the conductivity is not linear with time but changes after the second measurement. The change in conductivity can be evaluated as 12 ± 1 μS m^{-1} min^{-1}, smaller than for the open chamber.
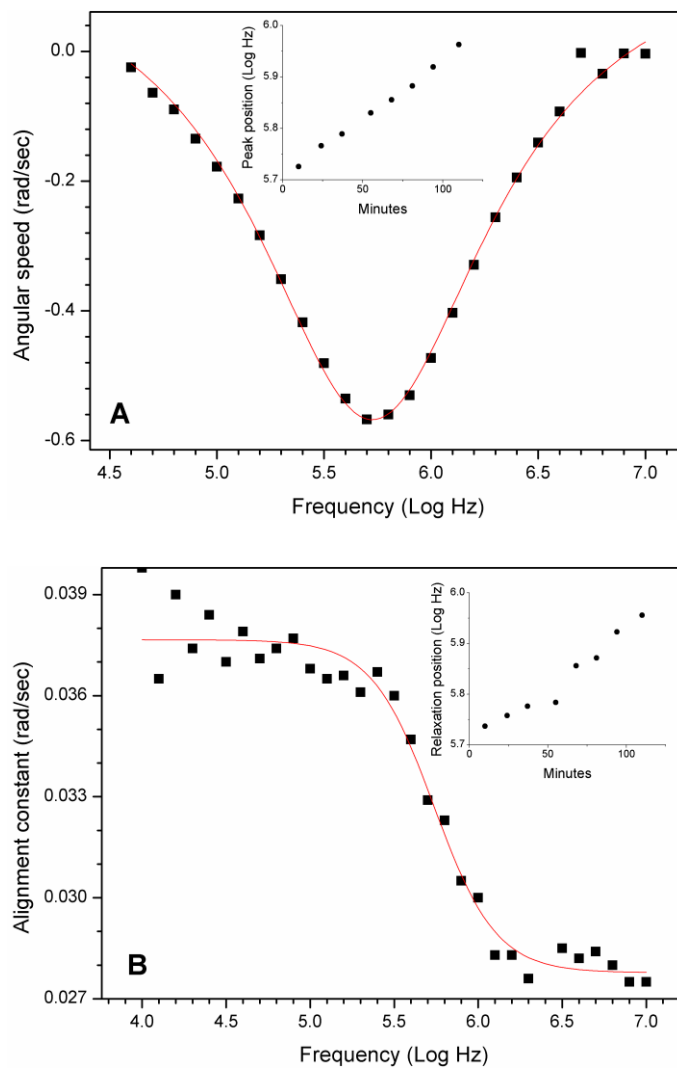
Figure 5-3. Variation in ER on ROT spectra for the open chamber. a) ROT spectrum for a particle at time t=0, the solid line is the resulting fit of the data using a Lorentzian, in the inset is plotted the position of the peak at different times for the same particle; b) the corresponding EO spectra at time t=0, the solid line is the resulting fit using a sigmoid, in the inset is plotted the position of the relaxation at different times for the same particle. All the spectra are normalized to 1V.
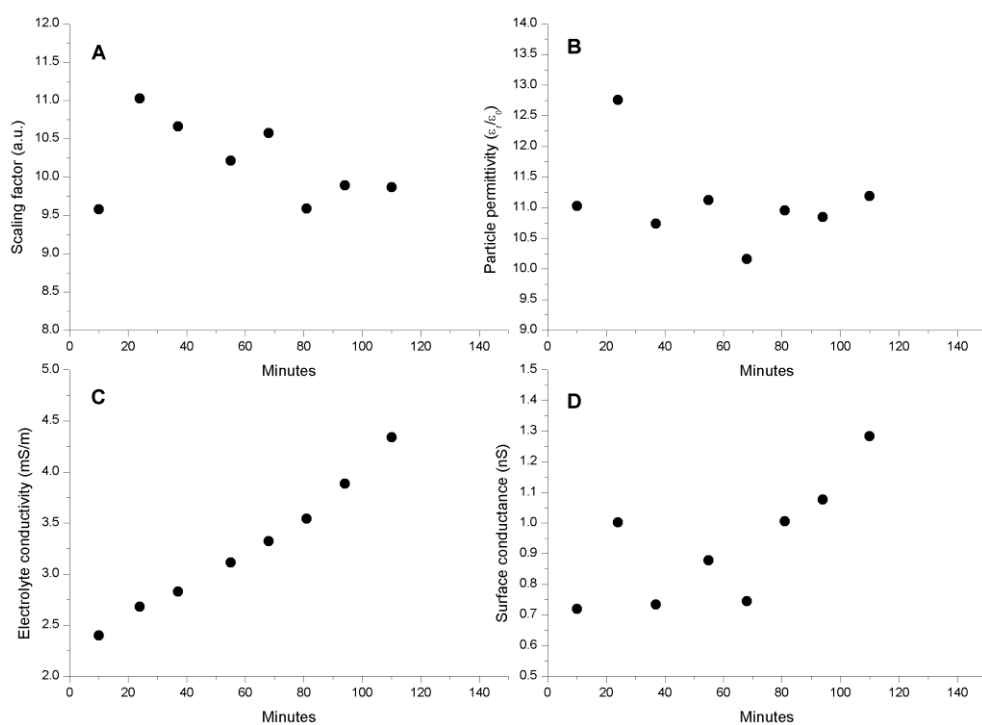
Figure 5-4. Fit results of the open chamber electrokinetic measurements. The ROT and EO spectra taken at different times for the same particle were fitted to obtain the four electric parameters which are plotted at the corresponding time to show the change with time. a) Scaling factor; b) particle permittivity; c) electrolyte conductivity; d) surface conductance.
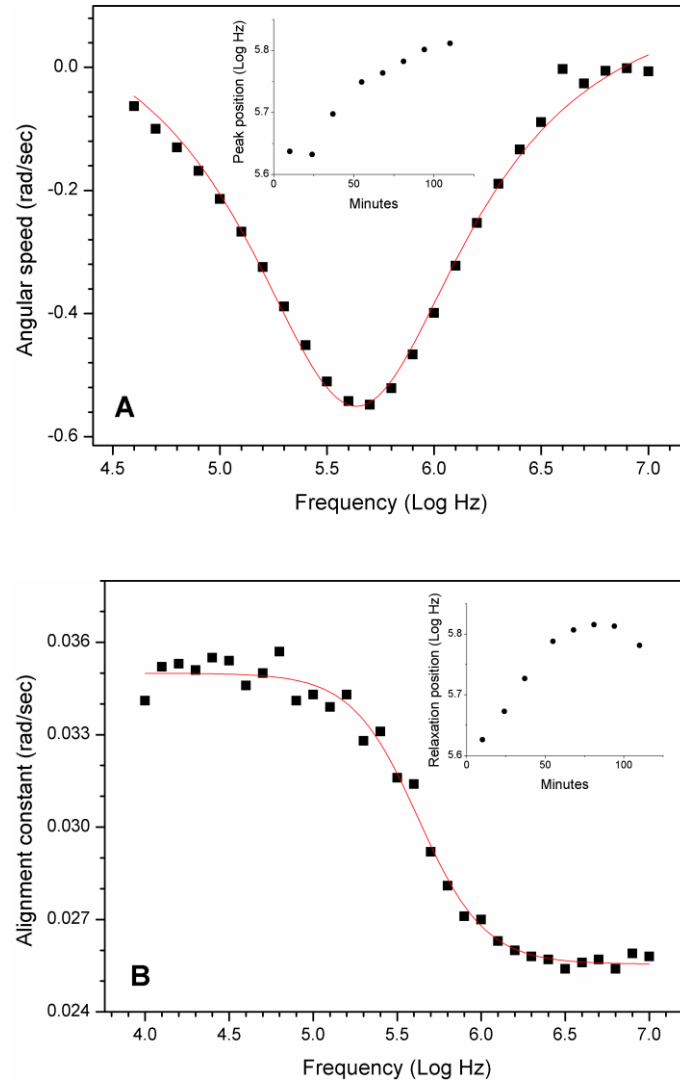
Figure 5-5. Change of the electrokinetic spectra for the closed chamber. a) ROT spectrum for a particle at time t=0, the solid line is the resulting fit of the data using a Lorentzian, inset shows the position of the peak at different times for the same particle; b) the corresponding EO spectra at time t=0, the solid line is the resulting fit using a sigmoid, in the inset is plotted the position of the relaxation at different times for the same particle. All the spectra are normalized to 1V.
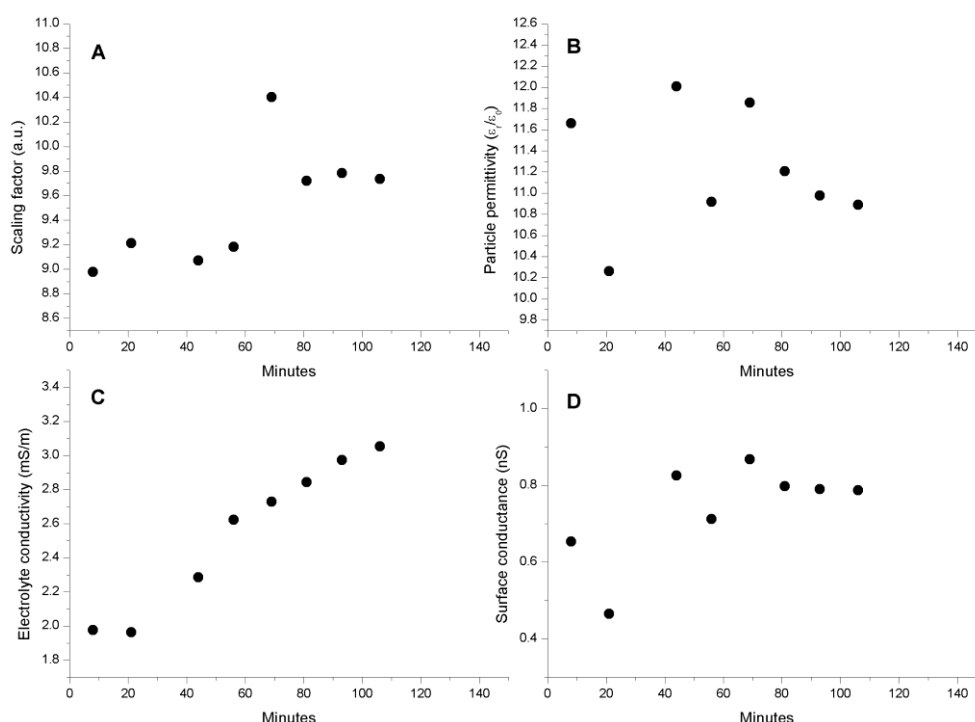
Figure 5-6. Fit results for the closed chamber electrokinetic measurements. The ROT and EO spectra taken at different times for the same particle were fitted to obtain the four electric parameters which are plotted at the corresponding time to show the change with time. a) Scaling factor; b) particle permittivity; c) electrolyte conductivity; d) surface conductance.

5.4 Discussion

Leaving the chamber open causes a faster evaporation of the suspending electrolyte, therefore a faster increase in the electrolyte conductivity: from 12 ± 1 µS m^{-1}min^{-1} to 18 ± 1 µS m^{-1}min^{-1} compared with a closed chamber. Keeping the chamber closed will slow down the change of electrolyte conductivity and therefore a change in the particle surface conductance. The change of conductivity is linear with time because the evaporation is constant and continuous. In the case of the closed chamber, after the initial stage, the conductivity seems to increase linearly but at a smaller rate. This behaviour is caused by the evaporation of the water in contact with the coverslip outside the chamber as shown in Figure 5-7. The water outside the chamber, hanging from the coverslip, forms a seal that stops the evaporation of the water inside the chamber. The very narrow gap between the coverslip and the chamber walls does not allow diffusion between outside and inside even if not actually sealed. This explains the stationary phase in Figure 5-5c: even as water on the outside evaporates and its conductivity increases, the water inside is not affected. When all the water outside is evaporated, the water inside starts to evaporate but slowly because of the coverslip closing the chamber: the process is still linear but the rate is smaller.
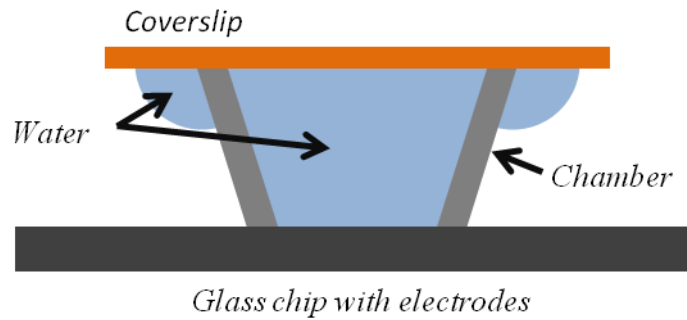
Figure 5-7. Schematic representation of the distribution of the water on the chip in the case of a closed chamber. The water hanging outside the chamber on the coverslip seals the chamber itself, slowing down the evaporation without affecting the electrolyte conductivity because of the slow diffusion between inside and outside.

Data in Figure 5-4 and Figure 5-6 show that the particle permittivity and scaling factor are roughly independent of time, while the suspending electrolyte conductivity and the particle surface conductance are time dependent.

5.5 Conclusions

In this Chapter the development of the optimal measurement methodology was presented. The best fitting strategy and the arrangement of the sample chamber that takes into account real experimental conditions such as friction on the glass and evaporation were investigated

Following the observation that particles move onto the glass substrate during EO but floats few microns above it during ROT, one more scaling factor was added to the fitting equations. This additional scaling factor was calculated by studying its relationship with the variation of the others fit parameters while fitting unfunctionalised SU-8 rod-shaped particles. The value of this additional factor was used as fixed parameter in Chapter 6 data fitting.

The time dependence of the fit values of the electrical parameters was also investigated. When the water in the chambers evaporates its conductivity increases and that could be seen clearly in the increase of the suspending electrolyte conductivity obtained with the data fit. This problem can be tackled closing that chamber with a glass coverslip. The coverslip forms a seal that slow down the evaporation and the change in conductivity. In particular, the conductivity does not change during the first minutes when using the coverslip. This suggests the strategy of replacing the suspending electrolyte with fresh one after 2 or 3 particles are measured.

Chapter 6

Biochemically Modified SU-8

Particles

6.1 Introduction

SU-8 particles offer a suitable substrate for electrokinetic based biosensing because they can be easily produced using standard photolithography and chemically modified to obtain a surface with a wide range of properties. The chemical modifications of SU-8 particles presented in Chapter 4 will be here studied using ROT and EO on a single particle basis, using the setup presented in Chapter 3 . SU-8 rod-shaped particles were analysed before and after a series of biochemical functionalisations aimed to obtain a surface with immobilised antibodies. At each step the particles changed their surface properties becoming positively charged, negatively charged or having immobilised proteins. In this Chapter the electrokinetic spectra of the particles at each stage of the biochemical modification will be presented and their electrical and physical properties will be discussed in relation to the chemical modification process involved.

6.2 Electrokinetic study of chemically modified SU-8 rods

6.2.1 Native SU-8 (P01)

Native SU-8 particles were prepared from a vacuum dried pellet and resuspended in the electrorotation buffer. They offer a reference point for the following chemical modifications. Comparing their chemical and electrical properties with the ones of the modified particles will give important information on the effect of the chemical reaction performed.

The ROT and EO spectra obtained from 12 particles from the same batch are in Figure 6-1. Average particle dimensions, as obtained from the snapshots, are reported in Table 6-1. Fit results are in Table 6-2.

	Particle sizes (aver ± std dev)
A (µm)	47 ± 2
B (µm)	11.8 ± 0.3

Table 6-1. Particle P01 average dimensions obtained from the snapshots of the particles analysed. A is the length of the rod, B is the diameter.

Figure 6-1. a) ROT and b) EO spectra of native SU-8 rods (particles P01). Spectra are normalized to 1V.

Scaling factor	σ_m (mS/m)	ϵ_p	K_S (nS)	Correlation
8.4 ± 0.3	2.4 ± 0.1	9.8 ± 0.3	0.48 ± 0.04	ROT 0.999 ± 0.001 EO 0.986 ± 0.005

Table 6-2. Fit results of the ROT and EO spectra of P01 particles. The error is the standard error.

6.2.2 Amino modified SU-8 rods

In this set of chemical reactions, the epoxide rings of the native particles are modified in order to obtain a surface rich in amine groups. Amine groups are positively charged at pH=7, while the epoxide rings do not have any net charge (they are polarized though), therefore the surface conductance should increase. Amine groups are important because they are common in biological molecules (such as proteins and DNA) and can easily react with carboxyl groups to achieve further modifications. Two different sets of reactions were performed using molecules with different lengths in order to test the reactivity (i.e. how much the surface conductance changed) and the effect of the distance of the amine group from the surface. We found that Jeffamine can heavily modify the bulk properties of the particles altering their permittivity.

The result of a modification with amine groups is determined using a Kaiser test, which is a colorimetric assay used to detect primary amine (-NH$_2$). The test is performed in ethanol at 115°C for 5 minutes and a deep blue colour is formed, proportional to the number of primary amines in solution, quantified by measuring the absorbance at 570 nm. The Kaiser test was performed after the reaction for the P03 particles to validate the reaction scheme in Reaction 4-2. The results of the absorbance measurements, after reaction with 0.55 mg of particles are in Table 6-3.

	Absorbance
blank sample	0.0331 ± 0.0004
P01 particles	0.076 ± 0.03
P03 particles	0.191 ± 0.002

Table 6-3. Absorbance measurements at 570 nm after the Kaiser test reaction on 0.55 mg of particles. Blank sample are the unreacted Kaiser test reagents, P01 are the native SU-8 particles, P03 are particles functionalised with Jeffamine. The error is the standard deviation of three measurements.

Using the extinction coefficient of the dye (15700 M^{-1}cm^{-1} [160]) and the light-path length (0.47cm for 150 μl of solution in a 96-well plate), the number of moles of amine groups is 26 ± 3 μmol, which corresponds to a loading level of 0.12 ± 0.01 mol/m^2 on the surface of the particles. The theoretical loading level is $1.8*10^{-5}$ mol/m^2, which was obtained comparing the

area of the surface of the particles with the area given by the lateral dimensions of an amine group sitting on a surface ($0.09 \ nm^2$). The ratio between the measured and the theoretical maximum surface loading level gives the corresponding number of monolayers of amine groups onto the particle surface, which is 6600 ± 500. This means that the modification of the particles is not purely on the surface, but also affects the bulk. The Kaiser test was not repeated on particles P02 modified with diaminopropane because the reaction pathway is the same but the molecule is much smaller than Jeffamine and therefore more reactive. For that reason diaminopropane in expected to react also inside the bulk of the particles as observed for P03.

The samples were prepared from a vacuum dried pellet and resuspended in the electrorotation buffer before the experiment.

6.2.2.1 Particles modified with diaminopropane (P02)

The ROT and EO spectra obtained from 10 particles from the same batch are in Figure 6-2. Average particle dimensions, as obtained from the snapshots, are reported in Table 6-4. Fit results are in Table 6-5.

	Particle sizes (aver ± std dev)
A (μm)	47 ± 1
B (μm)	12.1 ± 0.6

Table 6-4. Particle P02 average dimensions obtained from the snapshots of the particles analysed. A is the length of the rod, B is the diameter.
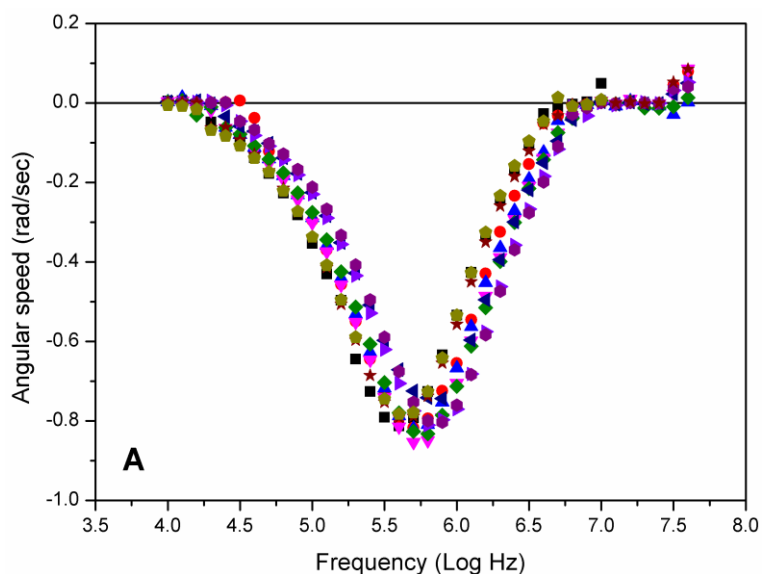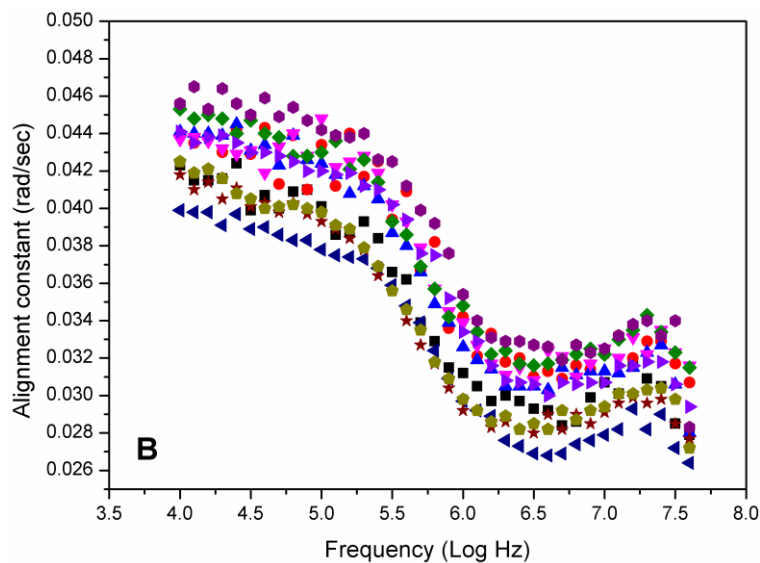
Figure 6-2. a) ROT and b) EO spectra of amino-modified SU-8 rods (particles P02). Spectra are normalized to 1V.

Scaling factor	σ_m (mS/m)	ϵ_P	K_S (nS)	Correlation
8.5 ± 0.4	2.4 ± 0.2	10.8 ± 0.3	0.47 ± 0.05	ROT 0.997 ± 0.001 EO 0.987 ± 0.005

Table 6-5. Fit results of the ROT and EO spectra of P02 particles. The error is the standard error.

6.2.2.2 Particles modified with Jeffamine (P03)

The ROT and EO spectra obtained from 14 particles from the same batch are in Figure 6-3. Average particle dimensions, as obtained from the snapshots, are reported in Table 6-6. Fit results are in Table 6-7.
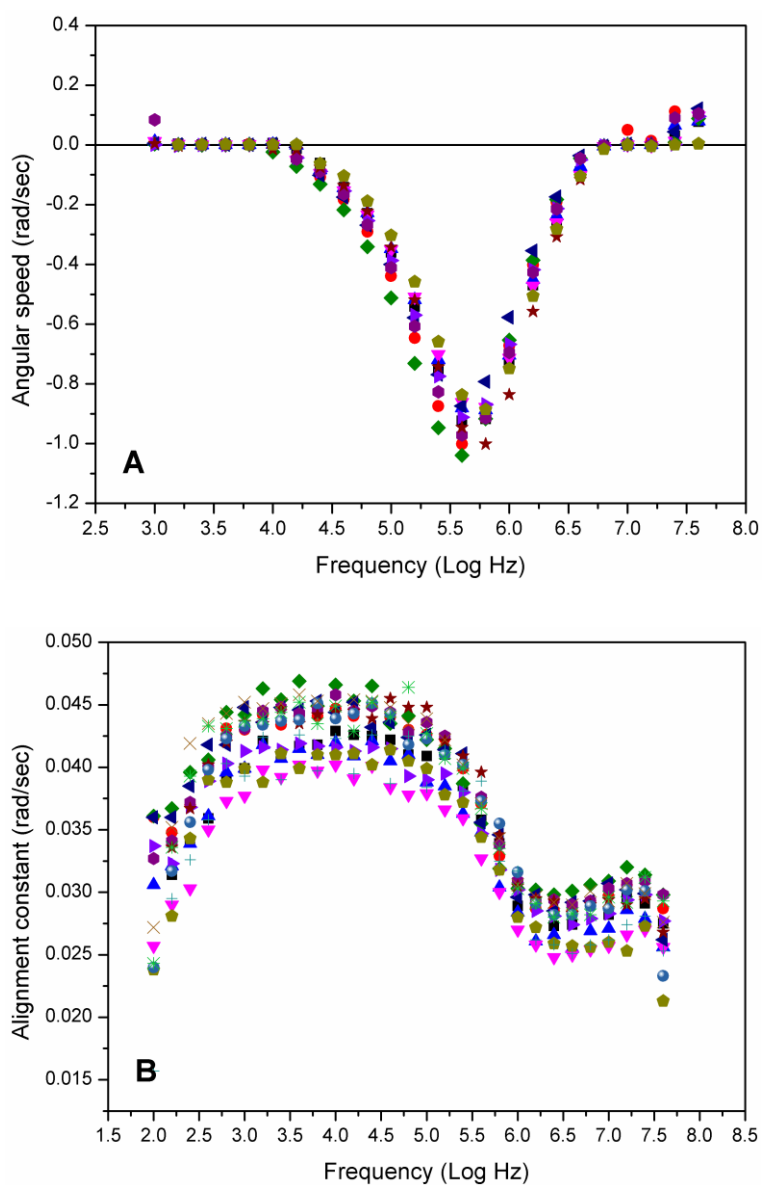
Figure 6-3. Extended a) ROT and b) EO spectra of SU-8 particles modified with Jeffamine (P03). Spectra are normalized to 1V.

	Particle sizes (aver ± std dev)
A (μm)	47.9 ± 0.7
B (μm)	12.1 ± 0.3

Table 6-6. Particle P03 average dimensions obtained from the snapshots of the particles analysed. A is the length of the rod, B is the diameter.

Scaling factor	σ_m (mS/m)	ϵ_P	K_S (nS)	Correlation
9.3 ± 0.2	2.04 ± 0.09	14.0 ± 0.4	0.65 ± 0.07	ROT 0.9959 ± 0.0009
				EO 0.992 ± 0.005

Table 6-7. Fit results of the ROT and EO spectra of P03 particles. The error is the standard error.

The decrease in the alignment constant at low frequency is not described by the Maxwell-Wagner theory, therefore in order to fit the data the low frequency EO spectra were trimmed at 10kHz, to leave only the plateau.

6.2.3 Particles modified with succinic anhydride (P05)

The aim of this experiment was to test the effect of a change in the sign of the charge on the surface of particles. The amino groups of the amino modified particles were reacted with succinic anhydride to have a surface rich in carboxyl groups, which are negatively charged at pH=7. The completeness of the reaction could be assessed using again the Kaiser test: when the reaction is completed virtually no primary amine groups should be left on the particles and the test result should be negative. The completeness of the reaction was not measured in this work, but the change in the electrokinetic spectra suggest a that a modification occurred. We found that the modification of the bulk of the particles was more evident then what was observed with the amino modified particles; a second relaxation at higher frequency appeared which was not expected from the Maxwell-Wagner model of interfacial relaxation.

The samples were prepared from vacuum dried particles P02 and resuspended in the electrorotation buffer before the experiment. The ROT and EO spectra obtained from 11 particles from the same batch are in Figure 6-4. Average particle dimensions, as obtained from the snapshots, are reported in Table 6-8. Fit results are in Table 6-9.

	Particle sizes (aver ± std dev)
A (μm)	50 ± 2
B (μm)	13.1 ± 0.4

Table 6-8. Particle P05 average dimensions obtained from the snapshots of the particles analysed. A is the length of the rod, B is the diameter.
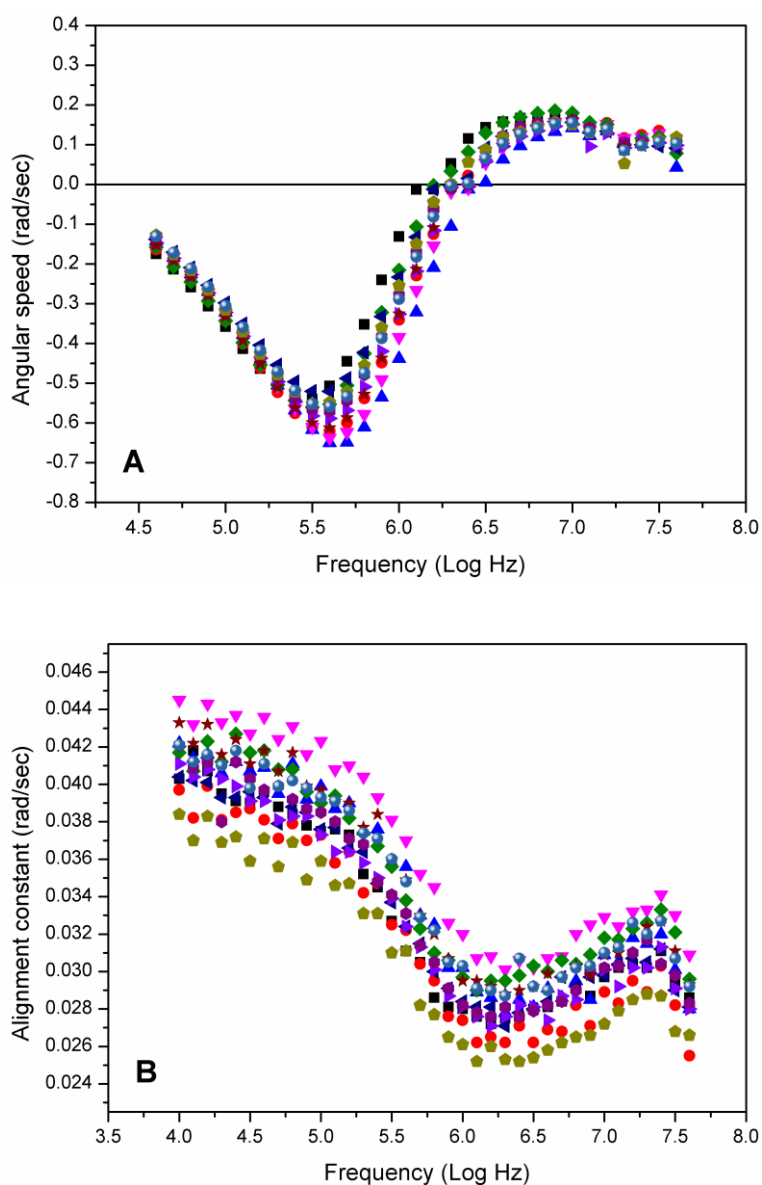
Figure 6-4. a) ROT and b) EO spectra of carboxyl-modified SU-8 rods (particles P05). Spectra are normalized to 1V.

Scaling factor	σ_m (mS/m)	ϵ_P	K_S (nS)	Correlation
8.1 ± 0.3	1.46 ± 0.06	13.7 ± 0.2	0.72 ± 0.02	ROT 0.990 ± 0.008 O 0.991 ± 0.002

Table 6-9. Fit results of the ROT and EO spectra of P05 particles. The error is the standard error.

6.2.4 Biotin modified SU-8 rods

This type of particle was obtained from the amino modified particles, through a reaction between the amine groups and the carboxylic groups from the biotin molecules. Unlike carboxyl or amine groups, biotin does not have any net charge at pH=7 (it is only polarized). These particles represent a foundation of a functionalisation process based on avidin, which is at the base of many binding assays used in molecular biology. We found that the particle's bulk was modified by the reaction: their permittivity increased compared to the amino modified particles and the electrokinetic spectra showed a secondary peak at high frequency, similar to the one obtained with succinilated particles. Also in this case, two different molecules were tested with a different spacer to place the biotin group at different distance from the surface. The presence of biotin can be assessed using fluorescently labelled avidin as reporting molecule. This is the same reaction that was used to obtain particles P08, where a fluorescence signal was observed (see Section 1.32.5 for details on the fluorescence observations of avidin).

The samples were prepared from a vacuum dried pellet and resuspended in the electrorotation buffer before the experiment.

6.2.4.1 Particles modified with biotin (P06)

The ROT and EO spectra obtained from 11 particles from the same batch are in Figure 6-5. Average particle dimensions, as obtained from the snapshots, are reported in Table 6-10. Fit results are in Table 6-11.

	Particle sizes (aver ± std dev)
A (μm)	50 ± 2
B (μm)	13.0 ± 0.2

Table 6-10. Particle P06 average dimensions obtained from the snapshots of the particles analysed. A is the length of the rod, B the diameter.

Scaling factor	σ_m (mS/m)	ϵ_P	K_S (nS)	Correlation
9.0 ± 0.2	2.1 ± 0.1	18.6 ± 0.4	0.99 ± 0.04	ROT 0.989 ± 0.004 EO 0.989 ± 0.00

Table 6-11. Fit results of the ROT and EO spectra of P06 particles. The error is the standard error.
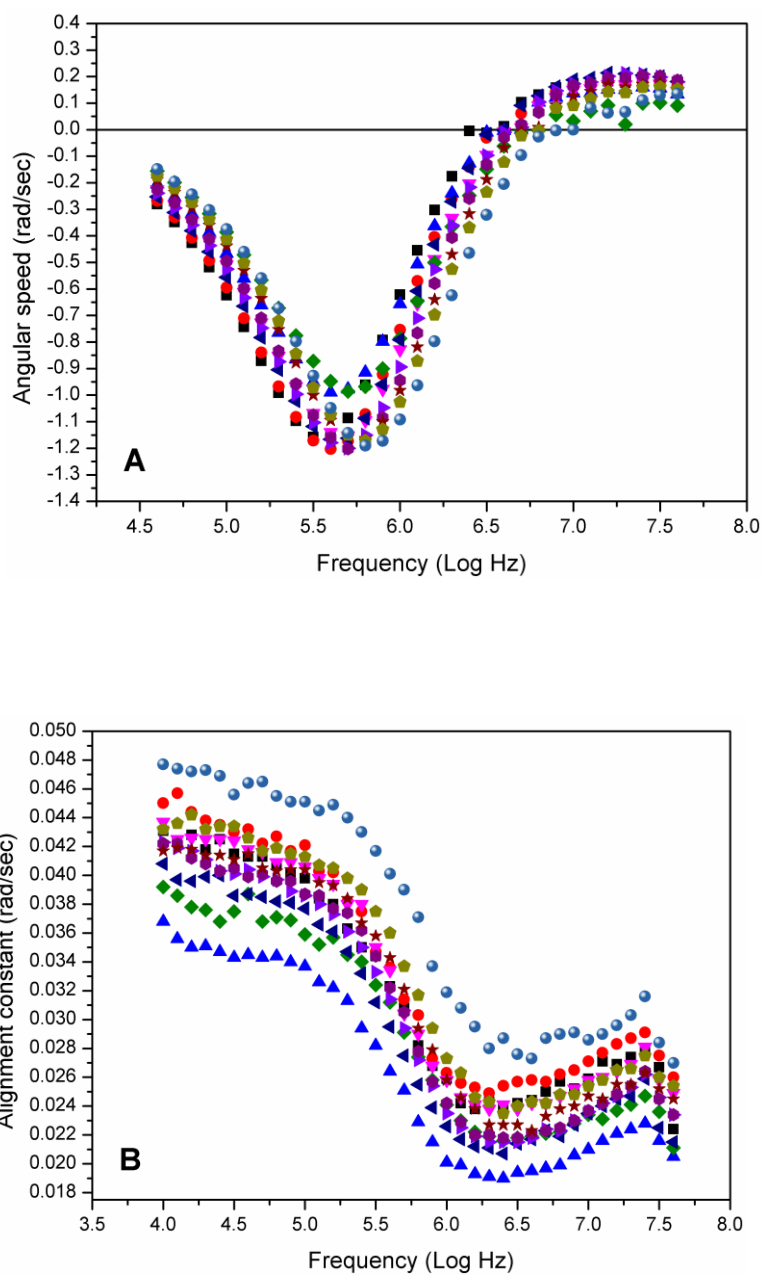
Figure 6-5. a) ROT and b) EO spectra of SU-8 rods modified with biotin (P06). Spectra are normalized to 1V.

6.2.4.2 Particles modified with LC-biotin (P07)

The ROT and EO spectra obtained from 10 particles from the same batch are in Figure 6-6. Average particle dimensions, as obtained from the snapshots, are reported in Table 6-12. Fit results are in Table 6-13.
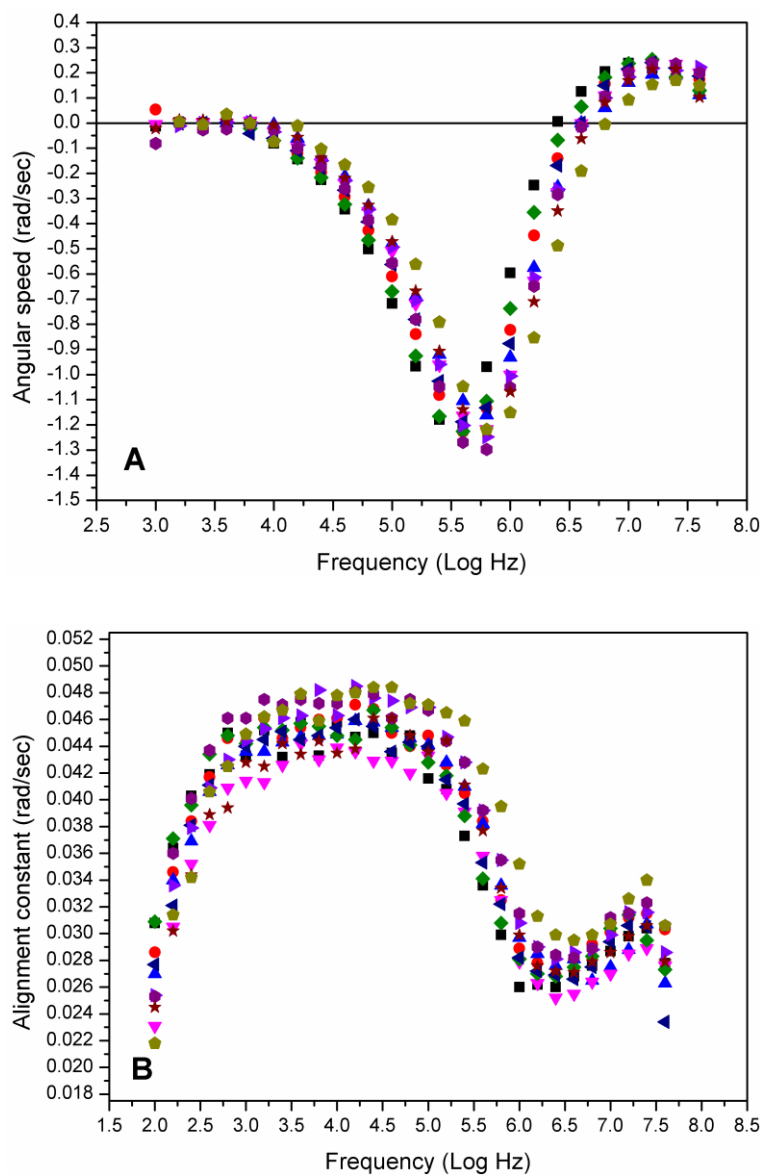
Figure 6-6. Extended a) ROT and b) EO spectra of SU-8 particles modified with LC-biotin (P07). Spectra are normalized to 1V.

	Particle sizes (aver ± std dev)
A (μm)	47.9 ± 0.6
B (μm)	11.9 ± 0.3

Table 6-12. Particle P07 average dimensions obtained from the snapshots of the particles analysed. A is the length of the rod, B is the diameter.

Scaling factor	σ_m (mS/m)	ϵ_P	K_S (nS)	Correlation
9.8 ± 0.5	2.1 ± 0.2	13.8 ± 0.7	0.32 ± 0.08	ROT 0.99 ± 0.02 EO 0.988 ± 0.003

Table 6-13. Fit results of the ROT and EO spectra of P07 particles. The error is the standard error.

As with the to P03 EO spectra, the low frequency EO spectral data were trimmed at 10 kHz, to leave only the plateau during data analysis.

6.2.5 Particles with immobilised avidin (P08)

This modification step represents a common binding assay, where a reporter molecule labelled with (fluorescent) avidin binds to the probe molecule labelled with biotin. Avidin is a protein and carries charges of different polarity, which should produce an increased surface conductance from the biotin modified particles.

The presence of avidin was assessed using fluorescence microscopy (Zeiss Axio Imager M1) comparing the images with non-modified particles as shown in Figure 6-7. SU-8 particles show a very low autofluorescence when excited with the same wavelength used to excite rhodamine: after 2 s integration time unfunctionalised particles cannot be distinguished from the background (see Figure 6-7b), while a 0.5 s integration time is enough to image funtionalised particles (see Figure 6-7a). The amount of proteins immobilised onto the SU-8 particles was not assessed, but it could be estimated by comparing the total brightness of the particles to the brightness of a known solution of rhodamine. The same objective should be used and care should be taken that the depth of field of the objective is large enough to capture the whole particle. The level of non-specific binding of avidin to the particles was not measured, but it could be done by exposing particles from all the previous modification steps to the same solution of fluorescently labelled avidin-D, followed by washing. The amount of fluorescence will be a measure of the amount of avidin on the particle surface, ideally the fluorescence should be observed only for biotin modified particles (because of specific binding). If non-specific binding is not observed in the native and amine modified particles, this test confirms the presence of biotin on the surface of the particles.
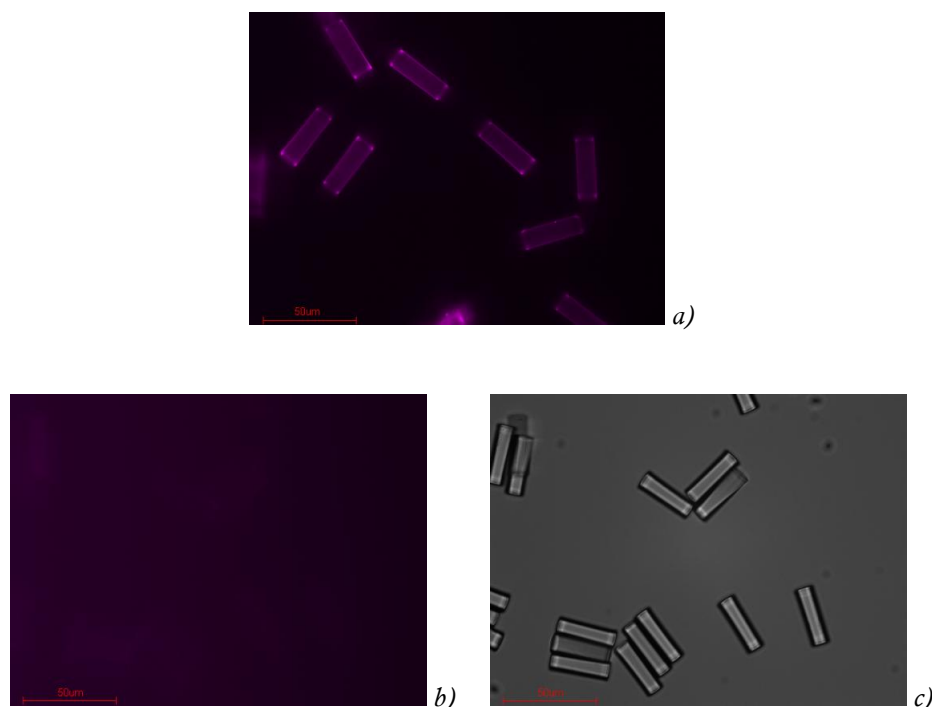
Figure 6-7. a) Fluorescence image of SU-8 rods with adsorbed rhodamine-labelled avidin D (particles P08), integration time 0.5 s; b) Fluorescence image of native SU-8 rods (particles P01), image taken with the same settings as a) but integration time 2 s; c) the same particles and area as b) but imaged with normal bright field to show the position of the particles. The images were taken with a Zeiss Axio Imager M1 using a 40x oil-immersion objective; fluorescence images were obtained using a rhodamine filter-set and are shown in pseudo-colours.

Despite the presence of the protein being confirmed, no appreciable change in surface conductance was observed. The secondary peak was still present with similar magnitude, which means the reaction did not affect the bulk, probably due to the size of avidin which cannot enter inside the particle polymer matrix.

The ROT and EO spectra obtained from 11 particles from the same batch are in Figure 6-8. Average particle dimensions, as obtained from the snapshots, are reported in Table 6-14. Fit results are in Table 6-15.

	Particle sizes (aver ± std dev)
A (μm)	51 ± 3
B (μm)	13.2 ± 0.5

Table 6-14. Particle P08 average dimensions obtained from the snapshots of the particles analysed. A is the length of the rod, B is the diameter.
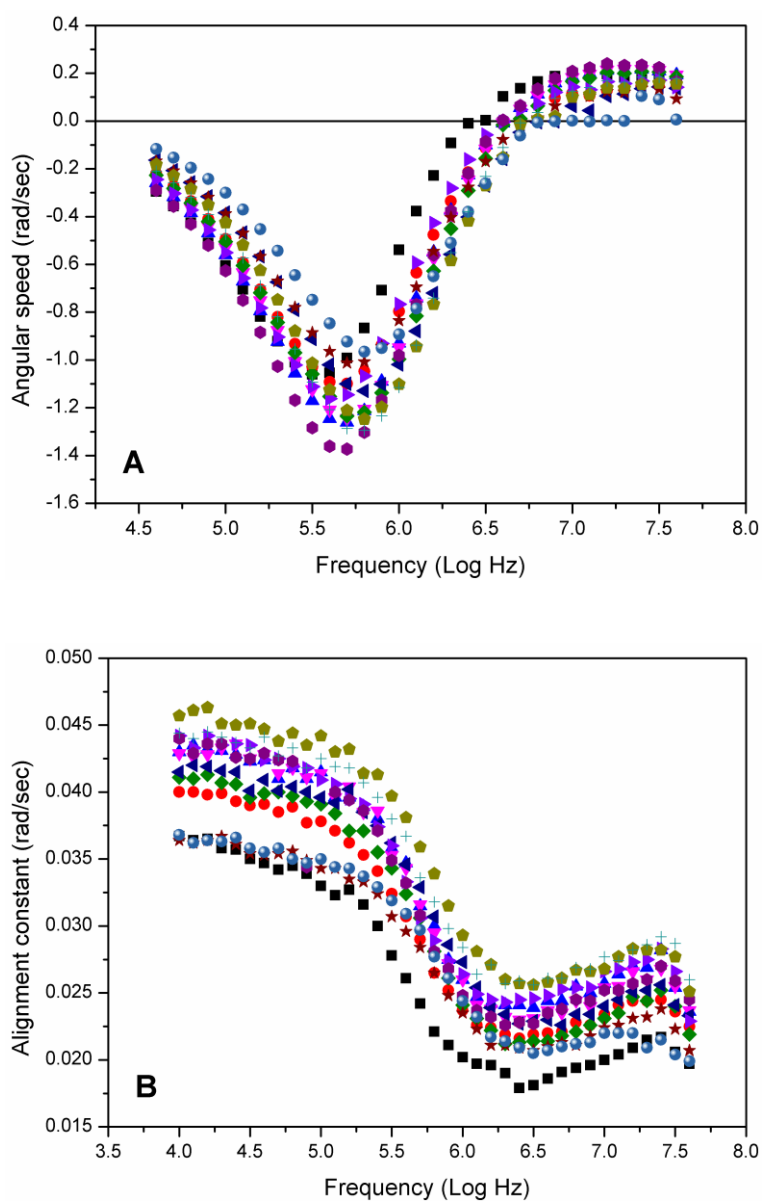
Figure 6-8. a) ROT and b) EO spectra of SU-8 rods with avidin immobilised onto the surface (P08). Spectra normalized to 1V.

Scaling factor	σ_m (mS/m)	ϵ_P	K_S (nS)	Correlation
8.6 ± 0.5	2.2 ± 0.1	18.4 ± 0.4	0.98 ± 0.04	ROT 0.989 ± 0.005 EO 0.990 ± 0.004

Table 6-15. Fit results of the ROT and EO spectra of P08 particles. The error is the standard error.

6.2.6 Particles with immobilised IgG (P09)

This is the final modification step, where biotinylated antibodies are bound to the avidin modified particles. This is how particles would be if used to detect antibody binding events: the reporting molecule (antibody) is bound to the particle and the probe molecules (antigens) would be free in solution. With this modification we aimed to increase even more the surface charge density increasing the number of proteins on the surface. The presence of the IgG on the particles was not assessed, as well as the non specific binding. The simpler way to confirm the presence of IgG is to use a fluorescently labelled IgG, with a fluorophore that can be detected independently of rhodamine (already present on the avidin molecules used in the previous modification step). The amount of IgG would be measured in the same way as explained in the previous Section for avidin, that is comparing the total brightness of the particles against a known solution of fluorophore. In the same way, non-specific binding could be measured exposing particles from all the previous modification steps to a solution of fluorescently labelled IgG and then washed. The fluorescent signal will give information on the non specific binding. Ideally, only the particles funcionalised with avidin should give a fluorescence signal.

The ROT and EO spectra obtained from 10 particles from the same batch are in Figure 6-9. Average particle dimensions, as obtained from the snapshots, are reported in Table 6-16. Fit results are in Table 6-17.
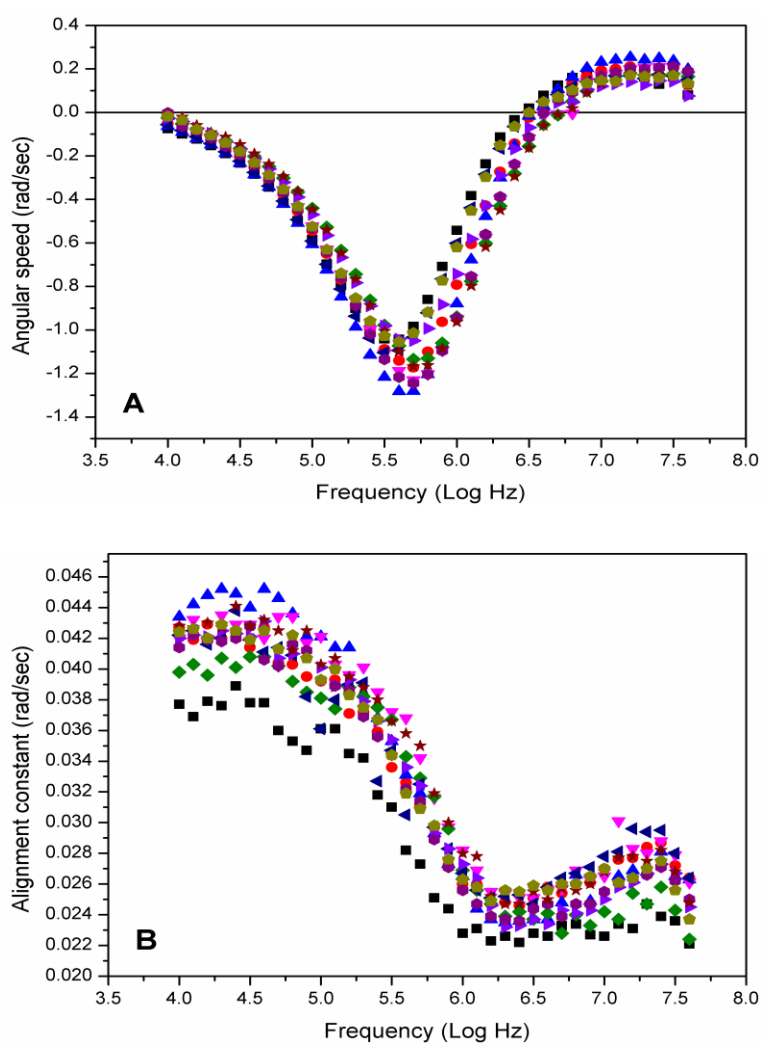
Figure 6-9. a) ROT and b) EO spectra of SU-8 rods with IgG immobilised onto the surface (P09). Spectra normalized to 1V.

	Particle sizes (aver ± std dev)
A (μm)	48.4 ± 0.9
B (μm)	13.1 ± 0.4

Table 6-16. Particle P09 average dimensions obtained from the snapshots of the particles analysed. A is the length of the rod, B is the diameter.
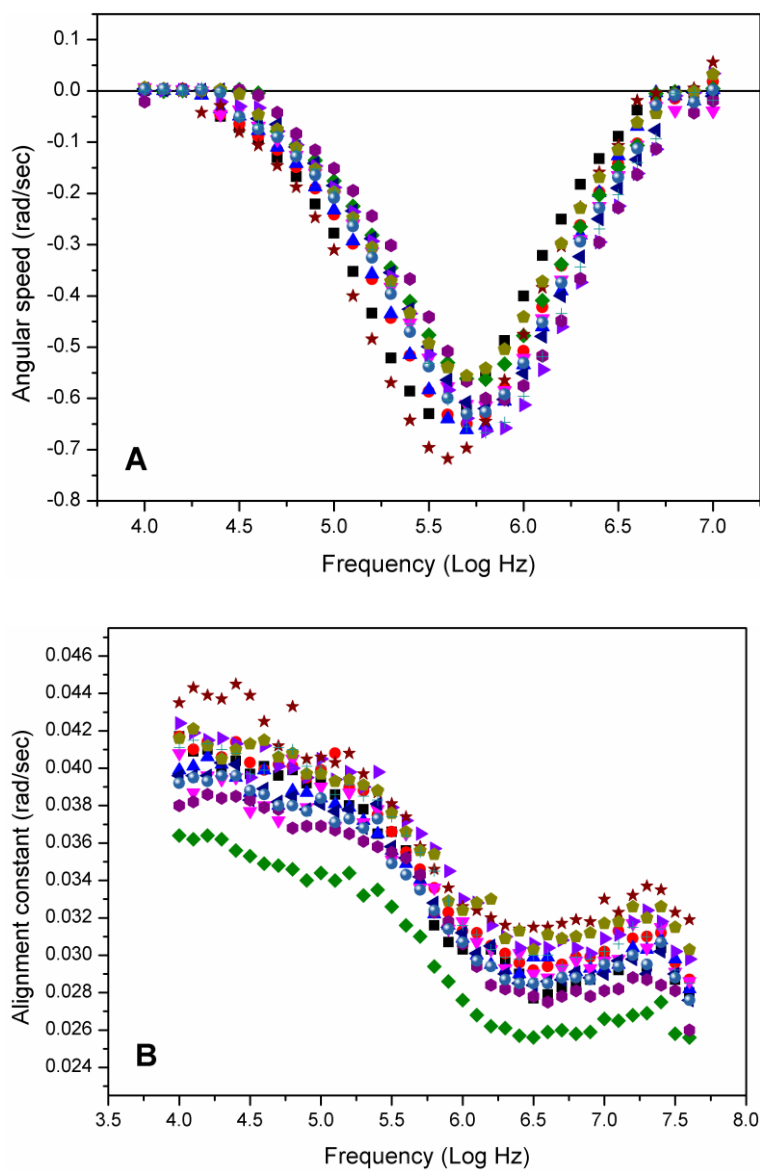
Scaling factor	σ_m (mS/m)	ϵ_P	K_S (nS)	Correlation
7.0 ± 0.3	2.0 ± 0.1	14.8 ± 0.7	$0.4 \pm 0.$	ROT 0.9988 ± 0.0005
				EO 0.992 ± 0.005

Table 6-17. Fit results of the ROT and EO spectra of P09 particles. The error is the standard error.

6.3 Experimental evidence of particle porosity

SU-8 is well known for its chemical and mechanical stability, but many observations in this work indicate that our SU-8 particles are porous. The first evidence comes from the result of the Kaiser test. As seen in section 1.32.2, the numbers of monolayers of amine groups estimated from the Kaiser test is 6600 ± 500. This result suggests that the reaction with Jeffamine happens mostly in the bulk of the particles. The reason for that can be traced to the use of DMF as a solvent and the interaction with Jeffamine as well.

The reaction schemes in 1.24.1 and 1.24.2, used to obtain particles P03, P04 and P05 respectively, require the use of DMF as solvent. DMF is well known to make many plastics swell, and the same happens to SU-8. In Table 6-18 and Figure 6-10 the effect of solvents and other chemicals used for functionalisation is shown. Particles P03 and P04 were measured after the reaction and washed with fresh DMF to remove the unreacted reagents, then washed three times with methanol and re-suspended in DI water. P01 native particles were studied after being resuspended in DMF and after the methanol wash. Figure 6-10 shows that DMF causes swelling of SU-8 particles. An additional contribution to the swelling comes from Jeffamine, used in the preparation of particles P03. While particles P01 and P04 swell about 33% when exposed to DMF, particles P03 swell about 45% (see Figure 6-10).

	P03	P04	P01
Particles suspended in DMF			
Particles washed in methanol and resuspended in DI water			
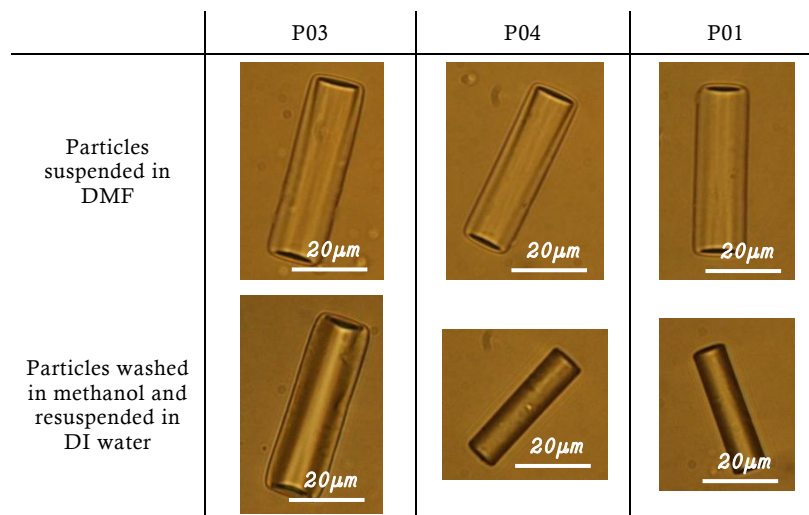
Table 6-18. Examples of particles from different chemical reactions in different suspending media. In the first row, particles are imaged while suspended in DMF; in the second row the pictures were taken after the particles were washed 3 times in methanol, then in DI water. The pictures are taken with the same objective and camera to aid comparison of particles.
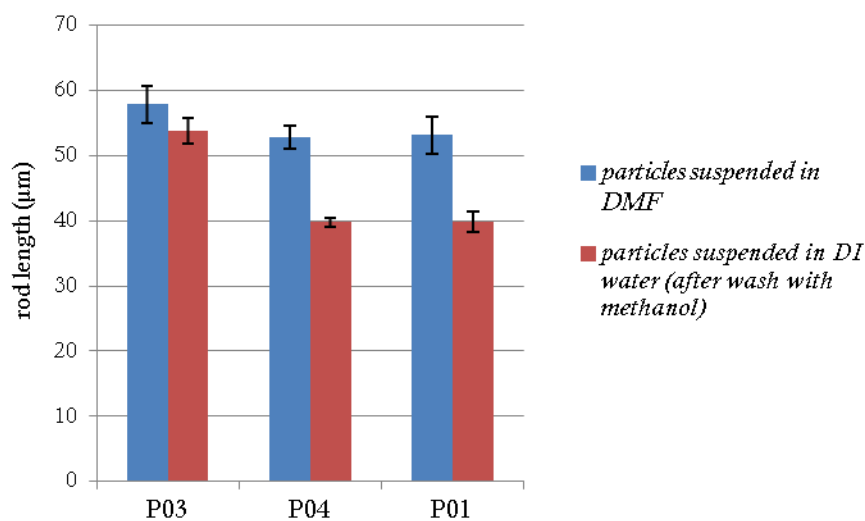
Figure 6-10. Graph comparing the size of different types of particles when suspended in DMF and DI water. Particles suspended in water were first washed with methanol to remove the DMF. Error bars are the standard deviations from 12 different particles.

That additional contribution confirms that the chemical modification is not just happening on the surface, but may occur also in the bulk as Jeffamine is penetrating into the SU8 matrix, as indicated by the Kaiser test. Particles P04 did not show any additional effect of swelling, probably because the long molecular chain is unlikely to penetrate deeply in the polymer matrix, therefore chemical modification occurred predominantly on the surface or inside a thin surface layer.

A wash with methanol removes the DMF and the unreacted chemicals, returning the particles back to their original size in the case of particles P01 and P04. Particles treated with Jeffamine (P03) did not return back to their original size probably because the solvent was retained in the bulk. This demonstrates that SU-8 particles are porous and can undergo permanent modification of the bulk as well as the surface, and they can also retain a certain amount of solvent in the bulk. For this reason, after every functionalisation, particles were vacuum dried to remove the solvents before resuspending in water.

Removing the solvents from the inside of the particles solved only partially the swelling of the particles. Using the particle dimensions and the fit results it is possible to build the graph in Figure 6-11. The graph shows that the increase of permittivity of the particles follows linearly the increase in particle size. A linear fit of the data (excluding P05) gave a value of 2.1 ± 0.3 for the slope and -90 ± 10 for the intercept. Using a length value of 44 μm (for dry particles), the corresponding relative permittivity is calculated as 2.4 ± 10 which is qualitatively in accord with the value of 3.2 for dry polymer. This result supports the idea that particles are porous and contain water (from the surrounding electrolyte) in the polymer matrix: swollen particles contain more water and the permittivity becomes higher. Using a simple linear model, the water content of the SU-8 can be estimated using the permittivity of dry polymer ($\varepsilon_r = 3.2$) and water (80) using the formula $\varepsilon_p=80x+3.2(1-x)$, where x is the percentage of water in the polymer matrix; a permittivity of 10 means 9% of water, while a particle permittivity of 20 means that 22% of the particle volume consists of water.

These experimental observations corroborate the hypothesis of porosity but also the possibility to have non-negligible contribution to the particle conductivity from the bulk conductivity. In case of porous particles the surface conductivity will not be effectively measured from the electrokinetic measurements: the fitting equations assume that the particle conductivity depends only on the surface conductance and not on the bulk conductivity, which is assumed to be zero.
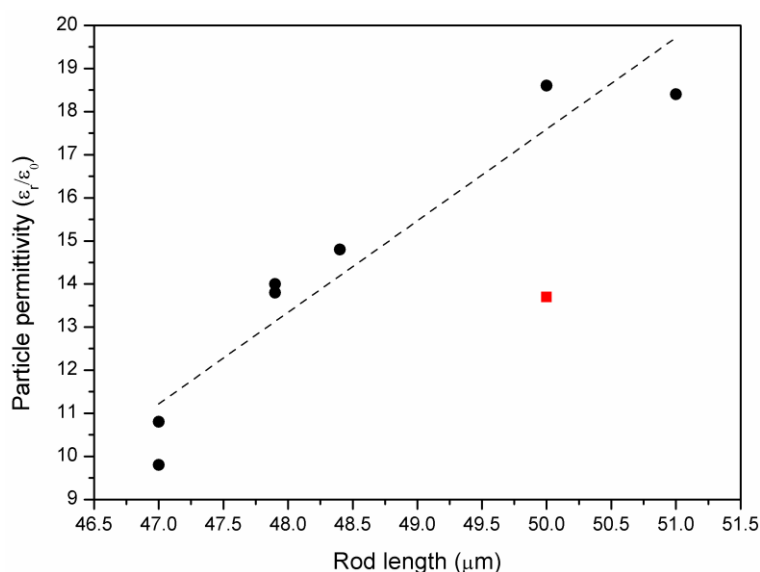
Figure 6-11. The particle permittivity plotted against the length of the rods using the data from Table 5-18 (solid circles). The dashed line is the linear fit to the solid circle data: slope=2.1 ± 0.3, intercept=-90 ± 10. The square represents data from particles P05; the fit to the electrokinetic data did not provide a reliable result, so this point is an outlier.

6.4 Discussion

In this section the results of the experimental work will be discussed starting from the features observed in the spectra and the electrical properties obtained with the fit. A summary of the electrokinetic data is shown in Figure 6-12 and the fit results are shown in Table 6-19.

6.4.1 The secondary relaxation

Electrokinetic spectra of particles P01, P02 and P03 appear as predicted by the theory: a single peak for the ROT spectra and a sigmoid for the EO. In both cases the electric torque that causes the alignment, instead of being constant at high frequency, has a slight increase at high frequency, followed by a decrease in the last three points. This feature is common to all particle types, and is enhanced after modification with biotin (particles P06 and P07). No other change in spectral features was observed in the spectra obtained from particles P08 and P09: no chemical modification was involved, just immobilization of proteins onto the surface of the particles. The reason for the decrease in the last three points of the EO spectrum might be due to a mismatch of the phase of the channels at high frequency that was not completely cancelled by the software correction explained in 1.21.5. When the phase difference between two energised channels is not 180°, the actual amplitude of the resulting electric field is decreased and so too the alignment torque.
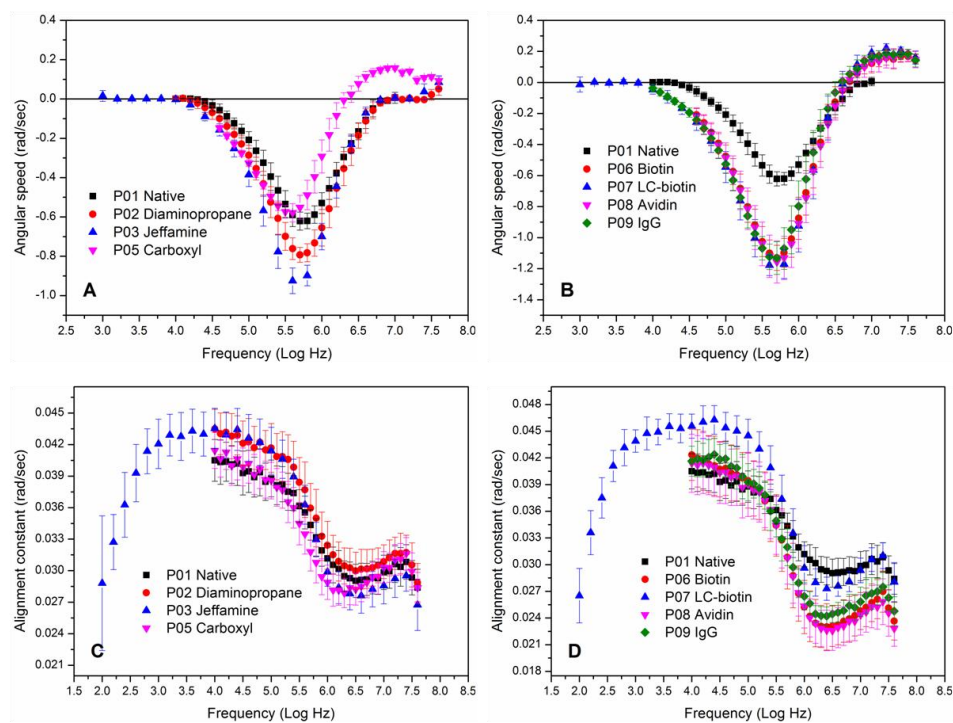
Figure 6-12. Summary of the electrokinetics spectra obtained in this work. a,b) ROT spectra; c,d) corresponding EO spectra. Particle types are indicated in the legends. Points are the average of the data for a given particle type, error bars are the standard deviation of the data. P01 results are shown in each graph as comparison.

Surface type	Particle sizes (μm)	Scaling factor	σ_m (mS/m)	ϵ_P	K_S (nS)
P01: Native SU-8	47 ± 2 11.8 ± 0.3	8.4 ± 0.3	2.4 ± 0.1	9.8 ± 0.3	0.48 ± 0.04
P02: Amine from diaminopropane	47 ± 1 12.1 ± 0.6	8.5 ± 0.4	2.4 ± 0.2	10.8 ± 0.3	0.47 ± 0.05
P03: Amine from Jeffamine	47.9 ± 0.7 12.1 ± 0.3	9.3 ± 0.2	2.04 ± 0.09	14.0 ± 0.4	0.65 ± 0.07
P05: Carboxyl	50 ± 2 13.1 ± 0.4	8.1 ± 0.3	1.46 ± 0.06	13.7 ± 0.2	0.72 ± 0.02
P06: Biotin	50 ± 2 13.0 ± 0.2	9.0 ± 0.2	2.1 ± 0.1	18.6 ± 0.4	0.99 ± 0.04
P07: LC-Biotin	47.9 ± 0.6 11.9 ± 0.3	9.8 ± 0.5	2.1 ± 0.2	13.8 ± 0.7	0.32 ± 0.08
P08: Avidin	51 ± 3 13.2 ± 0.5	8.6 ± 0.5	2.2 ± 0.1	18.4 ± 0.4	0.98 ± 0.04
P09: IgG	48.4 ± 0.9 13.1 ± 0.4	7.0 ± 0.3	2.0 ± 0.1	14.8 ± 0.7	0.4 ± 0.1

Table 6-19. Summary of the fit results for all the surface modifications of the SU-8 rods. The values are the average and the errors are the standard deviation of the average of the data.

The reason for the increase of the alignment constant with frequency is not clear, but it might be due to another relaxation at higher frequency. That effect gets more evident with the increase of the particle swelling, suggesting that it is related to the bulk of the particles. Possible explanations are related to the water content of the particles. For example, in literature it has been reported that the dielectric relaxation due to water molecules bound to hydrophilic gel matrixes is around 10^8Hz [161], the low frequency tail of that relaxation could appear in the electrokinetic spectra. Percolation of water in the polymer matrix could produce a similar relaxation as well, due to the change of the electrical properties with frequency because of the inclusions of small conductive elements inside an insulator.

The increasing importance of the high frequency feature in the EO spectra is mirrored by the appearance of the secondary relaxation peak in the ROT spectra. This is observed for particles P05, P06, P07, P08 and P09. The type of particle might play a role: particles P05 are rich in negatively charged groups, while P06 and P07 are rich in negatively polarised groups due to the oxygen atoms in the covalently bound molecules. Particles P02 and P03 are instead rich in positively charged groups and their electrokinetic spectra do not show the additional relaxation. This difference between positively and negatively charged particles cannot be related to a difference in mobility between ions, because K+ and Cl- have similar mobility: 7.6×10^{-8} and 7.9×10^{-8} $m^2V^{-1}s^{-1}$ respectively. H^+ and OH^- ions have instead a very different mobility (36×10^{-8} and 21×10^{-8} $m^2V^{-1}s^{-1}$ respectively), due to the different mechanism of transport. Their concentration at pH=7 is 10^{-7} mM while KCl ions concentration is 10^{-4} mM, therefore their contribution to the conductivity should be negligible. Therefore it must be due to the chemical modification steps that are increasing the water content in the particles making the bulk more hydrophilic.

Particles P08 and P09 have ROT spectra with a secondary peak at high frequency, but in this case the surface has a very high charge density because of immobilised protein. This suggests that high frequency secondary relaxation is related to the properties of the bulk of the particles. Proteins are not expected to reach the bulk of the particles because of their dimensions: a molecule of avidin, for instance, measures 4 x 5 x 5.6 nm. A molecule of Jeffamine is a ~11 nm long chain and it was shown in Section 4.3 that it can reach the bulk of the particle when used with DMF due to the large swelling (~40%) caused by the solvent. Avidin and IgG are instead used in water suspension, which causes a smaller swelling of the particles. Therefore, they should not penetrate into the bulk apart from a thin layer on the sidewalls where the polymer is just partially crosslinked and the structure is therefore more porous.

This phenomenon must be independent of a simple particle bulk conductivity change, because that will not alter the mathematical form of the Maxwell-Wagner relaxation shown in Chapter 2, therefore it cannot give rise to a secondary relaxation. In the framework of the

Maxwell-Wagner theory, a secondary relaxation is expected for shelled particles, but in this case particles did not show any inner structure under the optical microscope.

6.4.2 Percolation

The percolation theory describes the electrical properties of heterogeneous materials composed of conductive and non-conductive parts. Typically, a nonconductive polymer matrix is doped with different quantities of conductive particles and the behaviour studied as a function of the doping. Increasing the doping over a certain threshold results in the material changing from non conductive to conductive. The problem of predicting the behaviour of a nonconductive material, when parts of it are replaced by very small resistance and/or large capacitances in a random arrangement, is challenging and to date there are no analytical solutions. A model that gives the electrical properties of composite materials from first principles was published by Bergman and Imry [162]. The authors derived the electrical properties as a function of the difference between the volume fraction and the percolation threshold. More recently, some authors have used models based on effective-medium theory [163]-[165] or empirical models [166][167] to describe the experimental results, where parameters are usually calculated *a posteriori* through data fitting. The empirical models are based on the concept of universal dielectric response (UDR) introduced by Jonscher to describe the rich phenomenology of the dielectric relaxation of solids, which never follows a simple Debye relaxation model [168][169]. Following his work, the effect of percolation can be added by modifying the equations presented in Chapter 2 for the complex permittivity along two different axis of an ellipsoidal particle as follows [166][167]:

$$\varepsilon_{2,a} = \varepsilon_2 \varepsilon_0 + \frac{\Delta\varepsilon \cdot \varepsilon_0}{\left[1+\left(i\omega\tau_1\right)^{m_1}\right]^{(1-n_1)/m_1}} + \frac{1}{i\omega}\left(\frac{2K_S}{b}\right)$$

$$\varepsilon_{2,b} = \varepsilon_2 \varepsilon_0 + \frac{\Delta\varepsilon \cdot \varepsilon_0}{\left[1+\left(i\omega\tau_1\right)^{m_1}\right]^{(1-n_1)/m_1}} + \frac{1}{i\omega}\left(\frac{(a+b)K_S}{ab}\right)$$

(5.1)

where the particle surface conductivity is added as an independent effect. $\Delta\varepsilon$ is the difference between the static (DC) and the limiting permittivity at high frequency ($\omega\tau_1 >> 1$), τ_1 is the characteristic relaxation time, while m and n determine the low frequency and high frequency modelling of the relaxation respectively. In this context the Debye relaxation is just a special case of equation (5.1) with $m_1 = 1$ and $n_1 = 0$. Now the theoretical ROT and EO spectra can be derived as usual calculating $-\text{Im}[K_a+K_b]$ and $\text{Re}[K_a-K_b]$. The results are in Figure 6-13, where $\Delta\varepsilon$ was varied between 0 and 15.
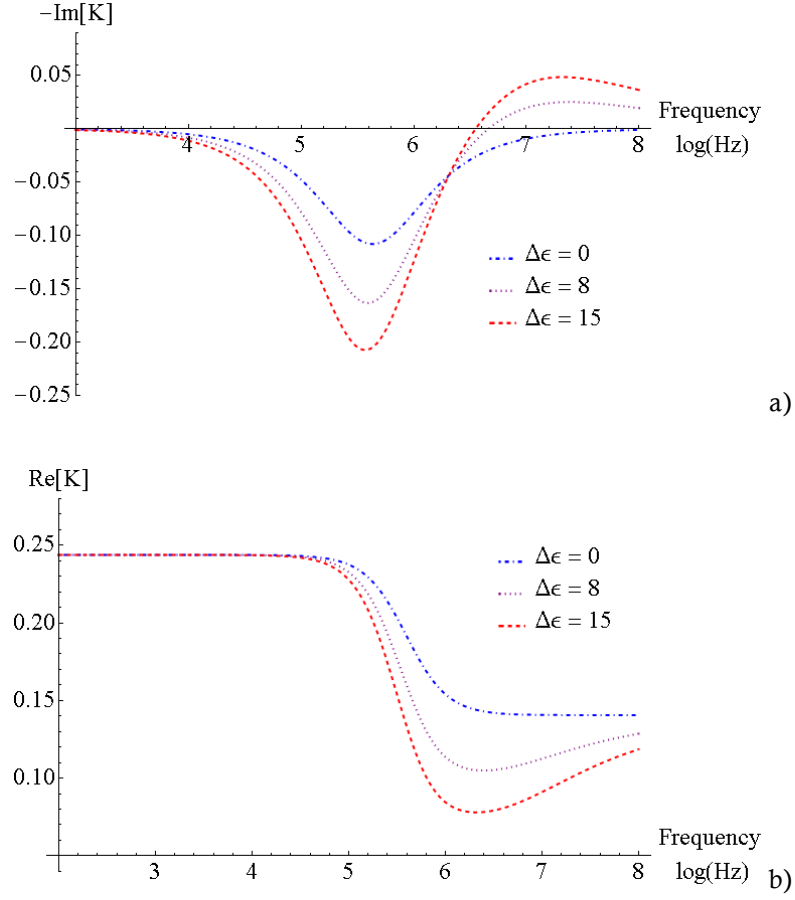
Figure 6-13. The graphs show the a) –Im[K_a+K_b] and b) Re[K_a-K_b] spectra for an ellipsoidal particle for different values of $\Delta\epsilon$. a) and b) are respectively proportional to the ROT and EO spectra. The other parameters were: 2a=40 μm and 2b=2c=10 μm. ε_m=76, ε_b=10, σ_m=2 mS/m, K_S=0.5 nS, τ_1=10$^{-7.5}$ s, m_1=0.8 and n_1=0.6.

This model produces a good representation of the experimental data at high frequency, but fails to reproduce the EO spectra at low frequency (independent of the chosen relaxation time) because the relaxation does not alter the term relative to the surface conductance of the particle.

A similar representation of the data could be obtained by adding one more relaxation as in the following equations:

$$\varepsilon_{2,a} = \varepsilon_2\varepsilon_0 + \frac{\Delta\varepsilon \cdot \varepsilon_0}{\left[1+\left(i\omega\tau_1\right)^{m_1}\right]^{(1-n_1)/m_1}} + \frac{1}{i\omega}\left(\frac{\Delta\sigma_b}{\left[1+\left(i\omega\tau_2\right)^{m_2}\right]^{(1-n_2)/m_2}} + \frac{2K_S}{b}\right)$$

$$\varepsilon_{2,b} = \varepsilon_2\varepsilon_0 + \frac{\Delta\varepsilon \cdot \varepsilon_0}{\left[1+\left(i\omega\tau_1\right)^{m_1}\right]^{(1-n_1)/m_1}} + \frac{1}{i\omega}\left(\frac{\Delta\sigma_b\, a/b}{\left[1+\left(i\omega\tau_2\right)^{m_2}\right]^{(1-n_2)/m_2}} + \frac{(a+b)K_S}{ab}\right)$$

(5.2)
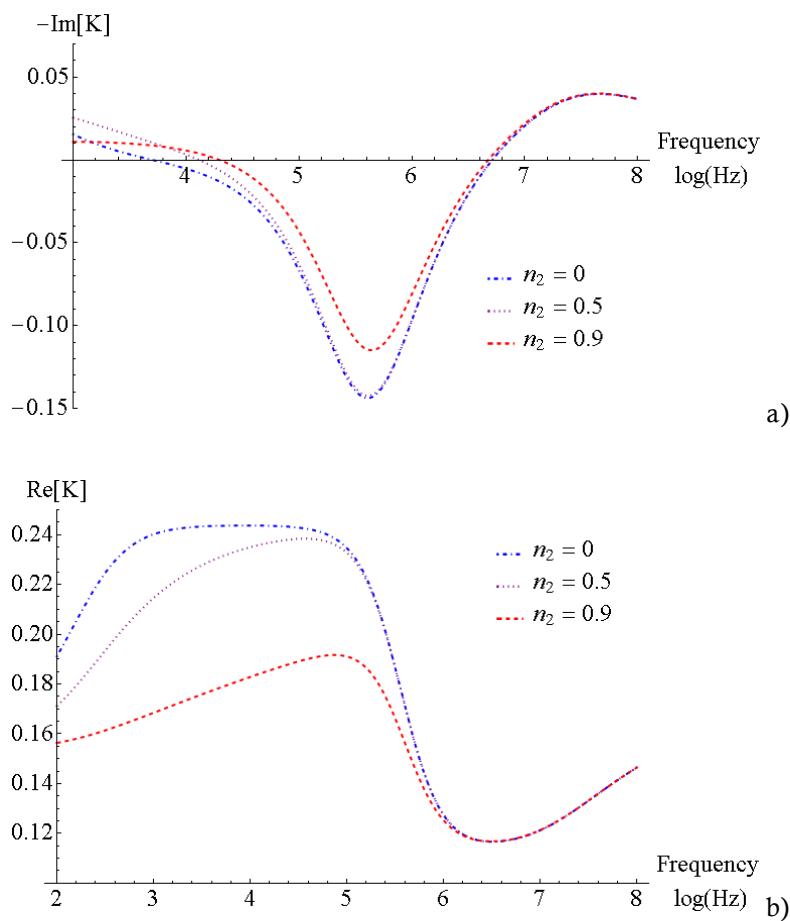
Figure 6-14. The graphs show the a) −Im[K_a+K_b] and b) Re[K_a-K_b] spectra for an ellipsoidal particle for different values of $\Delta\sigma_b$. a) and b) are respectively proportional to the ROT and EO spectra. The other parameters were: 2a=40 µm and 2b=2c=10 µm. ε_m=76, ε_b=10, σ_m=2 mS/m, K_S=0.5 nS, τ_1=10^{-8} s, τ_2=1 ms, $\Delta\varepsilon$=10, $\Delta\sigma_b$=0.05 mS/m, m_1=m_2=0.8 and n_1=0.6.

where τ_2, m_2 and n_2 are the relaxation time constant, and the low frequency and high frequency exponents respectively describing the process. $\Delta\sigma_b$ is the difference between the low frequency ($\omega\tau_2 \ll 1$) and high frequency ($\omega\tau_2 \gg 1$) value of the bulk conductivity. A factor a/b was added to take into account that the particle will have different bulk conductivities along different axes. For this case the Im[K_a+K_b] and Re[K_a-K_b] spectra are shown in Figure 6-14. The model presented in equation (5.2) gives a better representation of the experimental results, even if two independent percolation relaxations are used. The only problem is for the low frequency ROT spectra: experimentally no motion is observed while the model predicts a counterfield rotation. This discrepancy could be due to the fluid flow pushing the particle down onto the glass inhibiting any movement because of increased friction. The equations presented are not specific to percolation and can be applied to many different processes [170], but percolation is the more probable process involved.

This model gives an insight into the processes involved in the electrokinetic measurements but cannot be used to fit the data, because too many parameters are involved: along with the Scaling factor, particle permittivity, surface conductance and medium conductivity, also $\Delta\sigma_b$, $\Delta\varepsilon$, τ_1, τ_2, m_1, n_1, m_2, n_2 (8 more parameters than the normal Maxwell-Wagner model, respectively: the difference between the static and the high limit conductivity and permittivity, the relaxation time for the permittivity and conductivity relaxation, the high frequency and low frequency modelling of the permittivity and conductivity relaxation).

6.4.3 Suspending electrolyte conductivity

The suspending electrolyte conductivity obtained from the data fitting is comparable with the value measured with a calibrated conductivity meter. The different values obtained for native SU-8 particles could be due to the different ways in which it was measured, i.e. from the particle motion in an electric field instead of measuring current like a commercial conductivity meter. In the case of particles P01, contamination could be excluded because after crosslinking, particles were washed extensively in solvents and vacuum dried. The only possible contaminant could be the catalyst in the SU-8 matrix. Another cause of the different value for the conductivity could be a higher temperature in the chamber due to the lamp of the microscope and/or the electric field inside. Because the electrolyte conductivity is obtained from the fit and not imposed, the fit result should be independent of the actual phenomenon modifying the conductivity. The value obtained in the case of carboxyl-modified particles P05 is quite different because of the secondary relaxation; the same underestimation of conductivity (compared to the value obtained for P01) is present when fitting similar spectra. The co-field ROT peak at high frequency has the effect of shifting the Maxwell-Wagner peak at lower frequency (being of opposite polarity), causing an underestimate in conductivity. The contribution of this secondary peak could not be deleted from the data, because of insufficient data describing the tails of the peaks and a fit with a double Lorentzian curve did not have a single solution.

6.4.4 Particle permittivity

The relative permittivity of particles P01 was found to be higher (ε_r = 9.8) than the value of 3.2 expected for cross-linked and hard-baked (dry) polymer[4]. The discrepancy could be caused by an uptake of water in the polymer matrix [171]. This is confirmed by the increased dimensions of P01 particles compared to the size of dry particles (Table 4-1). Particle permittivity seems to increase at each modification step; however particles P07 have a lower permittivity. The result for particles P07 is an artefact due to the lack of a well defined plateau at high frequency and also the secondary relaxation. The fitted plateau is higher than the

---

[4] http://www.microresist.de/produkte/mcc/pdf/SU_8_2000_2000_5_bis_2015.pdf found on 02/10/2011

actual data, shifting the permittivity to smaller values. This is a common problem for all the particles, and can be severe when the contribution of the plateau is small compared to the secondary relaxation at high frequency. Trimming the data does not provide a solution to the problem, because the absence of a significant number of data points will lead to instability of the fit.

6.4.5 Surface conductance

The surface conductance K_S, measured for particles P01, is comparable to literature values for polystyrene beads (typically 0.5nS) [125]. Particles P02 had a surface conductance similar to native SU-8 particles. At pH 7 amine groups have a net charge, while epoxy rings do not, therefore a different (higher) surface conductance is expected. This suggests that the chemical modification does not happen onto the surface but in the bulk of the particle, so that the amine groups from diaminopropane (carbon chain length ~0.6 nm) are unavailable at the surface. This could be due a low reactivity of the surface itself, because the interaction with the environment can naturally open the more exposed epoxide rings making then nonreactive. In addition to that, the sidewalls of the rods are only partially crosslinked due to the geometry of the fabrication; therefore there will be only a certain number of unreacted epoxide rings available for chemical reactions, while the others (probably the majority) will be unavailable because they are embedded in a porous structure. That type of structure allows chemical reagents in organic solvents to percolate and modify its chemical properties in a layer of unknown thickness around the particle. Once solvents are removed the structure closes again and the charges are not available anymore. Particles P03 have a bigger surface conductance. Given the slightly different volume of the particles, chemical modification occurred in the bulk of the particles as well, as confirmed by the Kaiser test. Jeffamine provides a ~11 nm spacer for the amine group, therefore even if chemical modification does not happen on the surface the amine groups might well be more exposed than the amine group on the diaminopropane. The fit for the carboxyl modified particles (P05) gives a higher surface conductance than for P03, but the value of the medium conductivity (1.46 ± 0.06 mS/m) was found to be very different from the nominal one, suggesting that the fit might not be completely reliable. The fit for the IgG modified particles P09 gave an un-reliable result as well, as seen from the value of the *scaling factor* (7.0 ± 0.3), which is different from that obtained with P01 (8.4 ± 0.3). In the case of particles P05, P06 and P08 the scaling factor obtained has values near the one obtained for native SU-8 particles P01, as can be seen from Table 6-19. The results of the fit are only qualitative because of the interference of the secondary high frequency peak.

The water content of the particles might lead to an overestimate of particle surface conductance. We saw in Chapter 2 that the conductivity of a spherical particle is

$$\sigma_p = \sigma_b + \frac{2K_S}{a} \tag{5.3}$$

In our case, the fit gives the particle conductivity scaled to the particle size, which means:

$$\sigma_p = \frac{2K_S'}{a} = \frac{2\left(K_S + \sigma_b a/2\right)}{a} \tag{5.4}$$

Therefore $K_S' > K_S$. Particle bulk conductivity cannot be added to the fit as a free parameter because, for a given particle size, the effect of changing this parameter is un-distinguishable from changing just the surface conductance. The contribution of bulk permittivity (usually assumed to be negligible) could be extracted only by using particles of different size (but similar water content) but with the same surface conductance and measured in the same suspending electrolyte.

6.5 Conclusions

In this chapter we analysed SU-8 particles with different chemical properties, obtained via biochemical modifications in a step by step process. The aim was to develop a method to detect molecular binding events, such as antibody binding, using the surface conductance of elongated particles as indicator. The method developed in this work, which combines ROT and EO on a single particle basis, measures the electrical properties of the particles. The Maxwell-Wagner model of the interface relaxation was used to analyse the electrokinetic data obtained.

SU-8 particles seem unsuitable for this type of assay because the chemical reactions needed to modify them can also affect their bulk structure, particularly when reactions involve solvents like DMF. The results show that the particles undergo a chemical and physical modification of their bulk which can dominate over the surface modification which was the main goal. This modification is suggested by the observation of swelling of the particles, and causes the appearance of percolation effects in the electrokinetic spectra in the form of two additional relaxations at higher and lower frequencies than the Maxwell-Wagner relaxation, which is commonly used to describe the behaviour of particles in AC electric fields. Particle swelling could also lead to a wrong estimate of the surface conductance of the particles due to the contribution of the bulk conductivity, caused by the suspending liquid entering into the polymer matrix. Modification of the particles with proteins (avidin and IgG) did not lead to any significant change in surface conductance, which means that the charges carried by the proteins are not available for or do not modify the electrokinetic measurements. That could be due to the partially crosslinked sidewalls of the SU-8 rods, whose porous structure allows chemical modification in the inside only when organic solvents are used.

From this point of view, it will be better to work with particles which are not affected by swelling, for example silica particles. The particle permittivity could be considered constant and not a free parameter. Solid particles (i.e. not porous) may have a larger mass, causing even more friction on the substrate when moving, but that could be compensated by increasing the voltage of the signal (provided the particles do not show pDEP) or by changing the medium density. For the same reason the use of different methods such as DEP or ROT will produce sensible results only if the properties of the bulk of the particles are known. Spherical particles do not enable electroorientation measurements, so they could only be analysed using ROT and DEP, with the drawback of being unable to analyse single particles.

Chapter 7

Metal Coated Particles

7.1 Introduction

Gold coated particles behave quite differently from insulating particles. They are perfectly polarisable particles, but act as insulators at low frequencies, below the reciprocal of the charging time of the electrical double layer (EDL) at the metal-electrolyte interface, given by $T_{RC}=a\varepsilon_m / \sigma_m\lambda_D$ (where a is the particle radius, ε_m and σ_m are the permittivity and conductivity of the suspending liquid, and λ_D is the Debye length). This happens because the charged double layer acts like a capacitor, blocking the conduction from the liquid to the particle surface. At high frequency, the EDL is shorted and behaves like a conductor because there is no appreciable charge accumulated in the double layer, therefore the field lines do not run along the surface of the particle but intersect it perpendicularly. At high frequency, gold coated particles are perfectly polarisable, therefore the induced dipole is parallel to the electric field, while at low frequency the opposite occurs. This property could be applied to the sensing of biomolecules, for example using gold nanoparticles as electric labels instead of the common fluorescent labels: coating a particle with gold will change the behaviour at high frequency from insulator (showing nDEP) to conductor (showing pDEP), allowing easy separation or detection by electrokinetic methods.

Gold coated particles offer also an ideal support for immunoassays. Gold is a non reactive metal, but it can be easily functionalized with a monolayer of molecules using thiol
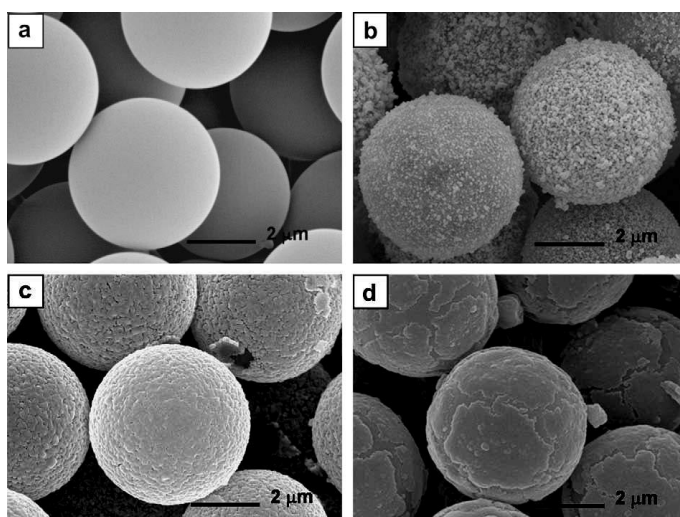
Figure 7-1. SEM images of a) pristine latex bead; b,c,d) gold coated beads obtained by 3 different chemical pathways. The quality of the coating is dependent on the process used, taken from [174].

chemistry. Thiol groups (-SH) are common in biological molecules such as proteins, where they appear in the amino acid cysteine.

In this Chapter the process to gold coat latex beads and the chemical modifications necessary to gold coat SU-8 particles are explained. Gold coated beads were analysed with ROT and DEP to study the effect of different medium conductivities on the EDL relaxation at low frequency. Rod shaped SU-8 particles were analysed after the adsorption of gold colloids onto the surface using ROT and EO in the Maxwell-Wagner frequency region, then after the gold coating with low frequency AC electric fields with only ROT. Gold coated rods were studied also after the functionalisation with uncharged biomolecules to decrease their surface charge. It was not possible to use EO at low frequency because of the strong pDEP and the friction with the glass substrate.

Metal deposition is usually achieved by metal sputtering or by electrochemical deposition, which means that the elements that need to be metal plated must be on a solid support. Although electroless deposition is similar to electrochemical deposition from the chemical point of view, no electrical current is needed for deposition and therefore the method can be used to coat particles in suspension. In electroless plating, metal ions are reduced to metal by a reducing agent, which is an electron donor, through a catalyst that is the same metal [172]. Electroless deposited metal is usually finer in grain than electrochemically deposited metal [173] and more compact because it does not depend on the electric field lines, which are more concentrated at apexes than on flat surfaces. Beads electroless coated with gold are shown in Figure 7-1.
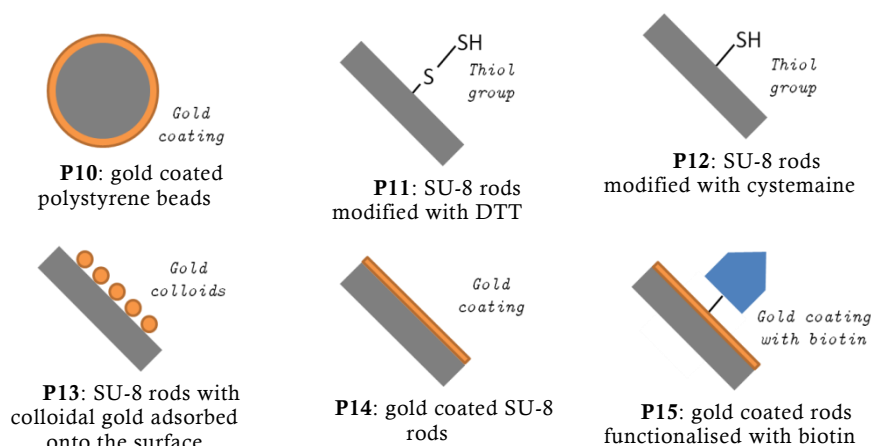
Table 7-1. Summary of the different types of particles treated in this chapter. Particles P10 were studied using DEP and ROT, particles P14 and P15 were studied only using ROT.

The first autocatalytic plating process dates to 1946 and was invented by Brenner and Riddell [175]. The original discovery involved nickel, but since then many other processes involving different metals have been published [172][173]. Of particular interest is the electroless deposition of gold. Many different methods have been published [176]. Many of those methods involve toxic compounds like cyanide and do not work at room temperature, therefore a substantial effort has been undertaken to develop less harmful electroless plating baths [177]. A cyanide free process at room temperature was proposed by Lam *et al.* [178] and adapted by Lim *et al.* [179]. This involves the sensitization of the particles obtained by coating them with cold colloidal nanoparticles. The gold nanoparticles will act as catalysts and seeds for the electroless deposition of gold. The gold nanoparticles were prepared following a modified version of the method proposed by Duff *et al.* [180] that used a rapid reduction of the metal in aged gold solutions.

A summary of the particles used in this Chapter is given in Table 7-1. The process of gold coating polystyrene beads and SU-8 rods is explained below.

7.2 Gold coated beads

This part of the thesis was done in collaboration with YuKun Ren (Harbin University).

Unfunctionalised 10 μm polystyrene beads were gold coated and studied using DEP and ROT at different suspending electrolyte conductivities. The process flow to obtain gold coated particles from unfunctionalised beads is shown in Figure 7-2. First, the beads are modified by adsorbing gold colloids onto their surface, followed by addition of gold ions until a compact shell is formed.
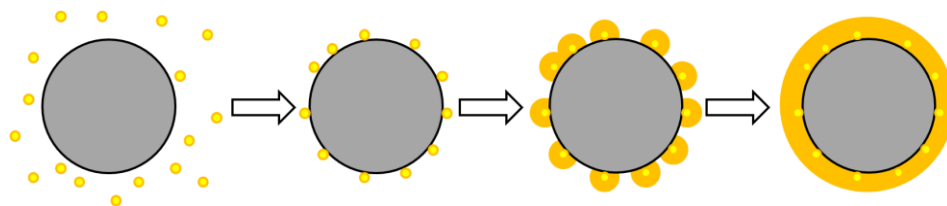
Figure 7-2. Steps involved in the fabrication of gold coated beads. Particles were firstly incubated overnight in a gold colloidal solution then gently washed to remove the excess of unbound colloids. Following the same protocol as for the SU-8 rods, more gold was catalytically deposited starting from the adsorbed gold seeds until a compact shell is formed.

7.2.1 Preparation of the colloidal gold

Gold colloids were prepared following the method proposed by Duff *et al.* [180] and adapted by Lim *et al*. [179] as summarized below.

Materials: Tetrakis (hydroxymethyl) phosphonium chloride (404861, Sigma), KOH (254169, Sigma), hydrogen tetrachloroaurate (Sigma).

Methods: A reduction solution was prepared by adding 12 μl of tetrakis (hydroxymethyl) phosphonium chloride and 1 ml of 1M KOH to 45 ml of DI water in a falcon tube. After 5 minutes, 2 ml of a 25 mM solution of hydrogen tetrachloroaurate were rapidly injected in the reducing solution. Vigorous shaking led to a gold-brown translucent solution in case of an aged gold solution. For a freshly prepared solution it took a few hours to develop the same colour. At this stage the colloids, according to Lim [179], are about 3 nm, but with time the solution changes colour – as can be seen in Figure 7-3 - turning red and developing a typical plasmonic resonance [180]. The colloids used were in the range of 10-20 nm (Figure 7-4). This difference in size was due to the difference in the protocol used in this work. Lim used an aged solution of tetrachloroaurate while a fresh solution was instead used in this work. It is our understanding that an aged solution would have had a large amount of nucleation centres of gold in metal state while a fresh solution would have had only a smaller amount, causing the gold nanoparticles to be bigger and less in number.
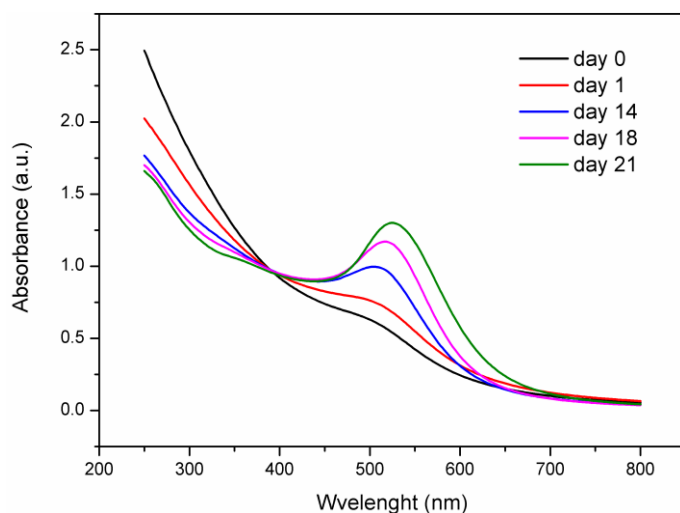
Figure 7-3. Absorbance measurements of the gold colloid suspension at different times. The data show the developing of a peak around 520 nm due to the increase in size of the colloids and the relative plasmonic resonance.
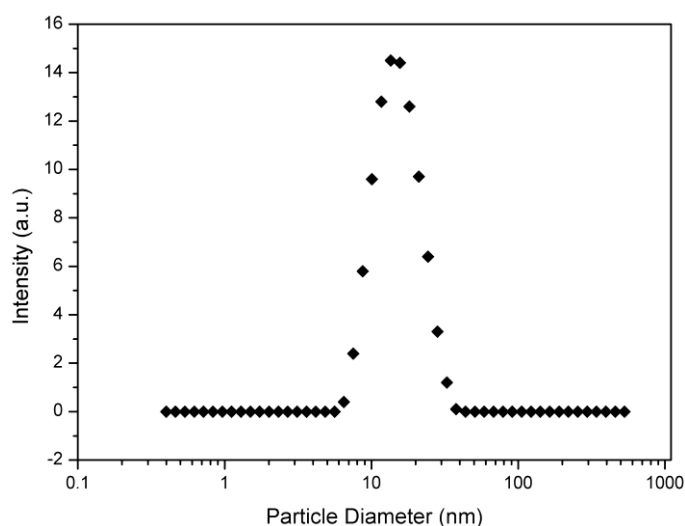
Figure 7-4. Size distribution of the gold colloids measured with Zetasizer Nano ZS (Malvern). Data points are the percentage of the particles with a given size.

7.2.2 Adsorption of the gold colloids

Materials: Gold colloidal solution prepared as in 1.37.1.

Methods: The gold-coated latex beads were fabricated from un-functionalised plain polystyrene beads. The lack of reactive groups on these beads required the use of adsorption methods rather than thiol chemistry. 2 mg of beads were incubated overnight in a gold colloidal solution prepared as explained in 1.37.1. The gold colloids adsorbed onto the surface

of the particles through van der Waals interaction. A gentle wash was used to remove excess colloids.

7.2.3 Electroless deposition of gold

Electroless deposition of gold was performed by adaptation of the method in Lim *et al.* [179].

Materials: Gold (I) sodium thiosulfate (39741, Alfa Aesar), L-ascorbic acid (A5960, Sigma), NaOH.

2 mg of particles modified with gold colloids and suspended in DI water were spun down and the supernatant was replaced with 200 μl of a plating solution composed of 34 mM gold (I) sodium thiosulfate and 57 mM L-ascorbic acid in 1 ml of DI water. 20 μl of 1M NaOH was then added to trigger the reducing reaction of gold and the test tube was mixed for a few minutes. The end of the chemical reaction was marked by a change in the colour (black) of the suspended particles. The reaction was then quenched adding 1ml of DI water and the supernatant discarded and replaced with other 200 μl of the plating solution to repeat the previous step. The plating was repeated again with 200 μl and finally with 400 μl of the plating solution, adding the correspondent amount of NaOH. The sample was washed 3 times (3 x 1ml) in DI water to remove the reagents. The presence of the shell was demonstrated by SEM imaging of the particles, as shown in Figure 7-5.
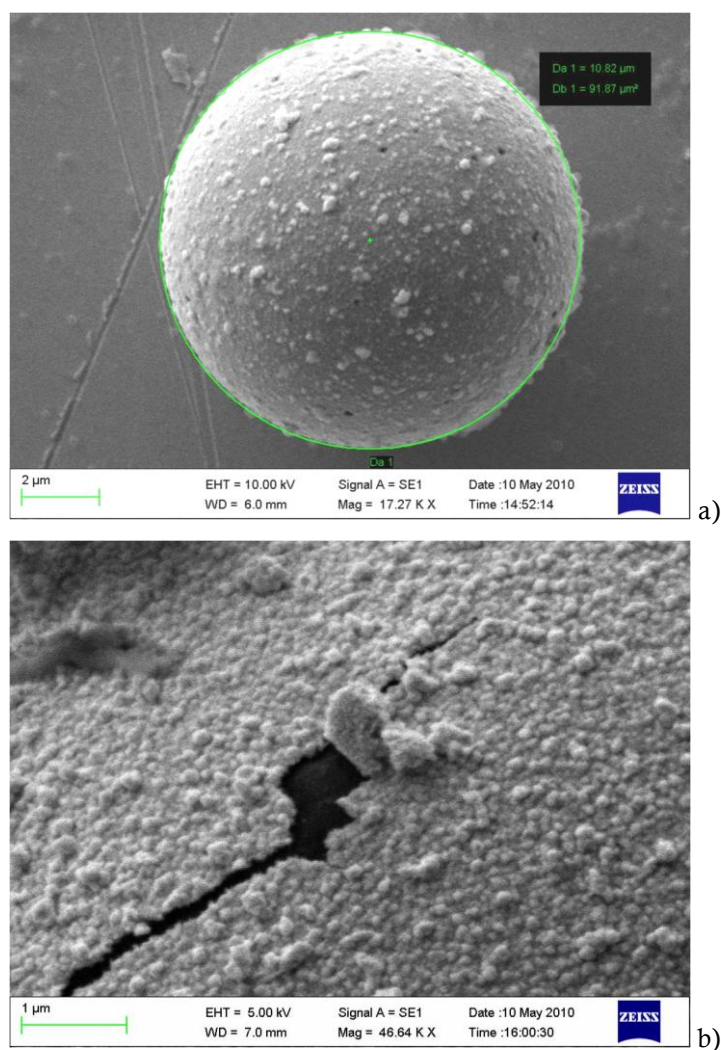
Figure 7-5. SEM images of gold coated beads. a) 10 µm bead after the gold coating. The small black spots are holes in the metal shell. b) High magnification SEM image of a cracked metal shell showing the thickness of the deposited layer. The black part is the native non conductive surface of the latex bead.

7.2.4 Electrokinetic measurements of gold coated beads (P10)

Particles were suspended in electrolytes with different conductivities adjusted with KCl to 0.7, 3.6, and 15.9 mS/m.

Results: For the ROT measurements, a gold coated bead was placed in the middle of a quadrupolar electrode array (500 µm between opposing electrodes), and was kept n position using a laser trap or a pipette tip. The laser cannot trap reflective particles, but can be used to push them. At least three complete rotations were recorded with a camera using a sinusoidal signal with a 4 Vpp amplitude, and the data was processed to obtain the angular speed of the particle as shown in Figure 7-6a. The rotation of the particles was counter-field as shown in
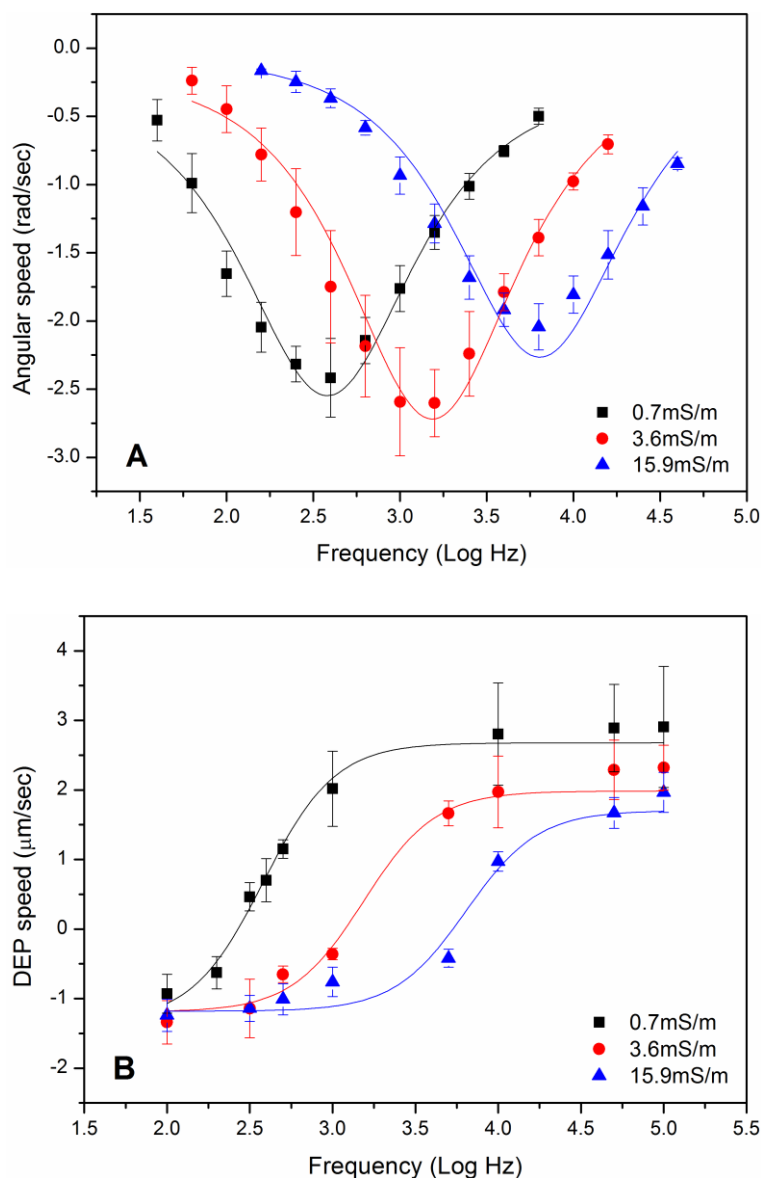
Figure 7-6. (a) ROT and (b) DEP spectra for gold coated 10μm beads. The particles were analysed with the three different conductivities of the suspending electrolyte indicated on the graphs. Error bars are the standard deviation of 10 different particle spectra. Solid lines are the resulting fit using a generic Debye relaxation. For ROT measurements a 500 μm gap array was used with 4Vpp; for DEP measurements a 200 μm gap electrodes with 5Vpp.

Figure 7-6a, meaning that the imaginary part of the polarizability is positive and therefore the real part should increase with frequency. This was confirmed by the DEP measurements.

For DEP measurements, particles were placed in the middle of the quadrupolar electrode array (200 μm gap) with adjacent electrodes energized with opposing phase. The centre of the quadrupole in this configuration has an approximately linear field gradient within an area of about 50% of the area between the electrodes. Therefore the movement of the particles was

recorded along any arbitrary radius from the centre of the electrodes. The results are shown in Figure 7-6b for each of the three conductivities. It shows that the DEP force increases with frequency as expected from ROT measurements, and counter to that observed for non-polarisable polymer particles.

At very low frequency and low conductivity (<10 mS/m) ACEO was observed to occur at the electrodes, moving the fluid from the centre above of the electrode arrays to the outside. From symmetry, the centre of the array - on the glass - is a stagnant point; therefore the movement of the particles was not affected by the fluid motion. That was confirmed by studying the motion of different sizes of particles: fluid flow would move any two particles with the same speed while DEP movement would scale with the square of the radius.

The ROT and DEP spectra can by fitted using a generic Debye relaxation

$$K_\infty + \frac{\Delta K}{1 + j\omega\tau} = K_\infty + \frac{\Delta K}{1+(\omega\tau)^2} - j\frac{\Delta K(\omega\tau)}{1+(\omega\tau)^2} \qquad (6.1)$$

to obtain the value of the relaxation frequency for each conductivity, as shown in Table 6-2:

σ_m (mS/m)	λ_D (nm)	f_{RC} measured (Log Hz ± fit error)	f_{RC} calculated (Log Hz)
0.7	45	2.58 ± 0.02	3.1
3.6	20	3.15 ± 0.02	3.5
15.9	9.4	3.79 ± 0.01	3.8

Table 7-2. Calculated and measured relaxation frequencies for the data in Figure 7-6. The corresponding Debye length (λ_D) is also shown, together with the calculated values for the relaxation frequencies. The errors are the uncertainty associated with the fit, because there are no complete spectra for single particles.

The relaxation frequency can also be easily calculated using an equivalent RC circuit following what is suggested in [108]: the EDL is the capacitive element while the resistive element depends on the conductivity of the solution. In that approximation the relaxation frequency is $f_{RC}=\sigma_m\lambda_D/a\varepsilon_m2\pi$ [107][181], where $t_{RC}=1/(2\pi f_{RC})$ is the RC time of the EDL, which means the time it takes to charge completely. σ_m is the suspending electrolyte conductivity, *a* is the radius of the particle, ε_m the suspending electrolyte permittivity and λ_D the Debye length associated with the corresponding ion strength. These data are also shown in Table 7-2. The measured values only approximately match the values calculated from the theory, but the trend is the same, a common problem in ACEO and ICEP [182]. The difference in behaviour is often related to contamination or oxidation of the surface (which gives effectively an additional insulating layer) or to the roughness of the metal which can suppress the fluid flow [183] and increase the effective capacitance. As shown in the SEM picture in Figure 7-5b, the surface of the particles is very rough (in nanometer scale) – this could provide an explanation for the difference in behaviour.

7.3 Gold coated rods

SU-8 rods were gold coated and studied using ROT. Native SU-8 rods (P01) only weakly bound the gold colloids, therefore the particles were chemically modified to produce a surface rich in thiol groups (-SH). Thiols react with gold forming a stable bond that will make the gold colloids adhere onto the surface of the particles.

7.3.1 Thiol modification of the particles

Two different methods were tested to produce a surface rich in thiol groups. The first method uses dithiothreitol (DTT) to obtain particles P12, while the second uses cysteamine to obtain particles P13, respectively C07 and C08 in Figure 7-7.

C07)   *C08)*
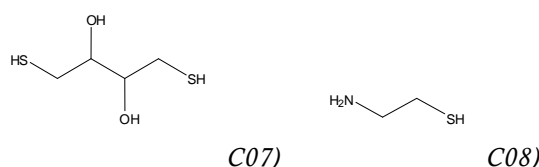
Figure 7-7. Molecular structure of dithiothreitol (DTT, C07) and cysteamine (C08), used in the modification of SU-8 to obtain a surface rich in thiol groups (-SH).

7.3.1.1 Modification with DTT (C07)

The reaction is a nucleophilic addition of a thiol group of a DTT molecule which reacts with an epoxy ring provided by a native SU-8 particle to obtain particles P11. The reaction is explained in Reaction 7-1.
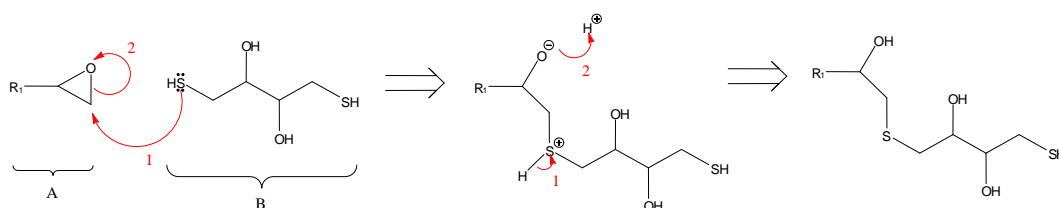
Reaction 7-1. Reaction scheme of DTT reacting with an epoxy ring. A is particle P01, B is DTT (C07). R_1 is an unspecified residue that does not participate in the reaction. Arrows indicate the movement of the electrons in the reaction.

Materials: DL-Dithiothreitol (43819, Sigma), Tris(2-carboxyethyl)phosphine hydrochloride (TCEP, C4706, Sigma), DMF, methanol.

Methods: 2 mg of native SU-8 particles was resuspended in DMF, spun down and the supernatant replaced with 1 M solution of DL-Dithiothreitol. The sample was sonicated for one minute to resuspend the particles and then left on a mixer for 4 hours. Particles where then washed 6 times (6 x 1 ml) in DMF, 3 times (3 x 1 ml) in methanol and three times (3 x 1 ml) in DI water with 0.02% Tween20 to remove any excess of reagents and organic solvents. The sample was then resuspended in a 0.5 M solution of TCEP in DI water and mixed for two hours and then washed 6 times in DI water and Tween-20. TCEP was used to re-activate the thiol groups oxidised to disulphide bonds and for that reason particles were exposed to gold colloids immediately afterwards to have the maximum reactivity. Disulfide bonds may form when thiol groups are interacting with nearby thiol groups on the surface and that could diminish the trapping of the gold colloids because of the smaller number of thiol groups available. The TCEP is a very strong reducing agent and cleaves the disulfide bonds. For that reason TCEP is used also in molecular biology to separate the two units forming the IgG molecular structure connected by disulfide bonds.

7.3.1.2 Modification with cysteamine (C08)

The reaction to obtain particles P13 is the same reaction described to obtain amino-modifed particles in 1.24.1. Also in this case a primary amine reacts with an epoxide ring to form an amide bond. Thiol groups may react as well following the scheme shown in Reaction 7-1, leaving in this case the amine groups exposed. According to the literature, amine groups can show an affinity for gold [184] even if the bond is less stable than that formed by thiol groups.
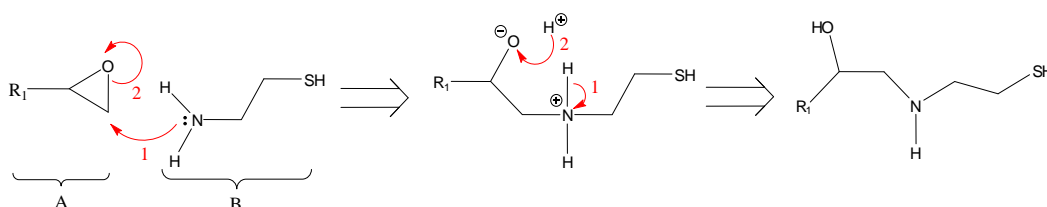
Reaction 7-2. Reaction of cysteamine with an epoxy ring. A is particle P01, B is cysteamine (C08). R_1 is an unspecified residue that does not participate in the reaction. Arrows indicate the movement of the electrons in the reaction.

Materials: Cysteamine (30070, Sigma), Tris(2-carboxyethyl)phosphine hydrochloride (TCEP, C4706, Sigma), DMF.

Methods: Native SU-8 particles were suspended in a mixture of 30 mg of cysteamine in 1 ml of DMF and shaked for 4 hours. The sample was then washed 6 times in DMF (5 x 1 ml), three in methanol (3 x 1 ml) and three times in DI water and Tween-20 (3 x 1 ml). The sample was then suspended in a 0.5 M solution of TCEP in DI water and mixed for two hours and then washed 6 times in DI water and Tween-20. TCEP was used to re-activate the thiol

groups oxidised to disulphide bonds because of a reaction with other cysteamine molecules in solution, leaving exposed in that case only an amine group which is less reactive and forms a less stable bond with gold than a thiol group.

7.3.2 Surface adsorption of gold colloids and electrokinetic measurements (P13)

Thiol modified particles P11 and P12, as in 1.38.1.2, were modified by immobilizing gold colloids onto their surface with the method described in 1.37.2 to obtain particles P13. The resulting particles were studied with ROT and EO.

Results: The washed pellet appeared to be darker in colour than the sample prepared with the method explained in 1.38.1.1, suggesting a higher level of gold colloid loading. The reaction of an amine group with an epoxide group seems more efficient than the reaction of a thiol group. Thus the particle surface modified with cysteamine is rich in thiol groups and poor in amine groups, because these prefer to react with the SU-8 epoxide rings.

The electrokinetic spectra of these rods are shown in Figure 7-8. They showed a different behaviour in the low frequency region of the EO spectrum compared to the spectra obtained in Figure 5-3 for the biochemically modified SU-8 particles. Data at low frequencies could not be collected because of positive DEP, which was so strong that the particles would not stay in the middle of the array for the entire measurement. Particles did not show any negative DEP in the frequency range used. Also, the laser trap could not be used because reflective particles are repelled by the laser beam instead of being trapped. The EO spectra for the rods could not be analysed with the Maxwell-Wagner model that predicts the alignment constant to have a constant value at low frequency, therefore a fit to the data using the model proposed in Chapter 2 was not possible. A generic fit with a Debye relaxation added to the Maxwell-Wagner relaxation would not produce sensible results because there are not ROT data points at frequencies low enough to determine the exact position of the relaxation.

The change of the alignment constant at low frequency could have a similar origin to the slope observed at low frequency in sections 1.32.2.2 and 1.32.4.2. This effect might be caused by percolation of the adsorbed gold colloids, causing a relaxation in the conductivity (see Figure 6-14, for $n_2 = 0.9$) at low frequency. The average size of the gold colloid (10 - 20 nm) is bigger than avidin (5 nm) so they should not be able to enter in the polymer matrix, therefore trapping must happen on the surface or only in a thin layer where the polymer is not fully crosslinked. Gold colloids belonging to the left-hand side tail of the distribution in Figure 7-4 could be small enough to enter in the bulk. Particles short-circuiting the electrodes could not cause this behaviour, as all the data were collected in three different steps, divided by the washing of the chamber and the mixing required to find and placing a single particle in the middle of the electrodes.
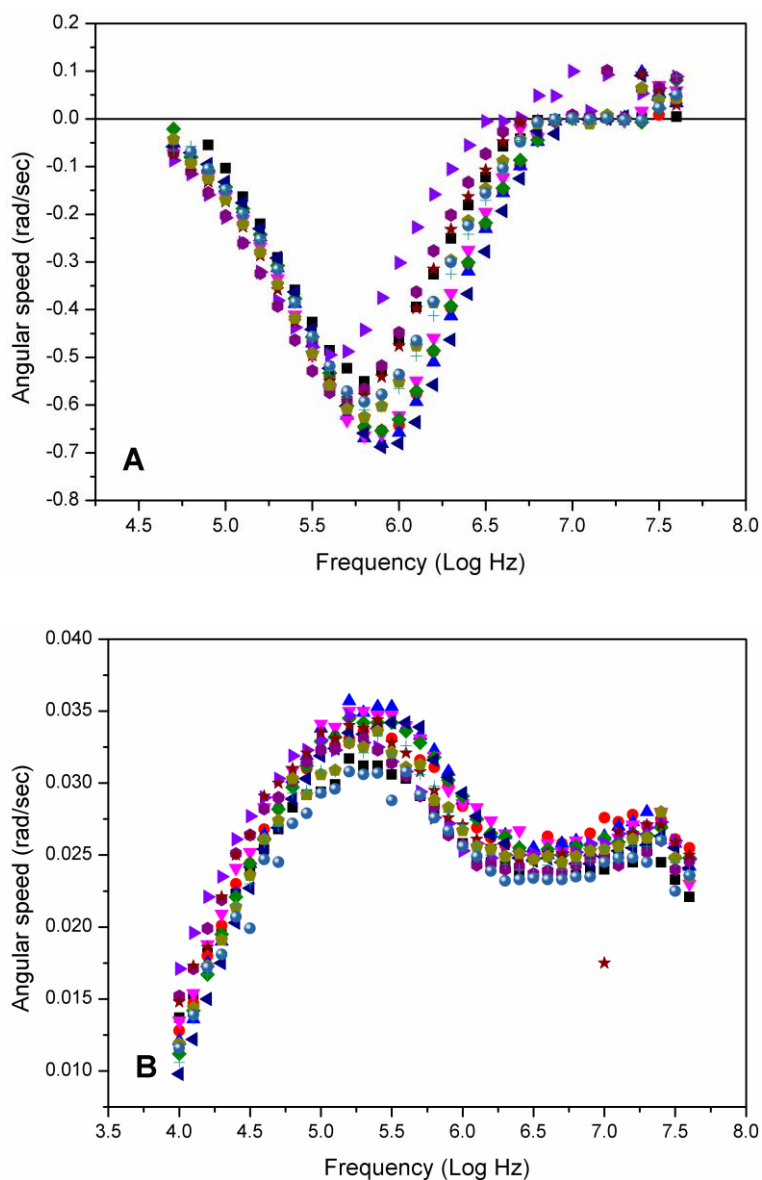
Figure 7-8. a) ROT and b) EO spectra of SU-8 rods with immobilized gold colloids onto their surface (P13). Spectra are normalized to 1V.

7.3.3 Electroless deposition of gold and ROT measurements (P14)

Electroless deposition of gold was performed by an adaptation of the method proposed by Lim [179] as explained above in 1.37.3 to obtain particles P14. The reaction produced a thick homogeneous gold layer about 200 nm thick, with only a few defects on the edge of the
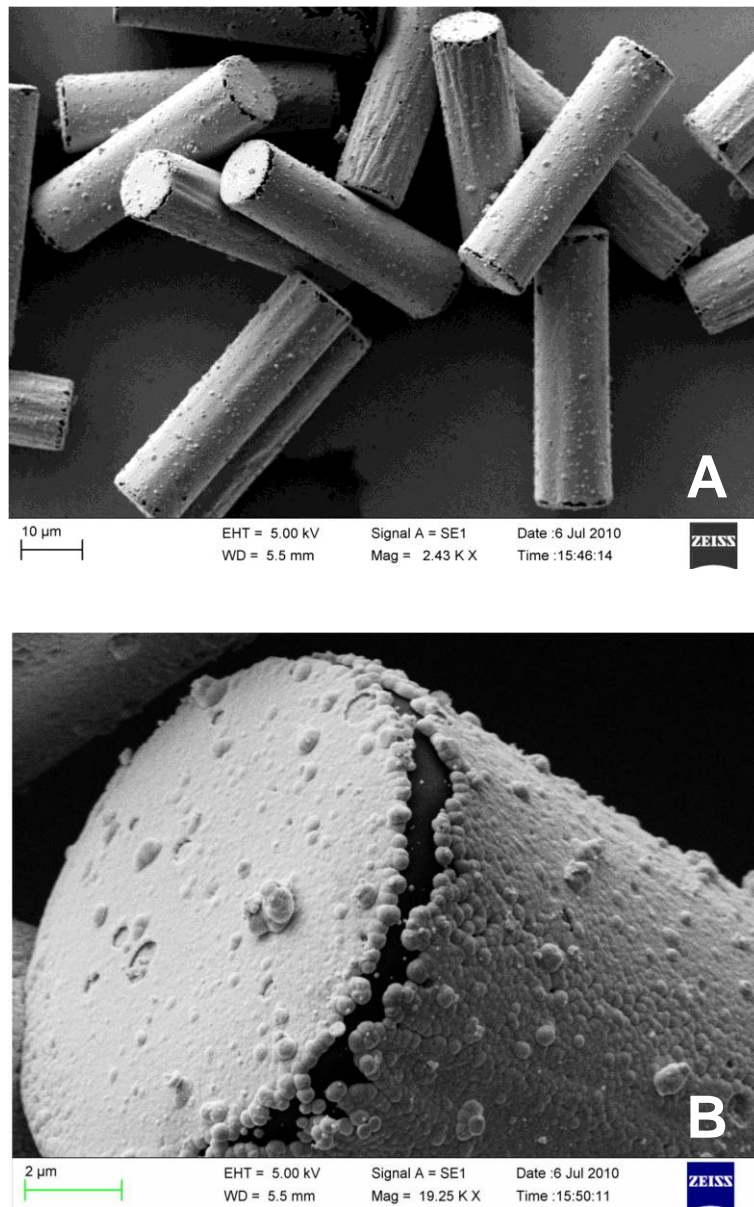
Figure 7-9. a) SEM image of the gold coated rods; b) detail of the metal coating showing the thickness and structure of the metal layer.

particles as shown in the SEM images in Figure 7-9 and as suggested by the gold colour of the pellet.

Results: 15 particles were analysed using ROT after being resuspended in the ROT buffer (σ_m=2.01 mS/m). In this case a chip with a 500 μm gap between opposite electrodes was used. Because of the strong positive DEP force due to the highly polarisable metal surface, it was impossible to work with the usual chips at the usual range of frequencies. A bigger gap between opposing electrodes leads to a weaker DEP force (due to the smaller gradient of the field in the middle of the chip) but on the other hand also the field strength is lower.
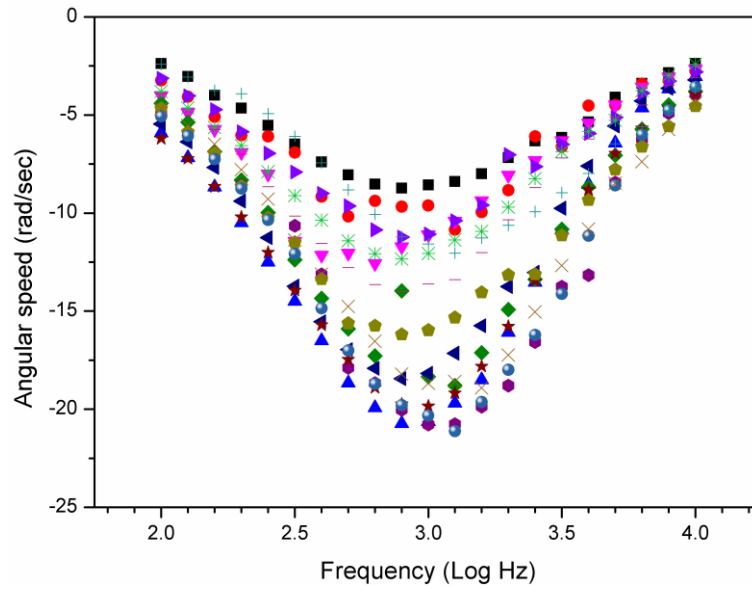
Figure 7-10. ROT spectra of 15 gold coated SU-8 rods. The measurements were taken with 500 μm gap electrodes and the spectra are normalized to 200 μm gap and 1V.

Consequently ROT experiments in the MHz range were not possible. However, a different rotation peak was observed at lower frequencies as shown in Figure 7-10.

This electrorotation peak is related to the relaxation of the double layer formed at the interface between the metal and the surrounding suspending electrolyte, as described in section 1.17 and 1.37.4. The difference between ROT spectra of particles is larger than observed with the chemically modified particles, probably because of differences in coating between particles, or because some particles short-circuit adjacent electrodes reducing the electric field strength in the chamber (randomly affecting particles analysis). There are no analytical models that describe the motion of elongated metal particles which could be used to fit the data, therefore the data was fitted to a Lorentzian peak to estimate the relaxation time. A Lorentzian function is the mathematical expression of a Debye relaxation in the imaginary part of the permittivity. The equation used to fit the data was:

$$y_{lorentzian} = A\frac{w}{\left(x - f_{RC}\right)^2 + w^2} \tag{6.2}$$

where A, w and f_{RC} were free parameters to be obtained from the fit. The fit results are in Table 7-3.

	A (rad/sec/Log Hz)	f_{RC} (Log Hz)	w (Log Hz)
SU-8 rods coated with gold	-10 ± 2	2.96 ± 0.07	0.62 ± 0.04

Table 7-3. Fit result of the SU-8 rods coated with gold using the data in Figure 6-9 using a Lorentzian curve for the fitting. The error is the standard deviation of 15 particles.

The amplitude of the peak is defined as $\Lambda=|A|*w$, which means $\Lambda=16 \pm 3$ (CV=19%) where the error is the standard deviation of 15 particles.

7.3.4 Gold coated particles functionalised with biotin - ROT measurements (P15)

Thiol chemistry was used to form a monolayer of biotin (C05) on the gold rods. Biotin does not have any thiol groups but the molecule can be easily modified using the pendant carboxyl group. Following Reaction 4-4, the surface was modified with cysteamine (C08) to provide amine groups that will react with the carboxyl group of the biotin, giving particles P15.

Materials: Biotin (B4639, Sgma), N-(3-Dimethylaminopropyl)-N'-ethylcarbodiimide hydrochloride (EDC.HCl, 03449, Sigma), N-Hydroxysulfosuccinimide sodium salt (sulfo-NHS, 56485, Sigma), Cysteamine (30070, Sigma), MES sodium salt (M5057, Sigma), NaCl, Tween-20.

Methods: 1 ml of the activation buffer, prepared as in 4.2.3.1, was used to dissolve a 1:1 mixture of biotin and cysteamine (~20 mg), 1 mg EDC.HCl and 1 mg sulfo-NHS together with ~2 mg of gold coated particles. The reaction was gently shaken overnight to allow the completeness of the reaction and the formation of the monolayer. Particles were washed in DI water and Tween-20 (0.02%) four times (4 x 1 ml) to remove the unreacted molecules and stored in DI water until further use.

Results: The monolayer of biotin should partially screen the metal surface and reduce the rotation speed. The experimental results are presented in Figure 7-11, while the fit results obtained using a Lorentzian peak are shown in Table 7-4.

	A (rad/sec/Log Hz)	f_{RC} (Log Hz)	w (Log Hz)
Gold coated SU-8 rods functionalised with biotin	-8 ± 1	2.9 ± 0.1	0.69 ± 0.04

Table 7-4. Fit results of the cold coated rods functionalised with biotin using the data in Figure 6-10 and a Lorentzian curve for the fitting. The error is the standard deviation of 14 particles.
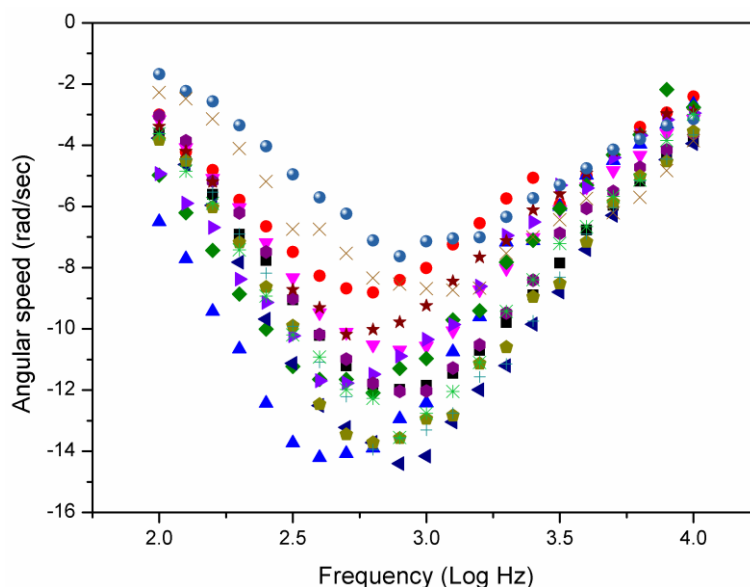
Figure 7-11. ROT spectra of 14 gold coated SU-8 rods functionalised with biotin. The measurements were taken with 500 μm gap electrodes and the spectra are normalized to 200 μm gap electrodes and 1V.

The average peak amplitude in this case is $\varLambda = 12 \pm 1$ (CV=8%), this means there is less variation in the experimental results after the functionalisation. The magnitude of the peaks is lower for unmodified gold coated rods by an amount equal to the error, which means that the difference is statistically significant.

7.4 Discussion

This chapter describes the behaviour of metal coated particles in electric fields. Rod shaped particles and beads were analysed using DEP and ROT. The effect of electrolyte conductivity and surface properties were also investigated.

SU-8 particles (rods) and latex particles (beads) were metal coated in suspension using a self-catalyzed reaction which deposited gold. The method started from Au nanoparticles adsorbed onto the surface of the particles. This method (used for the first time on microscopic polymer particles) formed a homogeneous and compact metal shell around particles of different shapes.

Metal-coated beads P10 were studied using DEP and ROT with different suspending electrolyte conductivities, and the data obtained were fitted using a standard Debye relaxation. The results are in qualitative agreement with the theory, although some discrepancies are observed, probably due to the roughness of the metal shell which increases the capacitance of the DL, shifting in frequency the position of the relaxation. The DL dominates particle behaviour: at low frequency it screens the metal from the electric field but

at high frequency it is transparent to the electric field (it behaves like a short-circuited capacitor) leaving the gold shell exposed. Such capacitor-like element gives rise to the relaxation observed.

The ROT spectra of rod shaped particles with different surface properties - gold colloids (P13), bare gold (P14) and biotin functionalised gold (P15) - were also analysed. A summary of the data for particles P14-15 is shown in Figure 7-12.

Particles P13 showed a different EO spectrum from the other particles seen in Chapter 6 , characterised by what seems to be a percolation effect that modifies the conductivity.

Particles P14 and P15 had a different peak magnitude; despite the large spread in the values (CV equal to 19% and 8% respectively), the difference in the value was statistically significant. This behaviour confirms that the addition of a dielectric layer on the metal screens the surface of the particle from the electric field, and the particle becomes similar to a dielectric particle and the electric torque vanishes (see [107], and [185] for a study on the related phenomena of ACEO over contaminated electrodes). The addition of a dielectric layer is in fact similar to the series addition of a capacitor to the double layer: the potential drop across the EDL becomes smaller and therefore the applied torque on the particle is reduced. Because the capacitance of the system decreases, also the charging time is expected to decrease accordingly. In fact, a thin dielectric layer (i.e. smaller then the Debye length: $\lambda_d < \lambda_D$) changes the ζ-potential of the surface of the particle by a factor

$$\delta = \left(1 + \frac{\varepsilon_w \lambda_d}{\varepsilon_d \lambda_D}\right)^{-1} \qquad (6.3)$$

where ε_w is the permittivity of the water and ε_d is the permittivity of the thin dielectric layer. In our case, if we consider the layer to have a thickness ~1.3 nm (the dimension of a biotin molecule) and relative permittivity equal to 3.3 [186] we obtain $\delta = 0.5$, smaller compared to the value of $\delta = 0.75$ obtained from the ratio of the peak amplitude of biotin modified gold coated particles and plain gold coated particles. Therefore, we overestimated the thickness of the layer or the coating was not homogeneous on the surface, some other effects might interfere as well, like the roughness of the surface. The relaxation time should change in the same way by a factor $\delta = 0.75$, which should be found between the results for the two types of particles. The expected f_{RC} would be 3.08 log(Hz), which is close to the error range of the f_{RC} obtained in the case of biotin modified particles (see Table 7-4). Concluding, the behaviour of these particles is qualitatively in accord with the theory commonly found in literature but the spread in the relaxation time between different particles, probably due to different sizes, partially masks the effect. There are no analytical solutions in the literature for the motion of
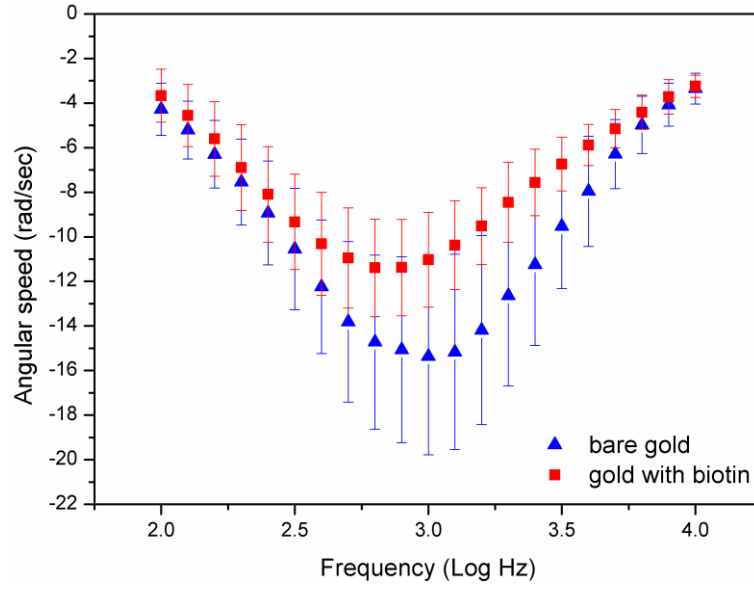
Figure 7-12. Summary of the electrokinetic results for the two surface types of gold coated rods: bare gold and gold functionalized with biotin. Triangles are particles P14, squares are particles P15. The error bars are the standard deviation of the data from all the particles of that type at that frequency. All the spectra are normalized to 1V and 200 μm electrode gap.

ellipsoidal metal particles in rotating electric fields and therefore the following considerations on their properties compared with beads are only qualitative.

The peak positions of the ROT spectra measured for gold coated beads and gold coated rods cannot be directly compared because the peak position is a function of particle dimensions. Calculating an equivalent spherical radius for an ellipsoid is probably non-trivial, therefore it was decided to adopt a simple method and average the contribution of each axis, similar to the method used for the conductivity of ellipsoidal particles in Section 2.4. This produces the following expression for the relaxation frequency:

$$f_{RC} = \frac{\sigma_m \lambda_D}{2\pi \varepsilon_m a'} = \frac{\sigma_m \lambda_D}{2\pi \varepsilon_m} \frac{1}{2} \left(\frac{1}{a} + \frac{1}{b} \right) = \frac{\sigma_m \lambda_D}{4\pi \varepsilon_m} \frac{a+b}{ab} \tag{6.4}$$

Where a' is the equivalent (spherical) radius of an ellipsoidal particle with semi-axis a and b on the same plane as the rotating electric field. For a particle with $2a=40$ μm and $2b=10$ μm, the equivalent radius is $2a'=16$ μm. All the data can be plotted together after rescaling the relaxation frequency as follows:

$$f_{RC} a = \frac{\sigma_m}{2\pi \varepsilon_m} \lambda_D = \frac{\sqrt{\sigma_m}}{2\pi} \sqrt{\frac{D}{\varepsilon_m}} \tag{6.5}$$

143
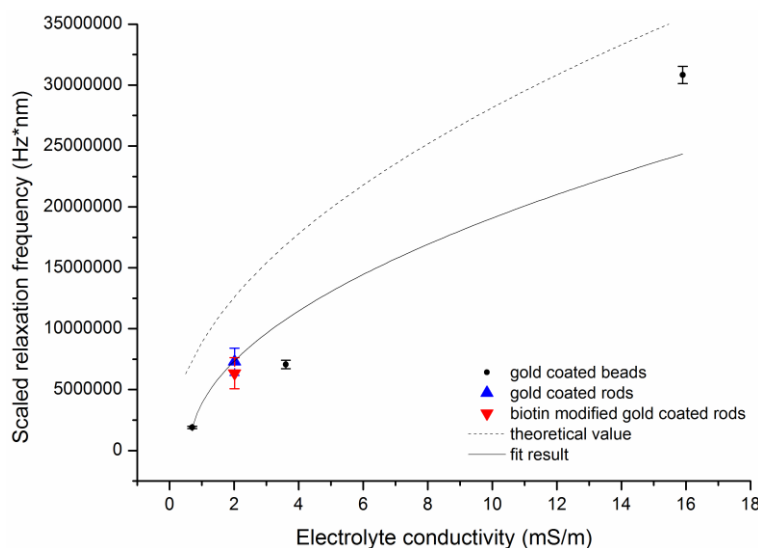
Figure 7-13. Scaled relaxation frequency for the gold coated beads and the gold coated rods (bare gold surface and biotin-modified). All the particles appear to follow the same trend, qualitatively similar to the theoretical value (dashed line) for 10 μm beads. Squares are particles P10, circles are particles P14 and triangles are particles P15. The solid line is the fit performed using equation (6.6).

The results are summarised in Figure 7-13 where it is shown that this theoretical model is able to describe the experimental results qualitatively even for ellipsoidal particles, after rescaling to take into account the different dimensions along different axes. The gold-coated rods follow the same trend as the gold coated beads, similar to the theoretical predicted behaviour.

Equation (6.5) can be generalized in the form:

$$f_{RC}a = A\frac{\sqrt{\sigma_m + B}}{2\pi}\sqrt{\frac{D}{\varepsilon_m}} \tag{6.6}$$

where the parameters A and B are to be found through data fitting. A represents a correction factor for the particle dimensions, and should take into account that the roughness of the surface is effectively increasing the overall surface of the particle. B represents a correction in the medium conductivity which may differ from the nominal value. The result of the fit is shown in Table 7-5 and in Figure 7-13

	A(unitless)	*B* (mS/m)
Gold coated particles	0.7 ± 0.1	-0.61 ± 0.09

Table 7-5. Fit result of the data in Figure 7-13 using equation (6.6). The error is the uncertainty of the fit.

Figure 7-14. Cartoon representation of a rough surface created by spherical caps having base diameter 2a *and height* h. *In a first order approximation the ratio between the area of the underlying surface and the surface of the caps is the same as the ratio between the surface area of a single cap and its base.*

The value of the correction factor *A* obtained from the fit is compatible with the hypothesis that the roughness of the surface can shift to lower frequency the value of the f_{RC} due to the increased capacitance of the EDL. The roughness of the surface can be estimated using a simple toy-model. Consider a surface tiled with spherical caps, as in Figure 7-14. The ratio between the area of the underlying flat surface and the overall surface area (due to the spherical caps) can be thought of as being roughly the same as the ratio between the surface area of the single spherical cap and the area of its base.

The surface area of the cap is given by $\pi(a^2+h^2)$ while the area of its base is πa^2. The ratio is therefore given by

$$\Phi = 1 + \frac{h^2}{a^2} \tag{6.7}$$

which for *0<h<a* gives *1<Φ<2*. The equivalent (and bigger) radius for a surface with ratio F is therefore

$$r' = r\sqrt{\Phi} = r\frac{1}{A} \tag{6.8}$$

where A is the parameter obtained with the fit. Using the value for A, *Φ=2.0±0.3* is obtained. That value of *Φ* represents a surface tightly packed with hemispheres, which is qualitatively in accord with the SEM images in Figure 7-5 and Figure 7-9.

7.5 Conclusions

Gold is an ideal substrate for the biochemical modifications aimed at biosensing applications: it is non-reactive, but can be easily functionalised using thiol chemistry to form a monolayer of molecules. Gold deposition transforms a surface from non-conductive to conductive, while a monolayer of uncharged molecules on gold will result in a non-conductive surface again.

An electroless method to gold coat particles in solution was presented in this Chapter. This method used an autocatalytic reaction to deposit gold starting from gold nanoparticles adsorbed onto the surface of particles. The gold nanoparticles can be adsorbed onto the surface of latex particles by Van der Waals forces, or they can be bound to SU-8 rod-shaped particles functionalised with thiol groups. The deposition of gold created a thin shell that surrounded the particles. The gold layer obtained with this method was rough, compact and around 200 nm thick.

Particles modified in that way behaved as perfectly polarisable particles due to the metal shell, and at low frequency (< 10 kHz) they showed a relaxation due to the polarization of the electrical double layer (EDL). Gold coated spherical particles were studied using DEP and ROT using different suspending electrolyte conductivities. Their behaviour was qualitatively in agreement with the theory, with discrepancies that can be related to the roughness of the surface. Surface roughness increases the effective surface of the particles and shifts the position of the relaxation towards lower frequencies.

SU-8 rod-shaped particles were first biochemically modified to have a surface rich in thiol groups, which were used to bind gold nanoparticles to the surface of the particles. The particles modified in that way were studied using ROT and EO and they showed clearly distinctive spectral features from unmodified particles. This result could be used for biosensing, where the reporting molecule has not attached a fluorescent label but an electric label instead, consisting of a gold nanoparticle. The change in surface properties would be detected using electrokinetics instead of using fluorescence microscopy.

A layer of gold was deposited on the particles with immobilised gold nanoparticles to form a conductive shell. The conductive shell of the particles was also modified to have a monolayer of non conductive molecules which screened the gold from the electric field making the particles less conductive. Gold coated particles were studied using only ROT, because when using EO they did not move freely on the glass due to their density. The ROT spectra showed the presence of the EDL relaxation in a position which is qualitatively in accord with the theory. The addition of a non-conductive monolayer of molecules caused a decrease in the relaxation peak magnitude. The difference in electrokinetic properties between the particles with immobilised gold nanoparticles and gold coated particles could be used as an amplification method when using the gold nanoparticles as electric label. Once the reporting molecules have been captured by the particle, the deposition of further gold will allow a clear distinction (visually as well) between particles carrying the reporting molecules and particles that do not. The difference in peak magnitude between the gold coated particles and those further functionalised with a non-conductive monolayer is consistent with the theory of EDL relaxation on contaminated electrodes and could be used again in the framework of biosensing. In this case the target molecules could bind to the gold coated particles modified

using thiol chemistry. The binding event would be seen as a change in the surface conductivity of the particles and consequently as a change in the peak magnitude. In this case no labelling would be required.

Chapter 8

Conclusions

In this thesis a new method has been presented for the study of the electrical properties of elongated particles. The method consists of a combined measurement of ROT and EO spectra of the same particles, and the method was used to obtain the particle permittivity and surface conductance. Up to this date, single particles have not been studied using EO on a single particle by particle basis. Traditionally, particles were analysed with EO in batches, therefore the measurements could not be directly related to the corresponding ROT data. The new technique was achieved by moving from a conventional parallel electrodes setup for EO to quadrupolar electrodes. Quadrupolar electrodes enable the electric field to be switched between orthogonal directions from one measurement to the next. In this way the particle under examination does not need to be moved and always rotates 90°. The quadrupolar electrodes were also used in a more conventional way to perform ROT on the same particle. The process was greatly simplified by the negative DEP that nearly all particles exhibit at all frequencies. Unfortunately, metal coated particles showed only positive DEP, limiting the measurements to ROT and DEP. The continuous motion of the particles observed with ROT necessitated the use of a laser to push the particle back in position at the centre of the electrode array.

8.1 Chemically modified SU-8 rods

The motion of SU-8 particles in AC electric fields was studied as a function of the chemical properties of their surface. The study started with native SU-8 particles, which do not have any charged group. The following modification steps used the reactive epoxide groups to add to the surface either positive or negative charges (at pH 7), respectively from the amine groups (NH_3^+) or carboxyl groups (COO^-). The amine groups were subsequently used to modify the surface of the particles, attaching uncharged molecules such as biotin. Avidin was also coupled to the surface of the particles. A fluorescently labelled avidin was used to check the binding of the protein to the surface. Avidin has 4 binding sites for biotin, one or two of which are used to attach the protein while the others were used to bind biotinylated IgG. Proteins like avidin and IgG carry many charges (both positive and negative) which might increase the surface conductance of the particles.

Our step-by-step study of the chemical functionalisation of SU-8 rod-shaped particles showed that the process of addition of charges onto the surface of particles modify the particle in other ways, as confirmed by measuring particle size and loading level (with the Kaiser test). The change in the particle permittivity was the main effect measured using AC electrokinetics. This change could be observed in the EO spectra in the high frequency region, where effects are dominated by the particle permittivity. The amount of surface charge (measured as surface conductance) changed in all the modification steps, but only from 0.5 nS to ~1 nS. It is possible that the modifications happened mostly in the bulk of the particles, making the charges not available for electrokinetic measurements, hence not allowing a clear differentiation of the particles on that basis.

The chemical modification of epoxides is well established, but the surface modification of SU-8 particles is less-so. Chemical modifications seem to occur in the bulk of the particles, probably because the epoxide rings at the surface are degraded to non-reactive hydroxyl groups when they interact with the environment after the development of the SU-8 particles. Modification of the surface with proteins (detected by fluorescence) did not change the surface conductance or permittivity. It is possible that their charges are "hidden" in a porous surface where the SU-8 is only partially crosslinked (like on the sidewalls of the rods).

Acquiring ROT and EO for the same particle provided quantitative data for the same particle. The contribution of bulk conductivity, caused by particle swelling, was not assessed because it is included in the contribution from the surface conductance (leads to an overestimation) and cannot be disentangled. ROT and EO spectra show two further relaxations. The origin of these is not clear, but they are related to chemical modification of the particles and probably come from percolation, which is the change in electrical behaviour of a dielectric due to the inclusion of small conductive parts. A percolation

model based on the Universal Dielectric Response (UDR) was able to reproduce the spectra. This model requires many parameters to describe the relaxation, hence a full fit to the data was not possible and the numerical results obtained when strong percolation related relaxations are present must be considered only in a qualitative manner.

8.2 Gold coated particles

In this work gold-coated SU-8 rods were studied in the low frequency region where the behaviour is dominated by the DL relaxation. This is the first time that the motion of elongated metal coated particles was measured on a single particle basis using ROT. The motion was recorded for three different surface properties: gold colloids, bare gold and biotin modified gold. Particles with adsorbed gold colloids showed a strong relaxation at low frequency in the EO spectra. This relaxation could be related to percolation of the gold colloids in the partially crosslinked sidewalls of the rods, causing at low frequency a relaxation in the conductivity of the particles. Particles coated with gold showed a single relaxation in the ROT spectra in the frequency range chosen. No Maxwell-Wagner relaxation was observed because of strong positive DEP. To circumvent this problem, electrodes with a larger gap were used. The biotin modified gold coated rods could be imagined having a thin dielectric layer formed by the uncharged biotin molecules that partially screen the gold. The results obtained are in qualitative accordance with this model, where particle behaviour is dominated by the DL at the metal/electrolyte interface. The biotin molecules screen the metal from the electric field and reduce the charge at the interface, decreasing the angular speed of the particles in rotating electric fields. The particles become similar to uncharged dielectric particles that do not rotate at low frequency. The EO spectra of the rod shaped particles could not be acquired because the rods do not orientate in a controlled way, probably because their density and rough surface facilitate adhesion to the glass substrate, causing a step-like movement.

The motion of spherical particles was studied using both ROT and DEP with suspending electrolytes of different conductivities. The DEP spectra were acquired by measuring the speed of particle movement over a short distance in a region close to the centre of the electrode array. ROT and DEP measurements were in agreement: the DEP force increased with the frequency (as suggested by the ROT measurements) from negative to positive DEP. The ROT peak position for metal coated rods was similar to the metal coated beads, despite differences in surface chemical properties. The results are qualitatively in agreement with theory. Deviations from the theoretical values are common in ACEO and ICEO, due to roughness of the surface or surface modification like oxides, in which case the system does not behave like an ideal capacitor. Through a simple calculation we found that rods and beads follow the same theoretical trend once the contribution to the different dimensions is taken into account. The deviation from the theoretical behaviour can be related to the roughness of

the surface, which underestimates the actual surface of the particle and the capacitance of the EDL.

8.3 Concluding remarks on biosensing

In this work a method that combines ROT and EO on a single particle basis was presented and applied to SU-8 particles functionalised in different ways. From the point of view of the application of this method for biosensing the results of this project represent a half-success. We successfully distinguished particles with different functionalisations but the differences were more related to the change in the properties of the bulk more than related to the change in surface properties as expected. We can therefore conclude that the method based on the combined use of ROT and EO measurement is effective in the determination of the electrical properties of elongated particles and therefore should be able to discriminate binding events of biomolecules onto the surface of the particles. On the other hand, the use of SU-8 as fabrication material appears to be not suitable. SU-8 can be easily functionalised but some of the reactions involved in the functionalisation of the particles need organic solvents (such as DMF) to happen. In this work it was demonstrated that SU-8 swells when exposed to DMF and that caused the chemical reactions to happen in the bulk of the particles as well, making them porous. Porosity implies bulk conductivity, which in this work prevented discrimination of the presence of proteins on the surface of the particles. Porosity is not acceptable in this type of measurements: the equations used to study the motion of the particles assume that the bulk conductivity of the particles is zero but with porous particles the bulk conductivity is dependent on the medium conductivity and could easily overpower the surface conductivity. Therefore for biosensing it would be more useful to have particles which are non-porous and allow chemical reactions only on their surface.

In this work we also investigated the electrokinetic properties of metal coated particles. Particles with adsorbed gold colloids and gold coated particles were studied. The particles coated with gold colloids showed electrokinetic spectra similar to the native SU-8 particles, but with a distinctive feature at low frequency in the EO spectra. That difference in behaviour could be used for biosensing, where the reporting molecule would have an electric label consisting in a gold nanoparticle instead of a fluorescent label. In case of a binding event, the nanoparticles will accumulate onto the surface changing its electrical properties. For the purpose of biosensing, the gold coating process presented in this work could be used also to amplify the effect of the nanoparticle labelled reporting molecules. A gold deposition step following the capture step will create a gold shell that would allow a clear discrimination (electrokinetic based but also visual) between particles where the binding event happened from particles where the binding did not happen. The gold coated particles obtained with the method proposed are not porous and behave like perfectly polarisable particles. These particles show a strong relaxation peak at low frequency due to the relaxation of the EDL.

The amplitude of the relaxation peak depends on the voltage drop across the double layer, therefore the addition of a monolayer of uncharged molecules reduced the peak amplitude and could see easily detected using ROT. This is an important finding for possible biosensing applications because gold particles can be easily functionalised using thiol chemistry to have reporting molecules on its surface. If the reporting molecules will bind to the target molecules the electric properties of the surface of the particle will change. That will appear as a change in the amplitude of the peak.

8.4 Future work

This project could be developed in different directions. The more important direction would be focussing on the optimization of the chemical reactions and the materials used in the fabrication. Ideally, the particles should not swell when chemically modified. That could be achieved with water based chemistry, which is milder than solvent based chemistry (particles swell less). Also, chemical reactions aimed to increase the surface charges in a controlled way (for example with a branching strategy) could give an insight into the resolution of the method. The method itself could be tested on solid particles to optimize the fitting strategy in a context where no percolation or swelling is involved. From the point of view of fabrication, the process could be refined to tackle the swelling, making the particles more solid without losing the reactivity of their surface. SU-8 is already a highly crosslinked polymer, so different materials should be investigated. The theoretical framework of this project could be expanded to include the contribution of other relaxation processes (for example caused by percolation) using *ab initio* calculations to obtain analytical expressions for the other relaxation processes involved (i.e. not empirical description descriptions). Simulations of the particle motion in the chamber considering those other processes might help developing a broader theoretical understanding of the complexity of the system.

The work done with the gold coated particles could be developed extending the theory already published in literature to non-spherical conductive particles and to include the effect of roughness of the metal shell. The gold coating method itself could be optimised to achieve a better control over the metal shell thickness and to assess if that has an influence on the electrokinetics results, especially aiming to reduce the CV between different particles from the same batch. Major work should be done on the actual application of those particles for biosensing. A similar step-by-step modification similar to what has been done in this work for SU-8 rods should be repeated on gold coated particles to understand the potential and limitations of the method.

Appendix 1

Publications and Conferences

A1.1 Papers published

D. Morganti and H. Morgan, "Characterization of non-spherical polymer particles by combined electrorotation and electroorientation," *Colloids and Surfaces A: Physicochemical and Engineering Aspects*, vol. 376, no. 1-3, pp. 67-71, Feb. 2011.

Y. K. Ren, D. Morganti, H. Y. Jiang, A. Ramos, and H. Morgan, "Electrorotation of Metallic Microspheres," *Langmuir*, vol. 27, no. 6, pp. 2128-2131, 2011.

A1.2 Conferences attended

Conference	Place	Presentation	Title
Nanotech 2008	Montreux	Poster	AC Electrokinetic studies of chemically modified SU-8 microparticles
Dielectrics 2009	Reading	Talk	Characterization of non-spherical polymer particles with electrorotation and electroorientation
Early Career Research in Electrostatics and Dielectrics 2009	London	Talk	AC electrokinetics of chemically modified SU-8 particles
ELKIN 2010	Turku	Talk	Combined electrorotation and electroorientation of rod-shaped polymer particles

Appendix 2

Fitting Script

The following script was used to fit the ROT and EO spectra in Mathematica 6.0, after importing the data from an Excel file.

```
rawdata = Import["file path"];
conductivities = Delete[rawdata[[1, 1]], 1]
np = Dimensions[conductivities][[1]];
frequencies = Delete[rawdata[[1, All, 1]], 1];
nf = Dimensions[frequencies][[1]];

rawdata2 = Delete[rawdata[[1]], 1];
data = Table[rawdata2[[t, {1, s + 1}]] , {s, 1, np}, {t, 1, nf}];
dataf = Table[ DeleteCases[data[[s]], Except[{_Real, _Real}]], {s, 1, np}];
dd = Dimensions[dataf][[1]]
lungh = Table[Dimensions[dataf[[t]]][[1]], {t, 1, dd}]

conductivitieseo = Delete[rawdata[[2, 1]], 1]
npeo = Dimensions[conductivitieseo][[1]];
frequencieseo = Delete[rawdata[[2, All, 1]], 1];
nfeo = Dimensions[frequencieseo][[1]];

rawdata2eo = Delete[rawdata[[2]], 1];
dataeo = Table[rawdata2eo[[t, {1, s + 1}]] , {s, 1, npeo}, {t, 1, nfeo}];
datafeo = Table[ DeleteCases[dataeo[[s]], Except[{_Real, _Real}]], {s, 1, npeo}];
ddeo = Dimensions[datafeo][[1]]
lungheo = Table[Dimensions[datafeo[[t]]][[1]], {t, 1, ddeo}]

rawsizes = rawdata[[3]];
sizes = Table[{rawsizes[[1, t]], rawsizes[[2, t]]} 1000, {t, 1, np}]
```

```
ecc = N[√(1 - b^2/a^2)]  (*a>b=c*)

Lpar = FullSimplify[b^2/a^2 (Log[2a/b] - 1)]

Lper = (1 - Lpar) / 2
e1 = em e0 - I ( beta) / (2 Pi 10^f);
e2 = ep e0 - I sp / (2 Pi 10^f);
scal = b^2/a^2 AA  1/(3 (Log[a / b] - 0.5));
epvalue = alfa;
fact = 0.82;
Ka = ( (e2 - e1)/(3 (e1 + (e2 - e1) Lpar)) /. {ep → (epvalue) , em → 76, e0 -> 8.85 × 10^(-12)}) /. sp → 2 kp/b
Kb = ( (e2 - e1)/(3 (e1 + (e2 - e1) Lper)) /. {ep → (epvalue) , em → 76, e0 -> 8.85 × 10^(-12)}) /. sp → (a + b) kp/(a b)
test2im = N[ComplexExpand[Im[Ka + Kb]]];
test2re = N[ComplexExpand[Re[Ka - Kb]]];
fitfuncim = -(180 / Pi) scal test2im (*inversion*) ;
fitfuncre = scal fact test2re ;


Needs["PlotLegends`"]
mark = {■, ●, ▲, ▼, ◆};
c01 =
 Table[
  NMinimize[
   {( Σ_{s=1}^{lungh[[t]]} ((fitfuncim /. {sm -> conductivities[[t]], f → dataf[[t, s, 1]], a -> sizes[[t, 1]]/2,

          b → sizes[[t, 2]] / 2, ep → epvalue}) - dataf[[t, s, 2]])^2) +

    ( Σ_{s=1}^{lungheo[[t]]} ((fitfuncre /. {sm -> conductivitieseo[[t]], f → datafeo[[t, s, 1]], a -> sizes[[t, 1]]/2,

          b → sizes[[t, 2]] / 2, ep → epvalue}) - datafeo[[t, s, 2]])^2), 0 < beta < 0.01, 15 > kp > 0.01,

    15 > AA > 1,  20 > alfa > 1}, {{kp, 0.1, 0.5}, {beta, 0.002, 0.003}, {AA, 2, 3}, {alfa, 6, 8}}], {t, 1, np}]
names = {alfa, beta, kp, AA};
numpar = Dimensions[names][[1]]
values = Table[names /. c01[[t, 2]], {t, 1, np}]
AAaverage =
 Table[{names[[s]], Mean[Table[values[[t, s]], {t, 1, np}]],
   StandardDeviation[Table[values[[t, s]] / √np , {t, 1, np}]]}, {s, 1, numpar}]
corim =
 Table[{(((((fitfuncim) /. c01[[t, 2]]) /. f → dataf[[t, All, 1]]) /. sm -> conductivities[[t]]) /.
    {a -> sizes[[t, 1]]/2, b → sizes[[t, 2]] / 2, ep → epvalue}, dataf[[t, All, 2]]}, {t, 1, np}];
corre =
 Table[{(((((fitfuncre) /. c01[[t, 2]]) /. f → datafeo[[t, All, 1]]) /. sm -> conductivities[[t]]) /.
    {a -> sizes[[t, 1]]/2, b → sizes[[t, 2]] / 2, ep → epvalue}, datafeo[[t, All, 2]]}, {t, 1, np}];
Table[Correlation[corim[[t, 1]], corim[[t, 2]]], {t, 1, np}]
{"Rot", Mean[%], StandardDeviation[%]}
Table[Correlation[corre[[t, 1]], corre[[t, 2]]], {t, 1, np}]
{"EO", Mean[%], StandardDeviation[%]}
```

```
Table[
 Show[Plot[((fitfuncre) /. c01[[t, 2]]) /. {sm → conductivities[[t]], a -> sizes[[t, 1]] / 2, b → sizes[[t, 2]] / 2},
   {f, 4, 8}, AxesLabel → {"Frequency
log(Hz)", "1/sec"}, PlotRange → {0.02, 0.07}, BaseStyle → {FontSize → Large},
   PlotStyle → {Thickness[0.007], Dashed},
   Epilog → {
     Inset[Graphics[Legend[{
             {Graphics[Text[Style[■, {Large, Black}], {0, 0}]], "native SU-8"},
           {Graphics[{Dashed, Thickness[0.4], Blue, Line[{{0, 0}, {1, 0}}]}], "fit result"}
          }, BaseStyle → {FontSize → Large}, LegendShadow → None, LegendSize → 50, LegendTextSpace → 5]],
        {7, 0.062}]
     }],
   ListPlot[datafeo[[t]], PlotMarkers → {■, 20}, PlotStyle → Black], AspectRatio → 0.75], {t, 1, np}]

Table[
 Show[Plot[((fitfuncim) /. c01[[t, 2]]) /. {sm → conductivities[[t]], a -> sizes[[t, 1]] / 2, b → sizes[[t, 2]] / 2},
   {f, 4, 8}, AxesLabel → {"Frequency
log(Hz)", "degree/sec"}, PlotRange → {0, 1.5}, BaseStyle → {FontSize → Large},
   PlotStyle → {Thickness[0.007], Dashed},
   Epilog → {
     Inset[Graphics[Legend[{
             {Graphics[Text[Style[■, {Large, Black}], {0, 0}]], "native SU-8"},
           {Graphics[{Dashed, Thickness[0.4], Blue, Line[{{0, 0}, {1, 0}}]}], "fit result"}
          }, BaseStyle → {FontSize → Large}, LegendShadow → None, LegendSize → 50, LegendTextSpace → 6]],
        {7.2, 1.2}]
     }],
   ListPlot[dataf[[t]], PlotMarkers → {■, 20}, PlotStyle → Black], AspectRatio → 0.75], {t, 1, np}]
```
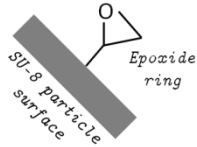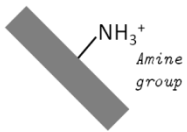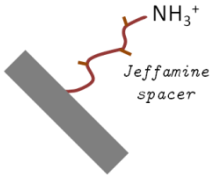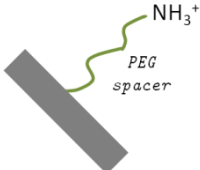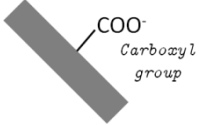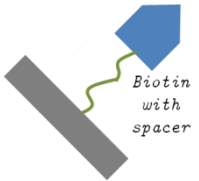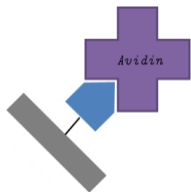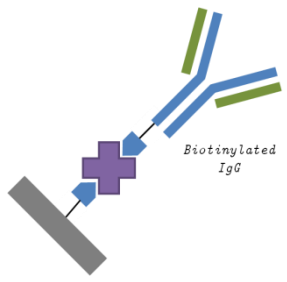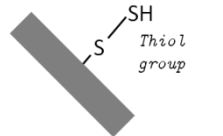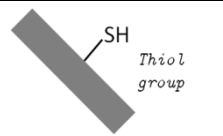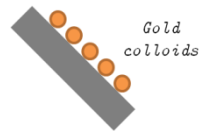
Appendix 3

Summary of Particle Types

The following table summarises the particle types involved in this work with the *Code* used in the text and the *Page* of the paragraph where the electrokinetics data can be found.

Code	Sketch	Type of particle	Page
P01		Native SU-8 particle.	95
P02		Amino modified SU-8 particle using diaminopropane.	97
P03		Amino modified particle with a Jeffamine spacer.	99
P04		Amino modified particle with a PEG spacer.	/
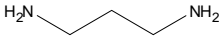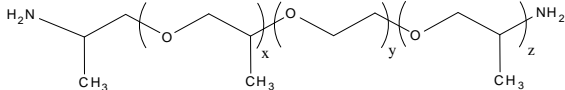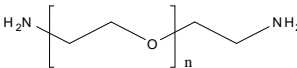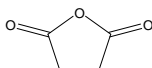
Code	Sketch	Type of particle	Page
P05		Carboxyl modified SU-8 particle.	100
P06		Biotin modified SU-8 particle	102
P07		Biotin modified SU-8 particle with a spacer.	104
P08		Avidin immobilized onto biotynilated particle.	105
P09		IgG immobilized onto avidin.	107
P10		Gold coated polystyrene beads	124
P11		SU-8 rods modified with DTT	/
P12		SU-8 rods modified with cystemaine	/
P13		SU-8 rods with colloidal gold adsorbed onto the surface	129
P14		Gold coated SU-8 rods	130
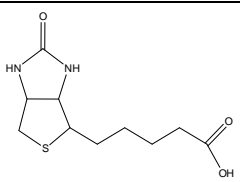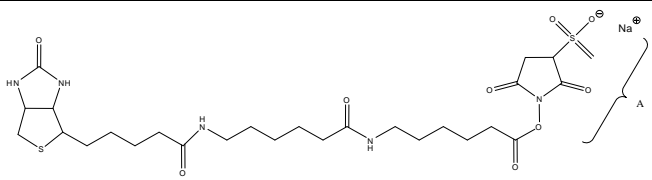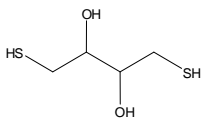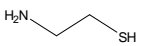
Code	Sketch	Type of particle	Page
P15	*Gold coating with biotin*	Gold coated rods functionalised with biotin	133

Appendix 4

Summary of Chemicals

The following table summarises the more important chemicals used during the functionalisation of the particles.

Code	Sketch	Use	Page
C01	H$_2$N — NH$_2$ Diaminopropane (D23602, Sigma)	To obtain a surface rich in amine groups.	78
C02	H$_2$N — (O)$_x$ — (O)$_y$ — (O)$_z$ — NH$_2$ CH$_3$ ... CH$_3$ ... CH$_3$ Jeffamine ED-900 (14527, Sigma)	Like above, but the amine group is connected to the surface through a spacer.	79
C03	H$_2$N — [O]$_n$ — NH$_2$ PEG-3000 (14502, Sigma)	Like above, but the spacer is longer.	79
C04	O = ⬠ = O Succinic anhydride (239690, Sigma)	Used to obtain a surface rich in carboxyl groups from a surface rich in amine groups.	79

Code	Sketch	Use	Page
C05	Biotin (B4639, Sigma)	Used as intermediate step before the immobilization with avidin.	82
C06	EZ-Link Sulfo-NHS-LC-LC-biotin (21338, Thermo)	Same as above, but with a longer spacer whose end is preactivated (A).	82
C07	DL-Dithiothreitol (43819, Sigma)	To obtain a surface rich in thios groups, as intermediate step prior to the immobilization of gold colloids.	127
C08	Cysteamine (30070, Sigma)	Same as above.	128

Bibliography

[1]   O. Smithies, "Zone electrophoresis in starch gels: group variations in the serum proteins of normal human adults," *Biochemical Journal,* vol. 61, pp. 629-641, 1955.

[2]   S. Raymond and L. Weintraub, "Acrylamide gel as a supporting medium for zone electrophoresis," *Science,* vol. 130, pp. 711-715, 1959.

[3]   K. Weber and M. Osborn, "The reliability of molecular weight determinations by dodecyl sulfate-polyacrylamide gel electrophoresis," *Journal of Biological Chemistry,* vol. 244, pp. 4406-4412, 1969.

[4]   D. C. Schwartz and C. R. Cantor, "Separation of yeast chromosome-sized DNAs by pulsed field gradient gel electrophoresis," *Cell,* vol. 37, pp. 67-75, 1984.

[5]   A. Görg, C. Obermaier, G. Boguth, A. Harder, B. Scheibe, R. Wildgruber, and W. Weiss, "The current state of two-dimensional electrophoresis with immobilized pH gradients," *Electrophoresis,* vol. 21, pp. 1037-1053, 2000.

[6]   A. Görg, W. Postel, A. Domscheit, and S. Günther, "Two-dimensional electrophoresis with immobilized pH gradients of leaf proteins from barley (*Hordeum vulgare*): Method, reproducibility and genetic aspects," *Electrophoresis,* vol. 9, pp. 681-692, 1988.

[7]   D. J. Harrison, K. Fluri, K. Seiler, Z. Fan, C. S. Effenhauser, and A. Manz, "Micromachining a miniaturized capillary electrophoresis-based chemical analysis system on a chip," *Science,* vol. 261, pp. 895-897, 1993.

[8]   M. Trojanowicz, "Recent developments in electrochemical flow detections - a review: Part I. Flow analysis and capillary electrophoresis," *Analytica Chimica Acta,* vol. 653, pp. 36-58, 2009.

[9]   H. A. Pohl, "The motion and precipitation of suspensoids in divergent electric fields," *Journal of Applied Physics,* vol. 22, pp. 869-871, 1951.

[10]   H. A. Pohl, *Dielectrophoresis*: Cambridge University Press, 1978.

[11]   N. G. Green and H. Morgan, "Dielectrophoretic investigations of sub-micrometre latex spheres," *Journal of Physics D: Applied Physics,* vol. 30, pp. 2626-2633, 1997.

[12]   N. G. Green and H. Morgan, "Dielectrophoresis of submicrometer latex spheres. 1. Experimental results," *The Journal of Physical Chemistry B,* vol. 103, pp. 41-50, 1999.

[13]   M. P. Hughes, H. Morgan, and M. F. Flynn, "The dielectrophoretic behavior of submicron latex spheres: influence of surface conductance," *Journal of Colloid and Interface Science,* vol. 220, pp. 454-457, 1999.

[14]   M. P. Hughes and H. Morgan, "Dielectrophoretic characterization and separation of antibody-coated submicrometer latex spheres," *Analytical Chemistry,* vol. 71, pp. 3441-3445, 1999.

[15]   F. F. Becker, X. B. Wang, Y. Huang, R. Pethig, J. Vykoukal, and P. R. Gascoyne, "Separation of human breast cancer cells from blood by differential dielectric affinity," *Proceedings of the National Academy of Sciences of the United States of America,* vol. 92, pp. 860-864, 1995.

[16]   R. Pethig, Y. Huang, X. B. Wang, and J. P. H. Burt, "Positive and negative dielectrophoretic collection of colloidal particles using interdigitated castellated microelectrodes," *Journal of Physics D: Applied Physics,* vol. 25, pp. 881-888, 1992.

[17]   H. Li and R. Bashir, "Dielectrophoretic separation and manipulation of live and heat-treated cells of *Listeria* on microfabricated devices with interdigitated electrodes," *Sensors and Actuators B: Chemical,* vol. 86, pp. 215-221, 2002.

[18]   M. P. Hughes, "Computer-aided analysis of conditions for optimizing practical electrorotation," *Physics in Medicine and Biology,* vol. 43, pp. 3639-3648, 1998.

[19]   Y. Huang and R. Pethig, "Electrode design for negative dielectrophoresis," *Measurement Science and Technology,* vol. 2, pp. 1142-1146, 1991.

[20]   X. Hu, P. H. Bessette, J. Qian, C. D. Meinhart, P. S. Daugherty, and H. T. Soh, "Marker-specific sorting of rare cells using dielectrophoresis," *Proceedings of the National Academy of Sciences of the United States of America,* vol. 102, pp. 15757-15761, 2005.

[21]   S. Junya, Z. Guangbin, and H. Masanori, "Fabrication of a carbon nanotube-based gas sensor using dielectrophoresis and its application for ammonia detection by impedance spectroscopy," *Journal of Physics D: Applied Physics,* vol. 36, pp. L109-L114, 2003.

[22]   D. Holmes, H. Morgan, and N. G. Green, "High throughput particle analysis: Combining dielectrophoretic particle focussing with confocal optical detection," *Biosensors and Bioelectronics,* vol. 21, pp. 1621-1630, 2006.

[23]   H. Morgan, D. Holmes, and N. G. Green, "3D focusing of nanoparticles in microfluidic channels," in *Nanobiotechnology, IEE Proceedings-*, 2004, pp. 76-81.

[24]   D. Holmes, N. G. Green, and H. Morgan, "Microdevices for dielectrophoretic flow-through cell separation," *Engineering in Medicine and Biology Magazine,* vol. 22, pp. 85-90, 2004.

[25]   C.-C. Chang, Z.-X. Huang, and R.-J. Yang, "Three-dimensional hydrodynamic focusing in two-layer polydimethylsiloxane (PDMS) microchannels," *Journal of Micromechanics and Microengineering,* vol. 17, pp. 1479-1486, 2007.

[26]   R. Yang, D. L. Feeback, and W. Wang, "Microfabrication and test of a three-dimensional polymer hydro-focusing unit for flow cytometry applications," *Sensors and Actuators A: Physical,* vol. 118, pp. 259-267, 2005.

[27]   G. H. Markx, Y. Huang, X.-F. Zhou, and R. Pethig, "Dielectrophoretic Characterization and Separation of Micro-Organisms," *Microbiology*, vol. 140, pp. 585–591, 1994.

[28]   H. O. Fatoyinbo, K. F. Hoettges, and M. P. Hughes, "Rapid-on-chip determination of dielectric properties of biological cells using imaging techniques in a dielectrophoresis dot microsystem," *Electrophoresis*, vol. 29, pp. 3–10, 2008.

[29]   K. V. Kaler and T. B. Jones, "Dielectrophoretic spectra of single cells determined by feedback-controlled levitation," *Biophysical Journal*, vol. 57, pp. 173–182, 1990.

[30]   K. V. I. S. Kaler, J.-P. Xie, T. B. Jones, and R. Paul, "Dual-frequency dielectrophoretic levitation of Canola protoplasts," *Biophysical Journal*, vol. 63, pp. 58–69, 1992.

[31]   Y. Huang, R. Hölzel, R. Pethig, and X.-B. Wang, "Differences in the AC electrodynamics of viable and non-viable yeast cells determined through combined dielectrophoresis and electrorotation studies," *Physics in Medicine and Biology*, vol. 37, pp. 1499–1517, 1992.

[32]   R. Hölzel, "Single particle characterization and manipulation by opposite field dielectrophoresis," *Journal of Electrostatics*, vol. 56, pp. 435–447, 2002.

[33]   N. A. M. Yunus and N. G. Green, "Continuous separation of submicron particles using angled electrodes," *Journal of Physics: Conference Series,* vol. 142, p. 012068, 2008.

[34]   N. G. Green, H. Morgan, and J. J. Milner, "Manipulation and trapping of sub-micron bioparticles using dielectrophoresis," *Journal of Biochemical and Biophysical Methods,* vol. 35, pp. 89-102, 1997.

[35]   T. B. Jones, *Electromechanics of particles*: Cambridge University Press, 1995.

[36]   G. H. Markx, "The use of electric fields in tissue engineering: A review," *Organogenesis,* vol. 4, pp. 11-17, 2008.

[37]   H. Kawai and M. Marutake, "The dispersion of the dielectric constant in Rochelle salt crystal at low frequencies," *Journal of the Physical Society of Japan,* vol. 3, pp. 8-12, 1948.

[38]   A. A. Teixeira-Pinto, L. L. Nejelski, J. L. Cutler, and J. H. Heller, "The behavior of unicellular organisms in an electromagnetic field," *Experimental Cell Research,* vol. 20, pp. 548-564, 1960.

[39]   J. L. Griffin, "Orientation of human and avian erythrocytes in radio-frequency fields," *Experimental Cell Research,* vol. 61, pp. 113-120, 1970.

[40]   R. D. Miller and T. B. Jones, "Electro-orientation of ellipsoidal erythrocytes. Theory and experiment," *Biophysical Journal,* vol. 64, pp. 1588-1595, 1993.

[41]   F. J. Iglesias, M. C. Lopez, C. Santamaria, and A. Dominguez, "Orientation of *Schizosaccharomyces pombe* nonliving cells under alternating uniform and nonuniform electric fields," *Biophysical Journal,* vol. 48, pp. 721-726, 1985.

[42]   F. J. Asencor, C. Santamaría, F. J. Iglesias, and A. Domínguez, "Dielectric energy of orientation in dead and living cells of *Schizosaccharomyces pombe.* Fitting of experimental results to a theoretical model," *Biophysical Journal,* vol. 64, pp. 1626-1631, 1993.

[43]   G. H. Markx, B. Alp, and A. McGilchrist, "Electro-orientation of *Schizosaccharomyces pombe* in high conductivity media," *Journal of Microbiological Methods,* vol. 50, pp. 55-62, 2002.

[44]   M. Kriegmaier, M. Zimmermann, K. Wolf, U. Zimmermann, and V. L. Sukhorukov, "Dielectric spectroscopy of *Schizosaccharomyces pombe* using electrorotation and electroorientation," *Biochimica et Biophysica Acta: General Subjects,* vol. 1568, pp. 135-146, 2001.

[45]   V. M. Fomchenkov, A. L. Mazanov, and V. N. Brezgunov, "Effect of dispersion of electric parameters of bacterial cells on their orientation in alternating electric fields," *Biofizika,* vol. 27, pp. 665-669, 1982.

[46]   A. I. Ivanov, V. M. Fomchenkov, L. A. Khasanova, Z. M. Kuramshina, and M. M. Sadikov, "Influence of heavy metal ions on the electrophysical properties of *Anacystis nidulans* and *Escherichia coli* cells," *Mikrobiologiia,* vol. 61, pp. 455-463, 1992.

[47]   O. I. Guliy, O. V. Ignatov, L. N. Markina, V. D. Bunin, and V. V. Ignatov, "Action of ampicillin and kanamicin on the electrophysical characteristics of *Escherichia coli* cells," *International Journal of Environmental Analytical Chemistry,* vol. 85, pp. 981-992, 2005.

[48]   O. I. Guliy, L. N. Markina, O. V. Ignatov, S. Y. Shchegolev, I. S. Zaitseva, V. D. Bunin, and V. V. Ignatov, "The effect of ampicillin on the electrophysical properties of *Escherichia coli* cells," *Microbiology,* vol. 74, pp. 111-115, 2005.

[49]   V. D. Bunin, O. V. Ignatov, O. I. Guliy, A. G. Voloshin, L. A. Dykman, D. O'Neil, and D. Ivnitski, "Studies of *Listeria monocytogenes*-antibody binding using electro-orientation," *Biosensors and Bioelectronics,* vol. 19, pp. 1759-1761, 2004.

[50]   O. I. Guliy, L. Y. Matora, G. L. Burygin, L. A. Dykman, N. A. Ostudin, V. D. Bunin, V. V. Ignatov, and O. V. Ignatov, "Electrophysical characteristics of

Azospirillum brasilense Sp245 during interaction with antibodies to various cell surface epitopes," *Analytical Biochemistry,* vol. 370, pp. 201-205, 2007.

[51] M. Radu, M. Ionescu, N. Irimescu, K. Iliescu, R. Pologea-Moraru, and E. Kovacs, "Orientation behavior of retinal photoreceptors in alternating electric fields," *Biophysical Journal,* vol. 89, pp. 3548-3554, 2005.

[52] A. Ivanov, V. G. Gogvadze, A. I. Miroshnikov, and B. I. Medvedev, "Electroorientation effect of isolated mitochondria in different functional states," *General Physiology and Biophysics,* vol. 4, pp. 483-491, 1985.

[53] I. Minoura and E. Muto, "Dielectric measurement of individual microtubules using the electroorientation method," *Biophysical Journal,* vol. 90, pp. 3739-3748, 2006.

[54] O. I. Guliy, V. D. Bunin, D. O'Neil, D. Ivnitski, and O. V. Ignatov, "A new electro-optical approach to rapid assay of cell viability," *Biosensors and Bioelectronics,* vol. 23, pp. 583-587, 2007.

[55] J. W. Choi, A. Pu, and D. Psaltis, "Optical detection of asymmetric bacteria utilizing electro orientation," *Biophysical Journal,* vol. 64, pp. 1588-1595, 1993.

[56] A. T. Poortinga, R. Bos, and H. J. Busscher, "Controlled electrophoretic deposition of bacteria to surfaces for the design of biofilms," *Biotechnology and Bioengineering,* vol. 67, pp. 117-120, 2000.

[57] A. Sebastian, A.-M. Buckle, and G. H. Markx, "Tissue engineering with electric fields: Immobilization of mammalian cells in multilayer aggregates using dielectrophoresis," *Biotechnology and Bioengineering,* vol. 98, pp. 694-700, 2007.

[58] A. Sebastian, A. M. Buckle, and G. H. Markx, "Formation of multilayer aggregates of mammalian cells by dielectrophoresis," *Journal of Micromechanics and Microengineering,* vol. 16, pp. 1769-1777, 2006.

[59] M. Yang, C. C. Lim, R. L. Liao, and X. Zhang, "Oriented and vectorial patterning of cardiac myocytes using a microfluidic dielectrophoresis chip - Towards engineered cardiac tissue with controlled macroscopic anisotropy," *Journal of Microelectromechanical Systems,* vol. 15, pp. 1483-1491, 2006.

[60] B. Alp, J. S. Andrews, V. P. Mason, I. P. Thompson, R. Wolowacz, and G. H. Markx, "Building structured biomaterials using AC electrokinetics," *Engineering in Medicine and Biology Magazine,* vol. 22, pp. 91-97, 2003.

[61] P. Makaram, S. Selvarasah, X. G. Xiong, C. L. Chen, A. Busnaina, N. Khanduja, and M. R. Dokmeci, "Three-dimensional assembly of single-walled carbon nanotube interconnects using dielectrophoresis," *Nanotechnology,* vol. 18, p. 395204, 2007.

[62] N. G. Green and T. B. Jones, "Numerical determination of the effective moments of non-spherical particles," *Journal of Physics D: Applied Physics,* vol. 40, pp. 78-85, 2007.

[63] T. Schnelle, R. Hagedorn, G. Fuhr, S. Fiedler, and T. Müller, "Three-dimensional electric field traps for manipulation of cells - calculation and experimental

verification," *Biochimica et Biophysica Acta: General Subjects,* vol. 1157, pp. 127-140, 1993.

[64] T. Müller, G. Gradl, S. Howitz, S. Shirley, T. Schnelle, and G. Fuhr, "A 3-D microelectrode system for handling and caging single cells and particles," *Biosensors and Bioelectronics,* vol. 14, pp. 247-256, 1999.

[65] C. Reichle, T. Müller, T. Schnelle, and G. Fuhr, "Electro-rotation in octopole micro cages," *Journal of Physics D: Applied Physics,* vol. 32, pp. 2128-2135, 1999.

[66] R. Arno', *Rendiconti Lincei,* vol. 1, 1892.

[67] W. M. Arnold, H. P. Schwan, and U. Zimmermann, "Surface conductance and other properties of latex-particles measured by electrorotation," *The Journal of Physical Chemistry,* vol. 91, pp. 5093-5098, 1987.

[68] H. Maier, "Electrorotation of colloidal particles and cells depends on surface charge," *Biophysical Journal,* vol. 73, pp. 1617-1626, 1997.

[69] M. P. Hughes, S. Archer, and H. Morgan, "Mapping the electrorotational torque in planar microelectrodes," *Journal of Physics D: Applied Physics,* vol. 32, pp. 1548-1552, 1999.

[70] K. Maswiwat, M. Holtappels, and J. Gimsa, "On the field distribution in electrorotation chambers - Influence of electrode shape," *Electrochimica Acta,* vol. 51, pp. 5215-5220, 2006.

[71] A. D. Goater, J. P. H. Burt, and R. Pethig, "A combined travelling wave dielectrophoresis and electrorotation device: applied to the concentration and viability determination of *Cryptosporidium*," *Journal of Physics D: Applied Physics,* vol. 30, pp. L65-L69, 1997.

[72] E. G. Cen, C. Dalton, Y. Li, S. Adamia, L. M. Pilarski, and K. V. Kaler, "A combined dielectrophoresis, traveling wave dielectrophoresis and electrorotation microchip for the manipulation and characterization of human malignant cells," *Journal of Microbiological Methods,* vol. 58, pp. 387-401, 2004.

[73] W. M. Arnold and U. Zimmermann, "Rotating-field-induced rotation and measurement of the membrane capacitance of single mesophyll-cells of *Avena sativa*," *Zeitschrift für Naturforschung C: A Journal of Biosciences,* vol. 37, pp. 908-915, 1982.

[74] R. Glaser, G. Fuhr, and J. Gimsa, "Rotation of erythrocytes, plant cells, and protoplasts in an outside rotating electric field," *Studia Biophysica,* vol. 96, pp. 11-20, 1983.

[75] C. Dalton, A. D. Goater, J. P. H. Burt, and H. V. Smith, "Analysis of parasites by electrorotation," *Journal of Applied Microbiology,* vol. 96, pp. 24-32, 2004.

[76] Y. F. Wu, C. J. Huang, L. Wang, X. L. Miao, W. L. Xing, and J. Cheng, "Electrokinetic system to determine differences of electrorotation and traveling-wave electrophoresis between autotrophic and heterotrophic algal cells," *Colloids and Surfaces A: Physicochemical and Engineering Aspects,* vol. 262, pp. 57-64, 2005.

[77]   R. Pethig, L. M. Jakubek, R. H. Sanger, E. Heart, E. D. Corson, and P. J. Smith, "Electrokinetic measurements of membrane capacitance and conductance for pancreatic beta-cells," *IEE Proceedings: Nanobiotechnology,* vol. 152, pp. 189-193, 2005.

[78]   G. Fuhr, T. Muller, and R. Hagedorn, "Reversible and irreversible rotating rield-induced membrane modifications," *Biochimica et Biophysica Acta,* vol. 980, pp. 1-8, 1989.

[79]   C. Cheng-Hsin, L. Chen-Zhong, Y. Chen-Che, and H. You-Ming, "Electrorotation of HL-60 cells uptake of metal and dielectric nanoparticles in a stationary AC electric field," in *Nano/Micro Engineered and Molecular Systems, 2008. NEMS 2008. 3rd IEEE International Conference on*, 2008, pp. 938-942.

[80]   C.-H. Chuang, Y.-M. Hsu, and C.-C. Yeh, "The effects of nanoparticles uptaken by cells on electrorotation," *Electrophoresis,* vol. 30, pp. 1449-1456, 2009.

[81]   C. Huang, A. Chen, M. Guo, and J. Yu, "Membrane dielectric responses of bufalin-induced apoptosis in HL-60 cells detected by an electrorotation chip," *Biotechnol Lett,* vol. 29, pp. 1307-13, 2007.

[82]   V. L. Sukhorukov, J. M. Endter, D. Zimmermann, R. Shirakashi, S. Fehrmann, M. Kiesel, R. Reuss, D. Becker, R. Hedrich, E. Bamberg, T. Roitsch, and U. Zimmermann, "Mechanisms of electrically mediated cytosolic Ca2+ transients in aequorin-transformed tobacco cells," *Biophysical Journal,* vol. 93, pp. 3324-3337, 2007.

[83]   D. Zimmermann, M. Kiesel, U. Terpitz, A. Zhou, R. Reuss, J. Kraus, W. A. Schenk, E. Bamberg, and V. L. Sukhorukov, "A combined patch-clamp and electrorotation study of the voltage- and frequency-dependent membrane capacitance caused by structurally dissimilar lipophilic anions," *The Journal of Membrane Biology,* vol. 221, pp. 107-121, 2008.

[84]   D. Zimmermann, A. Zhou, M. Kiesel, K. Feldbauer, U. Terpitz, W. Haase, T. Schneider-Hohendorf, E. Bamberg, and V. L. Sukhorukov, "Effects on capacitance by overexpression of membrane proteins," *Biochemical and Biophysical Research Communications,* vol. 369, pp. 1022–1026, 2008.

[85]   W. M. Arnold and U. Zimmermann, "Electro-rotation: development of a technique for dielectric measurements on individual cells and particles," *Journal of Electrostatics,* vol. 21, pp. 151-191, 1988.

[86]   T. B. Jones, "Quincke rotation of spheres," *IEEE Transactions on Industry Applications,* vol. IA-20, pp. 845-849, 1984.

[87]   G. von Quincke, "Rotationem im constanten electrischen Felde," *Annalen der Physik,* vol. 59, pp. 417-485, 1896.

[88]   A. S. Lampa, "Dielectric hysteresis," *Sitzungsberichte der Kaiserlichen Akademie der Wissenschaften,* vol. 115, pp. 1659-1690, 1906.

[89]   I. Sumoto, "An interesting phenomenon observed on some dielectrics," *Journal of the Physical Society of Japan,* vol. 10, p. 494, 1955.

[90]   P. E. Secker and M. R. Belmont, "A miniature multipole liquid-immersed dielectric motor," *Journal of Physics D: Applied Physics,* vol. 3, pp. 216-220, 1970.

[91]   P. E. Secker and I. N. Scialom, "A simple liquid-immersed dielectric motor," *Journal of Applied Physics,* vol. 39, pp. 2957-2961 1968.

[92]   L. Lobry and E. Lemaire, "Viscosity decrease induced by a DC electric field in a suspension," *Journal of Electrostatics,* vol. 47, pp. 61-69, 1999.

[93]   N. Pannacci, "How insulating particles increase the conductivity of a suspension," *Physical Review Letters,* vol. 99, p. 094503, 2007.

[94]   F. Peters, L. Lobry, A. Khayari, and E. Lemaire, "Size effect in Quincke rotation: a numerical study," *The Journal of Chemical Physics,* vol. 130, p. 194905, 2009.

[95]   H. Morgan, N. G. Green, M. P. Hughes, W. Monaghan, and T. C. Tan, "Large-area travelling-wave dielectrophoresis particle separator," *Journal of Micromechanics and Microengineering,* vol. 7, pp. 65-70, 1997.

[96]   S. Masuda, M. Washizu, and M. Iwadare, "Separation of small particles suspended in liquid by nonuniform traveling field," *IEEE Transactions on Industry Applications,* vol. IA-23, pp. 474-480, 1987.

[97]   S. Masuda, M. Washizu, and I. Kawabata, "Movement of blood cells in liquid by nonuniform traveling field," *IEEE Transactions on Industry Applications,* vol. IA-24, pp. 217-222, 1988.

[98]   M. S. Talary, J. P. H. Burt, J. A. Tame, and R. Pethig, "Electromanipulation and separation of cells using travelling electric fields," *Journal of Physics D: Applied Physics,* vol. 29, pp. 2198-2203., 1996.

[99]   L. Cui and H. Morgan, "Design and fabrication of travelling wave dielectrophoresis structures," *Journal of Micromechanics and Microengineering,* vol. 10, pp. 72-79, 2000.

[100] N. G. Green, A. Ramos, and H. Morgan, "Numerical solution of the dielectrophoretic and travelling wave forces for interdigitated electrode arrays using the finite element method," *Journal of Electrostatics,* vol. 56, pp. 235-254, 2002.

[101] T. Sun, H. Morgan, and N. G. Green, "Analytical solutions of AC electrokinetics in interdigitated electrode arrays: electric field, dielectrophoretic and traveling-wave dielectrophoretic forces," *Physical Review E,* vol. 76, p. 46610, 2007.

[102] Z. Yuejun, Y. Ui-Chong, and C. Sung Kwon, "Microparticle concentration and separation by traveling-wave dielectrophoresis (twDEP) for digital microfluidics," *Journal of Microelectromechanical Systems,* vol. 16, pp. 1472-1481, 2007.

[103] R. Pethig, J. P. H. Burt, A. Parton, N. Rizvi, M. S. Talary, and J. A. Tame, "Development of biofactory-on-a-chip technology using excimer laser micromachining," *Journal of Micromechanics and Microengineering,* vol. 8, pp. 57-63, 1998.

[104] G. Fuhr, T. Schnelle, and B. Wagner, "Travelling wave-driven microfabricated electrohydrodynamic pumps for liquids," *Journal of Micromechanics and Microengineering,* vol. 4, pp. 217-226, 1994.

[105] C. Grosse and V. N. Shilov, "Theory of the low-frequency electrorotation of polystyrene particles in electrolyte solution," *The Journal of Physical Chemistry,* vol. 100, pp. 1771-1778, 1996.

[106] C. Grosse and V. N. Shilov, "Theory of the low frequency electrorotation of disperse particles in electrolyte solution," *Colloids and Surfaces A: Physicochemical and Engineering Aspects,* vol. 140, pp. 199-207, 1998.

[107] T. M. Squires and M. Z. Bazant, "Induced-charge electro-osmosis," *Journal of Fluid Mechanics,* vol. 509, pp. 217-252, 2004.

[108] A. Ramos, H. Morgan, N. G. Green, and A. Castellanos, "AC electric-field-induced fluid flow in microelectrodes," *Journal of Colloid and Interface Science,* vol. 217, pp. 420-422, 1999.

[109] N. G. Green, A. Ramos, A. González, H. Morgan, and A. Castellanos, "Fluid flow induced by nonuniform ac electric fields in electrolytes on microelectrodes. III. Observation of streamlines and numerical simulation," *Physical Review E,* vol. 66, p. 026305, 2002.

[110] A. Ramos, A. González, A. Castellanos, N. G. Green, and H. Morgan, "Pumping of liquids with AC voltages applied to asymmetric pairs of microelectrodes," *Physical Review E,* vol. 67, p. 056302, 2003.

[111] A. Ramos, H. Morgan, N. G. Green, A. González, and A. Castellanos, "Pumping of liquids with traveling-wave electroosmosis," *Journal of Applied Physics,* vol. 97, p. 084906, 2005.

[112] J. A. Levitan, S. Devasenathipathy, V. Studer, Y. Ben, T. Thorsen, T. M. Squires, and M. Z. Bazant, "Experimental observation of induced-charge electro-osmosis around a metal wire in a microchannel," *Colloids and Surfaces A: Physicochemical and Engineering Aspects,* vol. 267, pp. 122-132, 2005.

[113] M. Z. Bazant and T. M. Squires, "Induced-charge electrokinetic phenomena: theory and microfluidic applications," *Physical Review Letters,* vol. 92, p. 066101, 2004.

[114] M. Z. Bazant and Y. Ben, "Theoretical prediction of fast 3D AC electro-osmotic pumps," *Lab on a Chip,* vol. 6, pp. 1455-1461, 2006.

[115] C. C. Huang, M. Z. Bazant, and T. Thorsen, "Ultrafast high-pressure AC electro-osmotic pumps for portable biomedical microfluidics," *Lab on a Chip,* vol. 10, pp. 80-85, 2010.

[116] S. Gangwal, O. J. Cayre, M. Z. Bazant, and O. D. Velev, "Induced-charge electrophoresis of metallodielectric particles," *Physical Review Letters,* vol. 100, p. 058302, 2008.

[117] J. Vykoukal, D. M. Vykoukal, S. Sharma, F. F. Becker, and P. R. C. Gascoyne, "Dielectrically addressable microspheres engineered using self-assembled monolayers," *Langmuir,* vol. 19, pp. 2425-2433, 2003.

[118] H. Morgan, M. P. Hughes, and N. G. Green, "Separation of submicron bioparticles by dielectrophoresis," *Biophysical Journal,* vol. 77, pp. 516-525, 1999.

[119] M. P. Hughes, M. F. Flynn, and H. Morgan, "Dielectrophoretic measurements of sub-micrometre latex particles following surface modification," *Electrostatics*, vol. 163, pp. 81–84, 1999.

[120] X.-F. Zhou, G. H. Markx, R. Pethig, and I. M. Eastwood, "Differentiation of viable and non-viable bacterial biofilms using electrorotation," *Biochimica et Biophysica Acta*, vol. 1245, pp. 85–93, 1995.

[121] C. E. Hodgson and R. Pethig, "Determination of the Viability of Escherichia Coli at the Single Organism Level by Electrorotation," *Clinical Chemistry*, vol. 44, pp. 2049–2051, 1998.

[122] J.-T. Huang, S.-Y. Hou, S.-B. Fang, H.-W. Yu, H.-C. Lee, and C.-Z. Yang, "Development of a biochip using antibody-coated gold nanoparticles to detect specific bioparticles," *Journal of Industrial Microbiology & Biotechnology*, vol. 35, pp. 1377–1385, 2008.

[123] V. L. Sukhorukov, R. Benkert, G. Obermeyer, F.-W. Bentrup, and U. Zimmermann, "Electrorotation of Isolated Generative and Vegetative Cells, and of Intact Pollen Grains of *Lilium longiflorum*," *Journal of Membrane Biology*, vol. 161, pp. 21–32, 1998.

[124] H. Morgan and N. G. Green, *AC Electrokinetics: colloids and nanoparticles*: Research Studies Press, Ltd, 2003.

[125] I. Ermolina and H. Morgan, "The electrokinetic properties of latex particles: comparison of electrophoresis and dielectrophoresis," *Journal of Colloid and Interface Science,* vol. 285, pp. 419-428, 2005.

[126] J. Lyklema, *Fundamentals of interface and colloid science*: Academic Pr, 2005.

[127] R. J. Hunter, L. R. White, and D. Y. C. Chan, *Foundations of colloid science*: Clarendon Press Oxford, 1989.

[128] S. S. Dukhin and B. V. Derjaguin, "Electrokinetic phenomena," *Surface and Colloid Science,* vol. 7, 1974.

[129] A. V. Delgado, F. González-Caballero, R. J. Hunter, L. K. Koopal, and J. Lyklema, "Measurement and interpretation of electrokinetic phenomena," *Journal of Colloid and Interface Science,* vol. 309, pp. 194-224, 2007.

[130] M. Smoluchowski, "Contribution to the theory of electro-osmosis and related phenomena," *Bulletin International de l'Academie des Sciences de Cracovie,* vol. 184, 1903.

[131] V. E. Shubin, R. J. Hunter, and R. W. O'Brien, "Electroacoustic and dielectric study of surface conduction," *Journal of Colloid and Interface Science,* vol. 159, pp. 174-183, 1993.

[132] H. Morgan, A. G. Izquierdo, D. Bakewell, N. G. Green, and A. Ramos, "The dielectrophoretic and travelling wave forces generated by interdigitated electrode arrays: analytical solution using Fourier series," *Journal of Physics D: Applied Physics,* vol. 34, pp. 1553-1561, 2001.

[133] C. T. O'Konski, "Electric properties of macromolecules. V. Theory of ionic polarization in polyelectrolytes," *The Journal of Physical Chemistry,* vol. 64, pp. 605-619, 1960.

[134] T. M. Squires, "Induced-charge electrokinetics: fundamental challenges and opportunities," *Lab on a Chip,* vol. 9, pp. 2477-2483, 2009.

[135] A. Ashkin, J. M. Dziedzic, J. E. Bjorkholm, S. Chu, "Observation of a single-beam gradient force optical trap for dielectric particles," *Optics Letters*, vol. 11, pp. 288–290, 1986.

[136] J. D. Gelorme, R. J. Cox, and S. A. R. Gutierrez, "Photoresist composition and printed circuit boards and packages made therewith," 1989.

[137] J. M. Shaw, J. D. Gelorme, N. C. LaBianca, W. E. Conley, and S. J. Holmes, "Negative photoresists for optical lithography," *IBM Journal of Research and Development,* vol. 41, pp. 81-94, 1997.

[138] H. Lorenz, M. Despont, N. Fahrni, N. LaBianca, P. Renaud, and P. Vettiger, "SU-8: a low-cost negative resist for MEMS," *Journal of Micromechanics and Microengineering,* vol. 7, pp. 121-124, 1997.

[139] R. Yang and W. Wang, "A numerical and experimental study on gap compensation and wavelength selection in UV-lithography of ultra-high aspect ratio SU-8 microstructures," *Sensors and Actuators B: Chemical,* vol. 110, pp. 279-288, 2005.

[140] A. Del Campo and C. Greiner, "SU-8: a photoresist for high-aspect-ratio and 3D submicron lithography," *Journal of Micromechanics and Microengineering,* vol. 17, pp. R81-R95, 2007.

[141] T. Sikanen, S. Tuomikoski, R. A. Ketola, R. Kostiainen, S. Franssila, and T. Kotiaho, "Characterization of SU-8 for electrokinetic microfluidic applications," *Lab on a Chip,* vol. 5, pp. 888-896, 2005.

[142] J. C. Ribeiro, G. Minas, P. Turmezei, R. F. Wolffenbuttel, and J. H. Correia, "A SU-8 fluidic microsystem for biological fluids analysis," *Sensors and Actuators A: Physical,* vol. 123-124, pp. 77-81, 2005.

[143] S. L. Tao, K. Popat, and T. A. Desai, "Off-wafer fabrication and surface modification of asymmetric 3D SU-8 microparticles," *Nature Protocols,* vol. 1, pp. 3153-3158, 2007.

[144] G. Cavalli, S. Banu, R. T. Ranasinghe, G. R. Broder, H. F. Martins, C. Neylon, H. Morgan, M. Bradley, and P. L. Roach, "Multistep synthesis on SU-8: combining microfabrication and solid-phase chemistry on a single material," *Journal of Combinatorial Chemistry,* vol. 9, pp. 462-472, 2007.

[145] G. R. Broder, R. T. Ranasinghe, J. K. She, S. Banu, S. W. Birtwell, G. Cavalli, G. S. Galitonov, D. Holmes, H. F. P. Martins, K. F. MacDonald, C. Neylon, N. Zheludev, P. L. Roach, and H. Morgan, "Diffractive micro bar codes for encoding of biomolecules in multiplexed assays," *Analytical Chemistry,* vol. 80, pp. 1902-1909, 2008.

[146] G. Kotzar, M. Freas, P. Abel, A. Fleischman, S. Roy, C. Zorman, J. M. Moran, and J. Melzak, "Evaluation of MEMS materials of construction for implantable medical devices," *Biomaterials,* vol. 23, pp. 2737-2750, 2002.

[147] G. Voskerician, M. S. Shive, R. S. Shawgo, H. v. Recum, J. M. Anderson, M. J. Cima, and R. Langer, "Biocompatibility and biofouling of MEMS drug delivery devices," *Biomaterials,* vol. 24, pp. 1959-1967, 2003.

[148] M. Evans, C. Sewter, and E. Hill, "An encoded particle array tool for multiplex bioassays," *Assay and Drug Development Technologies,* vol. 1, pp. 199-207, 2003.

[149] F. Walther, P. Davydovskaya, S. Zurcher, M. Kaiser, H. Herberg, A. M. Gigler, and R. W. Stark, "Stability of the hydrophilic behavior of oxygen plasma activated SU-8," *Journal of Micromechanics and Microengineering,* vol. 17, pp. 524-531, 2007.

[150] F. Walther, W. M. Heckl, and R. W. Stark, "Evaluation of nanoscale roughness measurements on a plasma treated SU-8 polymer surface by atomic force microscopy," *Applied Surface Science,* vol. 254, pp. 7290-7295, 2008.

[151] M. Joshi, N. Kale, R. Lal, V. Ramgopal Rao, and S. Mukherji, "A novel dry method for surface modification of SU-8 for immobilization of biomolecules in Bio-MEMS," *Biosensors and Bioelectronics,* vol. 22, pp. 2429-2435, 2007.

[152] M. Joshi, R. Pinto, V. R. Rao, and S. Mukherji, "Silanization and antibody immobilization on SU-8," *Applied Surface Science,* vol. 253, pp. 3127-3132, 2007.

[153] A. Deepu, V. Sai, and S. Mukherji, "Simple surface modification techniques for immobilization of biomolecules on SU-8," *Journal of Materials Science: Materials in Medicine,* vol. 20, pp. 25-28, 2009.

[154] M. Nordstrom, R. Marie, M. Calleja, and A. Boisen, "Rendering SU-8 hydrophilic to facilitate use in micro channel fabrication," *Journal of Micromechanics and Microengineering,* vol. 14, pp. 1614-1617, 2004.

[155] R. Marie, S. Schmid, A. Johansson, L. Ejsing, M. Nordström, D. Häfliger, C. B. V. Christensen, A. Boisen, and M. Dufva, "Immobilisation of DNA to polymerised SU-8 photoresist," *Biosensors and Bioelectronics,* vol. 21, pp. 1327-1332, 2006.

[156] S. L. Tao, K. C. Popat, J. J. Norman, and T. A. Desai, "Surface modification of SU-8 for enhanced biofunctionality and nonfouling properties," *Langmuir,* vol. 24, pp. 2631 - 2636, 2008.

[157] W. Dai and W. Wang, "Selective metallization of cured SU-8 microstructures using electroless plating method," *Sensors and Actuators A: Physical,* vol. 135, pp. 300-307, 2007.

[158] C.-H. Yeh, C.-Y. Hung, T. Chang, H.-P. Lin, and Y.-C. Lin, "An immunoassay using antibody-gold nanoparticle conjugate, silver enhancement and flatbed scanner," *Microfluidics and Nanofluidics,* vol. 6, pp. 85-91, 2009.

[159] M. Agarwal, R. A. Gunasekaran, P. Coane, and K. Varahramyan, "Scum-free patterning of SU-8 resist for electroforming applications," *Journal of Micromechanics and Microengineering,* vol. 15, pp. 130-135, 2005.

[160] V. K. Sarin, S. B. H. Kent, J. P. Tam, and R. B. Merrifield, "Quantitative monitoring of solid-phase peptide synthesis by the ninhydrin reaction," *Analytical Biochemistry,* vol. 117, pp. 147-157, 1981.

[161] T. Sakamoto, H. Nakamura, H. Uedaira, and A. Wada, "High-frequency dielectric relaxation of water bound to hydrophilic silica gels," *The Journal of Physical Chemistry,* vol. 93, pp. 357-366, 1989.

[162] D. J. Bergman and Y. Imry, "Critical behavior of the complex dielectric constant near the percolation threshold of a heterogeneous material," *Physical Review Letters,* vol. 39, pp. 1222-1225, 1977.

[163] V. Myroshnychenko and C. Brosseau, "Finite-element modeling method for the prediction of the complex effective permittivity of two-phase random statistically isotropic heterostructures," *Journal of Applied Physics,* vol. 97, p. 044101, 2005.

[164] V. Myroshnychenko and C. Brosseau, "Effective complex permittivity of two-phase random composite media: a test of the two exponent phenomenological percolation equation," *Journal of Applied Physics,* vol. 103, p. 084112, 2008.

[165] C. Chiteme and D. S. McLachlan, "AC and DC conductivity, magnetoresistance, and scaling in cellular percolation systems," *Physical Review B,* vol. 67, p. 024206, 2003.

[166] M. E. Achour, C. Brosseau, and F. Carmona, "Dielectric relaxation in carbon black-epoxy composite materials," *Journal of Applied Physics,* vol. 103, pp. 094103-094110, 2008.

[167] T. Bourdi, J. E. Rhazi, F. Boone, and G. Ballivy, "Application of Jonscher model for the characterization of the dielectric permittivity of concrete," *Journal of Physics D: Applied Physics,* vol. 41, p. 205410, 2008.

[168] A. K. Jonscher, "A new understanding of the dielectric relaxation of solids," *Journal of Materials Science,* vol. 16, pp. 2037-2060, 1981.

[169] A. K. Jonscher, "A new model of dielectric loss in polymers," *Colloid and Polymer Science,* vol. 253, pp. 231-250, 1975.

[170] A. K. Jonscher, "Dielectric relaxation in solids," *Journal of Physics D: Applied Physics,* vol. 32, pp. R57-R70, 1999.

[171] B. De'Neve and M. E. R. Shanahan, "Water absorption by an epoxy resin and its effect on the mechanical properties and infra-red spectra," *Polymer,* vol. 34, pp. 5099–5105, 1993.

[172] J. R. Henry, "Electroless (autocatalytic) plating," *Metal Finishing,* vol. 99, pp. 424-435, 2001.

[173] W. Goldie, *Metallic coating of plastics*: Electrochemical Publications Ltd., 1968.

[174] J.-H. Lee, Y. Lee, and J.-D. Nam, "Tunable surface metal morphologies and electrical properties of monodispersed polystyrene beads coated with metal multilayers via electroless deposition," *Intermetallics,* vol. 17, pp. 365-369, 2009.

[175] A. Brenner and G. E. Riddell, "Temperature coefficients for proving rings," *Journal of Research of the National Bureau of Standards,* vol. 37, p. 31, 1946.

[176] Y. Okinaka, *Gold plating technology* vol. 82, 1973.

[177] T. Osaka, Y. Okinaka, J. Sasano, and M. Kato, "Development of new electrolytic and electroless gold plating processes for electronics applications," *Science and Technology of Advanced Materials,* vol. 7, pp. 425-437, 2006.

[178] P. Lam, K. Kumar, G. E. Wnek, and T. M. Przybycien, "Electroless gold llating of 316 L stainless steel beads," *Journal of The Electrochemical Society,* vol. 146, pp. 2517-2521, 1999.

[179] J. Lim, A. Eggeman, F. Lanni, R. D. Tilton, and S. A. Majetich, "Synthesis and single-particle optical Detection of low-polydispersity plasmonic-superparamagnetic nanoparticles," *Advanced Materials,* vol. 20, pp. 1721-1726, 2008.

[180] D. G. Duff, A. Baiker, and P. P. Edwards, "A new hydrosol of gold clusters," *Journal of the Chemical Society: Chemical Communications,* vol. 9, pp. 96-98, 1993.

[181] Y. K. Ren, D. Morganti, H. Y. Jiang, A. Ramos, and H. Morgan, "Electrorotation of metallic microspheres," *Langmuir,* vol. 27, pp. 2128-2131, 2011.

[182] M. Z. Bazant, M. S. Kilic, B. D. Storey, and A. Ajdari, "Towards an understanding of induced-charge electrokinetics at large applied voltages in concentrated solutions," *Advances in Colloid and Interface Science,* vol. 152, pp. 48-88, 2009.

[183] R. J. Messinger and T. M. Squires, "Suppression of electro-osmotic flow by surface roughness," *Physical Review Letters,* vol. 105, p. 144503, 2010.

[184] K. Mukhopadhyay, S. Phadtare, V. P. Vinod, A. Kumar, M. Rao, R. V. Chaudhari, and M. Sastry, "Gold nanoparticles assembled on amine-functionalized Na−Y zeolite: A biocompatible surface for enzyme immobilization," *Langmuir,* vol. 19, pp. 3858-3863, 2003.

[185] A. J. Pascall and T. M. Squires, "Induced charge electro-osmosis over controllably contaminated electrodes," *Physical Review Letters,* vol. 104, p. 88301, 2010.

[186] D. M. Taylor, H. Morgan, and C. D'Silva, "Characterization of chemisorbed monolayers by surface potential measurements," *Journal of Physics D: Applied Physics,* vol. 24, pp. 1443-1450, 1991.